Karlsruher Institut für Technologie

The Early Universe as a Window to Particle Physics

Zur Erlangung des akademischen Grades eines

DOKTORS DER NATURWISSENSCHAFTEN (DR. RER. NAT.)

von der KIT-Fakultät für Physik
des Karlsruher Instituts für Technologie (KIT)

angenommene

DISSERTATION

von

M.Sc. Johann Plotnikov

aus Prokopjewsk (Russland)

Referentin:	Prof. Dr. Milada Margarete Mühlleitner (KIT, Karlsruhe)
Korreferent:	Prof. Dr. Rui Santos (ISEL & U. LISBOA, Lisbon)

Tag der mündlichen Prüfung: 05. Juni 2026

This document is licensed under a Creative Commons Attribution-ShareAlike 4.0 International License (CC BY-SA 4.0):

https://creativecommons.org/licenses/by-sa/4.0/deed.en

Disclaimer

Artificial Intelligence (AI) tools were employed during the making of this thesis to support the grammar and style of the text. ChatGPT[1] was used throughout the thesis to assist with spelling and grammar, as well as to paraphrase select sentences for improved clarity and conciseness. All suggested changes were carefully reviewed before incorporation.

Furthermore, ChatGPT and Claude[2] were utilized in Mathematica code generation to aid in plotting results and fixing occurring bugs in C++. All proposed changes were checked and tested to ensure factual correctness. No generative AI tools were used to derive or evaluate any of the results presented in this thesis.

[1] OpenAi's conversational AI model, `https://chatgpt.com/` (Access Date: 2026-04-27)
[2] Anthropic's constitutional AI model, `https://claude.ai/new` (Access Date: 2026-04-27)

Eidesstattliche Versicherung gemäß § 13 Absatz 2 Ziffer 3 der Promotionsordnung des Karlsruher Instituts für Technologie (KIT) für die KIT-Fakultät für Physik:

1. Bei der eingereichten Dissertation zu dem Thema

   The Early Universe as Window to Particle Physics

   handelt es sich um meine eigenständig erbrachte Leistung.

2. Ich habe nur die angegebenen Quellen und Hilfsmittel benutzt und mich keiner unzulässigen Hilfe Dritter bedient. Insbesondere habe ich wörtlich oder sinngemäß aus anderen Werken übernommene Inhalte als solche kenntlich gemacht.

3. Die Arbeit oder Teile davon habe ich bislang nicht an einer Hochschule des In- oder Auslands als Bestandteil einer Prüfungs- oder Qualifikationsleistung vorgelegt.

4. Die Richtigkeit der vorstehenden Erklärungen bestätige ich.

5. Die Bedeutung der eidesstattlichen Versicherung und die strafrechtlichen Folgen einer unrichtigen oder unvollständigen eidesstattlichen Versicherung sind mir bekannt.

Ich versichere an Eides statt, dass ich nach bestem Wissen die reine Wahrheit erklärt und nichts verschwiegen habe.

Karlsruhe, den 28. April 2026

. . . . . .

(Full name)

One step at a time.

Abstract

Understanding the nature of Dark Matter (DM) and the origin of the matter anti-matter asymmetry remain among the most challenging tasks in modern particle physics and cosmology. In this thesis we investigate theoretical frameworks that address both of these issues with an emphasis on production mechanisms that can be tested through current and upcoming experimental probes.

In the first part of this thesis we introduce a new tool that is able to compute the DM relic abundance for any model that provides a DM candidate stabilized by a $\mathbb{Z}_2$-symmetry via the freeze-out mechanism. Additionally, the code is able to perform efficient parameter scans on the given model to find parameter regions that generate the observed DM abundance. We give detailed descriptions of the algorithms and techniques used throughout the code as well as provide examples of how to use it.

In the second part of this thesis we finished an ongoing project, where we investigated the interplay between two DM generation mechanism, freeze-in and freeze-out, in the model CP in the Dark. Under certain circumstances, this model contains two DM candidates, both of which generate their own relic density through the aforementioned mechanisms. We demonstrate that via the interplay between the two, we can easily generate the observed relic density while also retaining the possibility of measurable signals in upcoming collider and direct detection searches.

The third, deals with the problem of the observed Baryon Asymmetry of the Universe (BAU). Here, we investigate the properties of the transport equations which are used to compute the BAU via the mechanism of Electroweak Baryogenesis (EWBG). More specifically, we check the convergence region of the moment expansion of the transport equations as well as its dependence on the choice of the truncation scheme. Additionally, we perform a phenomenological investigation of the Complex 2 Higgs-Doublet Model (C2HDM) with respect to the BAU. Lastly, we discuss the validity of the obtained BAU in the parameter space allowed by the current experimental and theoretical constraints.

Zusammenfassung

Das Verständnis der Natur der Dunklen Materie (DM) und des Ursprungs der Materie Antimaterie-Asymmetrie gehört zu den größten Herausforderungen der modernen Teilchenphysik und Kosmologie. In dieser Arbeit untersuchen wir Theorien, die beide Probleme adressieren, mit besonderem Fokus auf Produktionsmechanismen, die durch aktuelle und zukünftige Experimente überprüfbar sind.

Im ersten Teil präsentieren wir ein neues Programm, das in der Lage ist, die Reliktdichte der Dunklen Materie für jedes Modell, das einen $\mathbb{Z}_2$-Symmetrie stabilisierten DM-Kandidaten bereitstellt, mit dem freeze-out Mechanismus zu berechnen. Darüber hinaus ist der Code in der Lage, effiziente Parameterscans für das gegebene Modell durchzuführen, um Parameterbereiche zu identifizieren, die die beobachtete DM-Dichte erzeugen. Wir geben detaillierte Beschreibungen der im Programm verwendeten Algorithmen und Techniken sowie Beispiele für dessen Anwendung.

Im zweiten Teil dieser Arbeit haben wir ein bestehendes Projekt vollendent. In diesem untersuchten wir das Zusammenspiel zweier Mechanismen zur Erzeugung Dunkler Materie, Freeze-in und Freeze-out, im Modell „CP in the Dark“. Unter bestimmten Bedingungen enthält dieses Modell zwei DM-Kandidaten, die jeweils ihre eigene Reliktdichte über die genannten Mechanismen erzeugen. Wir zeigen, dass durch ihr Zusammenspiel die beobachtete Reliktdichte leicht reproduziert werden kann. Gleichzeitig besteht die Möglichkeit, messbare Signale an zukünftigen Teilchenbeschleuniger-Experimenten und Experimenten zum direkten Nachweis von Dunkler Materie zu erhalten.

Der dritte und letzte Teil befasst sich mit dem Problem der beobachteten Baryonenasymmetrie des Universums (BAU). Hier untersuchen wir die Eigenschaften der Transportgleichungen, die zur Berechnung der BAU über den Mechanismus der elektroschwachen Baryogenese (EWBG) verwendet werden. Insbesondere prüfen wir den Konvergenzbereich der Momentenentwicklung der Transportgleichungen sowie deren Abhängigkeit von der Wahl der Abbruchbedingung. Darüber hinaus führen wir eine phänomenologische Untersuchung des komplexen 2-Higgs-Dublett-Modells (C2HDM) im Hinblick auf die BAU durch. Abschließend diskutieren wir die Gültigkeit der erhaltenen BAU im Parameterraum, der durch aktuelle experimentelle und theoretische Einschränkungen erlaubt ist.

List of Abbreviations

BAU	Baryon Asymmetry of the Universe	**FLRW**	Friedmann-Lemaître-Robertson-Walker
BBN	Big Bang Nucleosynthesis	**FTFT**	Finite Temperature Field Theory
BP	Benchmark Point	**HTL**	Hard Thermal Loop
BSM	Beyond Standard Model	**KMS**	Kubo-Martin-Schwinger
C2HDM	Complex 2 Higgs-Doublet Model	**MB**	Maxwell-Boltzmann
CMB	Cosmic Microwave Background	**N2HDM**	Next-to-2-Higgs-Doublet Model
CxSM	Complex singlet extension of the Standard Model	**QCD**	Quantum Chromodynamics
		QFT	Quantum Field Theory
DD	Direct Detection	**SM**	Standard Model
DDP	Dark Doublet Phase	**SUSY**	Supersymmetry
DM	Dark Matter	**TAC**	Thermally Averaged Cross section
DS	Dark Sector		
EOM	Equations Of Motion	**TRSM**	Two-Real-Singlet Model
EW	Electroweak	**VEV**	Vacuum Expectation Value
EWBG	Electroweak Baryogenesis	**WIMP**	Weaky-Interacting-Massive-Particle
EWPT	Electroweak Phase Transition		
FIMP	Feebly-Interacting-Massive-Particle	**ΛCDM**	Λ Cold Dark Matter

Contents

CHAPTER 1

Introduction

Two theoretical frameworks underpin our current understanding of nature across vastly different scales. On microscopic distances, the Standard Model (SM) of particle physics provides a precise and experimentally validated description of the constituents of everyday matter and its interactions, as confirmed by decades of collider and precision measurements [1, 2]. On cosmological scales, the Λ Cold Dark Matter model (ΛCDM) successfully captures the large-scale structure and evolution of the universe, relying on a small set of parameters to explain observations ranging from the Cosmic Microwave Background (CMB) to the distribution of galaxies [3, 4].

Despite their individual successes, a tension emerges when these two models are considered together. The cosmological framework requires the existence of components such as Dark Matter (DM) and a generated primordial matter anti-matter asymmetry. However, neither of these ingredients can be accommodated within the SM. This mismatch highlights a fundamental incompleteness in our description of nature and provides a compelling motivation to search for new physics that consistently connects the microscopic laws of particle interactions with the macroscopic evolution of the universe. A promising approach to tackle this issue is to extend the current SM via additional particles capable of connecting these two regimes. In this context, such extensions not only provide viable candidates for DM, but can also introduce new sources of CP-violation and out-of-equilibrium dynamics required to generate the Baryon Asymmetry of the Universe (BAU) offering a unified framework to address both shortcomings.

One of the possible particle candidates to account for the DM content of the universe, are Weakly-Interacting-Massive Particle (WIMP). For couplings to the SM at the weak scale, such particles can naturally reproduce the observed relic abundance of DM in the universe, which is measured to be [4]

$$\Omega_{\mathcal{X}} h^2 = 0.120 \pm 0.001 \, . \tag{1.1}$$

However, the improving sensitivity of direct detection experiments [5,6] has led to increasingly stringent constraints, causing the viable parameter space of models containing WIMPs to shrink. This has led to an increase of complexity in current DM models, which, instead of providing a single candidate, contain an entire Dark Sector (DS) of particles. Although this solution manages to account for the null results observed by direct detection experiments, the

introduction of additional particles often complicates the generation of the observed DM relic abundance. To address this challenge, we develop a tool within this thesis that systematically explores the parameter space and identifies regions consistent with the observed dark matter relic abundance for a given model. The tool can be applied either to predefined models provided with the code or to user-defined DM models featuring a single candidate stabilized by a $\mathbb{Z}_2$-symmetry. It computes the corresponding DM relic abundance via thermal freeze-out and offers a set of algorithms for systematic parameter space searches.

Instead of increasing the complexity of our models, a second way to circumvent the experimental constraints is by considering Feebly-Interacting-Massive-Particles (FIMPs). In this approach, the DM candidate couples very weakly to the SM, such that it remain undetectable by current and near-future experiments. The DM relic abundance in such models is produced via the mechanism of freeze-in in the early universe. Although models that contain a FIMP work very well at generating the observed DM relic abundance they are very difficult to probe in experiments due to their small interaction with the SM. As a result, establishing their existence with current experimental techniques is highly challenging. In the second part of this thesis we finished a project that began prior to this theses, where we consider a model that contains two DM candidates, a FIMP and a WIMP. With this setup, the observed relic abundance can be easily generated by the FIMP component, while the WIMP sector can give rise to observable signals in upcoming experiments. Furthermore, depending on the measured signals, it may be possible to infer the fraction of the relic abundance contributed by the FIMP component.

We not turn to the problem of the observed BAU, which is characterized by the quantity [4]

$$\eta_{\text{obs}} = \frac{n_B - n_{\bar{B}}}{s} \simeq \frac{n_B}{s} \simeq (8.690 \pm 0.053) \cdot 10^{-11} \,. \tag{1.2}$$

To generate a matter anti-matter asymmetry from an initially symmetric state, a model has to fulfill the three Sakharov conditions [7]: Baryon-number violation, C and CP-violation, and departure from thermal equilibrium. A particularly promising approach to obtain the asymmetry is the mechanism called Electroweak Baryogenesis (EWBG). In this approach the Higgs field undergoes an electroweak phase transition in the early universe, during which its Vacuum Expectation Value (VEV) changes from a symmetric to a broken phase. If this transition is of first order, bubbles of the broken phase nucleate and expand throughout the Universe. Inside these bubbles, the Higgs field acquires its electroweak (true) VEV, while outside the bubbles the field remains in the symmetric (false) phase. As the plasma interacts with this expanding bubble, CP-violating processes create an asymmetry between matter and anti-matter which is subsequently absorbed by the expanding bubble. It was shown that the Higgs potential of the SM does not give rise to a first-order phase transition and is therefore not sufficient to explain the observed BAU [8, 9]. Therefore, additional scalar particles are necessary to obtain a strong first-order phase transition within the framework of EWBG. Given such models, we must solve the transport equations of the plasma to obtain the generated asymmetry and hence the BAU. To construct these equations we use the WKB method developed in Refs. [10–12], where the most recent developments include higher-order moment expansions [13]. In this work, we adopt this approach and investigate the convergence of the BAU as we increase the number of considered moments across different regions of parameter space. Doing so, our investigation shows that the computation of the BAU does not lead to stable results for small wall velocities or small wall thicknesses. We proceed to do a phenomenological investigation of the Complex 2 Higgs-Doublet Model (C2HDM) with respect to the BAU and show clear correlations between specific model parameters and the value of the BAU.

This thesis is structured as follows. We begin by providing the necessary prerequisites in Chapter 2 to enable the reader to follow the rest of the thesis. Here, we give a brief intro-

duction into the SM in Sec. 2.1, followed by an rough overview of the history of the universe in Sec. 2.2. We use Sec. 2.3 to introduce the Boltzmann equation, which is the central equation to describe the dynamics of the plasma that is present in the early universe. Lastly, we provide a rough overview on the topic of finite temperature field theory in Sec. 2.4.

With the necessary tools at hand, we continue with the three projects contained in this thesis. In Part I, we describe our developed DM tool `RelExt`, which is able to compute the relic density via freeze-out for an arbitrary DM model, where the DM candidate is stabilized by a $\mathbb{Z}_2$ symmetry, as well as to search the parameter space of the model for parameter regions which generate the observed DM abundance. First, we give an introduction into the WIMP paradigm in Chapter 3, where we derive the necessary Boltzmann equation to describe DM freeze-out. In Chapter 4, we provide an in depth description of our code `RelExt`, where we describe the overall structure of the tool as well as the algorithms used throughout the code. We give a few examples on how the code can be used to search parameter regions in Chapter 5 and give a conclusion of this part in Chapter 6.

In Part II of this thesis we consider the model CP in the Dark, which in a certain limit provides two DM candidates, one FIMP and one WIMP. We analyze the effect of having these two DM candidates with respect to experimental observables. In Chapter 7 we give a small introduction into the DM generation mechanism called freeze-in. Next, we derive the necessary Boltzmann equations in Chapter 8 to describe the generation of the DM abundance including both DM candidates. Lastly, we give a conclusion of this project in Chapter 9.

Part III contains the third project of this thesis, in which we compute the BAU using the WKB method and study its convergence behavior in the moment expansion of the transport equations as well as investigate the generated BAU within the C2HDM. To do so, we first provide an introduction into the mechanism of EWBG in Chapter 10. After that, in Chapter 11, we derive the transport equations as well as provide the formula to compute the BAU. In Chapter 12 we provide an updated value on one of the collision rates used in the transport equations, namely the top Yukawa rate. Lastly, we provide our numerical analysis in Chapter 13 and conclude this part in Chapter 14.

In Chapter 15 we give an overall summary and outlook of the projects contained in this thesis.

CHAPTER 2

Prerequisites

2.1. The Standard Model

The Standard Model of Particle Physics (SM) [14–16] is seen as one of the major achievements in theoretical physics of the 20th century. It manages to combine three of the four known fundamental forces of nature into one theory, i.e. the electromagnetic force, the weak force, and the strong force. So far, in the regime of particle interactions, there is no theory which is in better agreement with the experiments than the SM. In this section we will give a brief overview of the theory behind the SM and refer the reader to Ref. [17] for more details.

The SM is based on Quantum Field Theory (QFT) and consists of a renormalizable Lagrangian which is invariant under the local gauge group

$$SU(3)_c \times SU(2)_L \times U(1)_Y \,. \tag{2.1}$$

Here, $SU(3)_c$ is the gauge group of Quantum Chromodynamics (QCD) and represents the strong force. Since the Lagrangian is invariant under this group there exists a corresponding conserved charge, the color charge. This charge is mediated by its associated fields, which are called gluons denoted by G^a_μ ($a = \{1, .., 8\}$). They act as mediators between color triplet states, the quark fields $\{u, d, c, s, t, b\}$. The $SU(2)_L$ gauge group represents the weak force with the conserved charge which is the weak isospin I^3_W and which is mediated by the gauge fields W^i_μ ($i = \{1, 2, 3\}$). Finally, we have the $U(1)_Y$ gauge group, which conserves the hypercharge Y and is mediated by the gauge field B_μ. Together, the $SU(2)_L \times U(1)_Y$ builds up the Electroweak (EW) force which couples to left handed doublet fields and right handed singlet fields.

The SM Lagrangian can be split up into several distinct sectors which describe different properties of the SM particles [18],

$$\mathrm{L_{SM}} = \mathrm{L_{gauge}} + \mathrm{L_{fermion}} + \mathrm{L_{Higgs}} + \mathrm{L_{Yukawa}} + \mathrm{L_{GF}} + \mathrm{L_{ghost}} \,. \tag{2.2}$$

The first term is responsible for the dynamics and propagation of the gauge fields and is given by

$$\mathrm{L_{gauge}} = -\frac{1}{4} G^a_{\mu\nu} G^{a\mu\nu} - \frac{1}{4} W^i_{\mu\nu} W^{i\mu\nu} - \frac{1}{4} B_{\mu\nu} B^{\mu\nu} \,, \tag{2.3}$$

where the field strength tensor $F^a_{\mu\nu}$ for the gauge field A^a_μ is defined by

$$F^a_{\mu\nu} = \partial_\mu A^a_\nu - \partial_\nu A^a_\mu + g f^{abc} A^b_\mu A^c_\nu. \tag{2.4}$$

Further, the group structure constants satisfy

$$\left[T^a, T^b\right] = i f^{abc} T^c\,, \tag{2.5}$$

with T^a being the generators of the considered gauge group and a, b, c are the corresponding group indices. The last term in Eq. (2.4) is responsible for the self-coupling of the gauge fields and has a significant effect on the underlying physics leading to confinement and asymptotic freedom of the couplings in the case of QCD [19, 20]. This term appears only for non-abelian gauge groups and is zero in the abelian case.

Next, we have the kinetic term of the fermions ψ which is also responsible for their coupling to the gauge bosons

$$\mathrm{L}_{\text{fermion}} = \sum_\psi i\overline{\psi}\gamma^\mu D_\mu \psi \equiv \sum_\psi i\overline{\psi} \not{D} \psi\,. \tag{2.6}$$

Here, the covariant derivative is given by

$$D_\mu = \partial_\mu - i g_s T^a G^a_\mu - i g_1 \tau^i W^i_\mu - i g_2 Y B_\mu\,, \tag{2.7}$$

where the coupling constants g_y ($y \in \{s, 1, 2\}$) represent the strength of the strong, weak and hypercharge force, respectively. The covariant derivative ensures that the Lagrangian remains invariant under local gauge transformations. Important to note here is that the generators of the corresponding gauge group, T^a, τ^i and Y, have different representations based on the quantum field they are acting on. For example, for a color neutral and electroweak charged fermion (left-handed leptons) we take the trivial representation for the QCD generators $T^a = 0$, the fundamental representation for the weak force $\tau^i = \sigma^i/2$, where σ^i are the Pauli matrices, and set Y such that the electric charge Q of the fermion is reproduced via the relation

$$Q = \tau^3 + Y\,. \tag{2.8}$$

The appropriate choice of the representation of the generators leads to the observed behavior between matter fields and gauge fields.

Looking at the kinetic terms in Eq. (2.3) and Eq. (2.6) we notice that they do not contain any bilinear terms which would correspond to a particle mass. This is due to the fact that a mass term would break local gauge invariance of the SM gauge groups. However, in reality we observe that some gauge bosons and fermions have masses. To resolve this issue, Brout, Englert and Higgs introduced a mechanism which gives rise to the masses in an elegant way. In the Higgs mechanism, an additional scalar complex $SU(2)_L$ doublet, the Higgs doublet Φ, is added to the SM via

$$\mathrm{L}_{\text{Higgs}} = (D_\mu \Phi)^\dagger (D^\mu \Phi) + \mu^2 \Phi^\dagger \Phi - \lambda \left(\Phi^\dagger \Phi\right)^2\,, \tag{2.9}$$

where $\mu > 0$ and $\lambda > 0$ are free parameters of the Higgs potential

$$V(\Phi) \equiv -\mu^2 \Phi^\dagger \Phi + \lambda \left(\Phi^\dagger \Phi\right)^2\,. \tag{2.10}$$

We want to find the minimum of this potential to determine the ground state of our theory. This is done by requiring that

$$\frac{\partial V(\Phi)}{\partial \Phi} \stackrel{!}{=} 0\,, \tag{2.11}$$

which leads to the expectation value of

$$\langle \Phi \rangle = \sqrt{\frac{\mu^2}{2\lambda}} \equiv \frac{v}{\sqrt{2}} . \tag{2.12}$$

The v is called the EW Vacuum Expectation Value (VEV) and defines the ground state of the Higgs potential. This ground state breaks the EW symmetry of the SM potential from a $SU(2)_L \times U(1)_Y$ symmetry to the electromagnetic $U(1)_{\text{em}}$ symmetry. We can expand the Higgs doublet around the VEV by writing

$$\Phi = \begin{pmatrix} G^+ \\ \dfrac{v + h + iG^0}{\sqrt{2}} \end{pmatrix} . \tag{2.13}$$

Here, G^+ and G^0 are the charged and neutral Goldstone bosons, respectively, which emerge from breaking the $SU(2)_L \times U(1)_Y$ symmetry down to the electromagnetic symmetry and h is the Higgs boson. Inserting Eq. (2.13) into the covariant derivative term of Eq. (2.9) will lead to the mixing of the fields W^i and B, which after diagonalization will give the physical mass eigenstates

$$\begin{aligned} W^\pm_\mu &= \frac{1}{\sqrt{2}} \left(W^1_\mu \mp i W^2_\mu \right) , \\ Z_\mu &= \cos\theta_W W^3_\mu - \sin\theta_W B_\mu , \\ A_\mu &= \sin\theta_W W^3_\mu + \cos\theta_W B_\mu . \end{aligned} \tag{2.14}$$

The Weinberg angle θ_W fulfills the relations

$$\cos\theta_W = \frac{g_1}{\sqrt{g_1^2 + g_2^2}} \quad \text{and} \quad \sin\theta_W = \frac{g_2}{\sqrt{g_1^2 + g_2^2}} , \tag{2.15}$$

and the masses of the $W^\pm$-boson, Z-boson and photon γ (A_μ) are given by

$$m_W = \frac{1}{2} g v \quad , \quad m_Z = \frac{m_W}{\cos\theta_W} \quad , \quad m_\gamma = 0 . \tag{2.16}$$

Further, we can use the gauge freedom of $SU(2)_L$ to absorb the Goldstone fields into the longitudinal degrees of freedom of the massive gauge bosons. This choice is called the unitary gauge.

The Higgs mechanism gives rise to the masses of the massive gauge bosons trough its coupling to the Higgs boson with a non-zero VEV in the ground state. The masses of the fermions can be obtained in a similar manner via the Yukawa potential

$$\mathrm{L}_{\text{Yukawa}} = -\overline{L}_L \hat{Y}_l \Phi l_r - \overline{Q}'_L \hat{Y}_d \Phi d'_r - \overline{Q}_L \hat{Y}_u \tilde{\Phi} u'_r + \text{h.c.} , \tag{2.17}$$

where $\tilde{\Phi} = i\sigma^2 \Phi^*$, $\hat{Y}_{l/d/u}$ are complex Yukawa coupling matrices and Q'_L (L_L) are the left handed quark (lepton) doublets. After EW symmetry breaking and mass diagonlization the Yukawa terms will lead to bilinear fermion terms which give rise to their masses.

It is known that the gauge term in Eq. (2.3) is not enough to consistently quantize the gauge fields as it will lead to undefined propagators. The underlying reason for this is the fact that we have a gauge freedom in our theory. To address this, we need to introduce the gauge fixing terms with gauge parameters ξ which are given by

$$\mathrm{L}_{\text{GF}} = -\frac{1}{2\xi_G} F_G^2 - \frac{1}{2\xi_A} F_A^2 - \frac{1}{2\xi_Z} F_Z^2 - \frac{1}{2\xi_W} F_- F_+ , \tag{2.18}$$

with

$$\begin{aligned} F_G^a &= \partial^\mu G_\mu^a \,, \\ F_A &= \partial^\mu A_\mu \,, \\ F_Z &= \partial^\mu Z_\mu - \xi_Z m_Z G^0 \,, \\ F_+ &= \partial^\mu W_\mu^+ - i\xi_W m_Z G^+ \,, \\ F_- &= \partial^\mu W_\mu^- + i\xi_W m_Z G^- \,. \end{aligned} \tag{2.19}$$

These terms additionally remove the bilinear terms between Goldstone bosons and the corresponding gauge bosons appearing in Eq. (2.9), however, they also break the gauge invariance of the Lagrangian.

When introducing gauge fixing terms into a non-abelian gauge theory one naturally obtains additional ghost fields $\overline{c}$ and c which have the following Lagrangian

$$\begin{aligned} \mathrm{L}_{\mathrm{ghost}} = &\sum_{i=1}^{4} \left[\overline{c}_+ \frac{\partial(\delta F_+)}{\partial \alpha^i} + \overline{c}_- \frac{\partial(\delta F_-)}{\partial \alpha^i} + \overline{c}_Z \frac{\partial(\delta F_Z)}{\partial \alpha^i} + \overline{c}_A \frac{\partial(\delta F_A)}{\partial \alpha^i} \right] c_i \\ &+ \sum_{a,b=1}^{8} \overline{c}_G^a \frac{\partial(\delta F_G^a)}{\partial \beta^b} c_{G,b} \,, \end{aligned} \tag{2.20}$$

where the variation δ is taken with respect to the gauge group parameters α^i of the EW group and β^b of the QCD group.

Even though the SM is a very successful theory, there are several experimental phenomena and theoretical questions which it cannot account for. Examples for such shortcomings are:

- Dark Matter and Dark Energy [4],
- Gravity,
- Baryon asymmetry of the universe [8],
- Strong CP problem [21, 22],
- Hierarchy problem [23, 24],
- Neutrino masses [25, 26].

In this thesis we will focus on the problem of DM and the BAU by considering extensions of the SM via additional particles.

2.2. The Early and Current Universe

The standard model of cosmology, also called the Λ Cold Dark Matter model (ΛCDM), is at the time of this thesis the best description of the current universe and its evolution starting from the big bang. The validity of the ΛCDM model is experimentally tested by the space telescopes WMAP [3] and Planck [4]. In this section, we review the main evolutionary stages of the universe within the framework of the ΛCDM model.

According to this framework the age of the universe is $13.801 \pm 0.024\,\mathrm{Gyr}$. To account for the homogeneous and isotropic universe that we observe today, the universe had first to go through an inflationary stage. During this time period, the universe expanded at an exponentially increasing rate, leading to casual connections on large scales and its flatness. One common explanation for this rapid growth of the universe is the so called slow-roll inflation generated

via an Inflaton field. Slow-roll inflation is driven by the energy and form of the field's potential, and its time evolution ultimately leads to the termination of the inflationary phase. At the end of inflation, the Inflaton field oscillates around the minimum of its potential. These oscillations correspond to Inflaton particles, which decay into SM particles and, in some scenarios, Dark Matter. This process fills the universe with a hot plasma and marks the reheating phase. For a detailed review on slow-roll inflation and additional inflation models, see Refs. [27, 28]. Following the reheating phase, the universe contains a thermal plasma characterized by a temperature known as the reheating temperature T_{reh}. The exact temperature has no clear upper bound and depends on the considered inflation model. However, a lower bound can be derived from constraints on the neutrino density and its effect on Big Bang Nucleosynthesis (BBN), yielding [29]

$$T_{\mathrm{reh}} \gtrsim 4\,\mathrm{MeV}\,. \tag{2.21}$$

At this stage, the universe is composed of matter, radiation, and vacuum energy. The densities of these components determine the expansion rate of the universe, characterized by the Hubble parameter H, defined in terms of the scale factor $a(t)$

$$H(t) = \frac{\dot{a}(t)}{a(t)}\,. \tag{2.22}$$

Its time evolution is governed by the Friedmann equation [30]

$$\frac{H(t)^2}{H_0^2} = \Omega_{\mathrm{r}} + \Omega_{\mathrm{m}} + \Omega_\Lambda + \Omega_k\,, \tag{2.23}$$

where

$$\Omega_k = -\frac{k^2}{a(t)^2 H_0^2} \quad \text{and} \quad \Omega_i = \frac{\rho_i}{3M_{\mathrm{pl}}^2 H_0^2} \quad (i \in \{r, m, \Lambda\})\,, \tag{2.24}$$

with the free curvature k, the Planck mass M_{pl} and the densities $\rho_{\mathrm{r/m/\Lambda}}$ of radiation, matter and vacuum energy, respectively. The present-day value of the Hubble rate, referred to as the Hubble constant H_0, is inferred from two distinct observational methods. In the first approach the Hubble constant is determined by fitting the parameters of the ΛCDM model to the power spectrum of the Cosmic Microwave Background (CMB). The result obtained by the Planck collaboration using this method gives a rate of [4]

$$H_0 = (67.4 \pm 0.5)\,\mathrm{km\,s^{-1}Mpc^{-1}}\,. \tag{2.25}$$

The second approach determines the Hubble constant directly from the redshift–distance relationship of stars and supernovae, resulting in [31]

$$H_0 = (73.5 \pm 1.1)\,\mathrm{km\,s^{-1}Mpc^{-1}}\,. \tag{2.26}$$

The discrepancy between the two results is known as the Hubble tension and is an unresolved problem to this date. For a review of the Hubble tension and proposed solutions, we refer the reader to Ref. [32].

With the expansion of the universe, the temperature of the thermal bath decreases. This decrease in temperature leads to several out-of-equilibrium phenomena and phase transitions in the further evolution of the universe. One such transition is the Electroweak Phase Transition (EWPT) which could happen at the end of inflation and reheating, at a temperature of $T_{\mathrm{EWPT}} \simeq 100\,\mathrm{GeV}$.[3] During the EWPT the universe transitions from a vacuum state in which the electroweak symmetry is exact to one in which it is broken. As stated in the

[3] Should the EWPT take place at this temperature and be responsible for the BAU, it would establish a lower bound on the reheating temperature, $T_{\mathrm{reh}} > T_{\mathrm{EWPT}}$.

previous section, this gives rise to the masses of the fermions and gauge bosons. Additionally, it can also be a key ingredient in a dynamically generated baryon asymmetry used to explain the measured value in Eq. (1.2), which will be a central topic of this thesis. This can happen if the EWPT is of strong first-order, i.e. if the baryon wash-out condition [33]

$$\xi(T_c) = \frac{v(T_c)}{T_c} \gtrsim 1\,, \tag{2.27}$$

is fulfilled. Here, v is the VEV of the broken vacuum at the critical temperature T_c, which is the temperature at which the unbroken and broken vacuum are degenerate. As the universe transitions from the unbroken to the broken electroweak vacuum, bubbles begin to form, with the broken vacuum inside them. These bubbles expand with a wall velocity v_w, which can be determined by solving the scalar field equations of motion and the Boltzmann equations for the plasma [34, 35]. As these bubbles grow larger they fill the universe until the whole plasma is in the broken phase.

After the particles of the SM have acquired their masses, they are in thermal equilibrium. Since the SM particles have different masses, they follow different equilibrium distributions. This results in the fact that the density of the heavier particles is suppressed compared to that of the lighter ones. This effect can be tracked by examining the effective degrees of freedom $g_{\text{eff}}(T)$ in the plasma as a function of temperature via [36]

$$g_{\text{eff}}(T) = \frac{30}{\pi^2}\frac{\rho_{\text{tot}}}{T^4}\,. \tag{2.28}$$

Here, ρ_{tot} is the total energy density of the particles of the bath given by

$$\rho_{\text{tot}} = \sum_i g_i \int \frac{\mathrm{d}^3 p}{(2\pi)^3} E_i f_i(p)\,, \tag{2.29}$$

where

$$f_i = \frac{1}{e^{(E_i-\mu_i)/T} \pm 1}\,, \tag{2.30}$$

is the Bose-Einstein (upper sign) or Fermi-Dirac (lower sign) distribution. In addition, g_i are the internal degrees of freedom, $E_i = \sqrt{\mathbf{p}^2 - m_i^2}$ the energy, and μ_i the chemical potential of the considered particle i. For the SM, the maximum number of effective degrees of freedom is given by $g_{\text{eff}}(T > 175\,\text{GeV}) = 106.75$. As the temperature of the thermal bath decreases, the heavy SM particles will stop contributing to the effective degrees of freedom and therefore lowering it. For the evaluation of the effective degrees of freedom at the present temperature Eq. (2.28) cannot be used, since it assumes that all particle species remain in thermal equilibrium. Neutrinos, however, decouple from the thermal bath at a temperature T_{dec}, defined implicitly by the condition[4]

$$\Gamma(T_{\text{dec}}) \stackrel{!}{=} H(T_{\text{dec}})\,. \tag{2.31}$$

Here, Γ is the interaction rate between neutrinos, photons, and electrons. As the Hubble rate gets larger than the interaction rate ($H \gg \Gamma$) the neutrinos *freeze-out* of the thermal equilibrium at a temperature of approximately $T_{\text{dec}} \simeq 1\,\text{MeV}$, after which their comoving number density remains constant. Taking this into account, the current value for the effective degrees of freedom is $g_{\text{eff}}(T_0) = 3.36$ [36].

The mechanism by which particles freeze-out of thermal equilibrium can also account for the present dark matter abundance given in Eq. (1.1). In this thesis, we focus on this and

[4] This provides only an approximate definition of the decoupling temperature T_{dec}. A more precise determination requires solving the corresponding Boltzmann equation.

another (see below) thermal mechanism as the origin of the DM abundance. In particular, we study models featuring electrically neutral Weakly Interacting Massive Particles (WIMPs), which reproduce the observed relic abundance through thermal production. Their masses typically range from $\sim 1\,\mathrm{GeV}$ up to a few TeV, and they interact with the SM via weak-scale interactions. Again, we can use the condition given in Eq. (2.31) to estimate the temperature at which the DM particles decouple from the thermal bath. This temperature is also referred to as the freeze-out temperature T_{fo} and is approximated via the DM mass $m_{\mathcal{X}}$ to be at[5]

$$T_{\mathrm{fo}} \approx \frac{m_{\mathcal{X}}}{25}\,. \tag{2.32}$$

As in the case of neutrinos, after decoupling, the DM particles obtain a nearly constant comoving number density as the universe expands and cools, leading to the observed DM relic abundance. In the freeze-out scenario we assume that the DM particles are in thermal equilibrium with the SM after reheating. If we relax this assumption and start with a negligible DM density, the DM particles can obtain their relic density through a process known as *freeze-in*. In this scenario the SM continuously produces DM particles until the condition in Eq. (2.31) is fulfilled and production stops at a freeze-in temperature T_{fi} of approximately

$$T_{\mathrm{fi}} \approx \frac{m_{\mathcal{X}}}{5}\,. \tag{2.33}$$

In this scenario, the coupling between the SM and DM particles must be sufficiently small to prevent the overproduction or thermalization of DM.

At temperatures of $T = \mathcal{O}(100\,\mathrm{MeV})$ the SM plasma goes through another phase transition, the QCD phase transition [38]. During this epoch, the quark–gluon plasma hadronizes, forming bound states such as mesons and baryons. As the universe continues to cool to temperatures of $T = \mathcal{O}(1\,\mathrm{MeV})$, these hadrons combine to form nuclei of light elements like ^{2}H, ^{3}He, ^{4}H and ^{7}Li, marking the phase of Big Bang Nucleosynthesis [39]. As the universe keeps cooling it reaches the recombination epoch at a temperature of $T = \mathcal{O}(1\,\mathrm{eV})$ at which the electrons and protons of the thermal bath combine to atoms [40]. This leaves the photons with no interaction partners, as all charged particles have formed to neutral ones. These photons build up the CMB radiation we observe today.

The CMB provides a crucial probe of the universe's thermal and expansion history [4]. As already mentioned above, from its precise measurement, both the present Hubble rate and the dark matter relic density can be inferred. Moreover, the CMB spectrum allows us to determine the current temperature of the universe as

$$T_0 = (2.7255 \pm 0.0006)\,\mathrm{K}\,. \tag{2.34}$$

The analysis of the CMB temperature anisotropies further reveals the composition of the universe, yielding a baryon density of $\Omega_b h^2 = 0.0224 \pm 0.0001$, the vacuum energy density $\Omega_\Lambda h^2 = 0.3107 \pm 0.0082$ and a negligible radiation density $\Omega_r h^2 = \mathcal{O}\left(10^{-5}\right)$. Finally, the spatial curvature is measured to be $\Omega_k = 0.001 \pm 0.002$, which is fully consistent with a flat universe, completing our picture of the universe's thermal and compositional evolution.

2.3. The Boltzmann Equation

In this thesis we aim to compute observables originating from the early plasma of the universe. A possible approach to this would be to simulate the plasma and study its evolution in temperature (and thus time). However, such simulations are computationally demanding

[5] Note that the freeze-out temperature places a lower bound on the DM mass of approximately $m_\chi \gtrsim 100\,\mathrm{MeV}$, arising from constraints imposed by BBN [37].

and become infeasible for sufficiently large systems. The approach we will adopt in this work is to assign a phase space distribution function $f \equiv f(p^\mu, x^\mu)$ to each particle species and to study their evolution during the expansion of the universe. The equation which governs this evolution is the Boltzmann equation, which is given by

$$\mathcal{L}[f] = \mathcal{C}[f]\,. \tag{2.35}$$

On the left-hand side of the equation we have the Liouville operator $\mathcal{L}$ which will be responsible for the dynamical evolution of the system. The right-hand side, the collision operator $\mathcal{C}$, describes the interaction between different particle species within the plasma and is therefore able to link different particle species to generate a system of Boltzmann equations.

We will first focus on the Liouville operator. In its general covariant, relativistic form acting on a distribution function, it is given by [41]

$$\mathcal{L}[f] = \left(p^\mu \frac{\partial}{\partial x^\mu} - \Gamma^\mu_{\ \nu\rho} p^\nu p^\rho \frac{\partial}{\partial p^\mu} + m F^\mu \frac{\partial}{\partial p^\mu} \right) f\,, \tag{2.36}$$

with the Christoffel symbols (affine connection)

$$\Gamma^\mu_{\ \nu\rho} = \frac{1}{2} g^{\mu\alpha} (\partial_\nu g_{\alpha\rho} + \partial_\rho g_{\alpha\nu} - \partial_\alpha g_{\nu\rho})\,, \tag{2.37}$$

the external four-force F^μ and the particle mass m. We want to describe a spacetime that is expanding, homogeneous, isotropic, and has no curvature.[6] We do this by choosing the appropriate metric, the Friedmann-Lemaître-Robertson-Walker (FLRW) metric with $k = 0$, which can be written as a diagonal matrix with the elements

$$g_{00} = 1 \ \text{ and } \ g_{ii} = -a(t)^2\,, \tag{2.38}$$

and coordinates $x^\mu = (t, x, y, z)$. From this the relevant non-zero Christoffel symbols from Eq. (2.37) are given by

$$\Gamma^0_{\ ij} = \dot{a}(t) a(t) \delta_{ij} = H(t) a(t)^2 \delta_{ij} \ \ , \ \ \Gamma^k_{\ 0j} = \frac{\dot{a}(t)}{a(t)} \delta^k_{\ j} = H(t) \delta^k_{\ j} \ \ , \ \ (i,j,k) \in \{1,2,3\}\,. \tag{2.39}$$

Insertion into Eq. (2.36) gives

$$\mathcal{L}[f] = \left[E\partial_t + \mathbf{p}\nabla_{\mathbf{x}} - H(t)(a(t)^2 \mathbf{p}^2 \partial_E + E\mathbf{p}\nabla_{\mathbf{p}}) + m(F^0 \partial_E + \mathbf{F}\nabla_{\mathbf{p}}) \right] f\,, \tag{2.40}$$

where $\nabla_{\mathbf{A}} \equiv (\partial_{A_1}, \partial_{A_2}, \partial_{A_2})^T$ is the gradient with respect to the components of a vector $\mathbf{A}$. The Liouville operator can be separated into three distinct contributions. The first describes the natural evolution of the distribution function in phase space, while the second, proportional to $H(t)$, modifies the evolution of the distribution function due to the expansion of the universe. The last term accounts for possible external forces such as those arising from external electric or magnetic fields.

We now move on to the collision operator which is defined as [42]

$$\begin{aligned}
\mathcal{C}[f_1] = -\frac{1}{2} \int & \mathrm{d}\Pi_2 \cdots \mathrm{d}\Pi_m \mathrm{d}\Pi_{m+1} \cdots \mathrm{d}\Pi_n (2\pi)^4 \delta^4 (p_1 + p_2 + \cdots + p_m - p_{m+1} - \cdots - p_n) \\
& \left[|\mathcal{M}|^2_{1+2+\cdots+m \to m+1+\cdots+n} f_1 f_2 \cdots f_m (1 \pm f_{m+1}) \cdots (1 \pm f_n) \right. \\
& \left. - |\mathcal{M}|^2_{m+1+\cdots+n \to 1+2+\cdots+m} f_{m+1} \cdots f_n (1 \pm f_1)(1 \pm f_2) \cdots (1 \pm f_m) \right] \\
\equiv -\frac{1}{2} \int & \mathrm{d}\Pi_{\{2..n\}} (2\pi)^4 \delta^4 \left(\sum_{i=2}^{m} p_i - \sum_{i=m+1}^{n} p_i \right) \\
& \left[|\mathcal{M}|^2_{\{1..m\} \to \{m+1..n\}} f_1 f_2 \cdots f_m (1 \pm f_{m+1}) \cdots (1 \pm f_n) \right. \\
& \left. - |\mathcal{M}|^2_{\{m+1..n\} \to \{1..m\}} f_{m+1} \cdots f_n (1 \pm f_1)(1 \pm f_2) \cdots (1 \pm f_m) \right]\,,
\end{aligned} \tag{2.41}$$

[6] We implicitly assume that these conditions hold throughout the evolution of the universe.

where f_i are the distribution functions of the particle species i, the $(+)$ applies to bosons and the $(-)$ to fermions. Further, the matrix elements squared $|\mathcal{M}|^2_{\{X\}\to\{Y\}}$ with incoming particles X and outgoing particles Y are summed over the spins and polarizations of all initial and final state particles, except for particle 1. Additionally, we define the phase space integral measure

$$\mathrm{d}\Pi_i = \frac{\mathrm{d}^3 p_i}{(2\pi)^3 2E_i}\,. \tag{2.42}$$

Looking at Eq. (2.41) we notice that the integration goes over the phase space of all particles included in the $X \to Y$ process, except for the momenta of the particle species of interest p_1. This is because we want to solve the Boltzmann equation with respect to this variable. The equation also contains the Dirac distribution δ, which ensures that energy and momentum are conserved. In addition, we have two terms that appear in the square brackets. One represents the forward direction of the scattering process and the other the backward direction. Depending on the particle type appearing in the final state, we have either a Fermi-suppression $(-)$ or a Bose-enhancement $(+)$. In this thesis we will only consider matrix elements which are non CP-violating and therefore are equivalent in both directions. This simplifies Eq. (2.41) to

$$\mathcal{C}[f_1] = -\frac{1}{2}\int \mathrm{d}\Pi_{\{2..n\}}(2\pi)^4\delta^4\left(\sum_{i=2}^{m} p_i - \sum_{i=m+1}^{n} p_i\right)|\mathcal{M}|^2_{\{2..m\}\to\{m+1..n\}}\mathcal{P}[f_1]\,, \tag{2.43}$$

with

$$\mathcal{P}[f_1] = f_1 f_2 \cdot\cdot f_m(1\pm f_{m+1})\cdot\cdot(1\pm f_n) - f_{m+1}\cdot\cdot f_n(1\pm f_1)(1\pm f_2)\cdot\cdot(1\pm f_m)\,. \tag{2.44}$$

Note, that when we insert the thermal equilibrium distribution given in Eq. (2.30) ($\mu_i = 0$) for all involved particle species we obtain

$$\mathcal{P}[f_1] = f_{\mathrm{eq},1} f_{\mathrm{eq},2}\cdot\cdot f_{\mathrm{eq,n}}\left(e^{(E_1-\mu_1+\cdot\cdot+E_m-\mu_m)/T} - e^{(E_{m+1}-\mu_{m+1}+\cdot\cdot+E_n-\mu_n)/T}\right) = 0\,, \tag{2.45}$$

where we used the identity

$$1\pm f_{\mathrm{eq}} = f_{\mathrm{eq}} e^{(E-\mu)/T}\,, \tag{2.46}$$

in the first step and energy conservation to obtain zero as well as the chemical equilibrium condition $\mu_1 + \cdot\cdot + \mu_m = \mu_{m+1} + \cdot\cdot + \mu_n$. Inserting the Collision operator and the Liouville operator back into Eq. (2.35) we obtain our desired form for the Boltzmann equation

$$\begin{aligned}\mathcal{L}[f] &= \left[E\partial_t + \mathbf{p}\nabla_{\mathbf{x}} - H(t)(a(t)^2\mathbf{p}^2\partial_E + E\mathbf{p}\nabla_{\mathbf{p}}) + m(F^0\partial_E + \mathbf{F}\nabla_{\mathbf{p}})\right] f \\ &= -\frac{1}{2}\int \mathrm{d}\Pi_{\{2..n\}}\delta^4\left(\sum_{i=2}^{m} p_i - \sum_{i=m+1}^{n} p_i\right)|\mathcal{M}|^2_{\{2..m\}\to\{m+1..n\}}\mathcal{P}[f] = \mathcal{C}[f]\,.\end{aligned} \tag{2.47}$$

In general we need to couple many such Boltzmann equations, each describing the evolution of the respective particle species. The collision operator couples these equations such that we need to solve a system of coupled integro partial differential equations to determine the phase space evolution of the distribution functions. However, in practice we can assume that many of the involved particles are in thermal equilibrium and therefore we will not need a separate Boltzmann equation for each of them.

2.4. Finite Temperature Field Theory

The description of the SM we used in Sec. 2.1, based on QFT, is only valid for processes involving a small number of particles. In other words, it is only valid at zero temperature

with no background medium. However, for the purposes of this thesis, this is not sufficient as we want to study a thermal plasma containing a large number of particles and no isolated particle states. To account for the effects coming from a thermal background within QFT, we need to consider Finite Temperature Field Theory (FTFT). We will use this section to introduce the relevant concepts we need from FTFT, based on Refs. [43–46].

The key difference between QFT and FTFT is that we do not consider single quantum states but mixed states given by the density matrix

$$\rho = \sum_\alpha p_\alpha \left|\alpha\right\rangle\left\langle\alpha\right| \ , \tag{2.48}$$

where the states $|\alpha\rangle$ form an orthonormal basis and p_α is the probability of finding $|\alpha\rangle$ in a statistical ensemble. The expectation value of an operator $\mathcal{O}$ is then given by

$$\langle\mathcal{O}\rangle = \sum_\alpha p_\alpha \left\langle\alpha\right| \mathcal{O} \left|\alpha\right\rangle = \mathrm{tr}(\rho\mathcal{O}) \ , \tag{2.49}$$

where we used that $|\alpha\rangle$ is orthonormal. Due to the fact that p_α is a probability distribution, all p_α have to be real and fulfill

$$0 \leq p_\alpha \leq 1 \quad , \quad \sum_\alpha p_\alpha = 1 \quad , \quad \mathrm{tr}(\rho) = 1 \ . \tag{2.50}$$

Since p_α is real, this also implies that the density matrix ρ has to be hermitian. For a state in thermal equilibrium the density matrix can be represented by

$$\rho = \frac{1}{Z}\exp(-\beta H) \quad , \quad Z = \mathrm{tr}[\exp(-\beta H)] \ , \tag{2.51}$$

where $\beta = T^{-1}$ and H is the Hamiltonian of the system under consideration.

Let us first consider a free scalar field whose Hamiltonian is given by

$$H = \sum_k a_k^\dagger a_k \ , \tag{2.52}$$

where $a_k^\dagger$ and a_k are creation and annihilation operators fulfilling the commutation relations

$$[a_k, a_l^\dagger] = \delta_{kl} \quad , \quad [a_k, a_l] = [a_k^\dagger, a_l^\dagger] = 0 \ . \tag{2.53}$$

We define the number operator $N_k \equiv a_k^\dagger a_k$ with eigenvalues n_k to obtain for the partition function Z

$$\begin{aligned} Z =& \mathrm{tr}[\exp(-\beta\sum_k \omega_k N_k)] = \sum_n \left\langle n\right| \exp(-\beta\sum_k \omega_k N_k) \left|n\right\rangle = \sum_n \exp(-\beta\sum_k \omega_k n_k) \\ =& \sum_n \prod_k \exp(-\beta\omega_k n_k) = \prod_k \sum_{n_k} \exp(-\beta\omega_k n_k) = \prod \frac{1}{1-e^{-\beta\omega_k}} \ . \end{aligned} \tag{2.54}$$

With the partition function at hand, we can also calculate the average number of particles $\langle N_k\rangle$ and the average energy of the system $\langle H\rangle$

$$\begin{aligned} \langle N_k\rangle &= \mathrm{tr}(\rho N_k) = \frac{1}{Z}\sum_n \exp(-\beta\sum_{k'}\omega_{k'}n_{k'})n_k = -\frac{1}{\beta}\frac{\partial}{\partial\omega_k}\log Z = \frac{1}{e^{\beta\omega_k}-1} = f_{\mathrm{BE}}(\omega_k) \ , \\ \langle H\rangle &= \sum_k \omega_k \langle N_k\rangle = \sum_k \omega_k f_{\mathrm{BE}}(\omega_k) \ , \end{aligned} \tag{2.55}$$

where we recover the Bose-Einstein distribution $f_{\rm BE}$ from Eq. (2.30). From the above equation we then obtain the following identities

$$\langle a_k^\dagger a_l\rangle = f_{\rm BE}\delta_{kl} \quad , \quad \langle a_k a_l^\dagger\rangle = (1+f_{\rm BE})\delta_{kl} \quad , \quad \langle a_k a_l^\dagger\rangle = \langle a_k a_l^\dagger\rangle = 0 \; . \tag{2.56}$$

With these identities, we can now consider the time ordered causal 2-point thermal Green's function, i.e. the thermal propagator

$$\langle \mathcal{T}\phi(x)\phi(y)\rangle = \Theta(x_0-y_0)\langle\phi(x)\phi(y)\rangle + \Theta(y_0-x_0)\langle\phi(y)\phi(x)\rangle \; , \tag{2.57}$$

where $\phi(x)$ is the quantum field of a scalar particle given by

$$\phi(x) = \sum_k \frac{1}{\sqrt{2V\omega_k}}\left(a_k e^{-ikx} + a_k^\dagger e^{ikx}\right) \tag{2.58}$$

in a volume V. Without loss of generality we will set $y=0$ and calculate $\langle\mathcal{T}\phi(x)\phi(0)\rangle$. First, we calculate the 2-point function

$$\begin{aligned} G^>(x) \equiv \langle\phi(x)\phi(0)\rangle &= \sum_{kl}\frac{\langle a_k a_l^\dagger\rangle e^{-ikx} + \langle a_k^\dagger a_l\rangle e^{ikx}}{2V\sqrt{\omega_k\omega_l}} = \sum_k \frac{(1+f_{\rm BE}(\omega_k))e^{-ikx} + f_{\rm BE}(\omega_k)e^{ikx}}{2V\omega_k} \\ &= \int \frac{{\rm d}^3k}{(2\pi)^3 2\omega_k}\left[(1+f_{\rm BE}(\omega_k))e^{-ikx} + f_{\rm BE}(\omega_k)e^{ikx}\right] , \end{aligned} \tag{2.59}$$

where we took the limit $V\to\infty$ in the last step. We can now use the relation

$$\int \frac{{\rm d}^3k}{(2\pi)^3 2\omega_k} = \int \frac{{\rm d}^4k}{(2\pi)^4}\delta(k^2-m^2)\Theta(k_0) \; , \tag{2.60}$$

to bring $G^>$ in the following form

$$G^>(x) = \int \frac{{\rm d}^4k}{(2\pi)^4}\Delta^>_{\rm BE}(k)e^{-ikx} \quad \text{with} \quad \Delta^>_{\rm BE} \equiv (\Theta(k_0)+n_{\rm BE}(k_0))2\pi\delta(k^2-m^2) \; , \tag{2.61}$$

and $n_{\rm BE}(k_0) \equiv f_{\rm BE}(|k_0|)$. Similarly, we obtain for the other 2-point function $G^<(x) \equiv \langle\phi(0)\phi(x)\rangle$

$$G^<(x) = \int \frac{{\rm d}^4k}{(2\pi)^4}\Delta^<_{\rm BE}(k)e^{-ikx} \quad \text{with} \quad \Delta^<_{\rm BE} \equiv (\Theta(-k_0)+n_{\rm BE}(k_0))2\pi\delta(k^2-m^2) \; . \tag{2.62}$$

Combining these results, the causal 2-point function can be expressed as

$$\langle\mathcal{T}\phi(x)\phi(0)\rangle = \int \frac{{\rm d}^4k}{(2\pi)^4}\Delta_{\rm BE}(k)e^{-ikx} \; , \tag{2.63}$$

with

$$\Delta_{\rm BE} \equiv \frac{i}{k^2-m^2+i\epsilon} + 2\pi n_{\rm BE}(k_0)\delta(k^2-m^2) \; , \tag{2.64}$$

where we used the following relation

$$\begin{aligned} &\int \frac{{\rm d}^4k}{(2\pi)^3}[\Theta(x_0)\Theta(k_0)+\Theta(-x_0)\Theta(-k_0)]\delta(k^2-m^2)e^{-ikx} \\ &= \int \frac{{\rm d}^3k}{(2\pi)^3 2\omega_k}[\Theta(x_0)e^{-i\omega_k x_0} + \Theta(-x_0)e^{i\omega_k x_0}]e^{i\mathbf{kx}} = \int \frac{{\rm d}^4k}{(2\pi)^4}\frac{ie^{-ik_0x_0}}{k^2-m^2+i\epsilon}e^{i\mathbf{kx}} \\ &= \int \frac{{\rm d}^4k}{(2\pi)^4}\frac{ie^{-ikx}}{k^2-m^2+i\epsilon} \; , \end{aligned} \tag{2.65}$$

making use of the residue theorem in the second line. Thereby, we derived the thermal scalar propagator in Eq. (2.64). The first term is the known zero temperature result for the Feynman propagator, while the second term comes from the fact that we consider a thermal plasma. It acts as an additional on-shell contribution where the resulting particle follows the Bose-Einstein distribution. Following the same steps as above, one can derive the thermal propagators for gauge bosons and fermions [46]. For a gauge field A_μ, the result is

$$G^{>}_{\mu\nu}(x) = \int \frac{\mathrm{d}^4k}{(2\pi)^4} P_{\mu\nu}\Delta^{>}_{\mathrm{BE}}(k)e^{-ikx} \,, \tag{2.66}$$

$$G^{<}_{\mu\nu}(x) = \int \frac{\mathrm{d}^4k}{(2\pi)^4} P_{\mu\nu}\Delta^{<}_{\mathrm{BE}}(k)e^{-ikx} \,, \tag{2.67}$$

$$\langle \mathcal{T} A_\mu(x) A_\nu(0)\rangle = \int \frac{\mathrm{d}^4k}{(2\pi)^4} P_{\mu\nu}\Delta_{\mathrm{BE}}(k)e^{-ikx} \,, \tag{2.68}$$

where $P_{\mu\nu}$ is a gauge dependent tensor. For a fermion field ψ we obtain

$$S^{>}(x) = \int \frac{\mathrm{d}^4k}{(2\pi)^4} (\not{k} + m)\Delta^{>}_{\mathrm{FD}}(k)e^{-ikx} \,, \tag{2.69}$$

$$S^{<}(x) = \int \frac{\mathrm{d}^4k}{(2\pi)^4} (\not{k} + m)\Delta^{<}_{\mathrm{FD}}(k)e^{-ikx} \,, \tag{2.70}$$

$$\langle \mathcal{T}\psi(x)\bar{\psi}(0)\rangle = \int \frac{\mathrm{d}^4k}{(2\pi)^4} (\not{k} + m)\Delta_{\mathrm{FD}}(k)e^{-ikx} \,, \tag{2.71}$$

where

$$\Delta^{>}_{\mathrm{FD}} \equiv (\Theta(k_0) - n_{\mathrm{FD}}(k_0))2\pi\delta(k^2 - m^2) \,,\ \Delta^{<}_{\mathrm{FD}} \equiv (\Theta(-k_0) - n_{\mathrm{FD}}(k_0))2\pi\delta(k^2 - m^2) \,, \tag{2.72}$$

$$\Delta_{\mathrm{FD}} = \frac{i}{k^2 - m^2 + i\epsilon} - 2\pi n_{\mathrm{FD}}(k_0)\delta(k^2 - m^2) \,, \tag{2.73}$$

and n_{FD} is the Fermi-Dirac distribution. An important connection from FTFT to QFT is that the density operator can also be viewed as a time evolution operator with imaginary time such that $e^{\beta H}\mathcal{O}(t,\mathbf{x})e^{-\beta H} = \mathcal{O}(t - i\beta, \mathbf{x})$. With this, we obtain the Kubo-Martin-Schwinger (KMS) relation [43]

$$\langle \mathcal{O}_1(t)\mathcal{O}_2(t')\rangle = \langle \mathcal{O}_2(t')\mathcal{O}_1(t + i\beta)\rangle \,, \tag{2.74}$$

where we made use of the cyclicity of the trace.

2.4.1. Path Integral Formalism

So far we have only considered free particles without any interactions. To see how interactions appear in FTFT we will use the path integral formalism. In this formalism the n-point function is given by

$$\begin{aligned}
\langle \mathcal{T}\hat{\phi}(x_1)\dots\hat{\phi}(x_n)\rangle &= \int \mathcal{D}\phi \,\langle \phi, t_0|\, \rho\mathcal{T}\hat{\phi}(x_1)\dots\hat{\phi}(x_n)\,|\phi, t_0\rangle \\
&= \frac{1}{Z}\int \mathcal{D}\phi \,\langle \phi, t_0|\, e^{-\beta H}\mathcal{T}\hat{\phi}(x_1)\dots\hat{\phi}(x_n)\,|\phi, t_0\rangle \\
&= \frac{1}{Z}\int \mathcal{D}\phi \,\langle \phi, t_0 - i\beta|\, \mathcal{T}\hat{\phi}(x_1)\dots\hat{\phi}(x_n)\,|\phi, t_0\rangle \,,
\end{aligned} \tag{2.75}$$

where

$$\int \delta\phi(t)\,|\phi, t\rangle\langle\phi, t| = 1 \quad \text{with} \quad \delta\phi(t) \equiv \prod_{\mathbf{x}} \mathrm{d}\phi(t,\mathbf{x}) \,. \tag{2.76}$$

The object in Eq. (2.75) can be represented by a path-integral, following the procedure described in Ref. [47] (Sec. 9),

$$\langle \mathcal{T}\hat{\phi}(x_1)\dots\hat{\phi}(x_n)\rangle = \frac{1}{Z}\int \mathcal{D}\phi\,\hat{\phi}(x_1)\dots\hat{\phi}(x_n)\exp\left(i\int_C \mathrm{d}^4x\mathrm{L}(\phi)\right) , \tag{2.77}$$

with the partition function

$$Z = \int \mathcal{D}\phi \exp\left(i\int_C \mathrm{d}^4x\mathrm{L}(\phi)\right) . \tag{2.78}$$

From this, we obtain the generating functional in the presence of an external source $J(x)$ as

$$\mathcal{Z}(J) = \frac{1}{Z}\int \mathcal{D}\phi \exp\left(i\int_C \mathrm{d}^4x(\mathrm{L}+J(x)\phi(x))\right) , \tag{2.79}$$

with which we can obtain the n-point Green's function via

$$\langle \mathcal{T}\hat{\phi}(x_1)\dots\hat{\phi}(x_n)\rangle = \frac{1}{i^n}\frac{\delta^n}{\delta J(x_1)\dots J(x_n)}\mathcal{Z}(J)\bigg|_{J=0} . \tag{2.80}$$

At this stage there are two key differences to the zero temperature path integral formalism. First, the fields fulfill the periodicity boundary condition (anti-periodic in case of fermions)

$$\phi(t_0,\mathbf{x}) = \pm\phi(t_0-i\beta,\mathbf{x}) . \tag{2.81}$$

Second, the time integral in the exponential function is taken over a complex contour that starts at t_0 and ends at $t_0 - i\beta$. In the derivation of the path integral we insert a set of discrete times $x_1^0, x_2^0 \dots x_n^0$ between the boundaries, which means that we can choose the path ourselves. A simple choice would be a straight path from t_0 to $t_0 - i\beta$. This prescription would lead us to the imaginary time formalism (for more details see [43,48]). We will, however, take a different approach in which the Green's functions are calculated at real times, the so called real time formalism. Here, we take a path that starts at t_i and ends at a time t_f. We call this segment of the path C_+. Next, we go from t_f back to t_i which we call C_-, and lastly we go from t_i to $t_i - i\beta$ which we call C_3.[7] Now, taking $t_i \to -\infty$ and $t_f \to +\infty$, we are left with a time integral that can be written as

$$\int_C \mathrm{d}t\mathrm{L}(\phi) = \int_{-\infty}^{\infty}\mathrm{d}t_+\mathrm{L}(\phi_+) - \int_{-\infty}^{\infty}\mathrm{d}t_-\mathrm{L}(\phi_-) , \tag{2.82}$$

where introduced the notation for fields that lie on $C_{+/-}$ by giving them the corresponding index, effectively doubling the amount of fields. The contribution from C_3 has been dropped as it only contributes trivially to the generating functional [43].

2.4.2. Propagators in the Scalar Theory

With this setup, we can now consider a scalar theory given by

$$S_C(\phi) = S_0(\phi) + S_I(\phi) , \tag{2.83}$$

where

$$S_0(\phi) = -\frac{1}{2}\int_C \mathrm{d}^4x\phi(\partial_\mu\partial^\mu + m^2)\phi \quad \text{and} \quad S_I = \int_C \mathrm{d}^4x\mathrm{L}_I . \tag{2.84}$$

[7] One could have also introduced a fourth segment which goes from t_f to $t_f - i\sigma$ ($\sigma \in (0,\beta)$). However, this does not change any physical results as discussed in Ref. [45].

Here, S_0 corresponds to the unperturbed theory and S_I involves the interactions of the theory. With these, the perturbative series for $\mathcal{Z}$ is given by

$$\mathcal{Z}(J) = \frac{1}{Z}\exp\left(iS_I\left(\frac{1}{i}\frac{\delta}{\delta J}\right)\right)\mathcal{Z}_0(J)\ , \tag{2.85}$$

where $\mathcal{Z}_0$ is the functional of the unperturbed theory and is given by

$$\mathcal{Z}_0(J) = \exp\left(-\frac{i}{2}\int_C \mathrm{d}^4x\mathrm{d}^4y J(x)G(x-y)J(y)\right)\ . \tag{2.86}$$

To determine the dynamics of this theory, we want to investigate the above quantity. There, the Green's function $G(x-y)$ fulfills the relation

$$(\partial_\mu\partial^\mu + m^2)G(x-y) = -\delta_c(t-t')\delta^3(\mathbf{x}-\mathbf{y})\ , \tag{2.87}$$

where the delta distribution is extended to account for the path taken along the C_- branch

$$\delta_c(t-t') = \frac{\mathrm{d}\Theta_c(t-t')}{\mathrm{d}t} = \begin{cases}\delta(t-t') & t,t'\in C_+\\ -\delta(t-t') & t,t'\in C_-\\ 0 & \text{else}\end{cases}\ , \tag{2.88}$$

with

$$\Theta_c(t-t') = \begin{cases}\Theta(t-t') & t,t'\in C_+\\ \Theta(t'-t) & t,t'\in C_-\\ 0 & t\in C_+\ ,\ t'\in C_-\\ 1 & t'\in C_+\ ,\ t\in C_-\end{cases}\ . \tag{2.89}$$

Taking the Fourier transform of Eq. (2.87) with respect to the spacial coordinates gives

$$(\partial_t^2 + \omega_k^2)G(t-t',\omega_k) = -\delta_c(t-t')\ . \tag{2.90}$$

The Green's function which solves this equation while simultaneously fulfilling the KMS relation in Eq. (2.74) is given by [43]

$$\begin{aligned} iG_c(t-t',\omega_k) = \frac{n_{\mathrm{BE}}}{2\omega_k}\Big[&\Theta_c(t-t')\left(e^{\beta\omega_k - i\omega_k(t-t')} + e^{i\omega_k(t-t')}\right)\\ &+\Theta_c(t'-t)\left(e^{-i\omega_k(t-t')} + e^{\beta\omega_k + i\omega_k(t-t')}\right)\Big]\ . \end{aligned} \tag{2.91}$$

Taking the Fourier transform of this result with respect to time we obtain 4 different propagators based on which branch t and t' lie in,

$$iG_{++}(k) = \Delta_{BE}(k) \quad , \quad iG_{--}(k) = \Delta^*_{BE}(k)\ , \tag{2.92}$$

$$iG_{+-}(k) = \Delta^<_{\mathrm{BE}}(k) \quad , \quad iG_{-+}(k) = \Delta^>_{\mathrm{BE}}(k)\ , \tag{2.93}$$

where the $\Delta(k)$ are given in Eqs (2.61), (2.62) and (2.64), which we can write via a single 2×2 propagator matrix

$$i\hat{G} = \begin{pmatrix} iG_{++} & iG_{+-}\\ iG_{-+} & iG_{--}\end{pmatrix}\ . \tag{2.94}$$

This is the distinct feature of the real time formalism. By having two time branches, we introduce a second set of fields which lie on the C_- branch. Although these two sets do not have a direct interaction, they are connected via the propagator matrix given in Eq. (2.94) mixing the two. However, this mixing manifests itself only in higher-order corrections, as all

external lines carry exclusively either the (+) or the (−) index, corresponding to a single time direction. Similarly, although more involved, we obtain for the fermion propagator $\hat{S}$ and the vector boson propagator $\hat{G}_{\mu\nu}$ [46]

$$i\hat{S} = (\not{k} + m) \begin{pmatrix} iS_{++} & iS_{+-} \\ iS_{-+} & iS_{--} \end{pmatrix} \equiv (\not{k} + m) \begin{pmatrix} \Delta_{FD} & \Delta^{<}_{FD} \\ \Delta^{>}_{FD} & \Delta^{*}_{FD} \end{pmatrix} \quad , \quad i\hat{G}_{\mu\nu} = P_{\mu\nu} i\hat{G} \, . \tag{2.95}$$

2.4.3. Physical Propagators

In FTFT we are not interested in the causal propagators $G_{\pm\pm}$ since they do not have well defined analyticity properties as can be seen by the delta distribution appearing inside them. Further, they are not linearly independent from each other since they fulfill

$$G_{++} + G_{--} = G_{+-} + G_{-+} \, . \tag{2.96}$$

We can solve both issues by considering the physical Green's functions which are related to the causal ones via

$$\begin{aligned} iG_R &= iG_{++} - iG_{+-} = \frac{i}{k^2 - m^2 + i\epsilon} - 2\pi\Theta(-k_0)\delta(k^2 - m^2) \\ &= \mathcal{P}\frac{i}{k^2 - m^2} + \pi(1 - 2\Theta(-k_0))\delta(k^2 - m^2) \\ &= \mathcal{P}\frac{i}{k^2 - m^2} + \mathrm{sgn}(k_0)\pi\delta(k^2 - m^2) = \frac{i}{k^2 - m^2 + i\mathrm{sgn}(k_0)\epsilon} \, , \\ iG_A &= iG_{++} - iG_{-+} = \frac{i}{k^2 - m^2 - i\mathrm{sgn}(k_0)\epsilon} \, , \\ iG_K &= iG_{++} + iG_{+-} = (1 + 2n_{\mathrm{BE}}(k_0))2\pi\delta(k^2 - m^2) \, , \end{aligned} \tag{2.97}$$

where we used the Cauchy principle value $\mathcal{P}$ and the identity

$$\lim_{\epsilon \to 0^+} \frac{1}{x \pm i\epsilon} = \mp i\pi\delta(x) + \mathcal{P}\left(\frac{1}{x}\right) . \tag{2.98}$$

To obtain physical predictions the retarded propagator G_R is the relevant quantity we have to use when calculating quantities in FTFT. We can perform the basis change from the causal propagator matrix to the physical propagators matrix $\check{G}_{\mathrm{ph}}$ via

$$\check{G}_{\mathrm{ph}} = Q\check{G}Q^{-1} = \begin{pmatrix} 0 & G_A \\ G_R & G_K \end{pmatrix} \quad \text{with} \quad Q = \frac{1}{\sqrt{2}} \begin{pmatrix} 1 & -1 \\ 1 & 1 \end{pmatrix} \, . \tag{2.99}$$

In this basis the external fields are transformed via

$$\phi^+ = \frac{1}{\sqrt{2}}(\phi^{cl} + \phi^q) \quad , \quad \phi^- = \frac{1}{\sqrt{2}}(\phi^{cl} - \phi^q) \, , \tag{2.100}$$

in terms of new fields which we call the classical field ϕ_{cl} and the quantum field ϕ_q. The diagrammatic representation of the physical propagators is shown below:

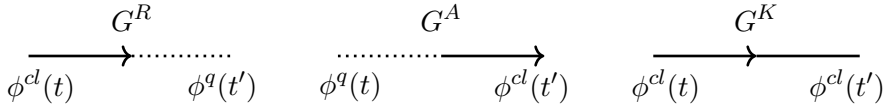

To see how this affects the Lagrangian and its couplings structure we will look at the kinetic fermion term involving the gluon gauge field (Eq. (2.6))

$$\mathrm{L}_F = ig_s T^a G_\mu^{a,+} \bar{\psi}^+ \gamma^\mu \psi^+ - ig_s T^a G_\mu^{a,-} \bar{\psi}^- \gamma^\mu \psi^- \ , \tag{2.101}$$

which in terms of the classical and quantum fields is then given by

$$\mathrm{L}_F = \frac{ig_s}{\sqrt{2}} T^a \left(G_\mu^{a,cl} \bar{\psi}^q \gamma^\mu \psi^{cl} + G_\mu^{a,cl} \bar{\psi}^{cl} \gamma^\mu \psi^q + G_\mu^{a,q} \bar{\psi}^{cl} \gamma^\mu \psi^{cl} + G_\mu^{a,q} \bar{\psi}^q \gamma^\mu \psi^q \right) \ . \tag{2.102}$$

In this basis we notice that now all the vertices carry the same sign and that each vertex carries an odd number of quantum fields. When constructing Feynman diagrams, one of the external legs is chosen as the *probed* one, while the remaining legs are taken to be classical. It does not matter which of the external legs is chosen to be the probed one, since they lead to the same results.

Part I.

Dark Matter in Extensions of the Standard Model

CHAPTER 3

Introduction into WIMP Dark Matter

Currently, there are three main ideas on the nature of DM which try to explain the observed phenomena. The first are primordial black holes, which are black holes that formed in the early radiation dominated universe and still govern the universe today [49]. In a second approach called modified Newtonian dynamics, the second law of Newton is modified by a scale factor such that it explains the correct velocity dependence of stars in the outer regions of galaxies [50]. In this thesis, we focus on the third class of scenarios, in which DM is assumed to be a new particle not contained within the SM. The theoretically allowed mass range for DM is extremely broad, spanning many orders of magnitude. Starting from ultralight candidates with masses as low as $m \sim 10^{-21}\,\mathrm{eV}$, up to the Planck scale at $m \sim 10^{28}\,\mathrm{eV}$. In this work we restrict ourselves to thermal dark matter, which typically lies in the mass range of a few GeV to a few TeV. For an extensive review on DM models for the entire mass range we refer the reader to Ref. [51].

3.1. Extensions Beyond the SM

Our goal is to construct models which provide a suitable DM candidate that is able to account for the observed relic density in Eq. 1.1. Additionally, the model should be able to explain the lack of DM evidence from current direct and indirect detection experiments as well as collider searches. We do this by extending the SM Lagrangian $\mathrm{L_{SM}}$ via an additional Beyond the SM (BSM) Lagrangian $\mathrm{L_{BSM}}$ such that

$$\mathrm{L_{model}} = \mathrm{L_{SM}} + \mathrm{L_{BSM}}\,. \tag{3.1}$$

A simple choice for $\mathrm{L_{BSM}}$ that explains the observed null results from experiments is

$$\mathrm{L_{BSM}} = \frac{1}{2}\partial_\mu \phi_S \partial^\mu \phi_S - \frac{1}{2} m^2 \phi_S^2\,. \tag{3.2}$$

Here, ϕ_s is a real scalar field with mass m. This Lagrangian does not couple to the SM and is therefore able to explain the null results of the experiments. To explain the observed relic density in this model one has to assume that the relic density was there from the very beginning of the universe as an initial condition or that it was produced via non thermal processes. We could add further fields to the BSM Lagrangian which can interact with each

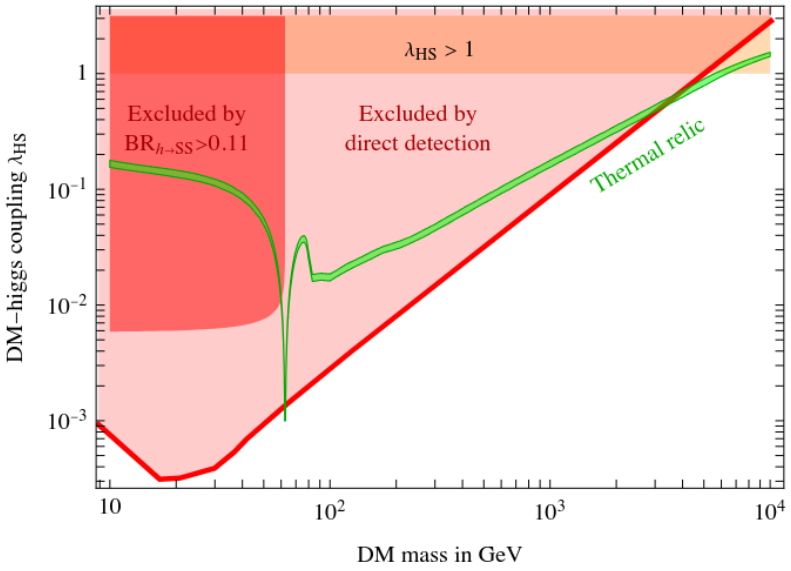

Figure 3.1.: DM-Higgs coupling over the DM mass. The green line shows the parameters which lead to the measured relic density. The red regions and orange are excluded by direct detection experiments, collider searches and pertubativity constraints. The figure is taken from Ref. [51].

other but not with the SM and construct a whole Dark Sector (DS) of particles. The issue with such models is that we can only study their influence on ordinary matter via gravitational effects, which are very weak and therefore currently impossible to probe in an experiment on particle level.

In this work we want to consider DM models which interact with the SM via forces besides gravity. However, their interaction with the SM should still be small to account for the experimental data. Depending on how small the coupling to the SM is, two classes of models emerge. In the first class of DM models the DS particles are in thermal equilibrium with the SM at the beginning of the universe. It was shown that for particles with a coupling at the order of the weak scale, so called WIMPs, the DM relic abundance can be obtained through the freeze-out mechanism [52].[8] In the second class of models the DS particles have a negligible initial abundance and are not in thermal equilibrium with the SM. In this case, the relic density is obtain through freeze-in and requires very small couplings to the SM of $\lambda \sim 10^{-10}$ to generate the observed relic abundance. Since the required couplings of the DM particles to the SM are very small, they are also referred to as FIMPs. In this part of the thesis we will focus on WIMPs as the source of the DM relic abundance, while in Part II we will investigate FIMPs as an additional source for the observed relic density.

To see how a connection between the BSM model and the SM might look like we extend our previous example in Eq. (3.2) by an additional term to obtain a coupling to the SM such that

$$\mathrm{L}_{\mathrm{BSM}} = \frac{1}{2}\partial_\mu \phi_S \partial^\mu \phi_S - \frac{1}{2}m^2\phi_S^2 - \lambda_{HS}\phi_S^2\Phi^2 - \frac{\lambda_s}{4}\phi_S^4\,, \tag{3.3}$$

where Φ is the SM Higgs doublet. Further, we have the portal coupling λ_{HS} between the DM field and the Higgs field, which ensures the thermal connection to the SM, and the self-coupling λ_s between four DM particles. Since, the DM candidate only couples to the Higgs boson after EW symmetry breaking, connecting the DM particles to the SM, the

[8] Even though freeze-out is the most commonly used mechanism to produce the relic abundance, there are many others which have been proposed, cf. [53–60].

model described by Eq. (3.3) is called a Higgs portal model. Further, we note that a $\mathbb{Z}_2$ was imposed such that $\phi_S \to -\phi_S$ and $\Phi \to \Phi$. This ensures that the DM is stable and cannot decay into two Higgs bosons.[9] The considered model is very constrained as can be seen by from Fig. 3.1. The green line shows the parameter space which generates the observed relic density of $\Omega_\chi h^2 = 0.12 \pm 0.001$. The dark red region is excluded by the upper bound on the invisible decays of the Higgs boson [61], while the light red region is excluded by direct detection experiments. Further, the orange region is the bound obtained from pertubativity constraints. The model under consideration allows only for DM masses in the range between 3-7 TeV, which will be covered by future DM experiments.

As a consequence we want to construct models which are able to explain the DM relic abundance and are not excluded by current experiments and as such have the chance at being tested in future experiments. Further, the toy model considered in Eq. 3.3 is only able to account for DM but no further observed phenomena. To build models which account for other phenomena besides DM, a richer particle spectrum with additional couplings is necessary. We want to consider a general model with potentially multiple DS particles that are $\mathbb{Z}_2$-odd and additional $\mathbb{Z}_2$-even particles. We divide the particle content of the BSM into a set of $\mathbb{Z}_2$-even fields Ψ_i a set of $\mathbb{Z}_2$-odd fields $\mathcal{X}_i$. From this a general Lagrangian can be constructed via

$$\mathrm{L}_{\mathrm{model}}\left(\{\Psi_i, \mathcal{X}_i\}\right) = \mathrm{L}_{\mathrm{even}}(\{\Psi_i\}) + \mathrm{L}_{\mathrm{odd}}(\{\mathcal{X}_i\}) + \mathrm{L}_{\mathrm{tri}}(\{\Psi_i, \mathcal{X}_i\}) + \mathrm{L}_{\mathrm{quar}}(\{\Psi_i, \mathcal{X}_i\})\,. \tag{3.4}$$

Here, $\mathrm{L}_{\mathrm{even}}$ contains only $\mathbb{Z}_2$-even Ψ_i fields, $\mathrm{L}_{\mathrm{odd}}$ contains only $\mathbb{Z}_2$-odd $\mathcal{X}_i$ fields, $\mathrm{L}_{\mathrm{tri}}$ contains the trilinear coupling between two $\mathcal{X}_i$ and one Ψ_i and $\mathrm{L}_{\mathrm{quar}}$ contains quartic couplings between two $\mathcal{X}_i$ and two Ψ_i. For the production of DM we mostly care about the last two parts of Eq. (3.4) as they are responsible for the thermal contact to the SM. In the next section we want to describe the thermal freeze-out of the $\mathcal{X}_i$ fields and derive the according collision terms necessary for the Boltzmann equation with processes allowed by the Lagrangian.

3.2. Dark Sector Boltzmann Equations

To derive the Boltzmann equation which describes the density evolution of a DS particle $\mathcal{X}_i$ we start at the-left hand side of Eq. (2.47) with no external force

$$\mathcal{L}[f_\mathcal{X}] = \left[E\partial_t + \mathbf{p}\nabla_\mathbf{x} - H(t)\left(a(t)^2\mathbf{p}^2\partial_E + E\mathbf{p}\nabla_\mathbf{p}\right)\right] f_{\mathcal{X}_i}\,. \tag{3.5}$$

Further, with the assumption that the universe is homogeneous and isotropic on large scales the distribution functions are only dependent on E and t such that

$$\mathcal{L}[f_{\mathcal{X}_i}] = \left[E\partial_t - H(t)a(t)^2\mathbf{p}^2\partial_E\right] f_{\mathcal{X}_i}(E,t)\,. \tag{3.6}$$

After transforming the momentum into the comoving frame

$$\mathbf{p} = \frac{\mathbf{p}'}{a(t)}\,, \tag{3.7}$$

we arrive at

$$\mathcal{L}[f_{\mathcal{X}_i}] = \left[E\partial_t - H(t)\mathbf{p}'^2\partial_E\right] f_{\mathcal{X}_i}(E,t)\,. \tag{3.8}$$

We now integrate both sides of Eq. (2.47) over the momentum of the DS particle with the integral measure in Eq. (2.42) multiplied by two and summed over the internal degrees of freedom g_i. With this we obtain for the integrated Liouville operator

$$\sum_{g_i}\int \frac{\mathrm{d}^3p}{(2\pi)^3E}\mathcal{L}[f_{\mathcal{X}_i}] = \dot{n}_{\mathcal{X}_i} + 3Hn_{\mathcal{X}_i}\,, \tag{3.9}$$

[9] Imposing a $\mathbb{Z}_2$ symmetry is not the only way to ensure that the DM particle is stable. There are many models which use different symmetry groups, which also lead to a stable DM candidate.

where

$$n = \sum_g \int \frac{\mathrm{d}^3 p}{(2\pi)^3} f(E,t)\,, \tag{3.10}$$

is the number density of a particle. For the first term of Eq. (3.9) we used the the fact that we can change the order between the derivative and the integration, while for the second term we used the energy momentum relation $E = \sqrt{\mathbf{p}^2 + m^2}$ and integrated by parts i.e.

$$\sum_g \int \frac{\mathrm{d}^3 p}{(2\pi)^3 E} \mathbf{p}^2 \partial_E f = \sum_g \int \frac{\mathrm{d}^3 p}{(2\pi)^3} \mathbf{p} \nabla_{\mathbf{p}} f = -3 \sum_g \int \frac{\mathrm{d}^3 p}{(2\pi)^3} f = -3n\,. \tag{3.11}$$

We now move on to the right-hand side of Eq. (2.47), the collision operator, where we will consider the $2 \to 2$ annihilation process

$$\mathcal{X}_i \mathcal{X}_j \leftrightarrow \Psi_k \Psi_l\,.$$

Again, we integrate over the momentum and sum over the internal degrees of freedom of the considered DS particle as in Eq. (3.9)

$$\sum_{g_i} \int \frac{\mathrm{d}^3 p_i}{(2\pi)^3 E_i} \mathcal{C}[f_{\mathcal{X}_i}] = -\int \mathrm{d}\Pi_{\{i,j,k,l\}} \delta^4(p_i + p_j - p_k - p_l) |\mathcal{M}|^2_{\mathcal{X}_i \mathcal{X}_j \leftrightarrow \Psi_k \Psi_l} \mathcal{P}[f_{\mathcal{X}_i}]\,, \tag{3.12}$$

where the indices of the momenta, energy and degrees of freedom are assigned such that they correspond to the respective particle and

$$\mathcal{P}[f_{\mathcal{X}_i}] = f_{\mathcal{X}_i} f_{\mathcal{X}_j} \left(1 \pm f_{\Psi_k}\right) \left(1 \pm f_{\Psi_l}\right) - f_{\Psi_k} f_{\Psi_l} \left(1 \pm f_{\mathcal{X}_i}\right) \left(1 \pm f_{\mathcal{X}_j}\right). \tag{3.13}$$

The sum over the internal degrees of freedom was absorbed into the definition of $|\mathcal{M}|^2$. To simplify Eq. (3.13) we assume that the Pauli blocking and Bose enhancement can be neglected and that the Ψ particles are in thermal equilibrium, since most of them are electrically charged and can interact with the thermal photons. This allows to do the replacement $f_\Psi \to f_{\Psi,\mathrm{eq}}$, from which we can apply the principle of detailed balance leading to

$$f^{\mathrm{eq}}_{\Psi_k} f^{\mathrm{eq}}_{\Psi_l} = f^{\mathrm{eq}}_{\mathcal{X}_i} f^{\mathrm{eq}}_{\mathcal{X}_j}\,. \tag{3.14}$$

With this, Eq. (3.13) is simplified into

$$\mathcal{P}[f_{\mathcal{X}_i}] = f_{\mathcal{X}_i} f_{\mathcal{X}_j} - f^{\mathrm{eq}}_{\mathcal{X}_i} f^{\mathrm{eq}}_{\mathcal{X}_j}\,. \tag{3.15}$$

Further, we assume that the DS particles are in kinetic equilibrium[10] and non-relativistic at the freeze-out temperature, i.e.

$$f_{\mathcal{X}_i}(E_i,t) = e^{\frac{-(E_i - \mu_i(t))}{T}} \equiv \xi_{\mathcal{X}_i}(t) f^{\mathrm{eq}}_{\mathcal{X}_i}(E_i) \;\;,\;\; \xi_{\mathcal{X}_i}(t) = e^{\frac{\mu_i(t)}{T}} \;\;,\;\; f^{\mathrm{eq}}_{\mathcal{X}_i}(E_i) = e^{\frac{-E_i}{T}}\,. \tag{3.16}$$

The assumption that the DS particles are non-relativistic is justified, since the freeze-out temperature is given by $T_{\mathrm{fo}} = m_{\mathcal{X}}/25$. After integrating Eq. (3.16) on both sides over the particle momentum and using Eq. (3.10) we arrive at

$$f_{\mathcal{X}_i} = n_{\mathcal{X}_i}(t) \frac{f^{\mathrm{eq}}_{\mathcal{X}_i}(E_i)}{n^{\mathrm{eq}}_{\mathcal{X}_i}}\,. \tag{3.17}$$

[10] This assumption was investigated in Ref. [62] and shown to be invalid for the model in Eq. (3.3) for DM masses close to the Higgs threshold.

We have now managed to express the distribution function in terms of the number density which has a time dependent and a time independent part. Inserting Eq. (3.15) and Eq. (3.17) into Eq. (3.12) we obtain

$$g_i \int \frac{\mathrm{d}^3 p_i}{(2\pi)^3 E_i} \mathcal{C}[f_{\mathcal{X}_i}] = -\langle \sigma v \rangle_{\mathcal{X}_i \mathcal{X}_j \leftrightarrow \Psi_k \Psi_l} \left(n_{\mathcal{X}_i} n_{\mathcal{X}_j} - n^{\mathrm{eq}}_{\mathcal{X}_i} n^{\mathrm{eq}}_{\mathcal{X}_j} \right), \tag{3.18}$$

where the Thermally Averaged Cross section (TAC) for a $2 \to 2$ process $\langle \sigma v \rangle$ is given by

$$\langle \sigma v \rangle_{\mathcal{X}_i \mathcal{X}_j \leftrightarrow \Psi_k \Psi_l} = \frac{\int \mathrm{d}\Pi_{\{i,j,k,l\}} \delta^4(p_i + p_j - p_k - p_l) |\mathcal{M}|^2_{\mathcal{X}_i \mathcal{X}_j \leftrightarrow \Psi_k \Psi_l} f^{\mathrm{eq}}_{\mathcal{X}_i} f^{\mathrm{eq}}_{\mathcal{X}_j}}{n^{\mathrm{eq}}_{\mathcal{X}_i} n^{\mathrm{eq}}_{\mathcal{X}_j}} . \tag{3.19}$$

Together with Eq. (3.9) we obtain the Boltzmann equation for a single DS particle

$$\dot{n}_{\mathcal{X}_i} + 3H n_{\mathcal{X}_i} = -\langle \sigma v \rangle_{\mathcal{X}_i \mathcal{X}_j \leftrightarrow \Psi_k \Psi_l} \left(n_{\mathcal{X}_i} n_{\mathcal{X}_j} - n^{\mathrm{eq}}_{\mathcal{X}_i} n^{\mathrm{eq}}_{\mathcal{X}_j} \right). \tag{3.20}$$

At this stage we would like to note a few things. We started out the derivation with an integro partial differential equation and ended up with a linear differential equation. The key assumption which led to this simplification is that the DS particles are in kinetic equilibrium such that their distribution functions fulfill Eq. (3.16). This assumption let us factorize the E_i dependence over which we then integrate in the TAC separately. Another thing to note is that although we are solving for the number density in Eq. (3.20), the number density itself only depends on the chemical potential and the temperature. This means that in this Boltzmann equation we are tracking the departure of the DS particles from chemical equilibrium, which in turn will give us the number density.

So far we only considered one annihilation process in the collision operator. To obtain the full collision operator we have to sum over all possible final states as well as over all annihilation partners $\mathcal{X}_j$. For the remainder of this thesis, the summation over the Ψ indices will be left implicit. Further, in Eq. (3.20) we considered only the annihilation processes in our Boltzmann equation. However, we have two additional process that are relevant for the density evolution of the corresponding DS particle. The first are conversion processes

$$\mathcal{X}_i \Psi_k \leftrightarrow \mathcal{X}_j \Psi_l ,$$

where $i \neq j$ [11] and the second are decays

$$\mathcal{X}_i \leftrightarrow \mathcal{X}_j \Psi_l . \tag{3.21}$$

Taking these into account, the Boltzmann equation for a single DS particle is given by [63]

$$\begin{aligned} \dot{n}_{\mathcal{X}_i} + 3H n_{\mathcal{X}_i} = &- \sum_j \langle \sigma v \rangle_{\mathcal{X}_i \mathcal{X}_j \leftrightarrow \Psi_k \Psi_l} \left(n_{\mathcal{X}_i} n_{\mathcal{X}_j} - n^{\mathrm{eq}}_{\mathcal{X}_i} n^{\mathrm{eq}}_{\mathcal{X}_j} \right) \\ &- \sum_{j \neq i} \left[\langle \sigma v \rangle_{\mathcal{X}_i \Psi_k \leftrightarrow \mathcal{X}_j \Psi_l} \left(n_{\mathcal{X}_i} n_{\Psi_k} - n^{\mathrm{eq}}_{\mathcal{X}_i} n^{\mathrm{eq}}_{\Psi_k} \right) - \langle \sigma v \rangle_{\mathcal{X}_j \Psi_k \leftrightarrow \mathcal{X}_i \Psi_l} \left(n_{\mathcal{X}_j} n_{\Psi_k} - n^{\mathrm{eq}}_{\mathcal{X}_j} n^{\mathrm{eq}}_{\Psi_k} \right) \right] \\ &- \sum_{j \neq i} \left[\Gamma_{\mathcal{X}_i \leftrightarrow \Psi_k \mathcal{X}_j} \left(n_{\mathcal{X}_i} - n^{\mathrm{eq}}_{\mathcal{X}_i} \right) - \Gamma_{\mathcal{X}_j \leftrightarrow \Psi_k \mathcal{X}_i} \left(n_{\mathcal{X}_j} - n^{\mathrm{eq}}_{\mathcal{X}_j} \right) \right] . \end{aligned} \tag{3.22}$$

In general we need to construct Eq. (3.22) for every DS particle included in the considered model, which would give us a set of N coupled Boltzmann equations, where N is the number of DS particles. However, this is not necessary as we can use the fact that there has to be

[11] The case $i = j$ has no relevance for the number density, since the particle number remains constant. However, they are important to retain kinetic equilibrium and must be taken into account if the assumption in Eq. (3.16) breaks.

a lightest DS particle $\mathcal{X}_1$ with mass m_1. Due to the enforced $\mathbb{Z}_2$ symmetry, all heavier DS particles eventually decay into the lightest one throughout the evolution of the universe. Even if their masses are almost degenerate, loop corrections will result in a non-zero decay width. This means that we can look at the DS as a whole, instead of looking at the individual DS particles. To do this we sum Eq. (2.47) over all DS particles and define

$$n_{\mathcal{X}} = \sum_{i=1}^{N} n_{\mathcal{X}_i} \,. \tag{3.23}$$

Due to the symmetry of the second and third term on the right hand side of Eq. (2.47) with respect to $i \leftrightarrow j$, they will cancel leaving us with

$$\dot{n}_{\mathcal{X}} + 3Hn_{\mathcal{X}} = -\sum_{i,j=1}^{N} \langle \sigma v \rangle_{\mathcal{X}_i \mathcal{X}_j \leftrightarrow \Psi_k \Psi_l} \big(n_{\mathcal{X}_i} n_{\mathcal{X}_j} - n_{\mathcal{X}_i}^{\mathrm{eq}} n_{\mathcal{X}_j}^{\mathrm{eq}} \big) \,. \tag{3.24}$$

Freeze-out occurs during the radiation dominated universe, meaning that the SM particles are still relativistic while the DS particle are not. This means that the number density of the latter is much stronger Boltzmann suppressed during this epoch compared to the former. This leads to the fact that the conversion/scattering rate $\langle \sigma v \rangle_{\mathcal{X}_i \Psi_k \leftrightarrow \mathcal{X}_j \Psi_l}$ is larger than the annihilation rate $\langle \sigma v \rangle_{\mathcal{X}_i \mathcal{X}_j \leftrightarrow \Psi_k \Psi_l}$ ensuring that the $\mathcal{X}_i$ remain in thermal equilibrium before freeze-out. This allows us to equate the ratios between the individual particle and the total density to their equilibrium values

$$\frac{n_{\mathcal{X}_i}}{n_{\mathcal{X}}} \simeq \frac{n_{\mathcal{X}_i}^{\mathrm{eq}}}{n_{\mathcal{X}}^{\mathrm{eq}}} \,. \tag{3.25}$$

Using this, Eq. (3.24) becomes

$$\dot{n}_{\mathcal{X}} + 3Hn_{\mathcal{X}} = -\langle \sigma v \rangle_{\mathrm{eff}} \big(n_{\mathcal{X}}^2 - (n_{\mathcal{X}}^{\mathrm{eq}})^2 \big) \,, \tag{3.26}$$

with

$$\langle \sigma v \rangle_{\mathrm{eff}} = \sum_{i,j=1}^{N} \langle \sigma v \rangle_{\mathcal{X}_i \mathcal{X}_j \leftrightarrow \Psi_k \Psi_l} \frac{n_{\mathcal{X}_i}^{\mathrm{eq}} n_{\mathcal{X}_j}^{\mathrm{eq}}}{(n_{\mathcal{X}}^{\mathrm{eq}})^2} \,. \tag{3.27}$$

As a next step, we want to bring Eq. (3.26) into a form where the change in the number density due to the expansion of the universe is absorbed into a new quantity called the yield

$$Y_{\mathcal{X}} = \frac{n_{\mathcal{X}}}{s} \,, \tag{3.28}$$

where s is the entropy density. Under the assumption that the entropy $S = a^3 s$ is constant, we obtain

$$\dot{Y}_{\mathcal{X}} = \frac{\dot{n}_{\mathcal{X}}}{s} + 3H \frac{n_{\mathcal{X}}}{s} \,. \tag{3.29}$$

Dividing Eq. (3.26) by s and using the above equation we obtain

$$\dot{Y}_{\mathcal{X}} = -s \langle \sigma v \rangle_{\mathrm{eff}} \big(Y_{\mathcal{X}}^2 - (Y_{\mathcal{X}}^{\mathrm{eq}})^2 \big) \,. \tag{3.30}$$

As a final step, we want to change the coordinates from the time t to a temperature dependent variable $x = m_1/T$. In order to do this, we calculate $\dot{Y}_{\mathcal{X}}$ in terms of x

$$\frac{\mathrm{d}Y_{\mathcal{X}}}{\mathrm{d}t} = \frac{\mathrm{d}Y_{\mathcal{X}}}{\mathrm{d}x} \frac{\mathrm{d}x}{\mathrm{d}t} = \frac{\mathrm{d}Y_{\mathcal{X}}}{\mathrm{d}x} \left(-\frac{x}{T} \frac{\mathrm{d}T}{\mathrm{d}t} \right) = \frac{\mathrm{d}Y_{\mathcal{X}}}{\mathrm{d}x} \left(-\frac{x}{T} \frac{\mathrm{d}s}{\mathrm{d}t} \frac{\mathrm{d}T}{\mathrm{d}s} \right) = \frac{\mathrm{d}Y_{\mathcal{X}}}{\mathrm{d}x} \left(3Hs \frac{x}{T} \frac{\mathrm{d}T}{\mathrm{d}s} \right) . \tag{3.31}$$

For the Hubble constant H we use Eq. (2.23), for which, in a radiation dominated, flat universe we have $\Omega_k = \Omega_m = \Omega_\Lambda = 0$. Together with

$$s = h_{\mathrm{eff}}(T) \frac{2\pi^2}{45} T^3 \quad , \quad \rho = g_{\mathrm{eff}}(T) \frac{\pi^2}{30} T^4 \,, \tag{3.32}$$

where $h_{\text{eff}}(T)$ are the effective degrees of freedom with respect to entropy, we obtain the final form for the Boltzmann equation of the DS particle density

$$\frac{\mathrm{d}Y_{\mathcal{X}}}{\mathrm{d}x} = -\sqrt{\frac{\pi}{45G}}\frac{g_*^{1/2}(T)m_1}{x^2}\langle\sigma v\rangle_{\text{eff}}\left(Y_{\mathcal{X}}^2 - (Y_{\mathcal{X}}^{\text{eq}})^2\right). \tag{3.33}$$

Here, G is the gravitational constant, $g_*^{1/2}(T)$ is defined as

$$g_*^{1/2}(T) = \frac{h_{\text{eff}}}{\sqrt{g_{\text{eff}}}}\left(1 + \frac{T}{3h_{\text{eff}}}\frac{\mathrm{d}h_{\text{eff}}}{\mathrm{d}T}\right), \tag{3.34}$$

and the equilibrium yield is given by

$$Y_{\mathcal{X}}^{\text{eq}} = \frac{n_{\mathcal{X}}^{\text{eq}}}{s} = \frac{1}{2\pi^2 s}\sum_{i=1}^{N} g_i \int \mathrm{d}E_i E_i\sqrt{E_i^2 - m_i^2}e^{-E_i/T} = \frac{45x^2}{4\pi^2 h_{\text{eff}}}\sum_{i=1}^{N} g_i\frac{m_i^2}{m_1^2}K_2\left(\frac{m_i}{m_1}x\right), \tag{3.35}$$

where K_n is the modified Bessel function of the second kind of order n.

To obtain the relic density we need to solve Eq. (3.33), starting at $x = 0$ with the initial condition $Y_{\mathcal{X}}(0) = Y_{\mathcal{X}}^{\text{eq}}(0)$ up to $x_0 = m_1/T_0$, where T_0 is given by Eq. (2.34). This will give us today's yield $Y_0 = n_0/s$ which we can plug into Eq. (2.24) together with today's entropy density to obtain the relic density

$$\Omega_{\mathcal{X}}h^2 = \frac{m_1 Y_0 s_0}{3M_{\text{pl}}^2 H_0^2}h^2 \approx 2.742\frac{m_1}{\text{GeV}}Y_0, \tag{3.36}$$

where h is a dimensionless constant given by

$$h = \frac{H_0}{100\frac{\text{km}}{\text{s Mpc}}}, \tag{3.37}$$

and we take the value of H_0 given by Eq. (2.25). In Part II of this thesis we will consider a model with two DM candidates. In this scenario we have to compute the respective Y_0 for each particle and add the two resulting contributions from Eq. (3.36) to obtain the full relic density.

3.3. Thermally Averaged Cross Section

The TAC given via Eqs. (3.19) and (3.27) consists of a 12-dimensional integral, where 4 of these can be eliminated by the delta distribution leaving an 8-dimensional integral we have to solve. The goal is to simplify this as far as possible to ensure a fast and efficient computation for our purposes. To do this we closely follow the derivation performed in Ref. [63]. As a first step we will look at the numerator of Eq. (3.27) and split up the integral into incoming and outgoing momenta such that

$$A \equiv \langle\sigma v\rangle_{\mathcal{X}_i\mathcal{X}_j\leftrightarrow\Psi_k\Psi_l} n_{\mathcal{X}_i}^{\text{eq}} n_{\mathcal{X}_j}^{\text{eq}} = \sum_{i,j}\int \mathrm{d}\Pi_i \mathrm{d}\Pi_j W_{ij}(s)e^{-(E_i+E_j)/T}. \tag{3.38}$$

Here, W_{ij} is the two-particle phase space involving the integrals over the final state momenta

$$W_{ij} = \frac{1}{S_{kl}}\sum_{g_i,g_j,g_k,g_l}\int \mathrm{d}\Pi_k \mathrm{d}\Pi_l |\mathcal{M}|^2_{\mathcal{X}_i\mathcal{X}_j\leftrightarrow\Psi_k\Psi_l}\delta^4(p_i + p_j - p_k - p_l), \tag{3.39}$$

where S_{kl} is a symmetry factor in case of identical final state particles. The two-body phase space in Eq. (3.39) is well known and simplifies to [64]

$$W_{ij}(s) = \frac{p_{kl}}{8\pi S_{kl}\sqrt{s}} \sum_{g_i,g_j,g_k,g_l} \int_{-1}^{1} |\mathcal{M}|^2_{\mathcal{X}_i\mathcal{X}_j\leftrightarrow\Psi_k\Psi_l} \mathrm{d}\cos\theta \,, \tag{3.40}$$

with

$$p_{kl}(s) = \frac{\sqrt{[s-(m_k+m_l)^2]\,[s-(m_k-m_l)^2]}}{2\sqrt{s}} \,, \tag{3.41}$$

the Mandelstam variable $s = (p_i + p_j)^2 = (p_k + p_l)^2$ and θ being the angle between the incoming momentum $\mathbf{p}_i$ and the outgoing momentum $\mathbf{p}_l$. Next, we rewrite the phase space volume over the initial state particles by using the energy momentum relation and integrating over trivial angle contributions giving

$$\mathrm{d}\Pi_i \mathrm{d}\Pi_j = \frac{1}{2(2\pi)^4} |\mathbf{p}_i||\mathbf{p}_j| \mathrm{d}E_i \mathrm{d}E_j \mathrm{d}\cos\beta \,. \tag{3.42}$$

Here, β is the angle between the incoming momenta $\mathbf{p}_i$ and $\mathbf{p}_j$. Following the prescription in Ref. [63] we perform a variable transformation such that

$$\begin{aligned} E_+ =& E_1 + E_2 \,, \\ E_- =& E_1 - E_2 \,, \\ s =& m_i^2 + m_j^2 + 2E_iE_j - 2|\mathbf{p}_i||\mathbf{p}_j|\cos\beta \,, \end{aligned} \tag{3.43}$$

which gives the Jacobian

$$\mathrm{d}E_i \mathrm{d}E_j \mathrm{d}\cos\beta \to \frac{\mathrm{d}E_+ \mathrm{d}E_- \mathrm{d}s}{4|\mathbf{p}_i||\mathbf{p}_j|} \,, \tag{3.44}$$

and the integration region

$$s \geq (m_i + m_j)^2 \,, \tag{3.45}$$

$$E_+ \geq \sqrt{s} \,, \tag{3.46}$$

$$2p_{ij}\sqrt{\frac{E_+^2 - s}{s}} \geq \left| E_- - E_+ \frac{m_j^2 - m_i^2}{s} \right| . \tag{3.47}$$

Note that Eq. (3.38) only depends on the variables E_+ and s. This allows us to integrate over E_- trivially and obtain for the phase space volume

$$\mathrm{d}\Pi_i \mathrm{d}\Pi_j = \frac{p_{ij}(s)}{2(2\pi)^4} \sqrt{\frac{E_+^2 - s}{s}} \mathrm{d}E_+ \mathrm{d}s \,. \tag{3.48}$$

Plugging Eq. (3.48) back into Eq. (3.38) and integrating over E_+ gives

$$A = \frac{T}{32\pi^4} \sum_{ij} \int p_{ij}(s) W_{ij}(s) K_1\left(\frac{\sqrt{s}}{T}\right) \mathrm{d}s \,. \tag{3.49}$$

For the denominator of Eq. (3.27) we only need to simplify $n_{\mathcal{X}}^{\mathrm{eq}}$ which gives

$$n_{\mathcal{X}}^{\mathrm{eq}} = \sum_i n_{\mathcal{X}_i}^{\mathrm{eq}} = \sum_{i,g_i} \int \frac{\mathrm{d}^3 p_i}{(2\pi)^3} e^{-E_i/T} = \frac{T}{2\pi^2} \sum_i g_i m_i^2 K_2\left(\frac{m_i}{T}\right) . \tag{3.50}$$

Putting everything together, we obtain for the TAC

$$\langle \sigma v \rangle_{\text{eff}} = \frac{\sum_{i,j} \int_{(m_i+m_j)^2}^{\infty} p_{ij}(s) W_{ij}(s) K_1\left(\frac{\sqrt{s}}{m_1} x\right) \mathrm{d}s}{8T \left[\sum_i g_i m_i^2 K_2\left(\frac{m_i}{m_1} x\right)\right]^2} . \tag{3.51}$$

An important feature of Eq. (3.51) is that co-annihilation channels where the DS mass is larger than the DM mass are exponentially suppressed. We can see this by approximating $K_1(x)$ for large x as [65]

$$K_n(x) \approx \sqrt{\frac{\pi}{2x}} e^{-x} . \tag{3.52}$$

Meaning the largest contribution to the integral in Eq. (3.51) will come from s values near the rest mass, while higher values are Boltzmann suppressed. This allows us to do a comparison of the strength of the DM annihilation processes compared to the ones from DS co-annihilations by considering the fraction between their respective Boltzmann suppression at the rest mass

$$\frac{K_1\left((m_i + m_j)\frac{x}{m_1}\right)}{K_1\left(2m_1 \frac{x}{m_1}\right)} \propto e^{-\frac{x}{m_1}(m_i+m_j-2m_1)} . \tag{3.53}$$

Since $m_{i,j} \geq m_1$, the exponent will always be negative resulting in a suppression for large DS particle masses. This means that to obtain efficient co-annihilation, the masses of the considered DS particles must be close to the DM mass.

CHAPTER 4

RelExt: A Tool for the Exploration of Dark Matter Models

Up until now we have discussed the theory needed to understand the mechanism of freeze-out from which the DM relic abundance can be generated thermally. The first major project of this thesis is to take the necessary formulas and implement them into a code which is able to compute the relic density numerically for an arbitrary model with a $\mathbb{Z}_2$ symmetry. The description of the code structure and its algorithms is based on our published manual [66].

Many codes exist which calculate DM observables such as `SuperIso Relic` [67], `DarkSUSY` [68], `MicrOMEGAs` [69–74], `MadDM` [75–77] and `DarkPACK` [78]. All of these codes are able to compute the relic density of WIMP particles via freeze-out. The codes `SuperIso Relic` and `DarkSUSY` were originally written for Supersymmetric (SUSY) models. In the case of `DarkSUSY` the user can additionally provide the TAC to compute the relic density in their given model. The codes `MicrOMEGAs` and `MadDM` automatically compute the relevant matrix elements via `CalcHep` [79] and `MadGraph5aMC@NLO` [80], respectively. `DarkPACK` also allows to compute the relic density for an arbitrary model using the `C++` package `MARTY` [81], which is a tool for symbolic calculations of BSM quantities such as matrix elements. For more details on the different tools we refer to Ref. [82].

In this chapter we will present our new code `RelExt`, which is based on `Mathematica` [83] and `C++`. The users solely have to provide their `FeynRules` [84] model files, which `RelExt` uses to automatically generate the necessary tree-level $2 \to 2$ matrix elements and to compute the relic density. What separates this code from the previously mentioned ones is that it includes scan procedures, which allow the user to search the parameter space such that the observed relic density is obtained within the experimental limits. This can be used to study the phenomenological implications for the considered model with respect to current collider and DM experiments. Further, it can be used to investigate which models are favored to produce the correct relic density, which will give insights into future model building. Although the code in the current version only includes the tree-level processes, it is set up such that higher-order corrections can be implemented in future updates.

The code is open-source and can be downloaded in its current version from

`https://github.com/jplotnikov99/RelExt`.

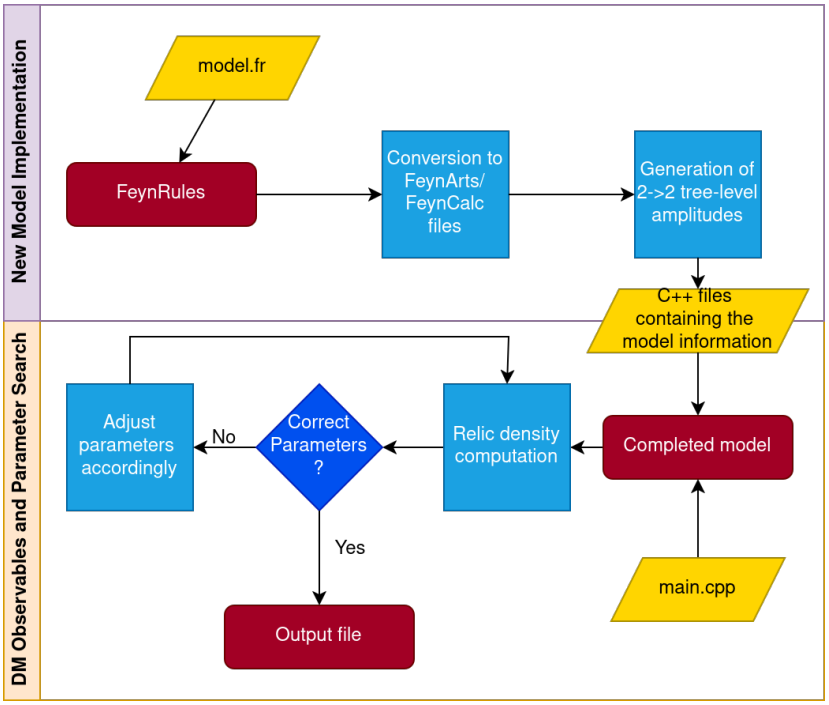

Figure 4.1.: Flowchart of `RelExt`. Taken from Ref. [66].

When downloading the code, it will include the following already implemented and tested models: the complex singlet extension of the Standard Model (CxSM) [85–92], the Next-to-2-Higgs-Doublet Model (N2HDM) in its dark doublet phase (DDP) [93, 94], the model CP in the Dark (CPVDM) [95, 96], the Two-Real-scalar-Singlet Model (TRSM) [97, 98], and the BDM5 [99, 100]. As already mentioned, new models can be implemented by providing the corresponding `FeynRules` model files. Important to note is that the code at this stage is only able to deal with models that have one DM candidate. Additionally, if the (co-)annihilation processes are CP-violating the derivation in Sec. 3.2 breaks down and as such cannot be treated by `RelExt`.

4.1. Code Overview

We start by giving a rough overview of the structure of the code. A more detailed breakdown will be given in the upcoming sections. As can be seen in Fig. 4.1, `RelExt` consists of two distinct parts. These two parts are denoted by "New Model Implementation" and "DM Observables and Parameter Search", respectively.

New Model Implementation
In the first part of the code the users can provide the `FeynRules` model files necessary for their model. Using these model files, `RelExt` generates the corresponding `FeynArts/FeynCalc` [101–103] model files. The code uses the packages `FeynArts` and `FeynCalc` to generate all necessary $2 \to 2$ (co-)annihilation matrix elements. Additionally, it will generate further quantities such as decay channels and information about s-channel resonances. All the information generated by this part of the code is then translated into `C++` files, that can be used in the second part of the code.

DM Observable and Parameter Search
Once a model is translated into `C++` the second part of the code can be used separately and does not rely on any components of the first part, i.e. `Mathematica` is not needed for this part. Here, the code is able to search the parameter space of the model for parameter configurations

which are able to saturate the experimental limit on the relic density. In order to do this, the code computes the TACs, the necessary total decay widths of the virtual particles, as well as the running of the couplings, which enter the interaction vertices. The Boltzmann equation given in Eq. (3.33) is then solved numerically to obtain today's relic density. Each model contains its own `main.cpp` file, which the users can modify and on which they apply different search algorithms on the parameter space of the model. The relic density as well as the needed parameters are then saved in an output file specified by the user. Appendix A.1 provides a more detailed discussion of the class structure underlying this part of the code.

4.2. Structure and Description of the Algorithms

Depending on the BSM model under consideration the set of input parameters can be more or less extensive. The interplay between these parameters can make it difficult to find viable relic density values necessary to perform meaningful phenomenological investigations. To find viable parameter regions, extensive parameter scans have to be performed, which can be quite time consuming. Because of this, there are two main objectives we want to accomplish with `RelExt`:

- Solve the Boltzmann equation given in Eq. (3.33) as fast and as precisely as possible, making large parameter scans feasible.
- Search the parameter space efficiently to obtain several viable parameter regions in a short amount of time.

In this section, we will describe the important algorithms and numerical methods used throughout the code, which allow for a fast computation of the relic density and subsequently enable an efficient parameter search. The code for the algorithms used in the `C++` part of `RelExt` is given in Appendix A.2.

4.2.1. Amplitude Generation

To calculate the relic density, we first need to generate the relevant (co-)annihilation matrix elements used in Eq. (3.40). As already mentioned, this is done by the first part of the code with the help of the `Mathematica` packages `FeynArts` and `FeynCalc`. The code automatically recognizes the DS particles provided by the model files and generates all possible tree-level $2 \to 2$ diagrams, with two DS particles in the initial state and two visible particles in the final state. To avoid unnecessary computation at later stages, we filter out processes which are identical up to a charge conjugation. From these diagrams we get the analytical expressions for the matrix elements using `FeynCalc`. Since BSM models can contain numerous additional particles, this can lead to matrix elements consisting of many diagrams already at tree-level. To ensure a fast calculation of the matrix elements squared we keep the analytical expression of each diagram in a list. We then loop over this list multiplying individual diagrams accordingly and sum them to obtain $|\mathcal{M}|^2$. In the example of a matrix element consisting of 2 diagrams with analytical expressions A and B, $|\mathcal{M}|^2$ is given by

$$|\mathcal{M}|^2 = |A|^2 + |B|^2 + 2\mathrm{Re}(A^* B)\,. \tag{4.1}$$

Many of these matrix elements will have similar coupling structures that need to be evaluated. We want to avoid computing the same coupling appearing in different amplitudes multiple times as they can be quite large depending on the model under consideration. In order to do this, the code recognizes couplings or combination of couplings that appear more than once throughout all amplitudes and stores them in tokens which will only be computed once per parameter point.

To obtain the TAC given in Eq. (3.51) we have to integrate over the Mandelstam variable s. In the amplitudes this can lead to divergencies resulting from s-channel propagators. To avoid this, we use the Breit-Wigner formula, and make the replacement

$$\frac{1}{s - m_{\text{med}}^2} \to \frac{1}{s - m_{\text{med}}^2 - i\Gamma_{\text{med}} m_{\text{med}}}\,, \tag{4.2}$$

where m_{med} and Γ_{med} are the mass and total decay width of the mediator particle, respectively. The code automatically identifies all s-channel mediator particles and is able to calculate their total decay widths. Here, the code differentiates between scalar particles, fermions and vector bosons. In the case of scalar and pseudoscalar particles, the code identifies all decay channels at tree level, saves their coupling modifiers and converts them into `C++` code. These coupling modifiers are used to compute the total decay widths including higher order QCD corrections for which we mostly follow the implementation provided by `HDECAY` [104, 105] as well as the formulas provided in Refs. [106, 107]. For all SM particles, except for the top-quark and the Higgs boson, the user has to provide the correct total decay width in the corresponding model file. The top-quark decay width, as well as the decay widths of additional non-scalar particles in the visible sector are calculated by the code at tree-level. Further, in some kinematic regions it is possible to encounter t/u-channel divergencies. To cure these, we use a similar approach as `MicrOMEGAs` and introduce a regulator width given by $\Gamma_j = m_j/1000$ [108]. Using this width leads to a deviation of less than 1% outside of the divergent regions compared to the zero width result.

In the case of DM (co-)annihilation into quarks we consider running quarks masses in the final states, expect for the top quark, where we take the pole mass. We evaluate the quark masses at next-to-next-to-next-to leading log order (N^3LL) taken at the scale given by twice the DM mass. `RelExt` always uses the following $\overline{\text{MS}}$ masses as input for the bottom, charm and strange quark at the scale Q given in the brackets, respectively: $\overline{m}_b(\overline{m}_b) = 4.18$ GeV, $\overline{m}_c(3\,\text{GeV}) = 0.986$ GeV, and $\overline{m}_s(2\,\text{GeV}) = 0.095$ GeV. For the first two quark generations as well as the leptons, the user has to provide the masses. The running masses are also used in the computation of the total decay widths of the scalars.

4.2.2. Computation of the TAC

The next step in obtaining the relic density, is to integrate over $\cos\theta$ in Eq. (3.40). Here, we first estimate the integrand using a composite Simpson's 3/8 method [109]. This estimate is then used in the termination criterion in the adaptive Simpson 3/8 computation of the integral. The usage of the estimate leads to rapid convergence as regions which are small compared to the estimate will terminate faster. Next we need to integrate Eq. (3.51) over the Mandelstam variable s. This is the most time consuming part of the whole relic density computation and requires therefore most optimization. We want to compute as little as possible while still retaining a good accuracy of the TAC. For this we make use of the relation shown in Eq. (3.53) by neglecting processes that are too far away from the DM rest mass. In order to accomplish this we first sort all the (co-)annihilation channels into batches of equal rest mass via the condition

$$\max(m_i + m_j, m_k + m_l)\,, \tag{4.3}$$

where $m_{i/j}$ are the initial state DS particles and $m_{k/l}$ are the outgoing SM particles. In Tab. 4.1 we can see an example of how this data structure looks like. Here, we consider a DS consisting of two real singlet fields, with masses chosen to better illustrate how the channel sorting works. We see that for most channels the DS particles are responsible for the rest mass of the given process. This is to be expected for WIMPs as they are heavier than most SM particles. However, some of the SM or BSM particles, such as the Higgs boson, the top-quark or a second Higgs particle, can be heavier than the DS particles. In such cases we

Rest mass [GeV]	Involved processes
200	$\mathcal{X}_1\mathcal{X}_1 \to e\bar{e}$, $\mu\bar{\mu}$, $\tau\bar{\tau}$, $u\bar{u}$, $d\bar{d}$, $c\bar{c}$, $s\bar{s}$, $b\bar{b}$, ZZ, W^+W^-
250	$\mathcal{X}_1\mathcal{X}_1 \to hh$
260	$\mathcal{X}_1\mathcal{X}_2 \to e\bar{e}$, $\mu\bar{\mu}$, $\tau\bar{\tau}$, $u\bar{u}$, $d\bar{d}$, $c\bar{c}$, $s\bar{s}$, $b\bar{b}$, ZZ, W^+W^-, hh
320	$\mathcal{X}_2\mathcal{X}_2 \to e\bar{e}$, $\mu\bar{\mu}$, $\tau\bar{\tau}$, $u\bar{u}$, $d\bar{d}$, $c\bar{c}$, $s\bar{s}$, $b\bar{b}$, ZZ, W^+W^-, hh
350	$\mathcal{X}_1\mathcal{X}_1$, $\mathcal{X}_1\mathcal{X}_2$, $\mathcal{X}_2\mathcal{X}_2 \to t\bar{t}$

Table 4.1.: Example of how `RelExt` internally sorts the processes for the computation of the TAC. In this example we have two DS singlet particles $\mathcal{X}_1$ and $\mathcal{X}_2$ with a mass of $m_{\mathcal{X}_1} = 100$ GeV and $m_{\mathcal{X}_2} = 160$ GeV, respectively.

obtain additional entries into the data structure as can be seen by the second and last row of Tab. 4.1. We can now define the following criterion that will decide whether or not certain (co-)annihilation processes will be taken into account during the computation [71]

$$B = e^{-x\frac{m_{i(k)}+m_{j(l)}-2m_1}{m_1}} > B_\epsilon\,. \tag{4.4}$$

Here, `RelExt` uses the default value of $B_\epsilon = 10^{-6}$, meaning that channels whose rest mass leads to a B below this number will not be included in the computation of the TAC.

Another trick that we use to speed up the computation, is to expand the modified Bessel functions of the second kind for both the numerator and the denominator. The asymptotic behavior for large x is given by [65]

$$K_n(x) = \sqrt{\frac{\pi}{2x}}e^{-x}\sum_{k=0}^{\infty}\frac{1}{k!(8x)^k}\prod_{j=1}^{k}\left(4n^2-(2j-1)^2\right) \equiv e^{-x}P_n^k(x)\,, \tag{4.5}$$

which allows us write the TAC in Eq. (3.51) in the following form

$$\langle\sigma v\rangle_{\text{eff}} = \frac{\sum_{i,j}\int_{(m_i+m_j)^2}^{\infty} p_{ij}(s)W_{ij}(s)P_1^k\left(\frac{\sqrt{s}}{m_1}x\right)e^{-\frac{\sqrt{s}}{m_1}x}\mathrm{d}s}{8T\left[\sum_i g_i m_i^2 P_2^k\left(\frac{m_l}{m_1}x\right)e^{-\frac{x}{m_1}m_l}\right]^2} \tag{4.6}$$

$$= \sum_{i,j}\int_{(m_i+m_j)^2}^{\infty}\frac{p_{ij}(s)W_{ij}(s)P_1^k\left(\frac{\sqrt{s}}{m_1}x\right)}{8T\left[\sum_l g_l m_l^2 P_2^k\left(\frac{m_l}{m_1}x\right)e^{-\frac{x}{m_1}(m_l-\sqrt{s}/2)}\right]^2}\mathrm{d}s\,. \tag{4.7}$$

To make sure that the error between the exact Bessel function and the approximation is sufficiently small we expand up to the sixth order. This already leads to a relative error of $\sim 1.74\cdot 10^{-5}$ at $x = 5$, while decreasing the evaluation time significantly. Looking at Eq. (4.6) we notice a problem. For large values of x (≈ 1000) the exponential functions in the numerator and the denominator cannot be evaluated anymore by `C++` as they will result in an underflow error. However, the value at today's temperature is roughly $x_0 \approx 10^{15}$ for a DM mass of 500 GeV. Even though the (co-)annihilation of the DS particles become less relevant at later times, i.e. larger x, we still want to solve the Boltzmann equation as far as possible to obtain a more precise result. This is done by casting Eq. (4.6) into Eq. (4.7). In this form, the exponential function only appears in the denominator and due to the exponents now being subtracted from each other, we can evaluate it for larger values of x. With this we can reach x values of up to $x = 10^7$. However, this results in another problem. In Eq. (4.6) we had to

evaluate the exponential functions in the denominator only once for a given x value, while in Eq. (4.7) we have to evaluate them every time we insert a new value of s, slowing down the computation. For this reason, `RelExt` first checks if it can evaluate the exponential functions in Eq. (4.6). If their arguments are too large Eq. (4.7) is used instead.

Optimizing the exponential functions might seem irrelevant at first sight, since the TAC also depends on W_{ij} which can contain large expressions for the amplitudes, especially in models with many additional particles. Having to evaluate large expressions will be of course more computationally demanding than simply computing the exponential functions. However, here we can use a clever trick by noticing that the combination $p_{ij}(s)W_{ij}(s)$ does not depend on x. While integrating over s, the integrator will choose always the same s-abscissas to obtain a value for the integral, meaning that $p_{ij}(s)W_{ij}(s)$ will be evaluated at the same s-values for different x. For this reason `RelExt` saves the results of the x-independent part in a hashmap, making it instant to evaluate them for the next iteration in x. This means that during the computation of the relic density, the first x-value called will take the most amount of time to evaluate, while the remaining ones will be bounded by the evaluation of the x-dependent part.

The next step is to integrate over s. Here, we have to make sure that we treat possible resonances appearing from s-channels accordingly. Simply integrating over s with an arbitrary numerical method can lead to the method missing these peaks if they are very sharp. To avoid this, the code integrates the peaks separately as it knows their locations which were provided by the `Mathematica` code. The algorithm to integrate over s is done in 4 steps:

1. Transform the integral to obtain finite boundaries via the substitution $x = (m_i + m_j)^2 + (1-u)/u$. This changes the boundaries such that $\left[(m_i+m_j)^2, \infty\right) \to (0, 1]$ and gives the Jacobian $1/u^2$.

2. Set additional boundaries inside the integration region which separate the peak regions from the remaining regions of the integrand.

3. Loop over the process batches with identical rest masses (see Tab. 4.1) and compute an estimate of the integral. The peaks are integrated precisely already at this stage.

4. Loop over the processes batches again, this time compute the integral precisely using the estimate obtained from the previous step.

`RelExt` does not create separate boundaries for each peak that occurs between the rest mass and infinity. If the peak is too far away from the boundary and therefore strongly Boltzmann suppressed it will not be treated separately, i.e. if the condition

$$e^{-x\frac{m_{\text{med}}-(m_i+m_j)}{m_1}} > B_\epsilon\,, \tag{4.8}$$

is fulfilled. The peak structure at the resonances given by Eq. (4.2) has the half-maximum points $m_{\text{med}} \pm \Gamma/2$. We want to encapsulate, however, the whole peak when integrating them separately and therefore choose the boundaries $m_{\text{med}} \pm 20\Gamma$ for the peak-integrator.[12] For the peak integration we use again an adaptive Simpson 3/8 method, while for the regions outside of the peaks or if there are no peaks at all we use the adaptive Gauss-Kronrod 15 point algorithm [109]. In Fig. 4.2 we see clearly how the algorithm resolves the integral over two peaks. There we show which of the two integrators evaluate the integrand of the TAC depending on the center-of-mass energy. In this example, we only consider the process $\mathcal{X}\mathcal{X} \to b\bar{b}$, where $\mathcal{X}$ is our DM particle with a mass of $m_{\mathcal{X}} = 60\,\text{GeV}$. The peaks result

[12] It can happen that the peak boundaries exceeds the integration boundary given by the rest mass or overlap with each other. In such a case the peak boundaries are adjusted accordingly (see Appendix A.2).

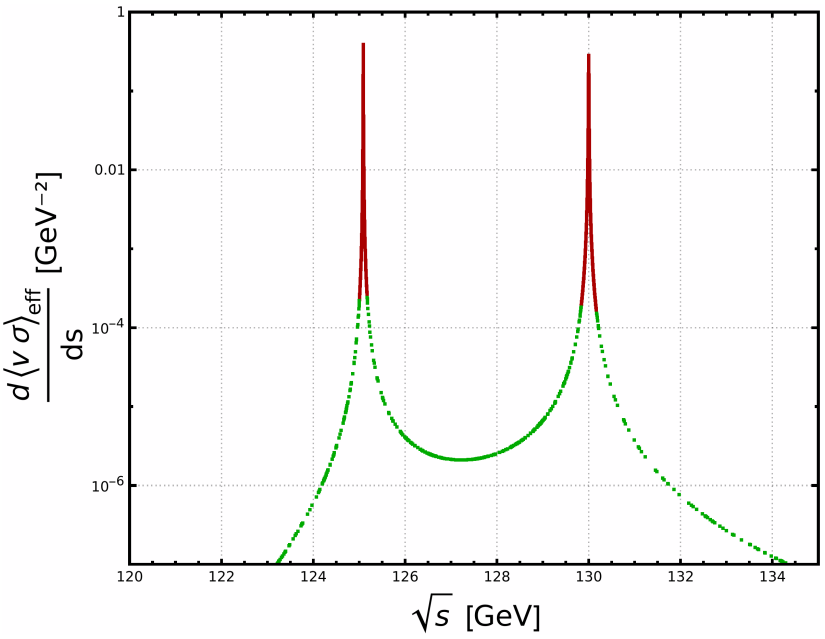

Figure 4.2.: Integrand of the TAC as a function of the center of mass energy. The red points are evaluated by the peak integrator and the green points by the usual integrator.

from the two Higgs bosons appearing in this example point at the masses of $m_{h_1} = 125\,\text{GeV}$ and $m_{h_2} = 130\,\text{GeV}$. We can see that the integrator evaluates a lot more points in the peak regions (red points) to obtain a more precise result, while for regions outside of the peaks the Gauss-Kronrod integrator needs much less points to reach a sufficient precision.

4.2.3. Solving the Boltzmann Equation

Now that we have optimized the computation of the TAC, the next step is to solve the Boltzmann equation in Eq. (3.33). We want to track the evolution of the yield starting from $x = 0$ up to the current temperature x_0. The first thing to realize is that for high temperatures, i.e. low x, the yield will remain in equilibrium with the thermal bath. So instead of starting our solver at $x = 0$ we want to start at a later time when the DS bath begins to decouple from the thermal bath. As already stated, we call this decoupling temperature, the freeze-out temperature x_f. To determine x_f we follow the derivation of Ref. [110]. We start by defining a new quantity $\tilde{Y}_\mathcal{X} = Y_\mathcal{X} - Y_\mathcal{X}^{\text{eq}}$ which turns Eq. (3.33) into

$$\frac{\mathrm{d}\tilde{Y}_\mathcal{X}}{\mathrm{d}x} = -\sqrt{\frac{\pi}{45G}}\frac{g_*^{1/2}(T)m_1}{x^2}\langle\sigma v\rangle_{\text{eff}}\tilde{Y}_\mathcal{X}\left(\tilde{Y}_\mathcal{X} + 2Y_\mathcal{X}^{\text{eq}}\right) - \frac{\mathrm{d}Y_\mathcal{X}^{\text{eq}}}{\mathrm{d}x}\,. \tag{4.9}$$

To first order we can neglect the left-hand side of Eq. (4.9) since $Y_\mathcal{X}$ follows the equilibrium distribution. We further introduce a new constant δ which is defined via $\tilde{Y}_\mathcal{X} = \delta Y_\mathcal{X}^{\text{eq}}$. Using the aforementioned definition and dividing Eq. (4.9) by $Y_\mathcal{X}^{\text{eq}}$ gives

$$\frac{\mathrm{d}\ln Y_\mathcal{X}^{\text{eq}}}{\mathrm{d}x} + \sqrt{\frac{\pi}{45G}}\frac{g_*^{1/2}(T)m_1}{x^2}\langle\sigma v\rangle_{\text{eff}}Y_\mathcal{X}^{\text{eq}}\delta\left(\delta + 2\right) = 0\,. \tag{4.10}$$

We arrived at a transcendental equation for x, which we have to solve to obtain the freeze-out point. We can choose δ freely as it is simply a measure of how much the yield should differ from its equilibrium value, when we solve Eq. (4.10). A δ which is too large will lead to a wrong estimate of the freeze-out point, while a small δ will be more accurate but requires us to solve more of the remaining evolution. The previous statement is true if we evolve

the Boltzmann equation starting from x_f until x_0 with any arbitrary ordinary differential equation solver. However, there is another way to solve the Boltzmann equation which is called the freeze-out approximation. In this approximation, we again determine the freeze-out point using Eq. (4.10), but instead of evolving the Boltzmann equation, we assume that $Y_\mathcal{X}^{\mathrm{eq}} \ll Y_\mathcal{X}$ in Eq. (3.33) which allows us to immediately integrate and obtain today's yield via

$$\frac{1}{Y_\mathcal{X}(x_0)} = \frac{1}{(1+\delta)Y_\mathcal{X}^{\mathrm{eq}}(x_\mathrm{f})} + \sqrt{\frac{\pi}{45G}} \int_{x_\mathrm{f}}^{x_0} \mathrm{d}x \frac{g_*^{1/2} m_\mathcal{X}}{x^2} \langle \sigma v \rangle_{\mathrm{eff}} \,. \tag{4.11}$$

In the freeze-out approximation we want a δ which is small enough to determine the freeze-out point accurately with sufficient accuracy, but at the same time is large enough to justify the assumption $Y_\mathcal{X}^{\mathrm{eq}} \ll Y_\mathcal{X}$. In `RelExt` we have the option to either use the faster freeze-out approximation or to solve the Boltzmann equation directly using a Dormand-Prince method. In the freeze-out approximation we use the recommended value of $\delta = 1.5$ to determine the freeze-out point. We found this to be accurate up to a few percent compared to the full numerical result. This behavior was also observed in Refs. [70, 110]. When we want to solve the Boltzmann equation using the Dormand-Prince method the freeze-out point is determined with $\delta = 0.1$.

We have not yet talked about how we actually solve Eq. (4.10) in `RelExt`. By experience we know that the freeze-out point for couplings at the weak scale is approximately at $x_f \sim 20-30$. For couplings much larger or much smaller than the weak scale this is not true. However, in such scenarios the relic density will either be heavily under-produced or over-produced. For this reason `RelExt` will search in the region $x \in [5, 50]$ for a solution of Eq. (4.10). One idea would be to simply run a bisection algorithm on this region. However, as discussed in Sec. 4.2.2 this will lead the code to include many channels in its computation for the lower boundary of x, which we ultimately might not care about at x_f and above. To circumvent this issue, we start at the upper boundary and move in steps of $\Delta x = -2$ towards the lower boundary while keeping track of the sign of Eq. (4.10). Once the sign flips we execute the bisection method between the current and the previous x-value to obtain the freeze-out point.

4.2.4. Parameter Search

With the solver of the Boltzmann equation set up we can now easily calculate the relic density via Eq. (3.36) and therefore move on to finding parameter regions which generate the observed relic density of Eq. (1.1). Finding these regions can become very cumbersome, especially for models with many parameters. To combat this difficulty, we implemented three algorithms into `RelExt` with different strengths to find viable parameter regions.

The first algorithm uses a Monte Carlo approach to filter out the good parameter regions and reuse them for future parameter scans. To accomplish this, we first lay a grid on the parameter region we want to investigate. This is done by dividing the parameter ranges of each parameter into N_b equally spaced bins, resulting in a total of $N_b^{N_p}$ number of cells that cover the parameter space, where N_p is the number of parameters. In classical Monte Carlo problems like e.g. the integration of higher-dimensional integrals, we want to adjust our sampling method to match the regions of interest. This means that we want to sample more regions where the integrand is large than regions where the integrand is small. The crucial point is that in such a case we still sample the whole region, but vary the sample density. In a parameter search we do not care about the regions which give us a bad relic density and

therefore do not want to keep sampling them. In this context we define how *good* or *bad* a parameter point is by assigning it a weight w which ranges from 0 to 1 via

$$w = \begin{cases} \left(\frac{\Omega_d h^2}{\Omega_c h^2}\right)^2, & \Omega_d h^2 < \Omega_c h^2 \\ \left(\frac{\Omega_c h^2}{\Omega_d h^2}\right)^2, & \Omega_d h^2 > \Omega_c h^2 \end{cases} . \tag{4.12}$$

Here, $\Omega_d h^2$ is the desired relic density, that we want to obtain and Ωh^2 is the computed relic density for the current parameter point. Now we can set up a random scan and `RelExt` will keep track of the N_{best} best cells during the process. The tracking of the best cells works as follows. When a new parameter point is generated it will be assigned to a unique cell of the grid. `RelExt` will first fill up an array with unique cells and their weights, until it reaches a length of N_{best}. While it fills up the array, it keeps track of the worst cell among them. If now a new point is generated whose w is larger than the one from the worst cell, it will be substituted with the new cell. However, if the array already contains the cell, it will only update the w value of this cell based on if its larger than the currently saved value. Once the array of best cells is full, we set a probability p_b which determines the probability that newly generated points are randomly generated from one of the best cells. This leaves a probability of $1 - p_b$ that the new point is generated randomly. After the scan is done `RelExt` generates an output file with the best cells, which can be reused for future scans.

In the Monte Carlo approach we hope that with a large enough sample size the good parameter regions will become apparent such that we can focus our sampling on these regions. However, in many cases this will not be sufficient as only very few cells are able to generate $\Omega_d h^2$ and within these cells we still have to find the parameter combination which results in $\Omega_d h^2$ with a reasonable uncertainty. This means that even if we keep scanning in the best cells, it might take a long time until we find points which generate the desired relic density. In such a case, the second algorithm can be employed - the random walk. With this algorithm, we start with an initial parameter point and try to improve it with each step. We do this by changing each parameter value x_i to a one new one x_i' via

$$x_i' = x_i(1 + \gamma_i) . \tag{4.13}$$

The γ_i is a randomly chosen step size in the range $[-\gamma_{\text{max}}, \gamma_{\text{max}}]$, where γ_{max} is a constant of our choice. At each step that we take we compute $\Delta\Omega h^2 = \Omega_c h^2 - \Omega_d h^2$ and compare it with its value before the step. If $\Delta\Omega h^2$ is larger than the previous value, we take a new step via Eq. (4.13). In the case that it gets smaller, we keep going in the same direction by repeating the same step. This process continues until $\Omega_d h^2$ is reached within the specified uncertainty or until the maximal number of iterations is reached.

The previous algorithms are designed for models with many parameters. But if we want to study models with few parameters we might want to investigate the influence of single parameters on the relic density more precisely. For such scenarios the third algorithm was developed. This algorithm tries to obtain $\Omega_d h^2$ by changing a single parameter of the model. To accomplish this, the algorithm operates in three modes, with the following goals.

Vanguard
Follows the gradient which minimizes $\Delta\Omega h^2$ in large steps. Its goal is to find out if $\Delta\Omega h^2$ can become 0 or if we are stuck in a local minimum.

Descent
If the Vanguard mode finds that we are stuck in a local minimum, this mode applies a gradient descent algorithm to find this minimum.

Bisect
If the Vanguard mode finds that $\Delta\Omega h^2$ can become zero, a bisection algorithm is used to determine the parameter which results in $\Delta\Omega h^2 \approx 0$.

The search algorithm always starts in the vanguard mode. While the mode tries to minimize $\Delta\Omega h^2$, we keep track of its sign and the sign of its derivative with respect to the parameter that we vary. This can result in two possible scenarios:

1. The sign of $\Delta\Omega h^2$ stays the same from one step to another, but the sign of its derivative flips. In this scenario we are stuck in a local minimum and switch to the Descent mode.
2. The sign of $\Delta\Omega h^2$ flips from one step to another. In this case, we crossed a line in the parameter space where $\Delta\Omega h^2 = 0$ and switch to the Bisect mode.

There are scenarios, in which the local minimum can be very sharp, but contains two or more lines which cross the $\Delta\Omega h^2 = 0$ line. The algorithm will first falsely identify that we have a local minimum, but still keeps track of potential sign flips while walking towards the minimum. If then a sign flip occurs, it will be able to switch to the Bisect mode and find one of the $\Delta\Omega h^2 = 0$ lines. To summarize, this algorithm will find the parameter value which results in either a local minimum of $\Delta\Omega h^2$ or in $\Delta\Omega h^2 \approx 0$ given an initial starting point.

4.3. Validation

To ensure that `RelExt` works as expected we compared the relic density computed by it, which we will call $\Omega_{\texttt{RelExt}} h^2$, with the one from `MicrOMEGAs` $\Omega_{\texttt{Micro}} h^2$. We made sure to test every model implemented in `RelExt` by sampling several random points and ensuring that the input parameters, the running quark masses and the decay widths match the ones from `MicrOMEGAs`. Further, we verified that `RelExt` works in more challenging scenarios, i.e. in the case of (co-)annihilation processes, resonant annihilation, and when threshold effects occur.

In Fig. 4.3 we compare the computed relic density $\Omega_c h^2$ over the DM mass of both codes in the real singlet extension of the SM. This model features a single DM particle and a SM-like-Higgs boson with a mass of 125 GeV who are connected via a trilinear portal coupling λ_{portal}. For the orange and green points we set $\lambda_{\text{portal}} = 0.1$, while for the red and black points we set $\lambda_{\text{portal}} = 6$. The curves show a dip in the relic density at a mass of $m_{\text{DM}} = m_h/2$, where m_h is the Higgs boson mass. This is expected since the annihilation channels become resonant and the relic density is inversely proportional to the TAC. The peaks and dips which follow after the resonant production are thresholds for the on-shell production of the Z-boson, W-boson and Higgs boson, respectively. From the figure it can be inferred that `RelExt` and `MicrOMEGAs` are in very good agreement with a maximum deviation of 6% between the two codes.

Next, we compare the codes in the model CP in the Dark [95,111]. This model is based on an N2HDM with an imposed $\mathbb{Z}_2$ such that the particle spectrum consists of the SM Higgs boson and five additional scalars in the DS, of which three are neutral and two are charged. The lightest neutral DS particle is the DM candidate. We will describe the model in more detail in Sec. 5.2. In Fig. 4.4 we show the relative difference between `RelExt` and `MicrOMEGAs` over the DM mass. The parameter sample was generated using the public code `ScannerS` [112] which checks for all relevant theoretical and experimental constraints. We find that the relative difference between the two codes does not exceed 2%, indicating good agreement.

Although the previous two examples show only small differences between the results of `RelExt` and `MicrOMEGAs`, larger deviations can be found in models where additional visible sector scalar particles get introduced. In such models, these additional scalars can obtain large total widths and can therefore have a large impact on (co-)annihilation channels with masses near the corresponding s-channel resonance. With this in mind, we will look next at the dark

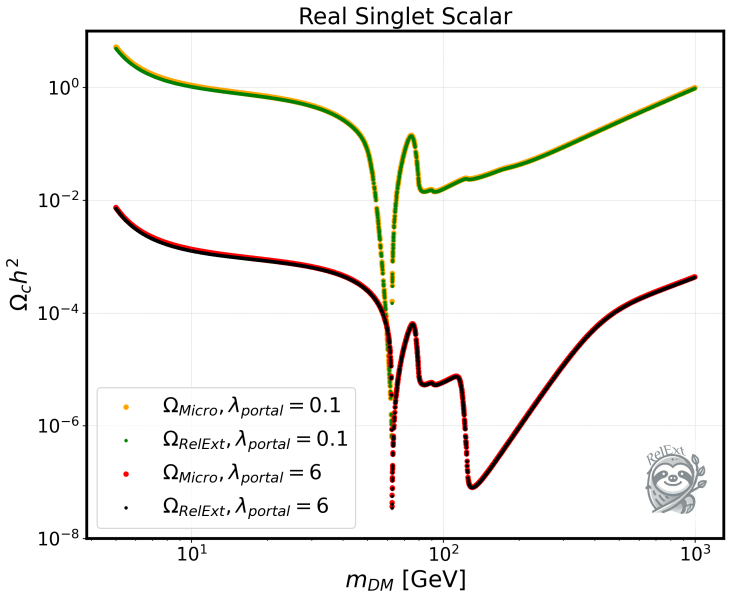

Figure 4.3.: Relic density computed by `RelExt` and `MicrOMEGAs` over the DM mass in the real singlet model. The orange and red points were computed by `MicrOMEGAs` with a Higgs portal coupling of 0.1 and 6, respectively. The green and black points were computed by `RelExt` for the portal couplings 0.1 and 6, respectively. Taken from Ref. [66].

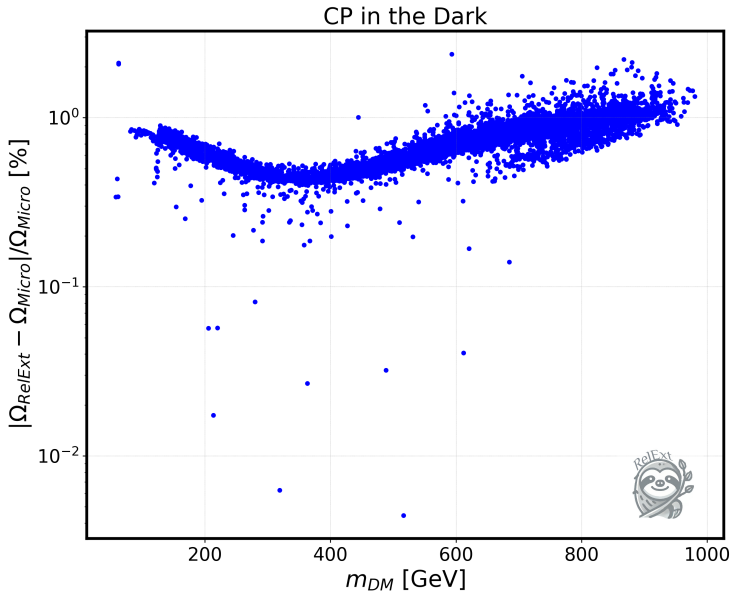

Figure 4.4.: Relative error of the computed relic density between `RelExt` and `MicrOMEGAs` over the DM mass for the model CP int the Dark. Taken from Ref. [66].

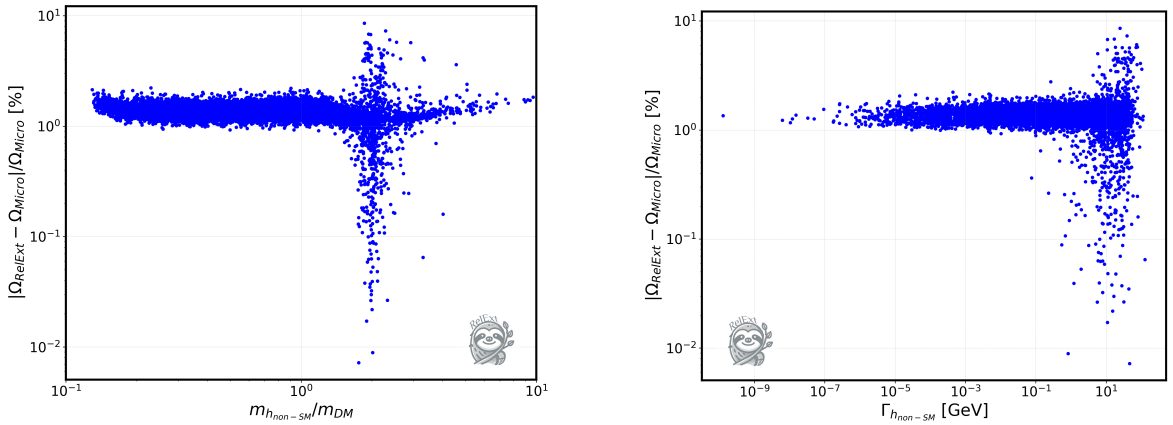

Figure 4.5.: Relative difference of the relic densities calculated with `RelExt` and `MicrOMEGAs` as a function of $m_{h_{\text{non-SM}}}/m_{\text{DM}}$ (left) and $\Gamma_{h_{\text{non-SM}}}$ (right), for the dark doublet phase of the N2HDM. Here, $m_{h_{\text{non-SM}}}$ is the mass of the non-SM-like Higgs boson in the visible sector, and $\Gamma_{h_{\text{non-SM}}}$ its total width. Taken from Ref. [66].

doublet phase of the N2HDM [93]. This model consists of two visible scalar particles, one of which is the SM Higgs boson, and four scalar DS particles, where two are neutral and two are charged. The second, visible, non-SM scalar which we will denote by $h_{\text{non-SM}}$ can obtain a large total width and will therefore be the focus of the following comparison. As in the case of CP in the Dark we performed a scan in the parameter space of the model using `ScannerS` ensuring that all relevant theoretical and experimental constraints are fulfilled. In Fig. 4.5 we show the relative difference in the relic density between the two codes as a function of the ratio between the mass of non-SM Higgs boson and the mass of the DM candidate in the left plot and as a function of the total width $\Gamma_{h_{\text{non-SM}}}$ of the non-SM Higgs boson on the right. We can see that near the resonance region, where $m_{h_{\text{non-SM}}} \approx 2m_{\text{DM}}$ and for large values of $\Gamma_{h_{\text{non-SM}}}$ we obtain points which show a relative difference of up to 9%. This difference comes from the way s-channel resonances are implemented in each code. In `RelExt`, the replacement in Eq. (4.2) is made independent of the current s-value that is used. However, `MicrOMEGAs` handles such resonances by introducing the aforementioned replacement only if the s-value is approaching this resonance. This means the authors of `MicrOMEGAs` obtain two regions between which they interpolate - the resonant and the non-resonant region. To show the difference more clearly, we will look at the DM DM $\to W^+W^-$ cross section for the benchmark point given Tab. 4.2 for which the relative difference in the relic density is 7.3%. The cross section is shown in Fig. 4.6 plotted as a function of the center mass energy $\sqrt{s}$. The plot shows a clear deviation between the two codes at a $\sqrt{s}$-value slightly below the resonance of the non-SM Higgs boson. This is exactly the region where `MicrOMEGAs` uses the interpolated values between the resonant and non-resonant regions. To confirm that the main reason for large deviations in the relic density between `RelExt` and `MicrOMEGAs` comes from the treatment of the resonances we set the width to zero outside the resonance peaks and as a result found good agreement also in these regions.

	N2HDM
$m_{h_{\text{SM}}}$	125.09
$m_{h_{\text{non-SM}}}$	927.082
m_{H_D}	405.215
m_{A_D}	595.853
$m_{H_D^\pm}$	628.737
α	-0.248593
v_s	292.978
m_{22}	133.912
λ_2	3.49988
λ_8	2.34688
$\Gamma_{h_{\text{SM}}}$	0.00490257
$\Gamma_{h_{\text{non-SM}}}$	38.9219
$\Omega_{\text{RelExt}}h^2$	0.000314878
$\Omega_{\text{Micro}}h^2$	0.000339666

Table 4.2.: Benchmark point shown in Fig. 4.6 for the dark doublet phase of the N2HDM. The first 12 lines contain the input parameters, lines 13 and 14 the relic densities from `RelExt` and `MicrOMEGAs`, respectively. More details on the model and its input parameters can be found in Refs. [93, 94]. Input parameters with units are given in GeV.

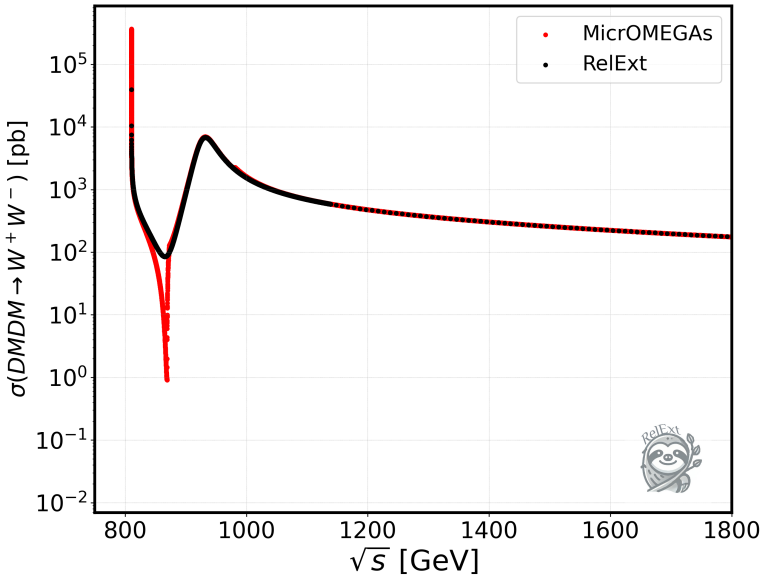

Figure 4.6.: Cross section over the center-of-mass energy for two DM particles annihilating into two W-bosons for the BP-defined in Tab. 4.2. The red curve shows the result computed by `MicrOMEGAs`, while the black curve shows the corresponding result by `RelExt`. Taken from Ref. [66].

CHAPTER 5

Application of RelExt on Different Dark Matter Models

We want to see how the code works in practice by showing different ways to search the parameter space for various models. We will structure this chapter by first introducing the model under consideration and then proceed to show how `RelExt` can be used to sample the parameters of the model.

5.1. The CxSM

To illustrate how the code can be used for parameter searches for a model with few parameters we will first look at the CxSM.

5.1.1. Model Description of the CxSM

The CxSM extend the SM scalar potential by an additional complex scalar singlet field $\mathbb{S}$. This singlet field and the SM Higgs doublet field Φ are parameterized after electroweak symmetry breaking as

$$\Phi = \begin{pmatrix} G^+ \\ \frac{1}{\sqrt{2}}\big(v + H + iG^0\big) \end{pmatrix} \ , \ \mathbb{S} = \frac{1}{\sqrt{2}}\big(v_S + S + i(v_A + A)\big)\,. \tag{5.1}$$

Here, H and S are real scalar fields, A is a pseudoscalar field and G^+ and G^0 are the charged and neutral Goldstone bosons, respectively. The parameters v, v_S and v_A are the VEVs to their respective fields H, S and A. We impose two separate $\mathbb{Z}_2$ symmetries on this model such that

$$\begin{array}{lllll} \mathbb{Z}_2^1\text{:} & H \to H & , & S \to -S & , \quad A \to A\,, \\ \mathbb{Z}_2^2\text{:} & H \to H & , & S \to S & , \quad A \to -A\,. \end{array}$$

Under consideration of these symmetries, we can write the most general renormalizable scalar potential as follows

$$V = \frac{m^2}{2}|\Phi|^2 + \frac{\lambda}{4}|\Phi|^4 + \frac{\delta_2}{2}|\Phi|^2|\mathbb{S}|^2 + \frac{b_2}{2}|\mathbb{S}|^2 + \frac{d_2}{4}|\mathbb{S}|^4 + \left(\frac{b_1}{4}\mathbb{S}^2 + c.c.\right)\,, \tag{5.2}$$

where the model parameters m, λ, δ_2, b_2, d_2 and b_1 are all real. By setting $v_A = 0$ the $\mathbb{Z}_2^2$ remains unbroken and A becomes a stable DM candidate. The first $\mathbb{Z}_2$, however, gets broken due to $v_S \neq 0$, which leads to mixing between the neutral scalar fields H and S. To obtain the mass eigenstates, which we will denote by h_i $(i = 1, 2)$ we need to perform a rotation defined by

$$\begin{pmatrix} h_1 \\ h_2 \end{pmatrix} = R_\alpha \begin{pmatrix} H \\ A \end{pmatrix} , \tag{5.3}$$

where the orthogonal rotation matrix R_α is given by

$$R_\alpha = \begin{pmatrix} \cos\alpha & \sin\alpha \\ -\sin\alpha & \cos\alpha \end{pmatrix} . \tag{5.4}$$

The mass eigenstates are ordered such that $m_{h_1} \leq m_{h_2}$. This rotation leads to a modification factor k_i for all interaction strength g_{h_i} between the CxSM Higgs bosons h_i and the SM particles given by

$$g_{h_i} = k_i g_{H_{\mathrm{SM}}} \, , \; k_i \equiv \begin{cases} \cos\alpha \, , & i = 1 \\ -\sin\alpha \, , & i = 2 \end{cases} , \tag{5.5}$$

where $g_{H_{\mathrm{SM}}}$ is the SM coupling between the SM Higgs boson and the SM particles. Our choice of input parameters for this model is

$$v \, , \; v_S \, , \; \alpha \, , \; m_{h_1} \, , \; m_{h_2} \, , \; m_A \, , \tag{5.6}$$

where m_A is the DM mass. The relations between the potential parameters and the input parameters are given in Appendix B.1.

5.1.2. Example Search in the CxSM

To illustrate how `RelExt` can be used to search for parameters, we will show two code examples of `main.cpp` files in which we adjust single parameters to obtain the observed relic density. Each `main.cpp` comes with a few settings the user can adjust. We give a brief description of the settings below. A more detailed description of these settings can be found in Ref. [66].

`MODE`	Can take the values 1, 2 or 3. Decides how new parameters are read in.
`SAVEPARS`	Parameter names, whose values will be saved in the output file.
`CONSIDERCHANNELS`	If not left empty, only these (co-)annihilation channels will be considered in the calculation of the relic density.
`NEGLECTCHANNELS`	Channels which will be ignored during the computation.
`NEGLECTPARTICLES`	Channels which contain these particles in their initial or final state will be ignored in the computation.
`BEPS`	Sets the value for B_ϵ in Eqs. (4.4) and (4.8).
`XTODAY`	Value of x_0 until which we solve the Boltzmann equation.

`FAST`	This is set to `true` if we want to use the freeze-out approximation and `false` if the Boltzmann equation should be solved with the ODE solver.
`CALCWIDTHS`	If this setting is set to `true`, the decay widths of particles appearing in the s-channels will be computed by `RelExt`. Otherwise they have to be provided by the user.
`SAVECONTRIBS`	If set to `true`, the relative contribution of individual channels to the computed relic density will be saved in the output file.

In the first example, we want to study how a change in α will influence the parameter v_S, on which we will perform a search to obtain the observed relic density. Below we give the settings we will use for the parameter scan.

```
/* Change to desired settings starting from here
**********************************************
 */
static constexpr int MODE = 1;
static const VecString SAVEPARS = {"MA1", "MS1", "alpha", "svev"};
static const VecString CONSIDERCHANNELS = {};
VecString NEGLECTCHANNELS = {};
static const VecString NEGLECTPARTICLES = {"u", "d", "e", "mu"};
static constexpr double BEPS = 1e-6;
static constexpr double XTODAY = 1e6;
static constexpr bool FAST = true;
static constexpr bool CALCWIDTHS = true;
static constexpr bool SAVECONTRIBS = false;
/*
**********************************************
 Until here */
```

Listing 5.1: Settings for the CxSM

As can be seen by the settings shown in Listing 5.1, we neglect the lightest quarks and the first two generations of leptons. We do this because we are considering a Higgs portal model, where the lightest particles will have the smallest couplings to the DS and therefore will only contribute negligibly. Doing this saves computation time since it forces `RelExt` to skip these channels when computing the relic density. By setting `MODE=1` we will read in a single parameter specified by the following input file

```
MA1      |10          , 1000       , 500
MS1      |10          , 1000       , 200
alpha    |-1.57079    , 1.57079    , -1.57
svev     | 0          , 1e6        , 300
```

The first two values for each parameter specify the lower and upper boundary values the parameter is allowed to obtain during a parameter search. The last entry for each parameter is the initial starting value when loading the parameter while using `MODE` 1. With the settings and the input file prepared we can run the `main.cpp` shown in Listing 5.2. The first 5 lines of the shown code are identical in every `main.cpp` file and are necessary to load in the settings. In line 6 we load the parameter point from the provided input file. Next, we save the initial value for α in line 7, i.e. `sav=1.57`, and keep increasing it in the for-loop until it reaches a value of `sav=-1.57` in line 8. While we loop over the `sav`-values we first set the value of α, then search for a v_s such that a relic density of $\Omega_d h^2 = 0.12 \pm 0.001$ is obtained and lastly

```
int main(int argc, char **argv) {
    clock_t begin_time = clock();
    Main M(argv, MODE, BEPS, XTODAY, FAST, CALCWIDTHS, SAVECONTRIBS);
    M.set_channels(CONSIDERCHANNELS, NEGLECTCHANNELS,
        NEGLECTPARTICLES);

    M.LoadParameters();
    double sav = M.GetParameter("alpha");
    for (sav; i < 1.57; sav += 0.01) {
        M.ChangeParameter("alpha", sav);
        M.FindParameter("svev", 0.12, 0.001);
        M.SaveData(SAVEPARS);
    }

    std::cout << "Computation time:\n"
              << float(clock() - begin_time) / CLOCKS_PER_SEC << "\n";
}
```

Listing 5.2: `main.cpp` file used to run the scan in α and v_S

save the parameters in the output file. Lines 14-16 simply print the computation time of the whole process.

After running this `main.cpp` file we plot the singlet VEV v_S over the mixing angle α shown in Fig. 5.1. The plot shows three minima at the points $\alpha_{\text{min}} = \{-\pi/2, 0, \pi/2\}$, which is due to the fact that one of the two coupling modifiers k_i $(i = 1, 2)$ goes to zero and blocks the according annihilation channels which have to be compensated by a small v_S to still obtain the observed relic density.[13] The peaks of the plot are located at $\alpha_{\text{max}} = \pm\pi/4$ since there both the sine and cosine coupling modifiers can contribute maximally.

We can also scan the mass of the DM candidate to study the influence of the resonance peaks on the choice of v_S. To do this we have to adjust only a few lines of code in the input file and the `main.cpp` file. In the input file we only modify the last entry for each parameter.

```
MA1     |10          , 1000       , 50
MS1     |10          , 1000       , 205
alpha   |-1.57079    , 1.57079    , 0.2
svev    | 0          , 1e6        , 50
```

For the `main.cpp` we only show the modified parts

```
double sav = M.GetParameter("MA1");
for (size_t i = 0; i < 150; i++) {
    M.FindParameter("svev", 0.12, 0.001);
    M.SaveData(SAVEPARS);
    M.ChangeParameter("MA1", ++sav);
}
```

The resulting plot is shown in Fig. 5.2. This time we show the singlet VEV over the DM mass. The two peaks which appear in this plot are exactly at the threshold of the two Higgs bosons contained in the model, i.e. at $m_{\text{DM}} = m_{h_i}/2$ $(i = 1, 2)$, with $m_{h_1} = 125\,\text{GeV}$ and $m_{h_2} = 205\,\text{GeV}$. In these regions annihilation becomes very efficient due to the resonance peaks and have to compensated by a increase in v_S to obtain the observed relic density.

[13] A small v_S leads to a larger TAC since the portal coupling is proportional to v_S^{-1}.

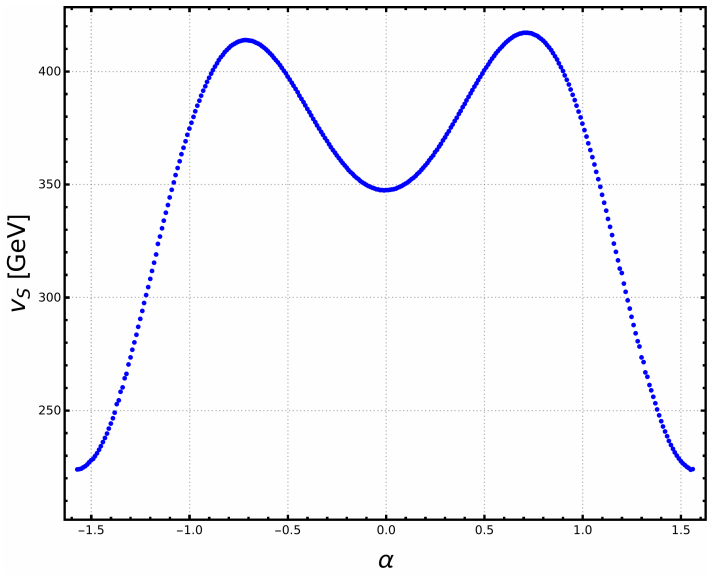

Figure 5.1.: The singlet VEV v_S over the mixing angle α for a benchmark point with $m_{h_1} = 125.09\,\text{GeV}$, $m_{h_2} = 200\,\text{GeV}$ and $m_A = 500\,\text{GeV}$ in the CxSM. All points shown generate the observed relic density.

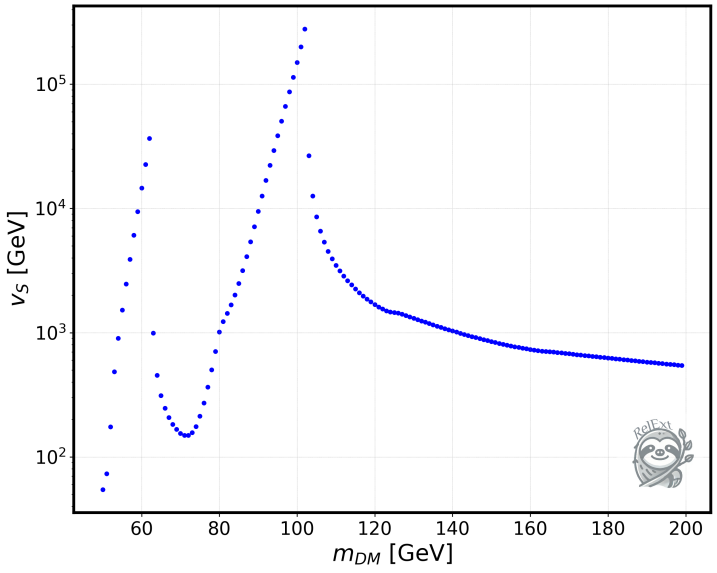

Figure 5.2.: The singlet VEV over the DM mass for a benchmark point with $m_{h_1} = 125.09\,\text{GeV}$, $m_{h_2} = 205\,\text{GeV}$ and $\alpha = 0.2$ in the CxSM. The points shown generate the observed relic density. Taken from Ref. [66].

5.2. CP in the Dark

To obtain the observed relic density for a simple model with only a few input parameter such as the CxSM is fairly straight forward. To show how we can find the relevant parameter regions in a more complicated model, we will look at the model CP in the Dark.

5.2.1. Model Description of CP in the Dark

In the model CP in the Dark we extend the scalar sector of the SM such that we have two complex doublet fields Φ_1 and Φ_2 as well as an additional real singlet field Φ_S. Although in general all the fields can acquire a non-zero VEV, we will consider a scenario in which only Φ_1 obtains a VEV. After electroweak symmetry breaking we can write the scalar fields as

$$\Phi_1 = \begin{pmatrix} G^+ \\ \frac{1}{\sqrt{2}}\big(v + h + iG^0\big) \end{pmatrix} \,,\; \Phi_2 = \begin{pmatrix} H^+ \\ \frac{1}{\sqrt{2}}\big(\rho_1 + i\eta\big) \end{pmatrix} \,,\; \Phi_s = \rho_s \,. \tag{5.7}$$

As in the case of the CxSM, the G^+ and G^0 fields are the charged and neutral Goldstone bosons. Further, we have the SM-like Higgs boson h, a charged scalar H^+, two CP-even neutral fields ρ_i ($i \in \{1, s\}$) and a CP-odd field η. To ensure that we have a stable DM candidate we enforce the following $\mathbb{Z}_2$ symmetry

$$\Phi_1 \to \Phi_1 \,,\; \Phi_2 \to -\Phi_2 \,,\; \Phi_s \to -\Phi_s \,. \tag{5.8}$$

After applying this symmetry, the most general renormalizable scalar potential is given by

$$\begin{aligned} V_{\text{Scalar}} = \; & m_{11}^2 \Phi_1^\dagger \Phi_1 + m_{22}^2 \Phi_2^\dagger \Phi_2 + \frac{\lambda_1}{2}\left(\Phi_1^\dagger \Phi_1\right)^2 + \frac{\lambda_2}{2}\left(\Phi_2^\dagger \Phi_2\right)^2 \\ & + \lambda_3 \Phi_1^\dagger \Phi_1 \Phi_2^\dagger \Phi_2 + \lambda_4 \Phi_1^\dagger \Phi_2 \Phi_2^\dagger \Phi_1 + \frac{\lambda_5}{2}\left[\left(\Phi_1^\dagger \Phi_2\right)^2 + \text{h.c.}\right] \\ & + \frac{1}{2} m_s^2 \Phi_\text{s}^2 + \frac{\lambda_6}{8}\Phi_\text{s}^4 + \frac{\lambda_7}{2}\Phi_1^\dagger \Phi_1 \Phi_\text{s}^2 + \frac{\lambda_8}{2}\Phi_2^\dagger \Phi_2 \Phi_\text{s}^2 + \left(A \Phi_1^\dagger \Phi_2 \Phi_s + \text{h.c.}\right) , \end{aligned} \tag{5.9}$$

where m_{11}, m_{22}, m_s and λ_i ($i \in [1, 8]$) are real parameters and A is complex. The term proportional to A introduces additional CP violation that is restricted to the DS. To obtain the mass eigenstates h_i ($i \in \{1, 2, 3\}$) we need to rotate the gauge eigenstates ρ_i and η via an orthogonal matrix R that is given by

$$R = \begin{pmatrix} c_{\alpha_1} c_{\alpha_2} & s_{\alpha_1} c_{\alpha_2} & s_{\alpha_2} \\ -(c_{\alpha_1} s_{\alpha_2} s_{\alpha_3} + s_{\alpha_1} c_{\alpha_3}) & c_{\alpha_1} c_{\alpha_3} - s_{\alpha_1} s_{\alpha_2} s_{\alpha_3} & c_{\alpha_2} s_{\alpha_3} \\ -c_{\alpha_1} s_{\alpha_2} c_{\alpha_3} + s_{\alpha_1} s_{\alpha_3} & -(c_{\alpha_1} s_{\alpha_3} + s_{\alpha_1} s_{\alpha_2} c_{\alpha_3}) & c_{\alpha_2} c_{\alpha_3} \end{pmatrix} . \tag{5.10}$$

This matrix is parameterized by three angles $\alpha_i \in \left[-\frac{\pi}{2}, \frac{\pi}{2}\right]$ ($i \in \{1, 2, 3\}$). Further, we used the notation $\sin\alpha \equiv s_\alpha$ and $\cos\alpha \equiv c_\alpha$ as an abbreviation. With the matrix R the mass and gauge eigenstates are related via

$$\begin{pmatrix} h_1 \\ h_2 \\ h_3 \end{pmatrix} = R \begin{pmatrix} \rho_1 \\ \eta \\ \rho_s \end{pmatrix} . \tag{5.11}$$

The mass eigenstates are ordered such that $m_{h_1} \leq m_{h_2} \leq m_{h_3}$. Our choice for the set of input parameters is the following

$$v \,,\; m_h \,,\; m_{h_1} \,,\; m_{h_2} \,,\; m_{H^+} \,,\; \alpha_1 \,,\; \alpha_2 \,,\; \alpha_3 \,,\; \lambda_2 \,,\; \lambda_6 \,,\; \lambda_8 \,,\; m_{22} \,,\; m_s. \tag{5.12}$$

The remaining parameters can be obtained from these and are given in Appendix B.2.

5.2.2. Example Search in CP in the Dark

In this model we not only have more parameters compared to the CxSM but also additional co-annihilation partners in the DS, which complicate the parameter search. We start of noticing that this model contains only a single Higgs boson which can act as Higgs portal to the SM. For such a scenario we expect the relic density to behave similar to the one shown in Fig. 4.3. There, we can divide the parameter space into two distinct regions. The first region is below the Higgs threshold at a mass of $m_{\text{DM}} < 125\,\text{GeV}$, which has many peaks and dips due to different particle thresholds and resonances. While the second region with $m_{\text{DM}} > 125\,\text{GeV}$ is very smooth and contains no such effects. For the following parameter scan we want to search these two regions separately to ensure that we find valid points in both of them and do not get stuck in one or the other while searching. We set up the two regions via the following input files

```
mH1     |10     ,   125
mH2     |10     ,   1000
mHc     |10     ,   1000
alph1   |0      ,   1.56
alph2   |0      ,   1.56
alph3   |0      ,   1.56
m22sq   |0      ,   1e+06
mssq    |0      ,   1e+06
```

```
mH1     |125.1  ,   1000
mH2     |125.1  ,   1000
mHc     |125.1  ,   1000
alph1   |0      ,   1.56
alph2   |0      ,   1.56
alph3   |0      ,   1.56
m22sq   |0      ,   1e+06
mssq    |0      ,   1e+06
```

Further, we adjust the settings by applying `MODE=2` to produce random parameter points between the given boundaries and changing `SAVEPARS` accordingly. With this setup, we do a first parameter scan using the Monte Carlo method described in Sec. 4.2.4. We choose $N_b = 100$ and track the best 500 cells during the scan, which will be saved at the end of the parameter scan. Further, we set $p_r = 1$ such that we only generate random parameters and do not produce any from the already found best cells. We do this because at this stage we only care about finding the best cells and do not worry about producing good parameter points yet. The corresponding `main.cpp` is given in Listing 5.3. The first 5 lines are identical to the CxSM example. In line 6 we initialize the grid by calling `InitMonteCarlo` and specify N_b, N_{best}, p_r and $\Omega_d h^2$ with the respective arguments. Next, we generate 10^5 random points for which we compute the relic density, track their weight according to Eq. (4.12) and save the parameter point in the output file.

```
1  int main(int argc, char **argv) {
2      clock_t begin_time = clock();
3      Main M(argv, MODE, BEPS, XTODAY, FAST, CALCWIDTHS, SAVECONTRIBS);
4      M.set_channels(CONSIDERCHANNELS, NEGLECTCHANNELS,
           NEGLECTPARTICLES);
5
6      M.InitMonteCarlo(100, 500, 1, 0.12);
7      for (size_t i = 1; i <= 1e5; i++) {
8          M.LoadParameters();
9          M.CalcRelic();
10         M.SetWeight();
11         M.SaveData(SAVEPARS);
12     }
13     std::cout << "Computation time:\n"
14               << float(clock() - begin_time) / CLOCKS_PER_SEC << "\n";
15 }
```

Listing 5.3: `main.cpp` file used to run a random scan to determine the best cell.

After running the code we obtain Fig. 5.3 where we plot the computed relic density over the DM mass. The gray, dashed line shows the desired, observed relic density we want to obtain.

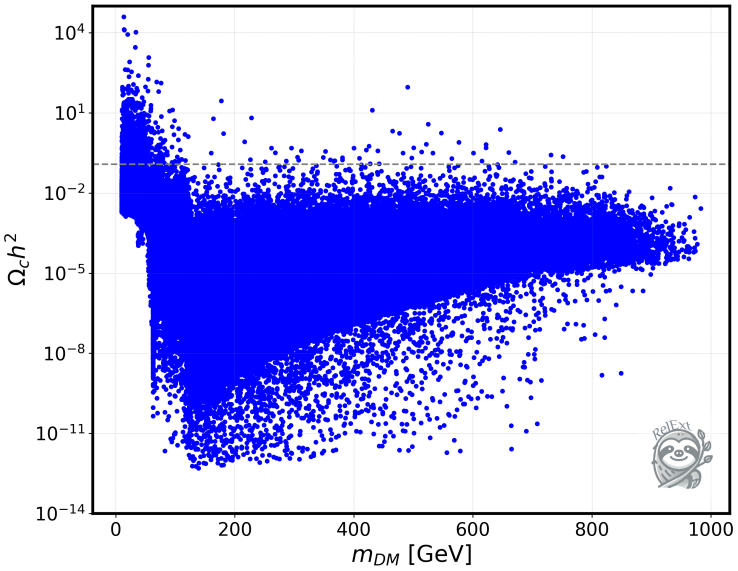

Figure 5.3.: Computed relic density over the DM mass for a random parameter scan in the model CP in the Dark. The gray, dashed line represents the observed relic density. Taken from Ref. [66].

Out of the $2 \cdot 10^5$ randomly generated points, only 27 (0.0135%) are within the 2σ range of the observed relic density $\Omega_d h^2 = 0.120 \pm 0.002$.

After the first scan, we can use the best cells tracked by `RelExt` to perform a second scan similar to the previous one. The main difference this time is that we set $p_r = 0$ and therefore generate points only from the already found best cells. This leads to the plot shown in Fig. 5.4, where the blue points are generated via the best cells, while the gray points are the randomly generated points from the original sample. Just by looking at the plot we notice a much better yield of good parameter points compared to the previous scan. This time, out of the $2 \cdot 10^5$ generated points, 3948 (1.97%) are within the 2σ range of the observed relic density. This is an increase by a factor of roughly ~ 100 in the amount of good points that we are able to produce.

As a further improvement, we will now also apply the random walk algorithm we described in Sec. 4.2.4. We again sample our points only from the best cells as in the previous scan, however, this time, we apply the random walk on these points to obtain the observed relic density. To do this, we only have to adjust line 9 in Listing 5.3 such that

```
M.CalcRelic(); -> M.RWalk(0.12, 0.002, 0.01, 400);
```

This will increase the computational effort since `RelExt` will now have to go through many iterations of the random walk for each newly generated point. Due to this reason we reduce the number of generated points to $2 \cdot 10^4$, i.e. changing

```
for (size_t i = 1; i <= 1e5; i++) -> for (size_t i = 1; i <= 1e4; i++)
```

After running the `main.cpp`, we obtain the plot shown in Fig. 5.5. The blue points are generated using the random walk on the best cells scan, the light and dark gray points originate from the two previously discussed scans. Additionally we marked a subset of the blue points, red. These red points are validated against all relevant experimental and theoretical

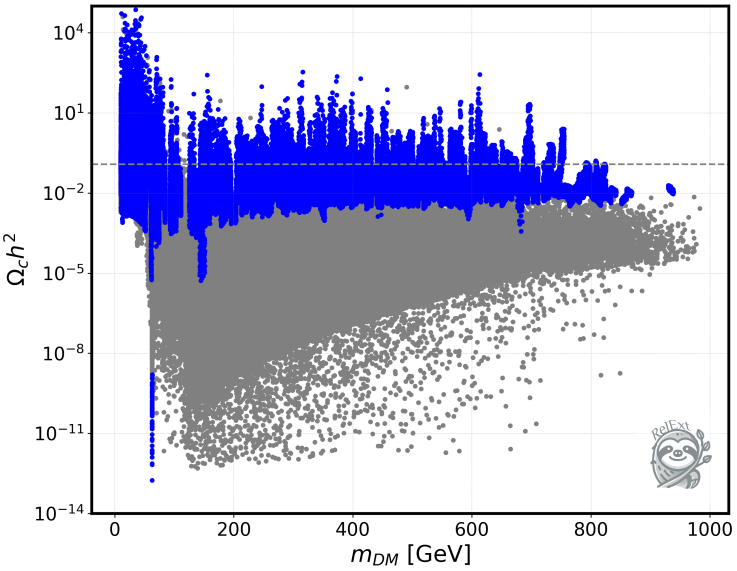

Figure 5.4.: Computed relic density over the DM mass in the model CP in the Dark. The blue points are generated from the best cells, while the gray ones are generated randomly. The dashed line represents the observed relic density. Taken from Ref. [66].

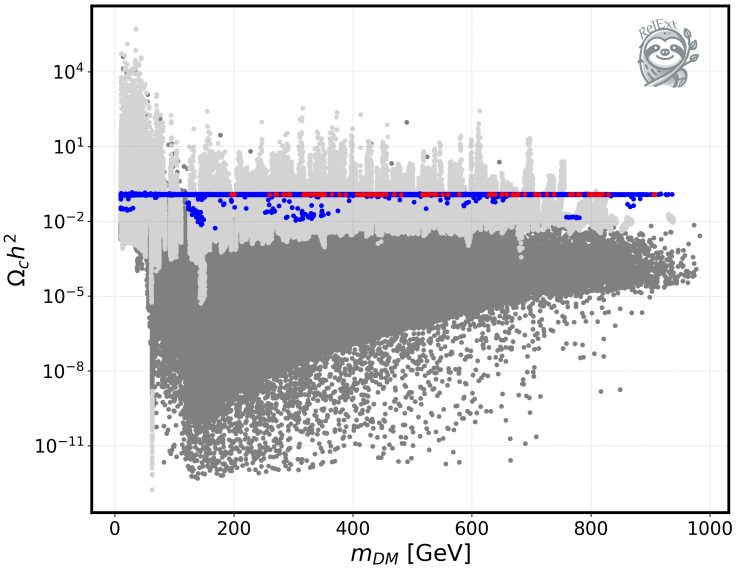

Figure 5.5.: Computed relic density over the DM mass in the model CP in the Dark. The blue points are generated from the best cells with a random walk applied onto them. The light gray points are generated from the best cells and the dark gray points are generated randomly. Further, the red points are validated against theoretical and experimental constraints by `ScannerS`. Taken from Ref. [66].

Method	points generated	% within 2σ	[good points] /[CPU time]
Random $m_{\rm DM} > m_h$	10^5	0.%	$\sim$0 s^{-1}
Random $m_{\rm DM} < m_h$	10^5	0.027%	$\sim$0.0012 s^{-1}
Best cells $m_{\rm DM} > m_h$	10^5	0.29%	$\sim$0.0178 s^{-1}
Best cells $m_{\rm DM} < m_h$	10^5	3.66%	$\sim$0.135 s^{-1}
Best cells with `RWalk` $m_{\rm DM} > m_h$	10^4	97.5%	$\sim$0.065 s^{-1}
Best cells with `RWalk` $m_{\rm DM} < m_h$	10^4	97.3%	$\sim$0.085 s^{-1}

Table 5.1.: The left column shows the total amount of points generated by the scan, the middle column shows the fraction of points for which the obtained relic density is within the 2σ limit and in the right column we present the number of good points (relic density within the 2σ limit) per second. We compare the random scan, the scan using only the best cells, and the scan in the best cells where a random walk is applied. The computations were performed on a liquid cooled AMD EPYC 7351 16-Core Processor machine with an x86_64 architecture, a base clock frequency of 1.2 GHz and maximum frequency of 2.4 GHz. We used 4 cores with a total of 4 GB of RAM for our scans. Taken from Ref. [66].

constraints by `ScannerS` [112]. Out of the $2 \cdot 10^4$ points, 19489 (97.45%) are within the 2σ limit.[14] We have to be a bit more nuanced when comparing the yield of these result to the previous ones. To obtain a better comparison we also need to take the computation time into account. We do this by looking at how many good points we generated per second, instead of simply comparing their amount. The results for the corresponding scan method are shown in Tab. 5.1. We see, as expected, the increase of the factor $\sim$100 in the good points per second between the random scan and the best cells scan throughout the whole $m_{\rm DM}$ region. However, when comparing the best cells scan with the random walk, we need to differentiate between the regions in which $m_{\rm DM} > m_h$ and $m_{\rm DM} < m_h$. In the former the increase in good points per second is a factor of $\sim$3.6. While in the latter case, the best cells scan outperforms the random walk by a factor of ~ 1.6. This can be attributed to the fact that in this region we have many peaks and dips, which lead to large changes in the relic density even if we change the parameters only slightly. Due to this, the random walk algorithm has a harder time to converge and therefore the computation time is increased. Nonetheless, it can still be beneficial to apply the random walk algorithm in this scenario as it is able to find further best cells from the already established ones, that can be used for future parameter searches.

[14] Points which are not within the 2σ bound have reached the maximum iteration limit of the random walk algorithm.

CHAPTER 6

Conclusion

As a part of this thesis we have developed the code `RelExt`, which is able to solve the Boltzmann equation needed to compute the relic density via freeze-out. To do this, it automatically computes the necessary amplitudes, thermally averaged cross sections and the decay widths of the s-channel mediators based on the model at hand. Further, it is also able to employ different parameter search strategies to find the parameter regions in which the model is able to generate the experimentally measured relic density. The code is shipped with the pre-installed and tested models CxSM, TRSM, the N2HDM in the dark doublet phase, the model CP in the dark, and the BDM5. The user has the option to implement additional models by providing the corresponding `FeynRules` model files. So far the code only covers models whose DM is stabilized by a discrete $\mathbb{Z}_2$. We described in depth the algorithms used throughout code which ensure a fast computation of the relic density as well as enable parameter searches to find the parameter regions in a given model which generate the observed relic density.

Further, we validated the correctness of our code by comparing it with `MicrOMEGAs`. During this comparison we found agreement throughout the tested models and also in parameter regions where resonance and threshold effects occur. However, in regions where a mediator particle with a large decay width occurs, we find disagreement due to the different ways our code and `MicrOMEAGs` treat resonances. This difference is highlighted in Fig. 4.6 for a benchmark point in the N2HDM.

The output of the code is designed such that it can be easily linked to other codes such as `ScannerS` [112] and `BSMPT` [113, 114]. Because of this, `RelExt` provides an excellent tool to test different DM models with respect to their capability to produce the experimentally measured relic density via thermal freeze-out while also respecting further experimental and theoretical constraints.

In its current version, `RelExt` can deal with models featuring one DM candidate. Future versions will aim to include multi-component DM models as well as models with feebly interacting massive particles in which the relic density is generated via freeze-in. Further upgrades, involve the inclusion of higher-order correction to the amplitudes present in the freeze-out/in processes.

Part II.

Simultaneous Freeze-in and Freeze-out in CP in the Dark

CHAPTER 7

Introduction

This part of the thesis is based on our published paper, which can be found in Ref. [115]. We will not show the numerical results here, since these were already discussed in my master thesis. For these we refer to the paper, i.e. [115], which based on the aforementioned thesis. Still, we will take the occasion to provide the necessary theoretical background in more detail than in the master thesis in the next chapter as well as a summary of the results in Chapter 9.

In the previous part of the thesis we focused our efforts on generating the correct relic abundance for an arbitrary freeze-out model with a DM candidate stabilized by a $\mathbb{Z}_2$ symmetry. In the process of doing that, we did not consider the second relevant DM constraint, the Direct Detection (DD) cross sections. As can be inferred from Fig. 3.1, the DD experiments exclude a large portion of the parameter region in the simplest WIMP scenario. This is a common feature of Higgs portal models since the interplay between DD constraints and generating the correct relic abundance is such that they counteract each other. More specifically, if we want to evade the DD experiments a small coupling to the SM is required. However, the same coupling will appear in the annihilation of DM particles during freeze-out leading to an overabundance of the relic density. On the other hand, if we increase the couplings to obtain the observed relic density, the DD constraints are jeopardized. One way to circumvent this issue is to introduce additional DS particles which are able to co-annihilate with the DM candidate, reducing the relic density without the need for large couplings. A simple way to illustrate this effect is by looking at a $\mathbb{Z}_2$ symmetric model with two real singlet fields ϕ_1 and ϕ_2 and the following renormalizable potential

$$\begin{aligned} V_{\text{Scalar}} = &\ \mu_h^2|\Phi|^2 + \lambda_h|\Phi|^4 + m_1^2\,\phi_1^2 + \frac{\lambda_1}{4!}\,\phi_1^4 + m_2^2\,\phi_2^2 + \frac{\lambda_2}{4!}\,\phi_2^4 \\ &+ \frac{\lambda_{1H}}{2}\,\phi_1^2|\Phi|^2 + \frac{\lambda_{2H}}{2}\,\phi_2^2|\Phi|^2 + \frac{\lambda_{12}}{4}\,\phi_1^2\phi_2^2 \\ &+ m_{12}^2\phi_1\phi_2 + \frac{\lambda_{112}}{4}\,\phi_1^3\phi_2 + \frac{\lambda_{122}}{4}\,\phi_1\phi_2^3 + \frac{\lambda_{12H}}{2}\,\phi_1\phi_2|\Phi|^2\,. \end{aligned} \tag{7.1}$$

Here, Φ is the SM doublet field and all parameters are real. To obtain the mass eigenstates of the DS, which we denote by h_{D1} and h_{D2}, we apply the rotation matrix with the angle θ_D as follows

$$\begin{pmatrix} h_{D1} \\ h_{D2} \end{pmatrix} = \begin{pmatrix} \cos\theta_D & \sin\theta_D \\ -\sin\theta_D & \cos\theta_D \end{pmatrix} \begin{pmatrix} \phi_1 \\ \phi_2 \end{pmatrix}\,, \tag{7.2}$$

where by convention we impose $m_{h_{D1}} < m_{h_{D2}}$. Compared to a singlet DM model, where we only have one coupling that is responsible for freeze-out, this model has three which are λ_{1H}, λ_{2H} and λ_{12H}. With these three couplings we can draw a plane in which the desired relic density constraint is obtained, as shown in Fig 7.1. Here, we plot the coupling λ_{1H} over λ_{2H} and show λ_{12H} via the color gradient for 3 different mass combinations of $m_{h_{D1}}$ and $m_{h_{D2}}$. All points that are shown generate the observed relic abundance within to uncertainty.

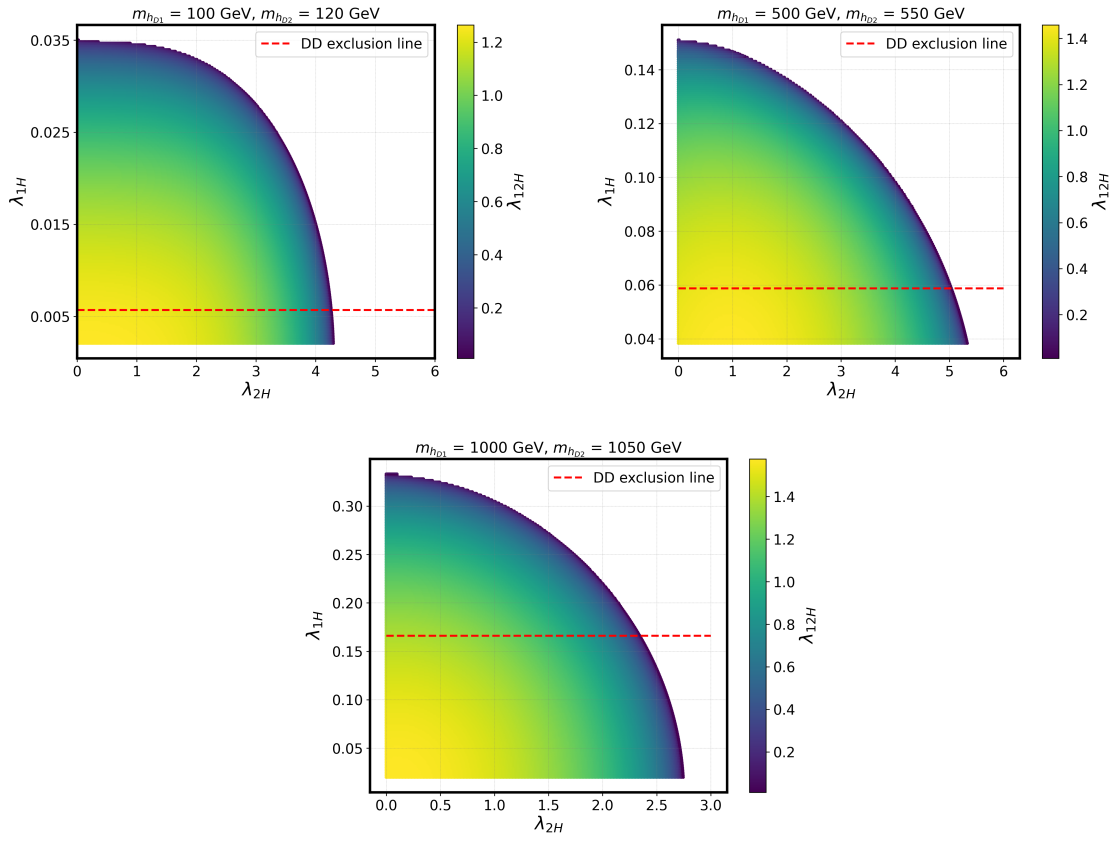

Figure 7.1.: Parameter points in the (λ_{1H}, λ_{2H}, λ_{12H}) plane for which $\Omega h^2 = 0.120 \pm 0.002$ for different $m_{h_{D1}}$, $m_{h_{D2}}$ mass combinations. The points above the red line are excluded by DD experiments. The points were generated using `RelExt`. Taken from Ref. [115].

The red line shows the DD exclusion limit, where points above the line are excluded. We see that in such a model it is much simpler to escape the limits from DD experiments since the coupling that is responsible for the DD constraints, λ_{1H}, can be arbitrarily small. This would lead to a large relic density in the scenario of single singlet, but with the additional singlet h_{D2} we can simply increase the couplings responsible for the co-annihilation channels to reduce the relic density. Although this approach works well for models where we can freely change all of the (co-)annihilation couplings, for models where gauge couplings are involved, which cannot be chosen arbitrarily, it becomes more difficult to obtain the observed relic density. We saw this phenomenon for CP in the Dark in Sec. 5.2, where we had to apply dedicated search algorithms to find parameter regions which are able to generate the desired relic density. However, there is another way to completely evade the DD constraints by considering a different DM production mechanism called freeze-in. We briefly mentioned freeze-in in Sec. 2.2 and will go into more detail in this part of the thesis.

7.1. Freeze-in

The mechanism of freeze-in is a natural explanation of the null results observed by current DM experiments while simultaneously accounting for the observed relic density. The key difference between the freeze-in mechanism compared to the freeze-out mechanism is the initial condition of the Boltzmann equation. While in the freeze-out scenario the DS particles start in thermal equilibrium with the SM bath, in the freeze-in scenario we begin with no initial DM abundance. The SM particles annihilate into DM until the freeze-in point x_{fi} is reached. To make sure that the DM particles do not immediately equilibrate with the SM bath, we need to choose a very small portal coupling λ of the order of $\lambda \sim 10^{-10}$. In the case where the coupling is larger than this value, the DM particles immediately reach thermal equilibrium and go through the freeze-out process at a later time.

The Boltzmann equation for the freeze-in mechanism is in general more involved than the freeze-out counterpart. This is attributed to the fact that freeze-in ends at early times of roughly $x_{\text{fi}} \approx 2 - 5$ [116]. As a result, the DM particles are still in the relativistic regime and the assumption that they follow the Maxwell-Boltzmann (MB) distribution is not valid. The effect of taking the non-relativistic MB distribution for the Boltzmann equation has been compared with a fully relativistic treatment in Ref. [74]. It was shown for a singlet DM model with a Higgs portal that the difference is a factor of two in the relic density for DM masses that are above half the Higgs mass and has no effect for masses below that. We will see that in our model the DM candidate going through freeze-in is a singlet and couples to the SM only via the Higgs portal. For this reason we will use the treatment in which we assume the MB distribution and adjust the result by this factor of two. In the case of a MB distribution the Boltzmann equation is identical to the one in the freeze-out case, i.e. Eq. 3.33. One common simplification at this stage is to neglect the $Y_\mathcal{X}^2$ term since the yield is negligible compared to its equilibrium value leading to

$$\frac{\mathrm{d}Y_\mathcal{X}}{\mathrm{d}x} = \sqrt{\frac{\pi}{45G}} \frac{g_*^{1/2}(T) m_1}{x^2} \langle \sigma v \rangle_{\text{eff}} (Y_\mathcal{X}^{\text{eq}})^2 \,. \tag{7.3}$$

Another quantity that becomes relevant in the freeze-in scenario is the reheating temperature which we discussed in Sec. 2.2. We have to decide how large it is after inflation as it determines the initial temperature of the SM bath and therefore the initial condition for the Boltzmann equation, i.e. $Y_\mathcal{X}(x_{\text{reh}}) = 0$. In this thesis we will set $x_{\text{reh}} = 10^{-4}$. We do this, because smaller values of x_{reh} will lead to the same results, while larger values move into the territory of a late reheating scenario [117, 118], which we do want to study in this thesis.

CHAPTER 8

Coupled Boltzmann Equations in CP in the Dark

A major deficit of freeze-in models is that due to their small couplings, its extremely difficult for upcoming experiments to detect their existence. We would prefer to construct a model which is testable, while also giving us information on the question whether parts or all of the DM abundance is generated via freeze-in. The idea that we follow in this thesis is to have two components which make up the full relic density, namely one component which is generated via freeze-out and which has testable consequences, and a second component, which is generated via freeze-in. The question then becomes: Can we make any statements about the freeze-in component in a given model if we obtain information from the freeze-out sector? In our paper we have shown that indeed through the combination of certain signatures we can infer the properties of the freeze-in component.

8.1. Coupling Freeze-out and Freeze-in

We will consider a model which has two DM candidates, where one evolves via the freeze-out mechanism and the other via the freeze-in mechanism. These are in general not independent since there can exist a mediator that connects the two. To account for this connection we need to consider a system of two coupled Boltzmann equations given by [119, 120]

$$\begin{aligned}\frac{dY_{\mathrm{FI}}}{dx} =&\sqrt{\frac{\pi}{45G}}\,\frac{g_*^{1/2}m_{\mathrm{FI}}}{x^2}\Bigg[\langle\sigma v\rangle_{\mathrm{FI}\leftrightarrow\mathrm{SM}}\left(\left(Y_{\mathrm{FI}}^{\mathrm{eq}}\right)^2-Y_{\mathrm{FI}}^2\right)\\ &+\langle\sigma v\rangle_{\mathrm{FI}\leftrightarrow\mathrm{FO}}\left(\left(\frac{Y_{\mathrm{FO}}}{Y_{\mathrm{FO}}^{\mathrm{eq}}}\right)^2\left(Y_{\mathrm{FI}}^{\mathrm{eq}}\right)^2-Y_{\mathrm{FI}}^2\right)\Bigg]\,, \qquad (8.1)\\ \frac{dY_{\mathrm{FO}}}{dx} =&\sqrt{\frac{\pi}{45G}}\,\frac{g_*^{1/2}m_{\mathrm{FI}}}{x^2}\Bigg[\langle\sigma v\rangle_{\mathrm{FO}\leftrightarrow\mathrm{SM}}\left(\left(Y_{\mathrm{FO}}^{\mathrm{eq}}\right)^2-Y_{\mathrm{FO}}^2\right)\\ &-\langle\sigma v\rangle_{\mathrm{FI}\leftrightarrow\mathrm{FO}}\left(\left(\frac{Y_{\mathrm{FO}}}{Y_{\mathrm{FO}}^{\mathrm{eq}}}\right)^2\left(Y_{\mathrm{FI}}^{\mathrm{eq}}\right)^2-Y_{\mathrm{FI}}^2\right)\Bigg]\,. \qquad (8.2)\end{aligned}$$

Here, we denote with the indices FI and FO, respectively, the freeze-in bath and the freeze-out bath. With the first equation we determine the yield of the freeze-in particle bath, while the second equation is responsible for the evolution of the freeze-out particles. We see that

the terms proportional to $\langle\sigma v\rangle_{\mathrm{FI}\leftrightarrow\mathrm{FO}}$ connect the two equations as $\langle\sigma v\rangle_{\mathrm{FI}\leftrightarrow\mathrm{FO}}$ describes the particle exchange between the FI and FO baths. In general, we would also need to consider a decay term for the freeze-in equation. However, in our study we will choose DM masses such that SM particles cannot decay into DM particles. As already stated in the previous chapter we can neglect the Y_{FI} terms which simplifies the equations to

$$\frac{dY_{\mathrm{FI}}}{dx} = \sqrt{\frac{\pi}{45G}}\frac{g_*^{1/2}m_{\mathrm{FI}}}{x^2}\left[\langle\sigma v\rangle_{\mathrm{FI}\leftrightarrow\mathrm{SM}}\left(Y_{\mathrm{FI}}^{\mathrm{eq}}\right)^2 + \langle\sigma v\rangle_{\mathrm{FI}\leftrightarrow\mathrm{FO}}\left(\frac{Y_{\mathrm{FO}}}{Y_{\mathrm{FO}}^{\mathrm{eq}}}\right)^2\left(Y_{\mathrm{FI}}^{\mathrm{eq}}\right)^2\right], \tag{8.3}$$

$$\frac{dY_{\mathrm{FO}}}{dx} = \sqrt{\frac{\pi}{45G}}\frac{g_*^{1/2}m_{\mathrm{FI}}}{x^2}\left[\langle\sigma v\rangle_{\mathrm{FO}\leftrightarrow\mathrm{SM}}\left(\left(Y_{\mathrm{FO}}^{\mathrm{eq}}\right)^2 - Y_{\mathrm{FO}}^2\right) - \langle\sigma v\rangle_{\mathrm{FI}\leftrightarrow\mathrm{FO}}\left(\frac{Y_{\mathrm{FO}}}{Y_{\mathrm{FO}}^{\mathrm{eq}}}\right)^2\left(Y_{\mathrm{FI}}^{\mathrm{eq}}\right)^2\right]. \tag{8.4}$$

Next, we are going to focus on the enhancement factor $\bar{Y}$ which we define as

$$\bar{Y}^2 \equiv \left(\frac{Y_{\mathrm{FO}}}{Y_{\mathrm{FO}}^{\mathrm{eq}}}\right)^2 . \tag{8.5}$$

It is a measure of how large the density of the freeze-out particles is compared to the their equilibrium value. We can determine how this enhancement factor behaves at different times of the evolution. Before freeze-out occurs this factor is going to be one, since at this stage the particles are still in thermal equilibrium. After freeze-out Y_{FO} becomes constant and therefore $\bar{Y} \propto \left(Y_{\mathrm{FO}}^{\mathrm{eq}}\right)^{-2}$. We know that freeze-in takes place at a value of $x_{\mathrm{FI}} = m_{\mathrm{FI}}/T_{\mathrm{FI}} \approx 2-5$, while freeze-out occurs at $x_{\mathrm{FO}} = m_{\mathrm{FO}}/T_{\mathrm{FO}} \approx 25$. This means that for similar masses m_{FI} and m_{FO} the freeze-out candidate will remain in thermal equilibrium throughout the entire freeze-in process. Meaning that we can safely set $\bar{Y} = 1$ in this scenario for the freeze-in equation. However, in a scenario where the freeze-out occurs before the freeze-in, this factor cannot be simply set to one and has to be taken into account. For both processes to happen simultaneously, i.e. $T_{\mathrm{FI}} = T_{\mathrm{FO}}$, the masses have to fulfill the relation

$$\frac{m_{\mathrm{FO}}}{m_{\mathrm{FI}}} \approx 5 - 12.5 . \tag{8.6}$$

This means that the mass of the freeze-out candidate has to be at least 5 times larger than the freeze-in counterpart. In our sample we make sure that such scenarios do not occur and therefore set $\bar{Y} = 1$ in the freeze-in equation. Further, we know that the freeze-in coupling are many orders of magnitude smaller than the freeze-out and SM couplings. This means that the TAC $\langle\sigma v\rangle_{\mathrm{FI}\leftrightarrow\mathrm{FO}}$ will be negligible compared to $\langle\sigma v\rangle_{\mathrm{FO}\leftrightarrow\mathrm{SM}}$ and can therefore be neglected in Eq. (8.4). These considerations lead to the decoupled Boltzmann equations

$$\frac{dY_{\mathrm{FI}}}{dx} = \sqrt{\frac{\pi}{45G}}\frac{g_*^{1/2}m_{\mathrm{FI}}}{x^2}\left[\langle\sigma v\rangle_{\mathrm{FI}\leftrightarrow\mathrm{SM}}\left(Y_{\mathrm{FI}}^{\mathrm{eq}}\right)^2 + \langle\sigma v\rangle_{\mathrm{FI}\leftrightarrow\mathrm{FO}}\left(Y_{\mathrm{FI}}^{\mathrm{eq}}\right)^2\right], \tag{8.7}$$

$$\frac{dY_{\mathrm{FO}}}{dx} = \sqrt{\frac{\pi}{45G}}\frac{g_*^{1/2}m_{\mathrm{FI}}}{x^2}\langle\sigma v\rangle_{\mathrm{FO}\leftrightarrow\mathrm{SM}}\left[\left(Y_{\mathrm{FO}}^{\mathrm{eq}}\right)^2 - Y_{\mathrm{FO}}^2\right] . \tag{8.8}$$

We can solve these equations independently of each other to obtain the relic density via

$$\Omega_{\mathcal{X}}h^2 = \Omega_{\mathrm{FO}}h^2 + \Omega_{\mathrm{FI}}h^2 , \tag{8.9}$$

where $\Omega_{\mathrm{FO/FI}}$ are the relic densities generated via freeze-out and freeze-in, respectively.

8.2. Freeze-in in CP in the Dark

We already gave an introduction of the model CP in the Dark in Sec. 5.2.1 and showed in Fig. 5.5 that we can obtain the observed relic density while considering all relevant constraints.

This was fairly involved and required dedicated parameter searches. As already mentioned, to avoid this we can invoke the freeze-in mechanism by reducing the couplings to the SM and choosing a different initial condition for the Boltzmann equation. However, in CP in the Dark we quickly run into a problem. Our DS particles couple to the SM via $SU(2)_L$ gauge couplings which are proportional to $g_1/\cos\theta_W \approx 0.74$. This value is much larger than the couplings required for freeze-in. In order to avoid them, we need to choose the rotation matrix given in Eq. (5.10) such that it decouples one of the mass eigenstates from the other two. In our case we choose to decouple the h_1 particle. This is done by setting $\alpha_2 = \pi/2$ such that the mass eigenstates are given by the gauge eigenstates via

$$\begin{aligned} h_1 &= \rho_s \,, \\ h_2 &= -\, s_{\alpha_1+\alpha_3}\rho_1 + c_{\alpha_1+\alpha_3}\eta \,, \\ h_3 &= -\, c_{\alpha_1+\alpha_3}\rho_1 - s_{\alpha_1+\alpha_3}\eta \,. \end{aligned} \tag{8.10}$$

We see that h_1 now only obtains a contribution from the $SU(2)_L$ singlet field ρ_s and can therefore not couple to the corresponding gauge bosons. All of the weak coupling strength has been moved into h_2 and h_3 via the doublet fields ρ_1 and η.

To describe the model CP in the Dark we need 13 independent input parameters, which are given in Eq. (5.12). As already mentioned, the remaining parameters in terms of the input parameters are given in App. B.2. We already set the rotation angle α_2 such that the gauge coupling of our freeze-in candidate is set to zero. Next, we need to ensure that the Higgs portal coupling λ_7 is sufficiently small to enable freeze-in. In the case that $\alpha_2 = \pi/2$ the λ_7 coupling is given by

$$\lambda_7 = \frac{2(m_{h_1}^2 - m_s^2)}{v^2} \,. \tag{8.11}$$

Therefore, to ensure that it is sufficiently small we need to impose $m_{h_1}^2 \approx m_s^2$. There are further consequences of fixing the α_2 parameter. The first is that the other neutral DS masses become degenerate, i.e. $m_{h_2} = m_{h_3}$. The second is that the parameter A becomes zero. As a result, decays of the form $h_{2/3} \to h_1 h$ are no longer possible and the CP violating properties of the model are lost. Further, the parameter λ_5 also becomes zero as a consequence. The fact that $A = 0$ and $\lambda_5 = 0$ is the same as imposing an additional $U(1)$ symmetry to the already exisiting $\mathbb{Z}_2$ symmetry on our lagrangian such that

$$\Phi_1 \to \Phi_1 \,,\; \Phi_2 \to e^{i\theta}\Phi_2 \,,\; \Phi_s \to \Phi_s \,. \tag{8.12}$$

This way we obtain two dark sectors. The first which only contains the h_1 particle which is going to responsible for the relic density generated via freeze-in. While the second, consisting of $h_{2/3}$ and $H^\pm$, will generate the relic density via freeze-out. Since the DM candidates $h_{2/3}$ are degenerate and also have the same couplings to the SM, they will contribute equally to relic density. We can now study the phenomenological consequences of this setup and check if we can find any signatures that could hint towards the existence of a freeze-in DM candidate.

CHAPTER 9

Conclusions

In this part of the thesis we investigated the model CP in the Dark and its phenomenological implications with respect to a scenario where simultaneous freeze-in and freeze-out is possible. In order to do this, we have first introduced the coupled Boltzmann equations in Sec. 8.1, which couple a thermal bath of freeze-out particles with a bath of freeze-in particles. We have then shown that we can decouple these equations and therefore treat freeze-in and freeze-out as independent processes since they occur at different times during the evolution of the universe.

The model CP in the Dark was already introduced prior to this part in Sec. 5.2.1. Due to the size of the gauge couplings that couple the DS of CP in the Dark to the SM, it is difficult to obtain couplings that are small enough for freeze-in. In Sec. 8.2 we address this issue by considering a scenario where the lightest gauge eigenstate decouples from the other two of the model giving us a freeze-in candidate. This was achieved by fixing one of the rotation angles to $\alpha_2 = \pi/2$. By doing this, we were able to obtain two DM candidates, one of which contributes to the relic density via freeze-out and one of which contributes via freeze-in. We also discussed the further implications of this scenario on the remaining model parameters.

In Ref. [115] we performed a numerical analysis of our setup by considering all relevant experimental and theoretical constraints. We have shown that throughout the entire parameter region freeze-in plays a crucial role in generating the observed relic abundance. In a majority of the scanned points that generated the desired relic density, freeze-in had to generate the majority of the relic abundance. We have shown that this effect is independent of the value of the DD cross section. The addition of a charged scalar contributes to the diphoton branching ratio of the SM Higgs boson. We have investigated this effect and found a signature that might hint towards a universe whose relic density is mostly generated via freeze-in. In a scenario where the diphoton branching ratio re-scaled to the SM value is measured to be below one, this model is able to generate the observed relic abundance only via dominant freeze-in contribution. If this model were to account for the entire observed relic density, this would give us a clear signal if the relic density was generated predominantly via freeze-in.

Part III.

Electroweak Baryogenesis in the C2HDM

CHAPTER 10

Introduction into Electroweak Baryogenesis

We will now shift our focus away from the problem of DM to an equally prominent one: the asymmetry between matter and anti-matter in the universe. In a universe that starts out in thermal equilibrium we expect there to be the same amount of matter as anti-matter. If this were the case, these two types of matter would have annihilated during the evolution of the universe and we would be left with a universe that consists mostly of photons. However, this is not what we observe. Instead, we have a universe that is full of matter and almost no anti-matter. We quantify the amount of asymmetry we observe via the Baryon Asymmetry of the Universe (BAU) η_{obs} which is given by Eq. 1.2. In order to explain the BAU we need to find a mechanism in the early universe that dynamically generates an asymmetry between matter and anti-matter.

10.1. Sakharov Conditions

In 1967, Sakharov proposed three conditions that have to hold true in order to dynamically generate the BAU [7]

- Baryon number violation
- C and CP violation
- Departure from thermal equilibrium

The first condition is self-explanatory. If we have no processes that violate the baryon number, we cannot obtain a baryon asymmetry. The second condition ensures that a process which produces a baryon excess does not produce the same anti-baryon access via the complementary process. If C and CP were exact the same amount of baryons and anti-baryons would be produced resulting in no net asymmetry. For the third condition we follow Refs. [121, 122] and consider the thermal equilibrium average of the baryon number operator $\hat{B}$ via the density operator $\rho = \exp(-\beta H)$, where H is the CPT-invariant world Hamiltonian

$$\langle \hat{B} \rangle_T = \text{tr}\left(e^{-\beta H}\hat{B}\right)$$

$$
\begin{aligned}
&= \mathrm{tr}\left((CPT)(CPT)^{-1}e^{-\beta H}\hat{B}\right) \\
&= \mathrm{tr}\left(e^{-\beta H}(CPT)^{-1}\hat{B}(CPT)\right) \\
&= -\mathrm{tr}\left(e^{-\beta H}\hat{B}\right) = -\langle\hat{B}\rangle_T \ . \qquad (10.1)
\end{aligned}
$$

Here, we used the CPT invariance of the Hamiltonian and the fact that $\hat{B}$ is odd under C and even under P and T. Therefore, $\langle\hat{B}\rangle_T = 0$ for a system that is always in thermal equilibrium. In the following sections we want to see if and how the SM can or cannot fulfill the three Sakharov conditions.

10.1.1. Baryon Violating Processes

In the SM we assign the baryon number and lepton number to the quarks and the leptons. These are classically conserved quantities due to the fact that the SM Lagrangian has a global $U(1)_B$ and $U(1)_L$ symmetry, i.e. it is invariant under the global phases

$$q(x) \to e^{i\omega/3}q(x) \ , \qquad (10.2)$$

$$\ell(x) \to e^{i\lambda}\ell(x) \ . \qquad (10.3)$$

Here, q and ℓ are the SM quarks and leptons, respectively. From Noether's theorem we obtain the associated conserved currents J_μ for the baryon number B and the lepton number L

$$\partial^\mu J^B_\mu = \partial^\mu \frac{1}{3}\sum_q \bar{q}\gamma_\mu q = 0 \ , \qquad (10.4)$$

$$\partial^\mu J^L_\mu = \partial^\mu \sum_\ell \bar{\ell}\gamma_\mu \ell = 0 \ . \qquad (10.5)$$

These currents are only conserved at the Born level. At the level of quantum fluctuations chiral currents are not conserved - they suffer from Adler-Bell-Jackiw anomalies [123,124]. For a gauge theory with a (non)abelian gauge group G of dimension d_G we obtain the following anomaly equations for the left- and right-chiral currents

$$\partial^\mu \bar{f}_L\gamma_\mu f_L = -c_L\frac{g^2}{32\pi^2}F^a_{\mu\nu}\tilde{F}^{a\mu\nu} \ , \qquad (10.6)$$

$$\partial^\mu \bar{f}_R\gamma_\mu f_R = +c_R\frac{g^2}{32\pi^2}F^a_{\mu\nu}\tilde{F}^{a\mu\nu} \ , \qquad (10.7)$$

where $f = q, \ell$, $F^a_{\mu\nu}$ is the field strength tensor, $\tilde{F}^{a\mu\nu}$ is the dual tensor, g is the gauge coupling corresponding to the gauge group under consideration and $c_{L/R}$ are constants that depend on the representation of f_L and f_R. We can now consider the above equations with respect to the SM gauge groups. For the QCD gauge group we have $c_L^{QCD} = c_R^{QCD}$ since the gluons couple with equal strengths to left- and right-handed quark currents. The weak gauge boson W only couples to the left-handed fermions giving $c_R^W = 0$, and lastly we have the hypercharge boson which couples differently to the different chiralities, i.e. $c_L^Y \neq c_R^Y$. Plugging these results into Eqs. (10.4) and (10.5) together with the decomposition

$$\bar{f}\gamma_\mu f = \bar{f}_L\gamma_\mu f_L + \bar{f}_R\gamma_\mu f_R \ , \qquad (10.8)$$

we obtain

$$\partial^\mu J^B_\mu = \partial^\mu J^L_\mu = \frac{n_F}{32\pi^2}\left(-g_1^2 W^i_{\mu\nu}\tilde{W}^{i\mu\nu} + g_2^2 B_{\mu\nu}\tilde{B}^{\mu\nu}\right) \ , \qquad (10.9)$$

where $W^i_{\mu\nu}$ ($i \in \{1,2,3\}$) and $B_{\mu\nu}$ are the $SU(2)_L$ and $U(1)_Y$ field strength tensors, respectively, $n_F = 3$ is the number of fermion generations and $g_{1/2}$ are gauge coupling constants.

From Eq. (10.9) we see that $\partial^\mu \left(J^B_\mu - J^L_\mu\right) = 0$, i.e. the quantum number $B - L$ is conserved in the SM, however $B + L$ is not. To see how this anomaly can result in baryon number violating processes we first rewrite the right-hand side of Eq. (10.9) as a divergence of a current K^μ [122]

$$\partial^\mu J^B_\mu = \partial^\mu J^L_\mu = n_F \partial^\mu K_\mu \,, \tag{10.10}$$

with

$$K^\mu = -\frac{g_1^2}{32\pi^2} 2\epsilon^{\mu\nu\alpha\beta} W^i_\nu \left(\partial_\alpha W^i_\beta + \frac{g_1}{3}\epsilon^{ijk} W^j_\alpha W^k_\beta\right) + \frac{g_2^2}{32\pi^2}\epsilon^{\mu\nu\alpha\beta} B_\nu B_{\alpha\beta} \,. \tag{10.11}$$

For a non-abelian gauge field whose field strength vanishes at infinity we can show that $2\epsilon_{\mu\nu\alpha\beta}\partial^\alpha F^{a\beta} = -g_1 \epsilon_{\mu\nu\alpha\beta} f^{abc} F^{b\alpha} F^{c\beta}$ which gives

$$\int \mathrm{d}^4x \partial^\mu K_\mu = \frac{g_1^3}{96\pi^2}\int_{\partial V_4} \mathrm{d}n^\mu \epsilon_{\mu\nu\alpha\beta}\epsilon^{ijk} W^{i\nu} W^{j\alpha} W^{k\beta} = N_{CS}(t_f) - N_{CS}(t_i) \equiv \Delta N_{CS} \,, \tag{10.12}$$

where N_{CS} is the Chern-Simons number and $t_{i/f}$ are some initial and final times, respectively. In a non-abelian gauge theory, like the $SU(2)_L$, there is an infinite number of ground states that carry different topological charges $\Delta N_{CS} = 0, \pm 1, \pm 2, \ldots$ which yield different physical vacuum states. These ground states are separated by a potential barrier. To see how this affects the baryon number we integrate Eq. (10.9) and obtain

$$\Delta \hat{B} = \Delta \hat{L} = n_F \Delta N_{CS} \,. \tag{10.13}$$

It was shown in Ref. [21] that large gauge fields $W^i_\mu \sim 1/g_1$ with non-zero topological charge can induce transitions that change the baryon and lepton number according to Eq. (10.13). In scenarios where the fermion masses can be neglected a more precise violation rule can be defined via

$$\Delta L_e = \Delta L_\mu = \Delta L_\tau = \frac{1}{3}\Delta B = \Delta N_{CS} \,. \tag{10.14}$$

So far we have found that there are different equivalent ground states which carry different topological charges. However, for a baryon number-violating process to occur there needs to be a transition from one vacuum state to another. In the case of a process where the gauge field connects one ground state to another we speak of an (anti-)instanton [125]. The cross section of such a process at zero temperature is of the order of [21]

$$\sigma_{\text{instanton}}(T = 0) \sim e^{-8\pi^2/g_1^2} \approx 10^{-164} \,. \tag{10.15}$$

Which means that at zero temperature a transition between two vacuum states is practically impossible. The situation changes at finite temperature where the SM is coupled to a heat bath, i.e. in the early universe. This enables processes where the transition between vacuua occurs not via a tunneling process as in the instanton case but by passing over the potential barrier separating the two minima. These transitions are called weak sphalerons [126] and have a rate that is Boltzmann suppressed such that [127]

$$\Gamma_{\text{sph}} \propto e^{-E_{\text{sph}}(T)/T} \,, \tag{10.16}$$

where E_{sph} is the minimal height of the barrier given by

$$E_{\text{sph}}(T) = \frac{4\pi}{g_1} B\left(\frac{\lambda}{g_1^2}\right) v(T) \,, \tag{10.17}$$

and B is a dimensionless constant which is tabulated in Ref. [126]. Plugging in numerical values for the temperature-independent constants the barrier height becomes

$$E_{\text{sph}}(T) \simeq 37 v(T) \,. \tag{10.18}$$

The rate given by Eq. (10.16), however, only applies in the case where the $SU(2)_L \times U(1)$ symmetry of the SM is already broken. For temperatures above $T_c \gtrsim 100$ GeV this symmetry is unbroken (more on that in the next section) and has therefore a different topological structure. In such a scenario the weak sphaleron rate has to be computed on the lattice and is given by [128]

$$\Gamma_{\text{sph}} \approx 8 \cdot 10^{-7} T \ . \tag{10.19}$$

So for large temperatures, where the electroweak symmetry is unbroken, we obtain an unsuppressed weak sphaleron rate that leads to baryon number-violating processes. However, once this symmetry is broken the rate is exponentially suppressed through the value of the VEV.

10.1.2. C and CP Violation

In the SM we also have C and CP violation via the weak interaction of the quarks given by

$$\mathrm{L}_{qqW} = -\frac{g_1}{\sqrt{2}} \bar{u}_L \gamma^\mu V_{\text{CKM}} d_L W_\mu^+ + h.c. \ , \tag{10.20}$$

in terms of the left-handed quark flavor triplets u_L and d_L for up-type and down-type quarks, respectively, as well as the Cabibbo-Kobayashi-Maskawa (CKM) matrix

$$V_{\text{CKM}} = U_{u_L}^\dagger U_{d_L} \ , \tag{10.21}$$

where U_{u_L} and U_{d_L} are unitary transformations which rotate the quark fields into their mass basis. The CKM matrix contains the KM phase angle δ_{KM} which is responsible for CP-violating processes. Processes where CP violation has been observed and can be explained by the KM phase are Kaon decays [129] as well as B meson decays [130].

10.1.3. Departure from Thermal Equilibrium

So far the SM can account for two out of the three Sakharov conditions. The last condition requires that we have a suitable event during the evolution of our universe which disturbs the thermal equilibrium of the SM plasma. As already implied in the previous section the breaking of electroweak symmetry is a key component in describing a possible mechanism that explains the BAU. So the question becomes: Does the electroweak phase transition cause a departure from thermal equilibrium? In order to answer this question we have to study the Higgs potential of the SM given in Eq. (2.10) at finite temperature. For large temperatures and small Higgs masses the effective Higgs potential $V_{\text{eff}}(\phi, T)$ is given at one loop by [122]

$$V_{\text{eff}}(\phi, T) = \frac{1}{2} a (T^2 - T_1^2) \phi^2 - \frac{1}{3} b T \Phi^3 + \frac{1}{4} \lambda \phi^4 \ , \tag{10.22}$$

with

$$a = \frac{3}{16} g_1^2 + \left(\frac{1}{2} + \frac{m_t^2}{m_h^2} \right) \lambda \quad , \quad b = \frac{9 g_1^3}{32 \pi} \quad , \quad T_1 = \frac{m_h}{2\sqrt{a}} \ . \tag{10.23}$$

Although we now know that Higgs mass is not small, it is still worth to investigate this example. We can check how this potential evolves as the universe cools down. Here, we can obtain two distinct scenarios with different phenomenological consequences which we show schematically in Fig. 10.1. In the first scenario shown on the left, there always exists a single simultaneous minimum as the universe cools down. As soon as a new minimum forms at the critical temperature T_c the VEV acquires this value and keeps decreasing smoothly until it reaches today's value. In such a case we speak of a second-order phase transition. The second scenario on the right shows that at the critical temperature we obtain two degenerate minima separated by a potential barrier. If such a scenario occurs, we call it a first-order phase transition. During this transition, as the universe cools down further, bubbles with a

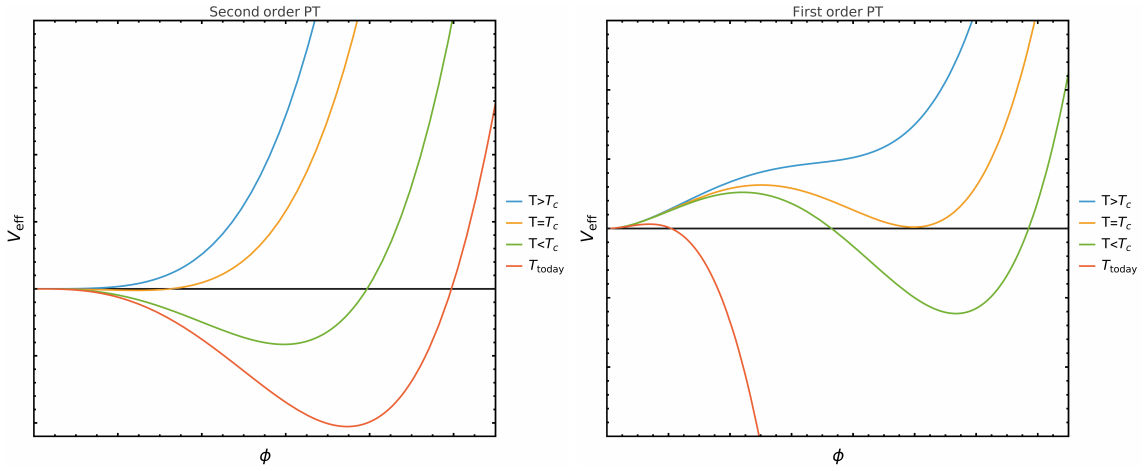

Figure 10.1.: Effective potential over the field value for different temperatures. On the left we show a second order phase transition, while on the right we show a first-order phase transition.

non-zero VEV begin to form in the universe where the fields inside these bubbles have either crossed the potential barrier due to temperature fluctuations or due to tunneling processes. These bubbles release latent heat and grow larger until they eventually fill the entire universe. The interaction of the plasma with the expanding bubble wall is exactly the out of equilibrium event we are looking for.

For the potential given in Eq. (10.22) we obtain a first-order phase transition at a critical temperature of

$$T_c = \frac{T_1}{\sqrt{1 - 2b^2/(9a\lambda)}} \,. \tag{10.24}$$

However, we need to remember that this potential is only valid if the mass of the Higgs boson is small compared to the relevant temperature. Since, we know that the Higgs boson has a mass of $m_h = 125.09$ GeV, this assumption is not valid since the phase transition occurs at the order of 100 GeV. A more dedicated investigation to determine if the SM has a first-order phase transition has been done on the lattice in Refs. [131, 132]. There it has been shown that for Higgs boson masses above $m_h \simeq 72$ GeV only a second-order phase transition is able to take place. This means that the SM by itself is not sufficient to explain the BAU we observe today. One ansatz to obtain a first-order-phase transition as well as sufficient C and CP violation, which we will follow in this thesis, is to introduce further scalar fields. These additional fields are able to produce potential barriers between the true and the false vacuum, necessary for baryogenesis at the cost of a more complicated vacuum structure.

10.2. Electroweak Baryogenesis

Suppose we are able to provide a model with enough C and CP violation as well as a first-order phase transition, we still need to provide the mechanism which produces the BAU. In this thesis we will consider the process of non-local baryogenesis, where the baryon asymmetry is ultimately generated away from the bubble wall in contrast to local baryogenesis where CP violation and baryon number violation takes place at the bubble wall. Non-local baryogenesis takes place in three steps. We will describe these steps with the help of Fig. 10.2 which shows the entire process schematically. We show a planar bubble wall with the false vacuum on the left side of the wall and the true vacuum on the right. The bubble wall has a wall velocity v_w with which it is expanding and a wall thickness L_w. In the first step left- and right-handed particles collide with the bubble wall that is expanding. Due to the fact that our model has CP violation, the left- and right-handed particles have different reflection coefficients

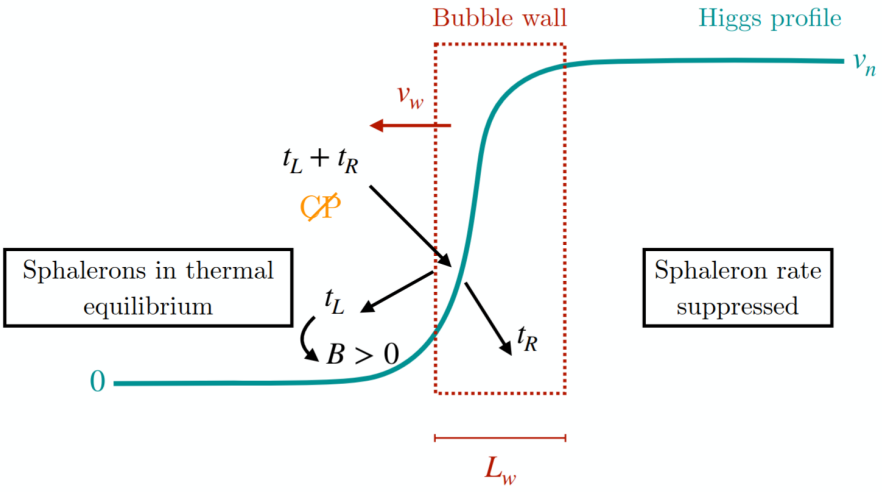

Figure 10.2.: A schematic graphic of electroweak baryogenesis showing the interaction of the left-handed and right-handed top quarks with the bubble wall and their conversion into a baryon asymmetry. Taken from Ref. [133].

at the bubble wall which induces an overabundance of left-handed particles outside of the bubble, i.e. left of the wall in Fig. 10.2. This abundance is then converted in the second step via the weak sphaleron processes, which are unsuppressed outside of the bubble wall, into a baryon asymmetry. This asymmetry would quickly equilibrate if left untouched and no net baryon asymmetry would be present. In such a case we speak of baryon asymmetry wash out. However, in the third step this momentary baryon asymmetry gets picked up by the expanding bubble wall. Since the sphaleron processes are Boltzmann suppressed inside the bubble the asymmetry remains and we are left with more matter than anti-matter.

One thing we have to make sure, is that the sphaleron rate is sufficiently suppressed in order to avoid wash out. Going back to Eqs. (10.16) and (10.17) we have to ensure that the exponential suppression is large to effectively turn off the sphaleron rate inside the bubble. This is done by imposing that our first-order phase transition is strong via the condition [33]

$$\frac{v(T_c)}{T_c} \gtrsim 1 \,. \tag{10.25}$$

This ensures that the Boltzmann suppression is sufficiently large and the generated baryon asymmetry is retained inside the bubble wall.

CHAPTER 11

Transport Equations

So far we only gave a rough outline on how electroweak baryogenesis (EWBG) can produce the observed BAU. In this chapter we will present the technical details and derive the transport equations necessary to compute the BAU. We will adopt the WKB ansatz first developed by Cline, Joyce and Kainulainen in [10] and Fromme and Huber in [11]. In these papers, the equations were only valid for small wall velocities. This approach was later generalized to arbitrary wall velocities by Cline and Kainulainen [12] and, with the most recent developments, was extended for arbitrary plasma velocity moments by Kainulainen and Venkatesan [13]. We will base this chapter on the work done in these references to derive the transport equations as well as the formula to calculate the baryon asymmetry.

11.1. CP-Violating Force

We want to start by deriving the force that acts on the plasma particles as they move through the bubble wall. Since the bubble wall interpolates between the true vacuum and the false one, we will look at a VEV that is dependent on the distance to the bubble wall z. To make sure that we obtain CP-violating effects, we will give the VEV also a complex phase such that it can be parameterized via

$$\langle 0|\phi|0\rangle_T \equiv \frac{\omega(z)}{\sqrt{2}} e^{i\theta(z)} \, . \tag{11.1}$$

Here we implicitly define the VEV to be the ground state of the field ϕ. To see the effect of such a ground state we will look at the Yukawa sector given in Eq. (2.17) and assume that ϕ couples to the fermions of the SM. This will lead to mass terms of the fermions that are given by

$$\mathrm{L}_{\mathrm{mass}} = -m_\psi(z)\bar{\psi}_L\psi_R - m_\psi^*(z)\bar{\psi}_R\psi_L \, , \tag{11.2}$$

where ψ is either a lepton or a quark field and $m_\psi(z)$ the respective mass defined via

$$m_\psi(z) = \frac{y_\psi}{\sqrt{2}}\omega(z)e^{i\theta(z)} \equiv |m_\psi(z)|e^{i\theta(z)} \, , \tag{11.3}$$

with y_ψ being the Yukawa coupling to the scalar field ϕ. Equation (11.3) tells us that fermions inside the plasma that are trying to pass into the bubble obtain a z-dependent mass with a

complex phase. Note that we cannot get rid of this phase by redefining the fermions fields. As it is a local phase, it will appear again via the derivatives of the kinetic terms. We can now write the equations of motion, i.e. the Dirac equation, for the fermions of this Lagrangian

$$\left(i\gamma^\mu\partial_\mu - m_\psi(z)P_R - m_\psi^*(z)P_L\right)\psi = 0\ , \tag{11.4}$$

where $P_{R/L} = (1 \pm \gamma^5)/2$ are the right- and left-chiral projectors, respectively. The key difference to the usual Dirac equation is that the above equation does not remain invariant under a C transformation and instead becomes

$$\left(i\gamma^\mu\partial_\mu - m_\psi^*(z)P_R - m_\psi(z)P_L\right)\psi^c = 0\ \ , \tag{11.5}$$

resulting in different equations of motion based on if we consider a particle or an anti-particle. For now we will focus on the particle case. We first boost into a frame where the momentum parallel to the wall is zero, meaning $p_x = p_y = 0$. To solve Eq. (11.4) in this frame we make an ansatz with a plane-wave time dependence with positive energy as well as a tensor product between chiral components and spin eigenstates χ_s

$$\psi_s(t,z) = e^{-iEt}\begin{pmatrix} L_s(z) \\ R_s(z)\end{pmatrix} \otimes \chi_s\ . \tag{11.6}$$

The spin is taken to be in z direction such that $\sigma_3\psi = s\psi$, with eigenvalues $s = \pm 1$. Inserting this into Eq. (11.4) we obtain two coupled equations for L_s and R_s

$$(E - is\partial_z)L_s = m_\psi R_s\ , \tag{11.7}$$
$$(E + is\partial_z)R_s = m_\psi^* L_s\ . \tag{11.8}$$

Inserting R_s from Eq. (11.7) into Eq. (11.8) we obtain

$$\left[(E + is\partial_z)\frac{1}{m_\psi}(E - is\partial_z) - m_\psi^*\right]L_s = 0\ . \tag{11.9}$$

To solve the above equation we will assume that the background, i.e. the VEV, varies slowly compared to the time scale at which the plasma particles move ($T \gg L_w^{-1}$). This allows us to do a gradient expansion with respect to the z variable. To enable us to do the gradient expansion we make the WKB ansatz for L_s

$$L_s(z) \equiv w(z)\exp\left[i\int^z p_{cz}(z')\mathrm{d}z'\right]\ , \tag{11.10}$$

with the amplitude $w(z)$ and the canonical momentum p_{cz}. At this stage we have to remember that we can do a field redefinition by a local phase, i.e. $\psi \to e^{i\alpha(z)}\psi$, which preserves the equations of motion but shifts the canonical momentum via

$$p_{cz} \to \tilde{p}_{cz} = p_{cz} + \alpha'(z)\ . \tag{11.11}$$

This ambiguity in the definition of p_{cz} shows that it cannot be the physical momentum of the particle. Inserting the ansatz of Eq. (11.10) into Eq. (11.9) and separating the real and imaginary parts we obtain

$$E^2 - |m_\psi|^2 - \tilde{p}_{cz}^2 + (sE + \tilde{p}_{cz})\theta' - \frac{|m_\psi|'}{|m_\psi|}\frac{w'}{w} + \frac{w''}{w} = 0\ , \tag{11.12}$$

$$2\tilde{p}_{cz}w' + \tilde{p}_{cz}'w - \frac{|m_\psi|'}{|m_\psi|}(sE + \tilde{p}_{cz}) - \theta' w' = 0\ . \tag{11.13}$$

Here, the prime denotes the derivative with respect to z. At lowest order, where we drop all the gradient terms, we recover the usual dispersion relation from Eq. (11.12), $E^2 = \tilde{p}_{cz}^2 + m_\psi^2$. We can also derive the dispersion relation to first-order in gradients. At this order the above equations decouple such that we obtain from Eq. (11.12)

$$p_{cz} \approx p_0 + s_{CP}\left(\frac{1}{2} + \frac{sE}{p_0}\right)\theta' - \alpha' \,, \tag{11.14}$$

to first-order in gradients, where $p_0 = \text{sign}(p_{cz})\sqrt{E^2 - |m_\psi|^2}$. With $s_{CP} = \pm 1$ we include the generalization of the equation to also include the anti-particle state, where $s_{CP} = -1$ refers to the anti-particle. Here, we made the phase dependence explicit again, so that we can later show its cancellation in the physical quantities. We can also obtain the energy via Eq. (11.12),

$$E = \sqrt{(p_{cz} + \alpha_{CP})^2 + |m_\psi|^2} - s_{CP}\frac{s\theta'}{2} \,, \tag{11.15}$$

with $\alpha_{CP} \equiv \alpha' \mp s_{CP}\theta'/2$ where the $(-)$ refers to left-handed and $(+)$ to right-handed particles. To restore the momenta parallel to the wall again we boost back to a general frame where $E^2 \to E^2 + p_x^2 + p_y^2$. This changes the dispersion relation in Eq. (11.15) to

$$\begin{aligned} E^2 &= (p_{cz} + \alpha_{CP})^2 + |m_\psi|^2 - s_{CP}s\sqrt{(p_{cz} + \alpha_{CP})^2 + |m_\psi|^2}\theta' + \frac{\theta'^2}{4} + p_x^2 + p_y^2 \\ &\approx E_0^2 - s_{CP}sE_{0z}\theta', \end{aligned} \tag{11.16}$$

where we neglect the θ'^2 term and define

$$E_0 \equiv \sqrt{(p_{cz} + \alpha_{CP})^2 + p_x^2 + p_y^2 + |m_\psi|^2} \quad , \quad E_{0z} \equiv \sqrt{(p_{cz} + \alpha_{CP})^2 + |m_\psi|^2} \,. \tag{11.17}$$

After taking the square root, only considering the positive energy solution, and performing a Taylor series we obtain[15]

$$E \approx E_0 - s_{CP}\frac{s\theta'}{2}\frac{E_{0z}}{E_0} \,. \tag{11.18}$$

Next, we calculate the physical kinetic momentum which is given by $p_z = Ev_{gz}$, where v_{gz} is the group velocity of the WKB wave-packet defined via

$$v_{gz} \equiv \frac{\partial E}{\partial p_{cz}} = \frac{p_{cz} + \alpha_{CP}}{E_0}\left(1 - s_{CP}\frac{s\theta'}{2}\frac{E_0^2 - E_{0z}^2}{E_0^2 E_{0z}}\right) \,. \tag{11.19}$$

With this, the kinetic momentum is given at leading order by

$$p_z \approx (p_{cz} + \alpha_{CP})\left(1 - s_{CP}\frac{s\theta'}{2E_{0z}}\right) \,. \tag{11.20}$$

Now we can use the kinetic momentum to substitute the canonical momentum in Eq. (11.17) to obtain

$$E_{0z} = \sqrt{p_z^2\left(1 - s_{CP}\frac{s\theta'}{2E_{0z}}\right)^{-2} + |m_\psi|^2} \approx \tilde{E}_{0z} + s_{CP}\frac{s\theta'}{2}\frac{p_z^2}{\tilde{E}_{0z}E_{0z}} \,. \tag{11.21}$$

Inserting the above equation back into Eq. (11.20) gives p_z to the order that we want to consider

$$\begin{aligned} p_z &= (p_{cz} + \alpha_{CP})\left[1 - s_{CP}\frac{s\theta'}{2}\left(\tilde{E}_{0z} + s_{CP}\frac{s\theta'}{2}\frac{p_z^2}{\tilde{E}_{0z}E_{0z}}\right)^{-1}\right] \\ &\approx (p_{cz} + \alpha_{CP})\left(1 - s_{CP}\frac{s\theta'}{2\tilde{E}_{0z}}\right) \,. \end{aligned} \tag{11.22}$$

[15] Although α_{CP} also depends on θ' we treat it as a constant in the expansion. For the derivation this means that we are taking higher-order terms of θ' into account. Doing this will make it easier to obtain the cancellation of α_{CP}.

Next, we can insert the obtained kinetic momentum into Eq. (11.17) to obtain to first-order in gradients

$$E = \tilde{E}_0 + s_{CP}\Delta\tilde{E} = \tilde{E}_0 - s_{CP}\frac{s\theta'|m_\psi|^2}{2\tilde{E}_0\tilde{E}_{0z}} , \tag{11.23}$$

where

$$\tilde{E}_0 \equiv \sqrt{p_z^2 + p_x^2 + p_y^2 + |m_\psi|^2} \quad , \quad \tilde{E}_{0z} \equiv \sqrt{p_z^2 + |m_\psi|^2} . \tag{11.24}$$

In the same manner we can write the group velocity in Eq. (11.19) with respect to the kinetic momentum

$$v_{gz} = \frac{p_z}{\tilde{E}_0}\left(1 + s_{CP}\frac{s\theta'|m_\psi|^2}{2\tilde{E}_0\tilde{E}_{0z}}\right) . \tag{11.25}$$

We see now that Eqs. (11.23) and (11.25) are independent of the phase α' and therefore represent physical quantities. Using the aforementioned equations we can use the Hamilton equations, $\dot{z} = v_{gz}$ and $\dot{p}_z = -\partial E/\partial z$, to obtain the CP-violating semiclassical force

$$F_z \equiv \dot{p}_z \approx -\frac{(|m_\psi|^2)'}{2\tilde{E}_0} + s_{CP}s\left[\frac{(|m_\psi|^2\theta')'}{2\tilde{E}_0\tilde{E}_{0z}} - \frac{|m_\psi|^2(|m_\psi|^2)'\theta'}{4\tilde{E}_0^3\tilde{E}_{0z}}\right] . \tag{11.26}$$

It is clear that we have two terms which act differently depending on the particle under consideration. The first term is CP-even and is therefore identical for particles and anti-particles, while the second term implies that the interaction with the wall leads to opposite forces acting on particles compared to anti-particles. This CP-violating force can also be derived from more fundamental principles via the Schwinger-Keldysh equation as was done in Ref. [134].

11.2. Liouville Operator

To describe how the plasma particles evolve as they interact with the bubble wall we will use the Boltzmann equation given in Eq. (2.47). We are looking for a time-independent solution with an external force, where we only take into account the z direction. This gives us the following form for the Liouville operator

$$\mathcal{L}[f] = (\dot{z}\partial_z + \dot{p}_z\partial_{p_z})f = (v_{gz}\partial_z + F_z\partial_{p_z})\, f = \mathcal{C}\,[f] \ . \tag{11.27}$$

To find a solution to this equation, we first consider a phase-space distribution in the moving wall frame that is in local equilibrium, i.e.

$$f_{0w}^i(z, \mathbf{p}) = f_{\mathrm{FD/BE}}[\gamma_w(\tilde{E}_0^i(z, \mathbf{p}) + v_w p_z)] , \tag{11.28}$$

for a particle species i with energy $\tilde{E}_0^i = \sqrt{\mathbf{p}^2 + |m_i(z)|^2}$ and a given wall velocity v_w with the Lorentz factor γ_w. Depending on the particle species we need to use the Fermi-Dirac $(+)$ or Bose-Einstein $(-)$ distribution functions which are given by

$$f_{\mathrm{FD/BE}}(x) = \frac{1}{e^{\beta x} \pm 1} \quad , \quad \beta = \frac{1}{T} . \tag{11.29}$$

In this thesis we will adopt the convention present in the literature for the derivatives of f_{0w}^i. Namely, that derivatives of f_{0w}^i are denoted by a prime and are taken with respect to the entire argument $\gamma_w(\tilde{E}_0^i + v_w p_z)$ such that $f_{0w}^{i\prime} = \partial_{\gamma_w(\tilde{E}_0^i + v_w p_z)} f_{0w}^i$. The prime for all other quantities still keeps the same meaning and denotes the derivative with respect to z.

Of course the plasma particles will not be in local thermal equilibrium since they are experiencing a force at the bubble wall. We want to track this disturbance away from equilibrium,

which we assume to be small, by including a chemical potential μ^i to capture changes in number density and a perturbation δf^i to track the departure from kinetic equilibrium. This gives us the ansatz

$$f^i(z,\mathbf{p}) = f_{\mathrm{FD/BE}}[\gamma_w(E^i + v_w p_z) - \mu^i] + \delta f^i(z,\mathbf{p})\,. \tag{11.30}$$

Note, that we also now take into account the change in the dispersion relation due to the interaction with the wall by using Eq (11.23). To make sure that δf only tracks the kinetic disturbance and not the number density of the equilibrium we impose

$$\int \mathrm{d}^3p\,\delta f^i(z,\mathbf{p}) = 0\,. \tag{11.31}$$

To linearize the equations with respect to μ^i and δf we again only consider the leading terms in the gradient expansion and treat μ^i to be of the same order as $\Delta\tilde{E}$. This gives us, up to the second order in gradients, the following expression

$$f^i \approx f^i_{0w} + f^{i\prime}_{0w}(\gamma_w s_{CP}\Delta\tilde{E} - \mu^i) + \frac{1}{2}f^{i\prime\prime}_{0w}(\gamma_w s_{CP}\Delta\tilde{E} - \mu^i)^2 + \delta f^i\,. \tag{11.32}$$

A natural way to continue is to split the chemical potential as well as δf into a CP-even and CP-odd part via

$$\mu^i \equiv \mu^i_e + \mu^i_o \quad , \quad \delta f^i \equiv \delta f^i_e + \delta f^i_o\,. \tag{11.33}$$

This allows us to arrange our ansatz in Eq. (11.32) via

$$f^i \equiv f^i_e + s_{CP} f^i_o\,, \tag{11.34}$$

where

$$f^i_e \approx f^i_{0w} - f^{i\prime}_{0w}\mu^i_e + \frac{1}{2}f^{i\prime\prime}_{0w}\gamma_w^2\Delta\tilde{E}^{i2} + \delta f^i_e\,, \tag{11.35}$$

$$f^i_0 \approx f^i_{0w}(\gamma_w\Delta\tilde{E}^i - \mu^i_o) - f^{i\prime\prime}_{0w}\gamma_w\Delta\tilde{E}^i\mu^i_e + \delta f^i_o\,. \tag{11.36}$$

With this split we can now extract the CP-odd and CP-even parts of the Boltzmann equation via the projections

$$\mathcal{L}[f]\big|_{CP-\mathrm{odd}} \equiv \frac{1}{2}\left(\mathcal{L}[f]|_{s_{cp}=+1} - \mathcal{L}[f]|_{s_{cp}=-1}\right)\,, \tag{11.37}$$

$$\mathcal{L}[f]\big|_{CP-\mathrm{even}} \equiv \frac{1}{2}\left(\mathcal{L}[f]|_{s_{cp}=+1} + \mathcal{L}[f]|_{s_{cp}=-1}\right)\,. \tag{11.38}$$

By applying the first projection we select the terms that change sign between particles and anti-particles, while applying the second projection collects terms that are not sensitive to the particle type. The CP-odd projection gives [135]

$$\begin{aligned}
\mathcal{L}[f]\big|_{CP-\mathrm{odd}} =& -\frac{p_z}{\tilde{E}^i_0}f^{i\prime}_{0w}\mu^{i\prime}_o + v_w\gamma_w\frac{(|m_i|^2)'}{2\tilde{E}^i_0}f^{i\prime\prime}_{0w}\mu^i_o - \frac{(|m_i|^2)'}{2\tilde{E}^i_0}\partial_{p_z}\delta f^i_o + \frac{p_z}{\tilde{E}^i_0}\partial_z\delta f^i_o \\
&+ sv_w\gamma_w\frac{|m_i|^2(|m_i|^2)'\theta'}{4\tilde{E}^{i2}_0\tilde{E}^i_{0z}}\left(\frac{f^{i\prime\prime}_{0w}}{\tilde{E}^i_0} - \gamma_w f^{i\prime\prime\prime}_{0w}\right)\mu^i_e + sv_w\gamma_w\frac{(|m_i|^2\theta')'}{2\tilde{E}^i_0\tilde{E}^i_{0z}}f^{i\prime\prime}_{0w}\mu^i_e \\
&+ \frac{sp_z|m_i|^2\theta'}{2\tilde{E}^{i2}_0\tilde{E}^i_{0z}}\left(\gamma_w f^{i\prime\prime}_{0w} - \frac{f^{i\prime}_{0w}}{\tilde{E}^i_0}\right)\mu^{i\prime}_e + \frac{sp_z|m_i|^2\theta'}{2\tilde{E}^{i3}_0\tilde{E}^i_{0z}}\partial_z\delta f^i_e \\
&+ \frac{s}{2\tilde{E}^i_0\tilde{E}^i_{0z}}\left((|m_i|^2\theta')' - \frac{|m_i|^2(|m_i|^2)'\theta'}{2\tilde{E}^{i2}_0}\right)\partial_{p_z}\delta f^i_e \\
&+ sv_w\gamma_w\frac{(|m_i|^2\theta')'}{2\tilde{E}^i_0\tilde{E}^i_{0z}}f^{i\prime}_{0w} + sv_w\gamma_w\frac{|m_i|^2(|m_i|^2)'\theta'}{4\tilde{E}^{i2}_0\tilde{E}^i_{0z}}\left(\gamma_w f^{i\prime\prime}_{0w} - \frac{f^{i\prime}_{0w}}{\tilde{E}^i_0}\right)\,,
\end{aligned} \tag{11.39}$$

where we expanded up to third order in gradients. For the CP-even projection we obtain

$$\begin{aligned}\mathcal{L}[f]\big|_{CP-\text{even}} =& -\frac{p_z}{\tilde{E}_0^i} f_{0w}^{i\prime}\mu_e^{i\prime} + v_w\gamma_w\frac{(|m_i|^2)'}{2\tilde{E}_0^i} f_{0w}^{i\prime\prime}\mu_e^i - \frac{(|m_i|^2)'}{2\tilde{E}_0^i}\partial_{p_z}\delta f_e^i + \frac{p_z}{\tilde{E}_0^i}\partial_z\delta f_e^i \\ & - \frac{sp_z|m_i|^2\theta'}{2\tilde{E}_0^{i3}\tilde{E}_{0z}^i} f_{0w}^{i\prime}\mu_o^{i\prime} - \frac{sv_w\gamma_w}{2\tilde{E}_0^i\tilde{E}_{0z}^i}\left[(|m_i|^2\theta')'\left(1+\frac{p_z}{v_w\tilde{E}_0^i}\right) - \frac{|m_i|^2(|m_i|^2)'\theta'}{2\tilde{E}_0^i}\right] f_{0w}^{i\prime\prime}\mu_o^i \\ & + \frac{s}{2\tilde{E}_0^i\tilde{E}_{0z}^i}\left[(|m_i|^2\theta')' - \frac{|m_i|^2(|m_i|^2)'\theta'}{2\tilde{E}_0^i}\right]\partial_{p_z}\delta f_o + \frac{sp_z|m_i|^2\theta'}{2\tilde{E}_0^{i3}\tilde{E}_{0z}^i}\partial_z\delta f_o \\ & - v_w\gamma_w\frac{(|m_i|^2)'}{2\tilde{E}_0^i} f_{0w}^{i\prime}\,, \end{aligned} \tag{11.40}$$

up to second order in gradients. In both equations the last line corresponds to the so-called *source* terms. These are independent of the variables we are trying to solve for and act as the force that drives our plasma out of equilibrium. Especially relevant for our purposes is the CP-odd source term

$$S_o^i \equiv -sv_w\gamma_w\frac{(|m_i|^2\theta')'}{2\tilde{E}_0^i\tilde{E}_{0z}^i} f_{0w}^{i\prime} - sv_w\gamma_w\frac{|m_i|^2(|m_i|^2)'\theta'}{4\tilde{E}_0^{i2}\tilde{E}_{0z}^i}\left(\gamma_w f_{0w}^{i\prime\prime} - \frac{f_{0w}^{i\prime}}{\tilde{E}_0^i}\right)\,. \tag{11.41}$$

Although we have derived the Liouville operator for a fermion with a complex mass, it is also valid for neutral scalars or fermions without a complex phase, by setting θ to zero.

One could already try and solve Eqs. (11.39) and (11.40) at this stage. However, this not easy at all and at the time of this thesis has only been done for the CP-even part, e.g. in Refs. [136–138]. By solving the CP-even part one can determine the friction at the wall and the wall velocity. However, for the CP-odd equation, we will follow a different approach in which we average our equations with suitable weights to obtain a closed system of first-order linear differential equations called the fluid network. This approach is more resourceful in terms of computational complexity as we do not have to deal with a system of integro-differential equations. For the CP-even equations, this approach was shown to lead to unreliable results and was therefore abandoned.

11.3. Moment Expansion

As already mentioned in the previous section, we want to construct a closed system of first-order differential equations from Eq. (11.39). For our further calculation we will neglect the terms proportional to the CP-even variables μ_e^i and δf_e^i as they are of higher order in ∂_z compared to the CP-odd counterparts. This leaves us with an equation depending solely on the CP-odd variables μ_o^i and δf_o

$$\begin{aligned}\mathcal{L}[f]\big|_{CP-\text{odd}} &= -\frac{p_z}{\tilde{E}_0^i} f_{0w}^{i\prime}\mu_o^{i\prime} + v_w\gamma_w\frac{(|m_i|^2)'}{2\tilde{E}_0^i} f_{0w}^{i\prime\prime}\mu_o^i - \frac{(|m_i|^2)'}{2\tilde{E}_0^i}\partial_{p_z}\delta f_o^i + \frac{p_z}{\tilde{E}_0^i}\partial_z\delta f_o^i \\ &= S_o^i + \mathcal{C}^i[f]\,. \end{aligned} \tag{11.42}$$

To proceed, we integrate the above equation over the momenta with the weight $(p_z/\tilde{E}_o^i)^\ell$, for different moments ℓ. At this point we define the average over a function $X(\mathbf{p})$ as

$$\langle X(\mathbf{p})\rangle \equiv \frac{1}{N_1}\int \mathrm{d}^3p X(\mathbf{p}) \quad \text{with} \quad N_1 = \int \mathrm{d}^3p f_{0w,\mathrm{FD}}'\big|_{m=0} = -\gamma_w\frac{2\pi^3}{3}T^2\,. \tag{11.43}$$

This gives us the ℓ'th moment equation

$$-\left\langle \frac{p_z^{\ell+1}}{\tilde{E}_0^{\ell+1}} f_{0w}^{i\prime} \right\rangle \mu_o^{i\prime} + v_w \gamma_w (|m_i|^2)' \left\langle \frac{p_z^{\ell}}{2\tilde{E}_0^{\ell+1}} f_{0w}^{i\prime\prime} \right\rangle \mu_o^i + \partial_z \left\langle \frac{p_z^{\ell+1}}{\tilde{E}_0^{\ell+1}} \delta f_o^i \right\rangle + \ell (|m_i|^2)' \left\langle \frac{p_z^{\ell-1}}{2\tilde{E}_0^{\ell+1}} \delta f_o^i \right\rangle$$
$$= \left\langle \frac{p_z^{\ell}}{\tilde{E}_0^{\ell}} \left(S_o^i + \mathcal{C}^i[f] \right) \right\rangle . \tag{11.44}$$

Following Ref. [13], we define the ℓ'th velocity moment $u_{o,\ell}^i$ and the dimensionless mass x via

$$u_{o,\ell}^i \equiv \left\langle \frac{p_z^{\ell}}{\tilde{E}_0^{\ell}} \delta f_o^i \right\rangle \quad \text{and} \quad x_i \equiv \frac{m_i}{T} . \tag{11.45}$$

Note, that the condition in Eq. (11.31) sets $u_{o,\ell}^i = 0$. With the above definitions we obtain for Eq. (11.44)

$$-D_{\ell+1}\mu_o^{i\prime} + u_{o,\ell+1}^{i\prime} + v_w \gamma_w (|x_i|^2)' Q_{\ell+1} \mu_o^i + \ell (|x_i|^2)' \bar{R} u_{o,\ell}^i = \hat{S}_{o,\ell}^i + \hat{\mathcal{C}}_\ell^i , \tag{11.46}$$

where we define the dimensionless coefficient functions D_ℓ, Q_ℓ and $\bar{R}$ via

$$D_\ell \equiv \left\langle \left(\frac{p_z}{\tilde{E}_0} \right)^\ell f_{0w}^{\prime} \right\rangle \quad , \quad Q_\ell \equiv T^2 \left\langle \frac{p_z^{\ell-1}}{2\tilde{E}_0^{\ell}} f_{0w}^{\prime\prime} \right\rangle \quad , \quad \bar{R} u_{o,\ell}^i \equiv T^2 \left\langle \frac{p_z^{\ell-1}}{2\tilde{E}_0^{\ell+1}} \delta f_o^i \right\rangle . \tag{11.47}$$

Further, the ℓ'th dimensionless source term $\hat{S}_{o,\ell}^i$ and collision term $\hat{\mathcal{C}}_\ell^i$ are given by

$$\hat{S}_{o,\ell}^i = -v_w \gamma_w \left[(|x_i|^2 \theta')' Q_\ell^{8o} - (|x_i|^2)' |x_i|^2 \theta' Q_\ell^{9o} \right] \quad , \quad \hat{\mathcal{C}}_\ell^i = \left\langle \left(\frac{p_z}{\tilde{E}_0} \right)^\ell \mathcal{C}^i \right\rangle , \tag{11.48}$$

with

$$Q_\ell^{8o} \equiv T^2 \left\langle \frac{s p_z^{\ell-1}}{2\tilde{E}_0^{\ell} \tilde{E}_{0z}} f_{0w}^{\prime} \right\rangle \quad , \quad Q_\ell^{9o} \equiv T^4 \left\langle \frac{s p_z^{\ell-1}}{2\tilde{E}_0^{\ell+2} \tilde{E}_{0z}} (f_{0w}^{\prime} - \gamma_w \tilde{E}_0 f_{0w}^{\prime\prime}) \right\rangle . \tag{11.49}$$

We have now obtained a system of n coupled first-order differential equations defined by Eq. (11.46), where ℓ goes from 0 to $n-1$. This system of equations depends on the universal functions D_ℓ, Q_ℓ, Q_ℓ^{8o} and Q_ℓ^{9o}, for which we provide an explicit form in Appendix C. These functions depend in general on the two variables x_i and v_w and have to be computed numerically. Computing them each time we solve the transport equations would be very time consuming, especially for large moments ℓ. However, since they are independent of the model under consideration, they can be evaluated beforehand. To do this, we build a 2-dimensional grid in x_i and v_w with the corresponding function values. In the code we then load these grids and use cubic splines to obtain continuous functions which are now orders of magnitude faster to evaluate.

11.4. Factorization and Truncation

Even though in Eq. (11.46) we have arrived at a much simpler form for our system of differential equations, there are still some things we have to address. The first one is that we have yet to specify $\bar{R}$ defined in Eq. (11.47). Here, we use the factorization rule first introduced in [11] and generalized in [13] to obtain

$$\bar{R} u_{o,\ell}^i = T^2 \left\langle \frac{p_z^{\ell-1}}{2\tilde{E}_0^{\ell+1}} \delta f_o^i \right\rangle \to \left[\frac{T^2}{2 p_z \tilde{E}_0} \right] u_{o,\ell}^i , \tag{11.50}$$

where

$$[X] \equiv \frac{1}{N_0} \int \mathrm{d}^3 p X f_{0w} \quad \text{with} \quad N_0 = \int \mathrm{d}^3 p f_{0w} = \gamma_w \int \mathrm{d}^3 p f_0 \equiv \gamma_w \hat{N}_0 \,. \tag{11.51}$$

We can now use Eq. (11.51) to obtain an explicit expression for $\bar{R}$

$$\bar{R} = \frac{\pi T^2}{\gamma_w^2 \hat{N}_0} \int \mathrm{d}E \, \ln \left| \frac{p - v_w E}{p + v_w E} \right| f_{\mathrm{FD/BE}}(E) \,. \tag{11.52}$$

Another issue we also have, is that the equations resulting from Eq. (11.46) have more variables than equations due to the velocity moment derivative $u^{i\prime}_{o,n}$. To obtain a closed set of equations we have to define a truncation scheme which relates $u^i_{o,n}$ to the previous velocity moments. A first approach which was introduced in Ref. [11] was to use the factorization rule of Eq. (11.50) which leads to

$$u^i_{o,n} = \left\langle \left(\frac{p_z}{\tilde{E}^i_0} \right)^n \delta f^i \right\rangle \to \left[\frac{p_z}{\tilde{E}^i_0} \right] u^i_{o,n-1} \equiv R u^i_{o,n-1} \,, \tag{11.53}$$

where R is the average longitudinal velocity of the boosted plasma and leads to $R = -v_w$. However, we have to remember that this choice for the truncation scheme is arbitrary. One could also set $R = 0$, setting the last moment to zero, or set $R = -1$, i.e. opposite to the previous moment. We will refer to the truncation choice, where the last moment is related to the previous one only via constant as the *constant truncation scheme*.

More recently, an alternative truncation scheme was proposed in Ref. [13], where the largest moment relates to all of the previous moments via the coefficients R_j

$$u^{i\prime}_{o,n} = \sum_{j=1}^{n-1} R_j u^{i\prime}_{o,i} \,. \tag{11.54}$$

To determine the different R_j's the authors defined the *variance truncation scheme*, where the n'th variance is set to zero such that

$$\left\langle \left(\frac{p_z}{\tilde{E}^i_0} - u^i_{o,1} \right)^n \delta f^i_o \right\rangle = 0 \,. \tag{11.55}$$

Expanding this expression and comparing coefficients with Eq. (11.54) leads to the following expressions for R_j

$$R_1 = -n^2 (-u^i_{o,1})^{n-1} + \sum_{k=2}^{n-1} \binom{n}{k} (n-k) u^i_{o,k} (-u^i_{o,1})^{n-k-1} \,, \tag{11.56}$$

$$R_j = -\binom{n}{j} (-u^i_{o,1})^{n-j} \quad , \; j \in [2, n-1] \,. \tag{11.57}$$

The choice of the truncation scheme should not affect the final BAU significantly. We will check if this is the case in Sec. 13.1.2.

Now that we have a closed system of equations we can define the vector $w^i_o = (\mu^i_o, u^i_{o,1}, \ldots, u^i_{o,n-1})^T$ to write Eq. (11.46) as a matrix equation of the form

$$\hat{\mathcal{A}} w_o^{i\prime} + \hat{\mathcal{B}} w_o^i = \hat{\mathcal{S}}_o^i + \hat{\mathcal{C}}^i[w_o^i] \,, \tag{11.58}$$

where $\hat{\mathcal{A}}$ and $\hat{\mathcal{B}}$ are $n \times n$-dimensional matrices defined via

$$\hat{\mathcal{A}} = \begin{pmatrix} -D_1 & 1 & \cdots & 0 & 0 \\ -D_2 & 0 & \cdots & 0 & 0 \\ \vdots & \vdots & \ddots & \vdots & \vdots \\ -D_{n-1} & 0 & \cdots & 0 & 1 \\ -D_n & R_1 & \cdots & R_{n-2} & R_{n-1} \end{pmatrix}, \quad \hat{\mathcal{B}} = (|x|^2)' \begin{pmatrix} v_w\gamma_w Q_1 & 0 & 0 & \cdots & 0 \\ v_w\gamma_w Q_2 & \bar{R} & 0 & \cdots & 0 \\ v_w\gamma_w Q_3 & 0 & 2\bar{R} & \cdots & 0 \\ \vdots & \vdots & \vdots & \ddots & \vdots \\ v_w\gamma_w Q_n & 0 & 0 & \cdots & (n-1)\bar{R} \end{pmatrix}, \tag{11.59}$$

and $\hat{\mathcal{S}}_o^i = (S_{o,1}^i, \ldots, S_{o,n}^i)$ is the source vector with its components given by Eq. (11.48). We will define and discuss the collision operator $\hat{\mathcal{C}}^i$ in the next section. To bring Eq. (11.58) into a numerically more suitable form, we invert $\hat{\mathcal{A}}$ to obtain

$$w_o^{i\prime} = \hat{\mathcal{A}}^{-1} \left[\hat{\mathcal{S}}_o^i + \hat{\mathcal{C}}^i - \hat{\mathcal{B}} w_o^i \right] \,, \tag{11.60}$$

with

$$\hat{\mathcal{A}}^{-1} = \frac{1}{\mathcal{D}_n} \begin{pmatrix} R_1 & R_2 & \cdots & R_{n-1} & -1 \\ R_1 D_1 & R_2 D_1 & \cdots & R_{n-1} D_1 & -D_1 \\ \vdots & \vdots & \ddots & \vdots & \vdots \\ R_1 D_{n-1} & R_2 D_{n-1} & \cdots & R_{n-1} D_{n-1} & -D_{n-1} \end{pmatrix} + \begin{pmatrix} 0 & 0 & \cdots & 0 \\ 1 & 0 & \cdots & 0 \\ \vdots & \ddots & \ddots & \vdots \\ 0 & \cdots & 1 & 0 \end{pmatrix} \,, \tag{11.61}$$

and

$$\mathcal{D}_n \equiv (-1)^n \det(\hat{\mathcal{A}}) = D_n - \sum_{i=1}^{n-1} R_i D_i \,. \tag{11.62}$$

The matrix $\hat{\mathcal{A}}$ has been chosen such that it fulfills the general truncation rule defined in Eq. (11.54).

11.5. Collision Operator

Until now we have only considered the equations for a single particles species i. However, the plasma consists of many different species that interact with each other, exchanging momentum and particle number. As already mentioned in Sec. 2.3, the separate Boltzmann equations of these particles will be coupled via the collision operator with each other. In general we have to consider all processes that provide an interaction between the plasma particles. For our purposes it is enough to restrict ourselves to the most relevant ones, which are 2-body decays and $2 \to 2$ scattering processes. After linearizing the collision operator in Eq. (2.41) we obtain the general expression for an inelastic process [13, 135]

$$\mathcal{C}_{\text{inel}}^i \approx -f_{0w}^i(p) \left(\sum_j s_{ij} \xi_j \right) \Gamma_{\text{inel}} - \delta f^i(p) \Gamma_{\text{inel}} \,. \tag{11.63}$$

Here, $s_{ij} = \pm 1$ if the particle j is incoming (+) or outgoing (−), $\xi_j = \mu_j/T$ and $\Gamma_{\rm inel}$ is the inelastic scattering rate. To obtain the collision operator for an elastic scattering process, one has to simply omit the first term of Eq. (11.63) as the chemical potentials cancel giving

$$\mathcal{C}^i_{\rm el} \approx -\delta f^i(p)\Gamma_{\rm el} \, . \tag{11.64}$$

After taking the thermal average as defined in Eq. (11.43) with the corresponding momentum weight, we obtain the ℓ'th moment collision operator

$$\hat{\mathcal{C}}^i_\ell = -K_\ell \kappa^i \bar{\mathcal{C}}^i - u^i_\ell \kappa^i \hat{\Gamma}^i_{\rm tot} \, , \tag{11.65}$$

where K_ℓ is another universal function defined by

$$K_\ell \equiv T^{-1} \left\langle \left(\frac{p_z}{\tilde{E}_0} \right)^\ell f_{0w} \right\rangle \, , \tag{11.66}$$

and κ_i is a normalization constant given by [135]

$$\kappa^i = \frac{T^3}{12 n^i} = \begin{cases} \dfrac{\pi^2}{9\zeta(3)} \simeq 0.912 & \text{FD} \\ \dfrac{\pi^2}{12\zeta(3)} \simeq 0.685 & \text{BE} \end{cases} \, . \tag{11.67}$$

Further, we have the collision term that contains decays and $2 \to 2$ scattering processes in terms of the thermally averaged rates $\hat{\Gamma}$,

$$\bar{\mathcal{C}}^i = \sum_{j,k} (\mu_i - \mu_j - \mu_k) \hat{\Gamma}^{\rm dec}_{i \to jk} + \sum_{j,k,l} (\mu_i + \mu_j - \mu_k - \mu_l) \hat{\Gamma}^{\rm scat}_{ij \to kl} \, , \tag{11.68}$$

and the total interaction rate given by

$$\hat{\Gamma}^i_{\rm tot} = \sum \left(\hat{\Gamma}^i_{\rm el} + \hat{\Gamma}^{\rm dec}_{i \to jk} + \hat{\Gamma}^{\rm scat}_{ij \to kl} \right) \, . \tag{11.69}$$

The computation of these thermally averaged rates is quite involved as one needs to consider finite temperature effects and in general the full 12 dimensional phase space in the case of $2 \to 2$ scattering. We will provide an explicit calculation for such a $2 \to 2$ rate in the next chapter.

At this stage we have to decide which particles and rates are the most relevant ones for the computation of the BAU. Before we talk about the rates, we first have to decide which particles generate the largest asymmetry. To determine this, we have to look at the source term in Eq. (11.48) as it is responsible for driving the particles out of equilibrium. The crucial part is that it is proportional to $|x_i|^2 \sim |m_i|^2$, meaning that fermions with a large mass will provide the largest CP-violating sources. In a scenario where the only fermions are the SM ones, the largest contribution will therefore come from the top-quark and the bottom-quark. Now that we have established which particles are the main contributors to the asymmetry, we need to find the dominant rates which try to equilibrate this asymmetry. The most relevant rates have been established long ago to be the following ones [10, 11]:

Top Yukawa Rate: $\mathbf{t_L h \leftrightarrow t_R g}$

The top Yukawa rate $\hat{\Gamma}_y$ is given by the annihilation of a left-handed top-quark with a Higgs boson into a right-handed top-quark and a gluon. The rate for this process has first been estimated in Ref. [139] to give $\hat{\Gamma}_y \approx 4.2 \cdot 10^{-3} T$, while the most recent calculation provides $\hat{\Gamma}_y \approx 1 \cdot 10^{-2} T$ [135]. In this work we present a new result, which does not rely on the leading

log approximation used in the aforementioned references. We calculate it in the next chapter in detail to obtain

$$\hat{\Gamma}_y \approx 6.0 \cdot 10^{-3} T \,. \tag{11.70}$$

Yukawa Helicity Flipping Rate: $\mathbf{t_L \leftrightarrow t_R}$

The Yukawa helicity flipping rate determines the rate at which a left-handed particles flips to a right-handed one via the interaction with the VEV. To calculate it, one has to work in the real-time Keldysh-Schwinger framework as in Ref. [140]. The rate is then obtained using the VEV-insertion approximation where the imaginary part of the retarded self-energy is expanded around the wall background. The most recent result is then given by [135]

$$\hat{\Gamma}_m \approx \frac{0.26 |m_t(z)|^2}{T} \,. \tag{11.71}$$

Higgs Number Violating Rate: $\mathbf{h \leftrightarrow W^+ W^-}$

The Higgs number-violating rate is the rate given by a Higgs boson decaying via the interaction with the thermal plasma into non Higgs particles. In the literature the imaginary part of the retarded Higgs self-energy induced by a thermal W-loop was used to calculate this rate. The most recent result is given by [135]

$$\hat{\Gamma}_h \approx \frac{1.5 |m_W(z)|^2}{T} \,. \tag{11.72}$$

W-Boson Scattering Rate: $\mathbf{t_L \leftrightarrow b_L W^+}$

The W-boson rate determines the particle exchange between bottom and top quarks via the W-boson. In the literature [11] it is defined via the total Higgs rate $\hat{\Gamma}^h_{\text{tot}}$, i.e.

$$\hat{\Gamma}_W = \hat{\Gamma}^h_{\text{tot}} \,. \tag{11.73}$$

Strong Sphaleron Rate: $\mathbf{q_L \leftrightarrow q_R}$

Similar to the weak sphaleron rate we discussed in Sec. 10.1.1 the strong sphaleron rate is a topological transition from one vacuum to another in QCD. This rate was computed using lattice methods in Refs. [141, 142] and gives with our normalization [135]

$$\hat{\Gamma}_{ss} \approx 2.7 \cdot 10^{-3} T \,. \tag{11.74}$$

The strong sphalerons provide a connection to the light quark states which will influence the heavier ones. Taking into account the chemical potentials of the involved particles we define the function

$$\tilde{\Gamma}_{ss}[\mu_i] \equiv \hat{\Gamma}_{ss} \sum_q (\mu_{q_L} - \mu_{q_R}) \,. \tag{11.75}$$

For light quarks, where the strong sphaleron rate is the only relevant one, we can assume that they have the same chemical potential

$$\mu_{q_L} = -\mu_{q_R} \equiv \mu_q \,. \tag{11.76}$$

Additionally, we use the baryon number conservation $B = \sum_q (n_q - \bar{n}_q) = 0$.[16] Since we consider only small perturbations in μ we have

$$n_q = \int \frac{\mathrm{d}^3 p}{(2\pi)^3} \left(e^{\beta[\gamma_w (E - v_w) - \mu_q]} \right) \approx n_q|_{\mu_q = 0} - \frac{N_1}{(2\pi)^3} D_0^q \mu_q \,, \tag{11.77}$$

[16] Note that the baryon number conservation is not a contradiction to the fact that we are trying to compute a baryon asymmetry. At the level of the transport equations the baryon number is conserved. Only in the final step (Sec. 11.7), where we consider the weak sphalerons, baryon number violation occurs.

where we wrote the result in terms of the universal function D_ℓ defined in Eq. (11.47). For anti-particles we can simply use the relation $\mu_q = -\mu_{\bar{q}}$. This means that when consider the two chiralities of a light quark we obtain for B

$$B = \sum_{q\in\{q_L,q_R\}} (n_q - \bar{n}_q) = -\frac{2N_1}{(2\pi)^3} D_0^q \mu_{q_L} - \frac{2N_1}{(2\pi)^3} D_0^q \mu_{q_R} = 0 \,. \tag{11.78}$$

This shows that light quarks cancel naturally in the sum if both the left- and right-handed partners appear. For our purposes we will treat all quarks up to the bottom quark as light such that we can assume the relation in Eq. (11.76) holds for them. For the left-handed bottom quark this assumption is not justified though, since it interacts via rates which are comparable in size to the strong sphaleron rate. Taking this into account, the baryon number gives

$$B = \sum_q = \frac{2N_1}{(2\pi)^3} D_0^b \mu_q - \frac{2N_1}{(2\pi)^3} D_0^b \mu_{b_L} - \frac{2N_1}{(2\pi)^3} D_0^t \mu_{t_R} - \frac{2N_1}{(2\pi)^3} D_0^t \mu_{t_L} = 0 \,, \tag{11.79}$$

which then gives the relation obtained in Ref. [12]

$$\mu_q = D_0^t \mu_{t_L} + D_0^t \mu_{t_R} + D_0^b \mu_{b_L} \,, \tag{11.80}$$

where we neglect the mass of the right-handed bottom quark to set $D_0^b = 1$ on the left hand side. Plugging Eqs. (11.76) and (11.80) into Eq. (11.75) we obtain

$$\tilde{\Gamma}_{ss}[\mu_i] = \hat{\Gamma}_{ss} \left[(1 + 9D_0^t)\mu_{t_L} + (1 + 9D_0^b)\mu_{b_L} - (1 - 9D_0^t)\mu_{t_L} \right] \tag{11.81}$$

We stress that this derivation requires that μ_{b_R} is not part of the reaction network. If one wants to include μ_{b_R} into the network, the above equation has to be adjusted accordingly.

Total Interaction Rates

Although the total interaction rate for a given particle can be defined via Eq. (11.69), in the formalism we are currently considering a different definition is used. It is given by [10,11,139]

$$\hat{\Gamma}^i_{\text{tot}} \equiv \frac{D_2^i}{D_0^i \hat{D}^i} \,, \tag{11.82}$$

where $\hat{D}^i$ is a diffusion constant containing the information about the interaction with the plasma. The diffusion constants for quarks and the Higgs boson are given by [135]

$$\hat{D}^{q_L} = \frac{7.1}{T} \quad , \quad \hat{D}^{q_R} = \frac{7.6}{T} \quad , \quad \hat{D}^h = \frac{14}{T} \,. \tag{11.83}$$

Now that we have established the most relevant interaction rates, we can build our interaction network. In this network we will include the left- and right-handed top quark, the left-handed bottom quark and the Higgs boson. Their respective collision operators at the ℓ'th moment are then given by Eq. (11.65) with [135]

$$\begin{aligned}
\bar{\mathcal{C}}^{t_L} &= \hat{\Gamma}_y(\mu_{t_L} - \mu_{t_R} + \mu_h) + 2\hat{\Gamma}_m(\mu_{t_L} - \mu_{t_R}) + \hat{\Gamma}_W(\mu_{t_L} - \mu_{b_L}) + \hat{\Gamma}_{ss}[\mu_i] \,, \\
\bar{\mathcal{C}}^{b_L} &= \hat{\Gamma}_y(\mu_{b_L} - \mu_{t_R} + \mu_h) + \hat{\Gamma}_W(\mu_{b_L} - \mu_{t_L}) + \hat{\Gamma}_{ss}[\mu_i] \,, \\
\bar{\mathcal{C}}^{t_R} &= -\hat{\Gamma}_y(\mu_{t_L} + \mu_{b_L} - 2\mu_{t_R} - 2\mu_h) + 2\hat{\Gamma}_m(\mu_{t_R} - \mu_{t_L}) - \hat{\Gamma}_{ss}[\mu_i] \,, \\
\bar{\mathcal{C}}^{h} &= \frac{3}{2}\hat{\Gamma}_y(\mu_{t_L} + \mu_{b_L} - 2\mu_{t_R} + 2\mu_h) + \hat{\Gamma}_h \mu_h \,.
\end{aligned} \tag{11.84}$$

Note that we neither included the W-boson, nor the gluon in our network even though they are involved in the presented interaction rates. This is due to the fact that they are thermalized at a much faster rate than the involved particles. Therefore, at the timescales we are investigating, they can be assumed to always be in thermal equilibrium, i.e. $\mu_{W/g} = 0$.

11.6. Full Equation Network

With the collision operators at hand, we can now extend the single species moment equations given in Eq. (11.58). As already mention, for each particle species we define a vector $w_o^i = (\mu_o^i, u_{o,1}^i, \dots, u_{o,n-1}^i)^T$. To include multiple particles species we can combine the individual particle vectors into a larger Nn-vector $\mathcal{W}^T = ((w_o^1)^T, (w_o^2)^T, \dots, (w_o^N)^T)$, where N is number of involved particles. This gives us the full equation network

$$\hat{\mathcal{A}}\mathcal{W}' + \hat{\mathcal{B}}\mathcal{W} = \hat{\mathcal{S}} + \hat{\mathcal{C}}[\mathcal{W}] \,, \tag{11.85}$$

where $\hat{\mathcal{A}} = \text{diag}(\hat{\mathcal{A}}_1, \dots, \hat{\mathcal{A}}_N)$ and $\hat{\mathcal{B}} = \text{diag}(\hat{\mathcal{B}}_1, \dots, \hat{\mathcal{B}}_N)$ are block diagonal matrices whose sub-matrices are defined via Eq. (11.59). Further, $\hat{\mathcal{S}}$ and $\hat{\mathcal{C}}[\mathcal{W}]$ are correspondingly defined Nn-vectors. Due to the block diagonal structure of Eq. (11.85), it is easy to invert

$$\mathcal{W}' = \hat{\mathcal{A}}^{-1}\left[\hat{\mathcal{S}} + \hat{\mathcal{C}}[\mathcal{W}] - \hat{\mathcal{B}}\mathcal{W}\right] \,, \tag{11.86}$$

with $\hat{\mathcal{A}}^{-1} = \text{diag}(\hat{\mathcal{A}}_1^{-1}, \dots, \hat{\mathcal{A}}_N^{-1})$ and $\hat{\mathcal{A}}_i^{-1}$ defined in Eq. (11.61).

11.6.1. A Note on Convergence

As we discussed in Sec. 11.5, our network consists of four species, meaning we have to solve a network consisting of $4n$ coupled equations. The boundary conditions are such that every component of $\mathcal{W}$ vanishes far outside and deep inside the bubble. At surface level, this system of equations seems to be over determined as we have $4n$ variables with $8n$ boundary conditions. However, by checking the asymptotic behavior of Eq. (11.86) we can check if some of the variables converge naturally, without enforcing boundary conditions. In the asymptotic limit, the source term vanishes and we are left with

$$\mathcal{W}' = \hat{\mathcal{A}}^{-1}\left[\hat{\mathcal{C}}[\mathcal{W}] - \hat{\mathcal{B}}\mathcal{W}\right] \equiv \hat{\mathcal{X}}\mathcal{W} \,. \tag{11.87}$$

By studying the eigenvalues λ_i of $\hat{\mathcal{X}}$, which can be real or complex, we can check if we have enough eigenmodes that converge naturally. In the limit $z \to \pm\infty$ the matrix $\hat{\mathcal{X}}$ becomes a constant and we obtain solutions that behave as $u_i \sim \exp(\lambda_i z)$. Since the λ_i are complex in general, the solutions we obtain, behave like damped oscillators at the edges of the integration region. We make sure that the real part of at least half of the eigenvalues leads to converging eigenmodes in this limit, before we begin solving the transport equations. For the remaining modes, that do not converge, we need to enforce the boundary condition to obtain a valid solution. We will look at the eigenvalue spectrum in more detail in Sec. 13.1.1.

11.7. Baryon Asymmetry

With the derived transport equations we can now compute the chemical potential of the relevant particles as a function of the distance to the bubble wall. The next step is to convert the generated left-handed chemical potential into a baryon asymmetry. As discussed in Sec. 10.2, we need to consider that sphalerons only couple to the left-handed particles. In order to continue, we define the baryon-left chemical potential

$$\mu_{B_L} \equiv \frac{1}{2}\sum_q \mu_{q_L}(z) \,. \tag{11.88}$$

We can use the relation given in Eq. (11.76) to eliminate the light quarks and obtain

$$\mu_{B_L} = \frac{1}{2}\left(1 + 4D_0^t\right)\mu_{t_L} + \frac{1}{2}\left(1 + 4D_0^b\right)\mu_{b_L} + 2D_0^t\mu_{t_R} \,. \tag{11.89}$$

The baryon asymmetry n_B can then be calculated via the diffusion equation

$$n_B'(z) = \frac{n_f}{2\gamma_w v_w}\Gamma_{ws}(z)(N_c\mu_{B_L}(z)T^2 - An_B(z)) \,, \tag{11.90}$$

where n_f is the number of flavors, N_c the number of colors, $A = 15/2$ and $\Gamma_{ws}(z)$ is the weak sphaleron rate given by

$$\Gamma_{ws} = \Gamma_{\rm sph} f_{\rm sph}(z) \quad \text{with} \quad f_{\rm sph}(z) = \min\left(1, \frac{1.7T}{\Gamma_{\rm sph}} e^{-37v(z)/T}\right) . \tag{11.91}$$

The function $f_{\rm sph}(z)$ is defined such that the sphaleron rate is interpolated between the symmetric and the broken phase using the rates discussed in Sec. 10.1.1 and $\Gamma_{\rm sph}$ from Eq. (10.19). Since Eq. (11.90) is a first-order linear equation we can solve it exactly

$$n_B(z) = -\int_z^\infty \mathrm{d}z' \frac{n_f N_c}{2v_w\gamma_w}\Gamma_{ws}(z')\mu_{B_L}(z')T^2 \exp\left[-\frac{An_f}{2v_w\gamma_w}\int_z^{z'}\Gamma_{ws}(z'')\mathrm{d}z''\right] , \tag{11.92}$$

where we set $n_B(+\infty) = 0$. To relate n_B to the BAU given in Eq. (1.2) we need to evaluate $n_B(-\infty)$ and divide by the entropy density given in Eq. (3.32) with $h_{\rm eff} = 106.75$,

$$\eta_B = -\frac{45 n_f N_c}{4\pi^2 v_w\gamma_w h_{\rm eff} T}\int_{-\infty}^{\infty}\mathrm{d}z\Gamma_{ws}(z)\mu_{B_L}(z)\exp\left[-\frac{An_f}{2v_w\gamma_w}\int_{-\infty}^{z}\Gamma_{ws}(z')\mathrm{d}z'\right] . \tag{11.93}$$

Using this formalism, we notice that the integral appearing in the exponent of Eq. (11.93) diverges since the VEV in Eq. (11.91) reaches a constant value inside the bubble. This effect occurs because we consider a time-independent solution. Its easy to see that if we allow for a change in temperature (time) the cooling of the universe would further suppress the sphaleron rate until it nearly vanishes at $T = 0$. Further, because the time between the phase transition and today is finite, the particles could have only traversed a finite volume and not an infinite one. In practice, we simply truncate the integration boundaries at some large constant relative to the bubble wall thickness. Varying this constant changes the final result only negligibly.

CHAPTER 12

Top Yukawa Rate

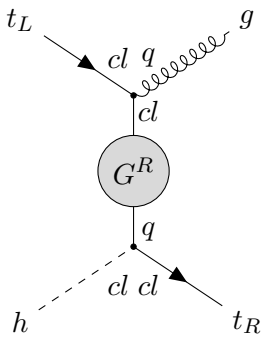

Figure 12.1.: Feynman diagram of the process that leads to the top Yukawa rate.

As already alluded to in the previous chapter, we want to provide an update of the top Yukawa rate $\hat{\Gamma}_y$. The first analytical estimate for this rate was provided in Ref. [139] and since then has been used throughout the literature for nearly two decades. Recently, new estimates were published using the VIA method in Ref. [143] giving $\hat{\Gamma}_y \approx 3 \cdot 10^{-2} T$ and the leading log approximation in Ref. [135] giving $\hat{\Gamma}_y \approx 10^{-2} T$. In this chapter we want to provide an updated calculation, where we include the full dispersion relation of the corrected fermion propagator as well as a full numerical integration of the collision operator. The diagram we want to evaluate is shown in Fig. 12.1, where cl and q denote classical and quantum fields, respectively, as introduced in Sec. 2.4.3. Similar to the aforementioned references, we consider only the t-channel contribution.

12.1. Self-Energy

To obtain finite temperature effects, the self-energy of the retarded propagator has to be calculated. We will do so for the massless case as was done in Ref. [144], but without taking the Hard Thermal Loop (HTL) limit.[17] For clarity we will denote four vectors of kinematical

[17] In the reference, in contrast to the retarded propagator, they considered the Feynman propagator which gives the same result as our calculation in the HTL limit.

variables with capital letters and absolute values of the spatial components with small letters in this section. The self-energy Σ for a massless fermion at zero temperature has the form

$$\Sigma_{T=0} = -a\not{K} \,, \tag{12.1}$$

which results in a propagator correction given by $S = \not{K}/(1+a)K^2$, where the pole remains at $K^2 = 0$. At finite temperature the situation changes since we have an additional kinematical quantity we have to consider, the plasma velocity U_μ with $U_\mu U^\mu = 1$. We will perform our calculation in the plasma rest frame where $U^\mu = (1,0,0,0)$. With this in mind, the self-energy changes to

$$\Sigma_T = -a\not{K} - b\not{U} \,, \tag{12.2}$$

where a and b are Lorentz invariant functions, which depend on the energy k_0 and the momentum k. This changes the propagator structure in a non trivial way to

$$S(K) = \frac{(1+a)\not{K} + b\not{U}}{(1+a)^2K^2 + 2(1+a)bk_0 + b^2} \,. \tag{12.3}$$

The pole of this structure can be determined by solving the equation

$$k_0(1+a) + b = k(1+a) \,, \tag{12.4}$$

which in the HTL limit gives $k_0 = m_f$ as $k \to 0$, where m_f is the thermal mass given by [144]

$$m_f^2 \equiv \frac{g^2 C_2}{8} T^2 \tag{12.5}$$

and C_2 is the quadratic Casimir invariant. The thermal mass was used in the previous results to obtain the top Yukawa rate, where it acted as a regulator mass in the propagator. In the more general case, we obtain the coefficient functions via the projections

$$t_K \equiv \frac{1}{4}\mathrm{tr}(\not{K} i\Sigma_T) = -aK^2 - bk_0 \quad \text{and} \quad t_U \equiv \frac{1}{4}\mathrm{tr}(\not{U} i\Sigma_T) = -ak_0 - b \,, \tag{12.6}$$

which results in

$$a = \frac{1}{k^2}(t_K - t_U k_0) \quad \text{and} \quad b = \left(\frac{k_0^2}{k^2} - 1\right) t_U - \frac{k_0}{K^2} t_K \,. \tag{12.7}$$

The self-energy for the retarded fermion propagator with an arbitrary gauge boson in the loop is given by

$i\Sigma^R(K) =$ 

$$= -\frac{1}{2} i g^2 C_2 \int \frac{\mathrm{d}^4 P}{(2\pi)^4} G^R_{\mu\nu}(P)\gamma^\mu S^K(P-K)\gamma^\nu + G^K_{\mu\nu}(P)\gamma^\mu S^R(P-K)\gamma^\nu \,, \tag{12.8}$$

with loop momentum P. Inserting the expressions for the propagators given in Eq. (2.97) and extracting the temperature-dependent contributions we obtain

$$\begin{aligned} i\Sigma^R_T(K) = &- g^2 C_2 \int \frac{\mathrm{d}^4 P}{(2\pi)^3} (\not{P} - \not{K}) \left[\frac{-2n_{\mathrm{FD}}(p_0 - k_0)}{P^2 + i\mathrm{sgn}(p_0)\epsilon} \delta\left((P-K)^2\right) \right. \\ &\left. + \frac{2n_{\mathrm{BE}}(p_0)}{(P-K)^2 + i\mathrm{sgn}(p_0 - k_0)\epsilon} \delta(P^2) \right] . \end{aligned} \tag{12.9}$$

After performing the transformation $P \to P + K$ on the first term and $P \to -P$ on the second term the expression simplifies to

$$\begin{aligned} i\Sigma_T^R(K) &= 2g^2 C_2 \int \frac{\mathrm{d}^4 P}{(2\pi)^3} \frac{\delta(P^2)}{(P+K)^2 + i\mathrm{sgn}(p_0+k_0)\epsilon} \left[(\not{P} + \not{K}) n_{\mathrm{BE}}(p_0) + \not{P} n_{\mathrm{FD}}(p_0)\right] \\ &= g^2 C_2 \int \frac{\mathrm{d}p \mathrm{d}x}{(2\pi)^2} \frac{p}{(P+K)^2 + i\mathrm{sgn}(p_0+k_0)} \left[(\not{P} + \not{K}) n_{\mathrm{BE}}(p_0) + \not{P} n_{\mathrm{FD}}(p_0)\right] \Big|_{p_0=\pm p}, \end{aligned} \tag{12.10}$$

where $x \equiv \cos\theta$ and the angle θ between the three-momentum vectors $\mathbf{p}$ and $\mathbf{k}$.

12.1.1. Integral Intermezzo

Before we apply the projectors from Eq. (12.6), we will first evaluate the integrals that will appear due to them. These are the following,

$$I_1(P) = \int_{-1}^{1} \mathrm{d}x \frac{1}{(P+K)^2 + i\mathrm{sgn}(p_0+k_0)\epsilon} \Big|_{p_0=\pm p}, \tag{12.11}$$

$$I_2(P) = \frac{1}{p} \int_{-1}^{1} \mathrm{d}x \frac{p_0}{(P+K)^2 + i\mathrm{sgn}(p_0+k_0)\epsilon} \Big|_{p_0=\pm p}, \tag{12.12}$$

$$I_3(P) = \int_{-1}^{1} \mathrm{d}x \frac{P\cdot K}{(P+K)^2 + i\mathrm{sgn}(p_0+k_0)\epsilon} \Big|_{p_0=\pm p}. \tag{12.13}$$

We will evaluate the first integral $I_1(P)$ to showcase how we deal with them. As a first step we split it up into the real and imaginary part using Eq. (2.98)

$$I_1(P) = \int_{-1}^{1} \mathrm{d}x \left[\mathcal{P}\frac{1}{K^2 - 2p(kx \mp k_0)} - i\pi\delta(K^2 - 2p(kx \mp k_0))\mathrm{sgn}(p_0+k_0)\right]. \tag{12.14}$$

We use a shorthand notation with the $(\mp)$, with which we mean the addition of the two branches that result from the respective sign. For the real part we obtain

$$\begin{aligned} \mathrm{Re}(I_1) &= \int_{-1}^{1} \mathrm{d}x \mathcal{P}\frac{1}{K^2 - 2p(kx \mp k_0)} = -\frac{1}{2pk}\left[\log|K^2 - 2p(k \mp k_0)|\right]_{-1}^{1} \\ &= \frac{1}{2pk}\log\left|\frac{K^2 + 2p(k \pm k_0)}{K^2 - 2p(k \mp k_0)}\right| = \frac{1}{2pk}\log\left|\frac{(k_0 \pm p)^2 - (k-p)^2}{(k_0 \pm p)^2 - (k+p)^2}\right| \\ &\equiv \frac{1}{2pk} L_{\pm}(P) = \frac{1}{2pk}(L_+(P) + L_-(P)) \equiv \frac{1}{2pk} L_1(P), \end{aligned} \tag{12.15}$$

where

$$L_1(P) = \log\left|\frac{(k-2p)^2 - k_0^2}{(k+2p)^2 - k_0^2}\right|. \tag{12.16}$$

Moving on to the imaginary part, we obtain

$$\mathrm{Im}(I_1) = -\pi\mathrm{sgn}(k_0 \pm p) \int_{-1}^{1} \mathrm{d}x \delta(K^2 - 2p(kx \mp k_0)). \tag{12.17}$$

Here we have to distinct between two cases $k_0 > k$ and $k_0 < k$ since it will determine the area in which the argument of the delta distribution can be evaluated to zero. For $k_0 > k$ the first branch $(-)$ never contributes since $K^2 - 2p(kx - k_0) < 0$ and we are left with

$$\begin{aligned} \mathrm{Im}(I_1) &= -\mathrm{sgn}(k_0 - p)\pi \int_{-1}^{1} \mathrm{d}x \delta(K^2 - 2p(kx + k_0)) \\ &= -\mathrm{sgn}(k_0 - p)\frac{\pi}{2pk} \int_{-1}^{1} \mathrm{d}x \delta\left(\frac{K^2 - 2pk_0}{2pk} - x\right) \\ &= -\mathrm{sgn}(k_0 - p)\frac{\pi}{2pk} \Theta\left(\frac{k_0 + k}{2} - p\right) \Theta\left(p - \frac{k_0 - k}{2}\right). \end{aligned} \tag{12.18}$$

Plugging in the upper boundary for p, $p = \frac{k_0+k}{2}$ into the sgn function gives

$$k_0 - \frac{k_0+k}{2} = \frac{k_0-k}{2} > 0 \,,$$

and therefore

$$\mathrm{Im}(I_1) = -\frac{\pi}{2pk}\Theta\left(\frac{k_0+k}{2}-p\right)\Theta\left(p-\frac{k_0-k}{2}\right) \,. \tag{12.19}$$

For the case $k_0 < k$ we obtain

$$\mathrm{Im}(I_1) = -\frac{\pi}{2pk}\left[\mathrm{sgn}(k_0+p)\Theta\left(p-\frac{k-k_0}{2}\right)+\mathrm{sgn}(k_0-p)\Theta\left(p-\frac{k+k_0}{2}\right)\right], \tag{12.20}$$

and similar to the previous case, due to

$$k_0 - p \leq k_0 - \frac{k+k_0}{2} = \frac{k_0-k}{2} < 0,$$

we are left with

$$\mathrm{Im}(I_1) = -\frac{\pi}{2pk}\left[\Theta\left(p-\frac{k-k_0}{2}\right)-\Theta\left(p-\frac{k+k_0}{2}\right)\right]. \tag{12.21}$$

Combining the real and imaginary part, the integral I_1, and similarly I_2 and I_3, are obtained as

$$I_1(P) = \frac{1}{2pk}\left[L_1(P) - i\pi\begin{cases}\Theta\left(\frac{k_0+k}{2}-p\right)\Theta\left(p-\frac{k_0-k}{2}\right) & k_0 > k\\ \Theta\left(p-\frac{k+k_0}{2}\right)-\Theta\left(p-\frac{k-k_0}{2}\right) & k_0 < k\end{cases}\right], \tag{12.22}$$

$$I_2(P) = \frac{1}{2pk}\left[L_2(P) + i\pi\begin{cases}\Theta\left(\frac{k_0+k}{2}-p\right)\Theta\left(p-\frac{k_0-k}{2}\right) & k_0 > k\\ \Theta\left(p-\frac{k+k_0}{2}\right)+\Theta\left(p-\frac{k-k_0}{2}\right) & k_0 < k\end{cases}\right], \tag{12.23}$$

$$I_3(p) = 2 - \frac{K^2}{2}I_1(P) \,, \tag{12.24}$$

where

$$L_2(P) \equiv L_+(P) - L_-(P) = \log\left|\frac{(k_0+k)^2((k_0-k)^2-4p^2)}{(k_0-k)^2((k_0+k)^2-4p^2)}\right| \,. \tag{12.25}$$

12.1.2. Applying Projectors

With the relevant integrals at hand we apply the projectors defined in Eq. (12.6) on Eq. (12.10) to obtain

$$t_K = \frac{g^2C_2}{4\pi^2}\int \mathrm{d}pp\left[\left(2+\frac{K^2}{2}I_1(P)\right)n_B + \left(2-\frac{K^2}{2}I_1(P)\right)n_F\right], \tag{12.26}$$

$$t_U = \frac{g^2C_2}{4\pi^2}\int \mathrm{d}pp\left[(pI_2(P)+k_0I_1(P))n_B(p_0) + pI_2(P)n_F(p_0)\right] \,, \tag{12.27}$$

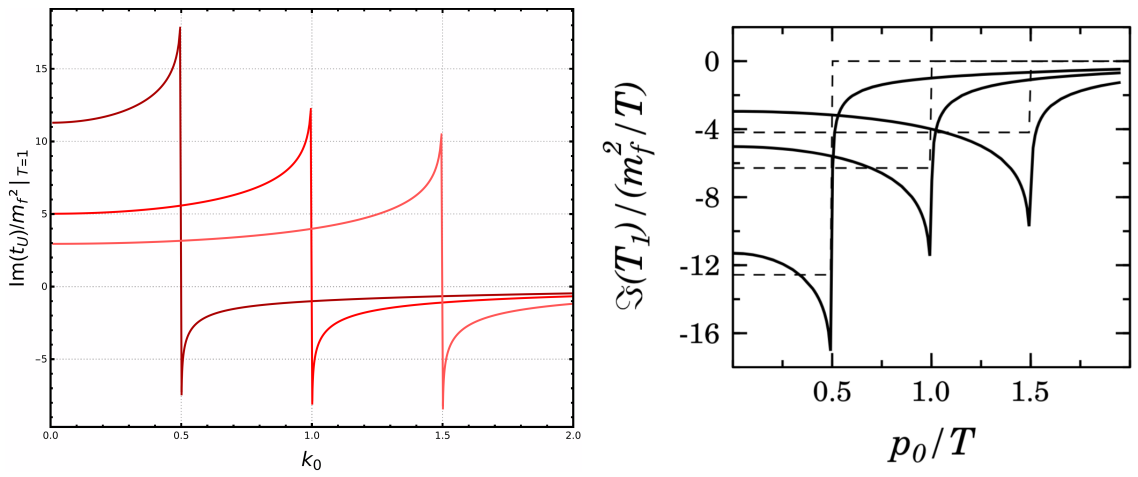

Figure 12.2.: Imaginary part of t_U divided by m_f^2 at $T = 1$ over k_0. On the left our result and on the right the result obtained in Ref. [145]. The different lines show, from dark red to light red, the respective result for a fixed value of $k = 0.5, 1, 1.5$.

with the real and imaginary parts given by

$$\begin{aligned}
\mathrm{Re}(t_K) &= \frac{g^2 C_2}{8\pi^2} \int \mathrm{d}p \left[\left(4p + \frac{K^2}{2k} L_1(P) \right) n_B + \left(4p - \frac{K^2}{2k} L_1(P) \right) n_F \right] , \\
\mathrm{Im}(t_K) &= \frac{g^2 C_2 K^2}{16\pi k} \int_{\frac{|k_0-k|}{2}}^{\frac{k_0+k}{2}} \mathrm{d}p (n_F - n_B) , \\
\mathrm{Re}(t_U) &= \frac{g^2 C_2}{8\pi^2 k} \int \mathrm{d}p \left[(pL_2(P) + k_0 L_1(P)) n_B + pL_2(P) n_F \right] , \\
\mathrm{Im}(t_U) &= \frac{g^2 C_2}{8\pi k} \begin{cases} \int_{\frac{k_0-k}{2}}^{\frac{k_0+k}{2}} \mathrm{d}p \left[(p-k_0) n_B + p n_F \right] & k_0 > k \\ \int_{\frac{k_0+k}{2}}^{\infty} \mathrm{d}p \left[(p-k_0) n_B + p n_F \right] + \int_{\frac{k-k_0}{2}}^{\infty} \mathrm{d}p \left[(p+k_0) n_B + p n_F \right] & k_0 < k \end{cases} .
\end{aligned} \tag{12.28}$$

The real parts of the above expressions agree with the results obtained in Ref. [145], in which the imaginary time formalism was used. However, for the $\mathrm{Im}(t_U)$ our result differs in the $k_0 < k$ regime by an overall minus sign. This difference can be seen in Fig. 12.2, where we show our computed imaginary part of t_U normalized by m_f^2 as a function of k_0 for different values of k in the left plot and the same quantity computed in Ref. [145] on the right. We checked that this has only a negligible effect on the final result.

12.1.3. Collision Operator

We want to consider the collision operator defined in Eq. (2.43) for a $2 \to 2$ process averaged via Eq. (11.43). For a general $2 \to 2$ process this gives

$$\langle \mathcal{C}[f] \rangle = \frac{1}{N_1} \int \mathrm{d}\Pi_{\{1..4\}} (2\pi)^4 \delta^4 (P_1 + P_2 - P_3 - P_4) \, |\mathcal{M}|^2_{12\to34} \mathcal{P}[f] , \tag{12.29}$$

with

$$\mathcal{P}[f] = f_1 f_2 (1 \pm f_3)(1 \pm f_4) - f_3 f_4 (1 \pm f_1)(1 \pm f_2) . \tag{12.30}$$

Since the collision operator is Lorentz invariant, we will calculate it in the plasma frame. With the identity

$$(1 \pm f_i) = f_i e^{\beta E_i - \beta \mu_i} , \tag{12.31}$$

we can write $\mathcal{P}[f]$ as

$$\begin{aligned}\mathcal{P}[f] &= f_1 f_2 f_3 f_4 \left(e^{\beta(E_3+E_4-\mu_3-\mu_4)} - e^{\beta(E_1+E_2-\mu_1-\mu_2)}\right) \\ &\approx f_1^0 f_2^0 (1 \pm f_3^0)(1 \pm f_4^0) \left(\frac{\mu_1+\mu_2-\mu_3-\mu_4}{T}\right) ,\end{aligned} \tag{12.32}$$

where we expanded around $\mu \approx 0$ and used energy conservation in the second line. For our purposes we only consider a scenario where all particles are massless and will therefore do the derivation with this in mind. We extract the temperature dependence of the collision operator by rescaling the momenta via $P_i \to P_i T$ such that

$$\langle \mathcal{C}[f] \rangle = \frac{T^4}{N_1} \int \mathrm{d}\Pi_{\{1..4\}} (2\pi)^4 \delta^4 \left(P_1 + P_2 - P_3 - P_4\right) |\mathcal{M}|^2_{12\to 34} \mathcal{P}[f] . \tag{12.33}$$

We can immediately integrate out the fourth particle, such that

$$\langle \mathcal{C}[f] \rangle = \frac{T^4}{N_1} \int \mathrm{d}\Pi_{\{1..3\}} 2\pi \delta\left((P_1 + P_2 - P_3)^2\right) |\mathcal{M}|^2_{12\to 34} \mathcal{P}[f] . \tag{12.34}$$

With the remaining δ distribution we can integrate out the momentum of the third particle using

$$\delta\left((P_1 + P_2 - P_3)^2\right) = \frac{\delta\left(p_3 - \frac{p_1 p_2 - \mathbf{p_1}\mathbf{p_2}}{F}\right)}{2|F|} , \tag{12.35}$$

where

$$F \equiv p_1 + p_2 + \hat{\mathbf{p}}_3(\mathbf{p_1} + \mathbf{p}_2) \quad \text{with} \quad \hat{\mathbf{p}}_3 = \frac{\mathbf{p}_3}{p_3} . \tag{12.36}$$

This leaves us with

$$\begin{aligned}\langle \mathcal{C}[f] \rangle &= \frac{T^4}{N_1} \int \mathrm{d}\Pi_{\{1,2\}} \int \mathrm{d}\Omega \frac{p_3}{16\pi^2} |\mathcal{M}|^2_{12\to 34} \mathcal{P}[f] \Big|_{p_3 = \frac{p_1 p_2 - \mathbf{p_1}\mathbf{p_2}}{2|F|}} \\ &= \hat{\Gamma}_{12\to 34}(\mu_1 + \mu_2 - \mu_3 - \mu_4) ,\end{aligned} \tag{12.37}$$

where

$$\hat{\Gamma}_{12\to 34} \equiv \frac{T^3}{N_1} \int \mathrm{d}\Pi_{\{1,2\}} \int \mathrm{d}\Omega \frac{p_3}{16\pi^2} |\mathcal{M}|^2_{12\to 34} f_1^0 f_2^0 (1 \pm f_3^0)(1 \pm f_4^0) . \tag{12.38}$$

All that is left to do is to plug in the amplitude for the processes $t_L h \to t_R g$, c.f. Fig. 12.1, which in terms of the coefficients a and b as well as the mandelstam variables $s = (P_1 + P_2)^2$ and $t = (P_1 - P_3)^2$ is given by

$$\begin{aligned}|\mathcal{M}|_{t_L h \to t_R g} = &- 4 g_s^2 y_t^2 \big[|1+a|^2 st + |b|^2 (s + t - 4p_2 p_3) + 2\mathrm{Re}(ab^* + b)(p_1(s+t) + p_2 t - p_3 s) \\ &- 4\mathrm{Im}(a^* b + b) U^\mu P_1^\nu P_2^\rho P_3^\sigma \epsilon_{\mu\nu\rho\sigma} \big] / |(1+a)^2 t + 2(1+a) b (p_1 - p_3) + b^2|^2 ,\end{aligned} \tag{12.39}$$

After plugging in the numerical values $g_s = \sqrt{4\pi\alpha_s}$, $\alpha_s = 0.12$, $y_t = 1$, $C_2 = 4/3$ and integrating the collision operator using the Cuba library [146] we obtain a value of

$$\hat{\Gamma}_y = (0.00596747 \pm 5.93 \cdot 10^{-6}) T . \tag{12.40}$$

Our result differs by 41% compared to the most recent result using the leading log approximation calculated in Ref. [135].

CHAPTER 13

Numerical Analysis

In the following we perform a thorough numerical and phenomenological analysis of the transport equation and therefore the BAU, using two models. The first model is the benchmark model given in [13] (Sec. 7). We will use this model to study the effects of different transition temperatures, wall velocities, wall thicknesses and truncation schemes as these are direct input parameters of the model. The second model which we will consider, is the Complex 2-Higgs Doublet Model (C2HDM). In this model, we perform a phenomenological investigation and study the impact of changing the parameters of the C2HDM potential on the BAU. The results which we will show in this section are new and have not been published. A publication is in preparation.

13.1. Benchmark Model

We begin by introducing the benchmark model used in Ref. [13]. In this model the bottom quark and the Higgs boson are assumed to be massless. To obtain a complex top mass, the additional dimension 5-operator $i(s/\Lambda)\bar{Q}_3 H t_R$ is introduced, where s is an additional scalar field and the new physics scale is called Λ. Taking this operator into account, the top mass is given by

$$m_t(z) = y_t h(z)\left(1 + i\frac{s(z)}{\Lambda}\right) = |m_t(z)|e^{i\theta(z)} \,, \tag{13.1}$$

with

$$|m_t(z)| = y_t h(z)\sqrt{1 + \frac{s(z)^2}{\Lambda}} \quad , \quad \theta(z) = \arctan\frac{s(z)}{\Lambda} \,. \tag{13.2}$$

The VEV-profiles $h(z)$ and $s(z)$ of the scalar fields are modeled via so-called kink solutions

$$h(z) = \frac{v_n}{2}\left(1 - \tanh\frac{z}{L_w}\right) \quad , \quad s(z) = \frac{w_n}{2}\left(1 + \tanh\frac{z}{L_s}\right) \,, \tag{13.3}$$

where the input parameters are defined as

$$v_n = \frac{1}{2}w_n = T_n \quad , \quad \Lambda = 1\,\text{TeV} \quad , \quad L_w = L_s = \frac{5}{T_n} \quad , \quad T_n = 100\,\text{GeV} \,. \tag{13.4}$$

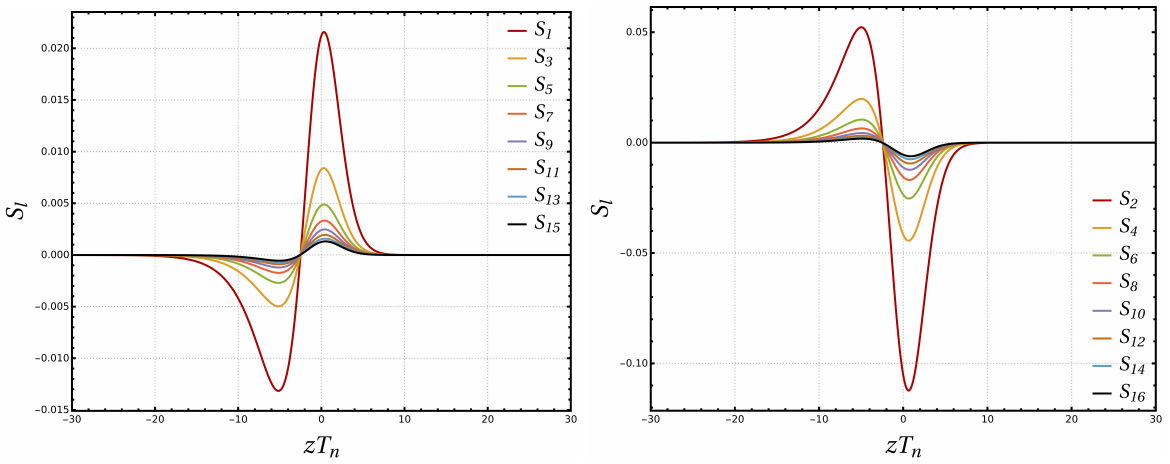

Figure 13.1.: Source terms for the left-handed top quark in the benchmark model as a function of zT_n. Left: odd-numbered source terms, right: the even-numbered source terms.

We will use these parameters with a wall velocity of $v_w = 0.1$ and Eq. (11.84) for the collision network as our base scenario which we will use throughout this section. In Fig. 13.1 we show the source terms as defined in Eq. (11.48) for the left-handed top quark in this model for moments up to $\ell = 16$. We see that as we increase ℓ the magnitude of the source terms decrease. With the source terms at hand we solve Eq. (11.86) to obtain the chemical potentials depending on the distance to the bubble wall z. Since it is impossible to display the modes in $z \in (-\infty, \infty)$, we will compress the interval to $u \in (-1, 1)$ such that

$$u = \frac{\sqrt{1+z^2} - 1}{z} \,. \tag{13.5}$$

We show the chemical potentials over u in Fig. 13.2 for all particles involved in the fluid network with number of equations per particle of up to $n = 50$ with the truncation scheme $R = -v_w$. The chemical potentials μ_{t_L} and μ_{t_R} have the same order of magnitude and have a similar dependence on u up to a difference in sign. They are also not fully identical in size or shape, otherwise they would exactly cancel and the BAU would be close to zero. As can be inferred from the plots, the chemical potential of μ_{b_L} is almost an order of magnitude smaller than that of μ_{t_L} and will therefore only have a small impact on the final BAU. We show the chemical potential of μ_h for completeness, but it impacts the BAU only indirectly as an interaction partner. For all curves we notice that larger moments lead to oscillatory modes at the edges, which is something we expect as already mentioned in Sec. 11.6.1. The reason for these large distance oscillations comes likely from the high energy modes of δf, which tend to decay more slowly compared to the low energy ones. Large moments pick up these high energy modes of δf and as a result show up as large distance oscillations. Additionally, the magnitude of the chemical potentials decreases with larger moments and is not as sharp as the low moment ones. Both, the oscillations and the decreasing magnitude, are effects which are also observed in Ref. [13].

In Fig. 13.3 we show the BAU normalized to the observed value, i.e. $\bar{\eta} \equiv \eta/\eta_{obs}$, as a function of the number of moments for three different truncation schemes which we introduced in Sec. 11.4. On the left we show the numerical results obtained using the collision network and rates that we defined in Chapter 11 and which we call the Barni network, on the right we show our results using the collision network and rates from Ref. [13], which we call the KV network. We observe that the BAU generated from the Barni network is smaller in magnitude than the one computed with the KV network. This is expected, since the collision rates which try to equilibrate the chemical potentials are larger in our network compared

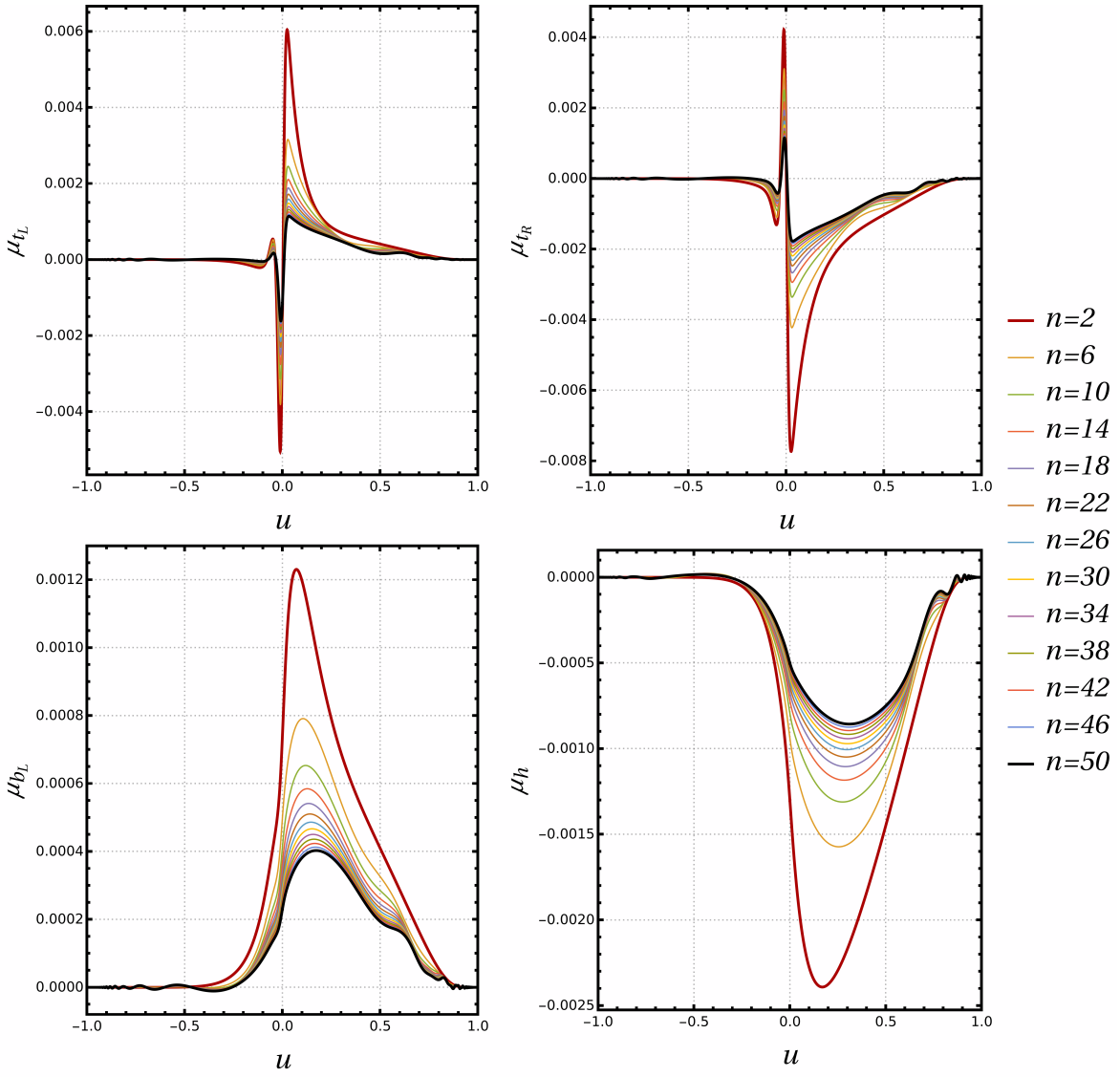

Figure 13.2.: Computed chemical potentials of the particles involved in the fluid network over u as defined in Eq. (13.5) for moments up to $n = 50$ for $R = -v_w$.

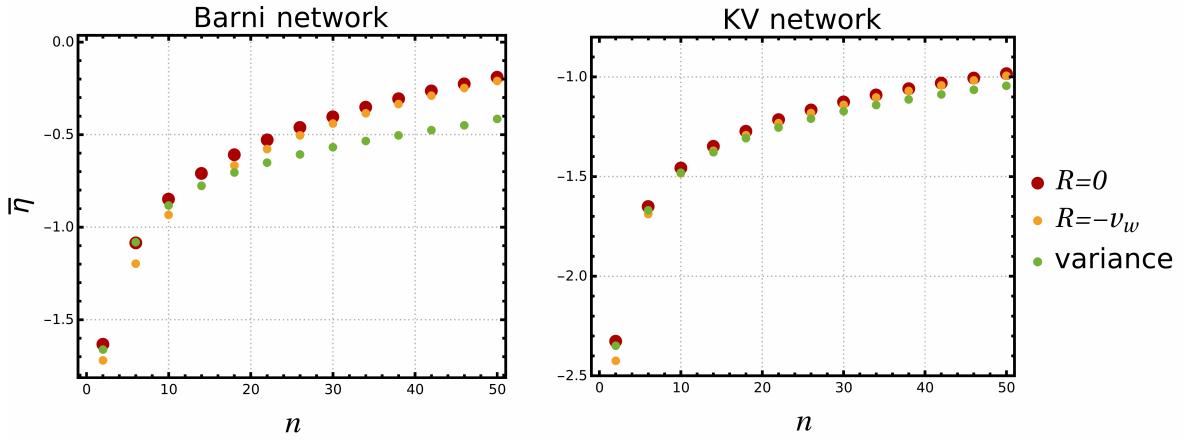

Figure 13.3.: The normalized BAU $\bar{\eta} \equiv \eta/\eta_{\text{obs}}$ over the number of moments. Left: the results for the collision network defined in Eq. (11.84) and the rates presented in Sec. 11.5, right: results for the collision network and rates used in Ref. [13]. The different colors represent different truncation scheme choices, where $R = 0, -v_w$ correspond to a constant truncation choice and *variance* to the variance truncation introduced in Sec. 11.4.

to the ones in [13]. Nonetheless, both networks exhibit the same behavior as we increase n. Namely, the absolute value of $\bar{\eta}$ decreases as we increase the number of moments, but does not stabilize to a constant value after taking into account a maximum of 50 moment equations, independent of the truncation scheme we choose. We will be investigate the scheme dependence in further detail in Sec. 13.1.2. The result we obtained using the KV network matches the result obtained in Ref. [13] very well. The minor differences are most likely attributed to a difference in the definition of V_h (see App. C) as well as in the equation used to obtain the final BAU (Eq. (11.93) in our case). However, a key discrepancy to the aforementioned reference is that we do not observe a significant difference in convergence behavior depending on the truncation choice.

We would like to also note that, since the BAU is negative, this model describes a universe that is full of anti-matter compared to matter. This cannot be solved by a simple relabeling of names as it ultimately emerges from the Lagrangian, where the labels for what matter and anti-matter are set to match the observed experiments. Hence, this parameter point does not lead to physical scenario.

13.1.1. Eigenvalue Spectrum

We can investigate the oscillatory and decaying/growing eigenmodes of the fluid network by considering the transport equations in the asymptotic limits $z \to \pm\infty$. In this limit, the equations reduce to $\mathcal{W}' = \hat{\mathcal{X}}\mathcal{W}$, where $\hat{\mathcal{X}}$ is the constant matrix defined in Eq. (11.87). As already mentioned, the solutions of this equation will be a linear combination of $u_i \sim \exp(\lambda_i z)$, where the λ_i are the complex eigenvalues of $\hat{\mathcal{X}}$. We show the eigenvalue spectrum of $\hat{\mathcal{X}}$ in Fig. 13.4 for different numbers of equations per particle n. In the upper row we show the eigenvalues for $z \to +\infty$ and in the lower row, the eigenvalues for $z \to -\infty$. We see that for $n = 2$ (left column) all eigenvalues are real and therefore do not lead to oscillations far away from the bubble wall. This is in concordance with what we observed in Fig. 13.2. For larger moments we obtain more and more eigenvalues with a small real part and a large imaginary part which leads to slowly decaying and highly oscillatory modes. Another important feature is that exactly half of the eigenvalues have a negative real part, ensuring that we have a sufficient amount of decaying modes to obtain a converging solution to the transport equations. Further, we see for the $n = 12$ scenario that we obtain very small

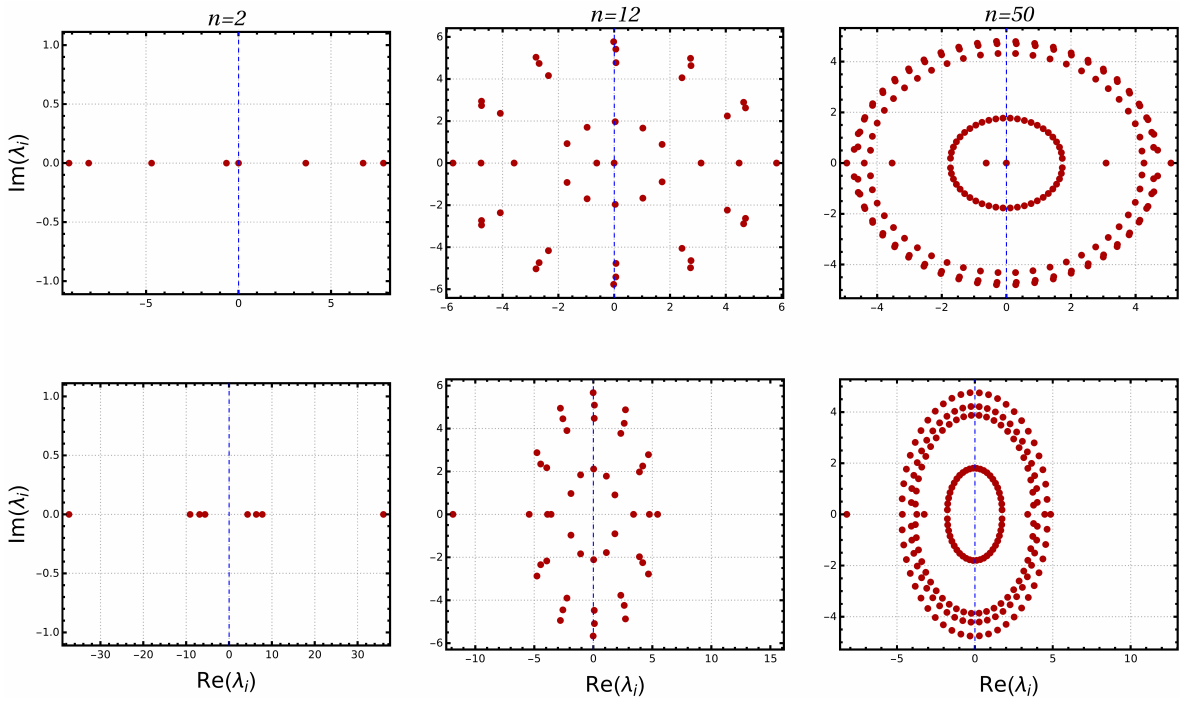

Figure 13.4.: Eigenvalue spectrum of $\hat{\mathcal{X}}$ with the imaginary part of λ_i on the y-axis and the real part on the x-axis for different number of equations per particle, left to right column: $n = 2, 12, 50$. The upper row shows the eigenvalues for $z \to \infty$ and the lower row for $z \to -\infty$.

negative real parts for the eigenvalues and leads to very slow decaying modes, which cannot be handled consistently by our numerical solver. This occurs, more generally, for the sequence $n = 4, 8, 12, \ldots$ as was also observed in Ref. [13].

13.1.2. Truncation Dependence

We saw in Fig. 13.3 that depending on the truncation scheme the moment expansion may lead to different results. In this section we want to check if the results which we obtain, are independent of the choice for R in the constant truncation scheme. To do this, we vary this constant and compute how the results change based on the largest moment we consider. In Fig. 13.5 we show the dependence of the normalized BAU depending on the R constant for different wall velocities. The different lines show the largest considered moment of the transport equations and the dashed blue line marks the truncation choice $R = -v_w$. We observe that for small wall velocities at low moment order, the result depends heavily on our truncation choice. As we increase the number of moments the lines start to lose their curved shape and begin to tend towards a constant, truncation scheme independent, value. Since, this calculation is very computationally demanding for large moments, we only go up to $n = 50$. To check if the BAU truly converges to a constant R-independent value in this framework, larger moments have to be taken into account. However, for large v_w, here from $v_w = 0.5$ on, we already observe a convergence at $n = 50$, making these results more robust than the ones obtained at small v_w. We would like to point out that as $R \to -1$ the numerical results for large v_w can break down. This comes from the fact that the eigenvalues of the exponentially growing eigenmodes are of $\mathcal{O}(100)$ and cannot be stabilized reliably by our algorithm.

We do the same analysis for different wall thicknesses instead of wall velocities as shown in Fig. 13.6. As in the case with v_w, the results depend strongly on the truncation choice at low moment orders, while for larger ones they begin to flatten out. Although, similar to the

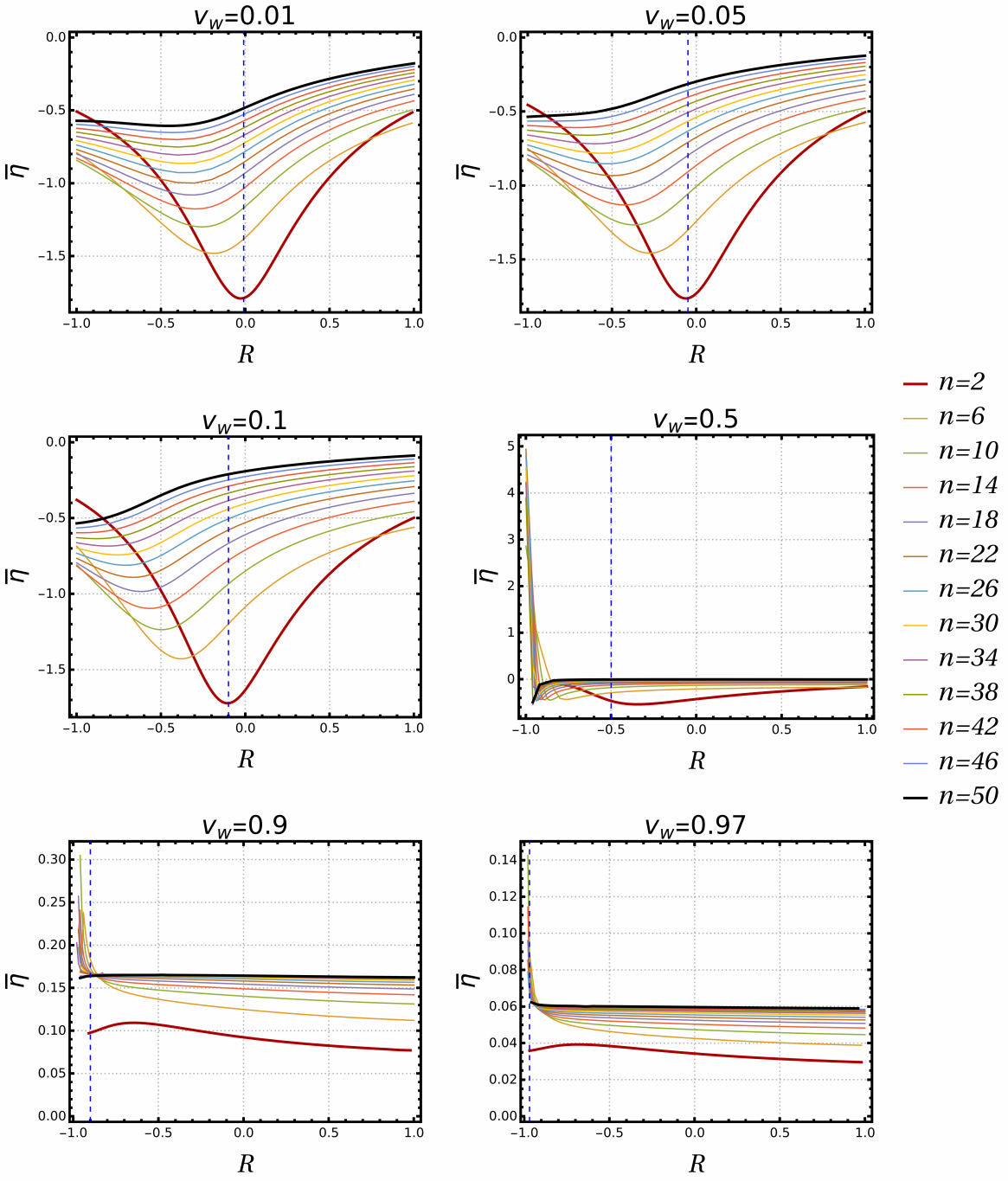

Figure 13.5.: The normalized BAU $\bar{\eta}$ over the R-value used in the constant truncation scheme for different wall velocities. The lines represent the largest moment taken into account in the transport equations and the dashed blue line marks the truncation choice $R = -v_w$.

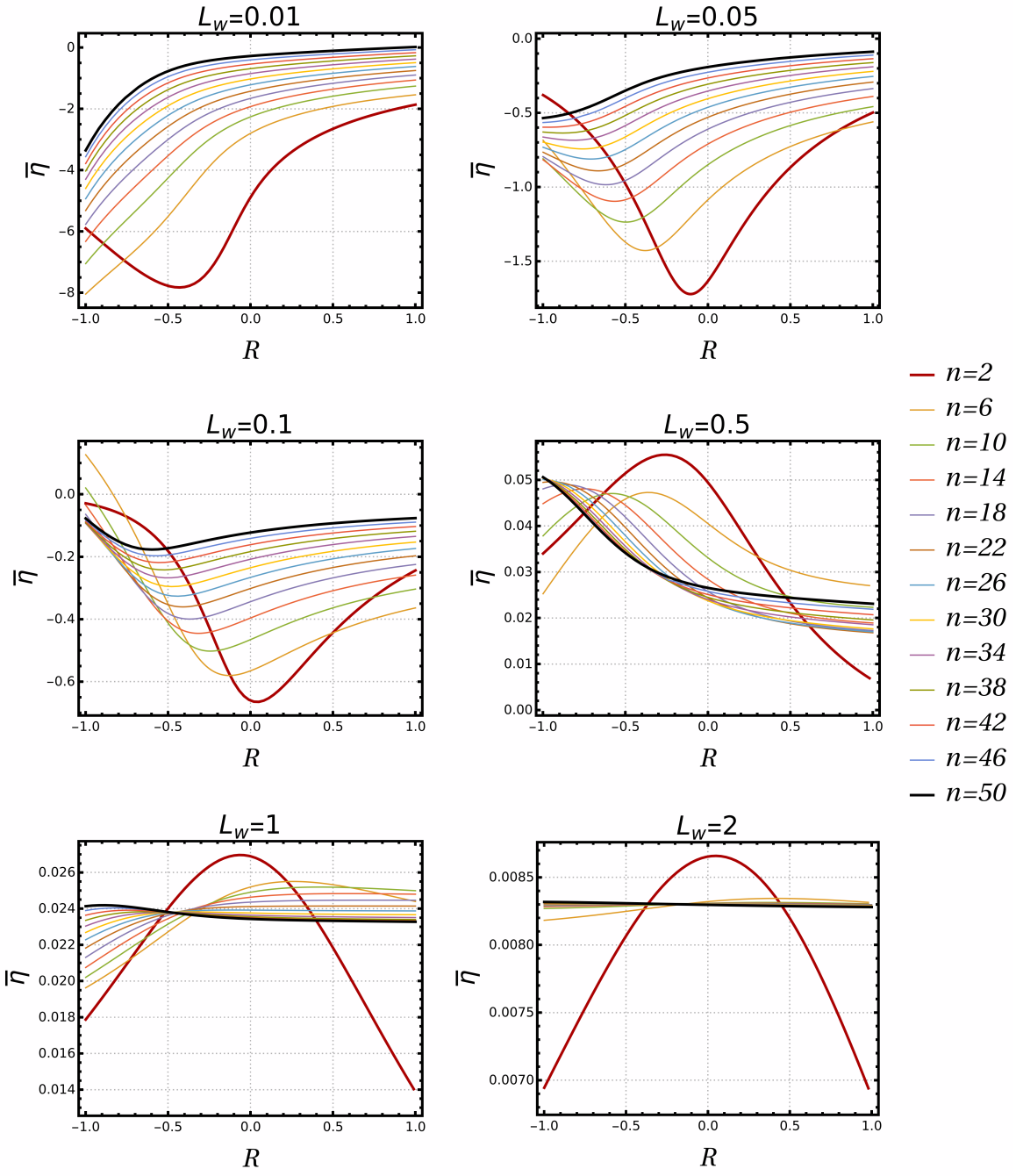

Figure 13.6.: The normalized BAU $\bar{\eta}$ over the R-value used in the constant truncation scheme for different wall thicknesses. The lines represent the largest moment taken into account in the transport equations.

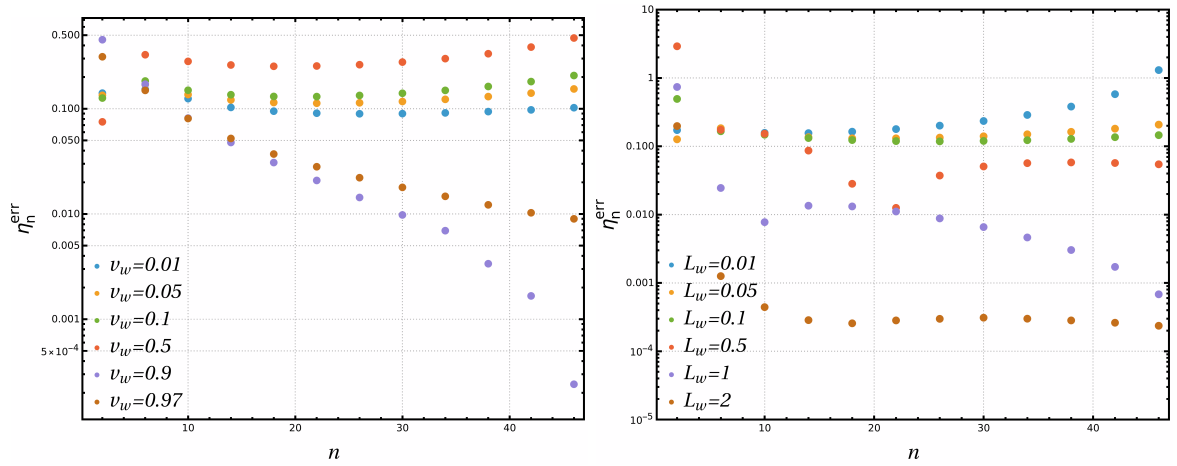

Figure 13.7.: Error of the BAU as defined in Eq. (13.6) over the number of moments for different v_w on the left and different L_w on the right.

v_w case, it is not clear at all that for small L_w, i.e. $L_w < 1$, they will reach a constant value as $n \to \infty$. For $L_w = 2$ the moment expansion converges already at $n = 14$. For large L_w, however, the BAU turns out to be smaller. A rapid convergence for large L_w is expected as it is the underlying assumption of the WKB ansatz, which is $L_w T_n \gg 1$.

However, at this stage it is not clear that the BAU will converge to a constant value even if the result is independent of the truncation choice. To investigate if the results for the BAU really converge to a constant value for large v_w and L_w, when large n values are chosen, we will consider the quantity

$$\eta_n^{\mathrm{err}} \equiv \left| \frac{\eta_{n+4} - \eta_n}{\eta_n} \right| . \tag{13.6}$$

If the BAU converges to a constant value we should see that $\eta_n^{\mathrm{err}} \to 0$ as we increase n. In Fig. 13.7 we plot η_n^{err} as a function of n for different v_w and L_w. For small wall velocities as well as small wall thicknesses we see that η_n^{err} reaches either a constant value or starts to increase for large n. This suggests that for these values the method does not lead to a reliable and stable result. Only for large parameter values v_w, L_w, we observe a convergent behavior.[18]

There could be several causes why smaller values of L_w and v_w do not reach a stable solution. The obvious cause is that we did not take sufficiently large n into account and that the result might stabilize for larger n values. However, looking at the trends observed in Fig. 13.7, this seems unlikely. As already mentioned in Ref. [13] another possibly large source of error could come from the estimates used to obtain the ℓ'th collision operator in Eq. (11.65). A more detailed study of the collision rates for large moments might lead to a more stable solution for the BAU. Another reason might be that the moment expansion approach is only valid in the limit of large v_w or large L_w as these fulfill the requirement that μ and δf are sufficiently small perturbations allowing us to consider only linear terms in the transport equations. Hence, the following results have to be evaluated, keeping in mind the discussed uncertainties.

13.2. Complex 2-Higgs Doublet Model

We will now switch from the simple toy model to a phenomenologically more relevant model, the C2HDM [147–155]. In this model we add a second doublet to the SM scalar sector with same gauge representation as the SM Higgs doublet and impose a softly broken $\mathbb{Z}_2$ symmetry,

[18] The fact that the $L_w = 2$ does not keep decreasing is due to the maximum precision of our algorithm.

where $\Phi_1 \to \Phi_1$ and $\Phi_2 \to -\Phi_2$. Following the model description in Ref. [156], we write the scalar potential as

$$\begin{aligned} V =& m_{11}^2|\Phi_1|^2 + m_{22}^2|\Phi_2|^2 - \left(m_{12}^2\,\Phi_1^\dagger\Phi_2 + h.c.\right) + \frac{\lambda_1}{2}(\Phi_1^\dagger\Phi_1)^2 + \frac{\lambda_2}{2}(\Phi_2^\dagger\Phi_2)^2 \\ &+ \lambda_3(\Phi_1^\dagger\Phi_1)(\Phi_2^\dagger\Phi_2) + \lambda_4(\Phi_1^\dagger\Phi_2)(\Phi_2^\dagger\Phi_1) + \left[\frac{\lambda_5}{2}(\Phi_1^\dagger\Phi_2)^2 + h.c.\right] , \end{aligned} \tag{13.7}$$

where, due to the hermicity of the potential, all couplings are real, except for m_{12}^2 and λ_5 which are complex. We parameterize the doublets in terms of neutral components ρ_i and η_i as well as charged components ϕ_i^+, where $i \in \{1, 2\}$ as

$$\Phi_1 = \begin{pmatrix} \phi_1^+ \\ \dfrac{\rho_1 + i\eta_1}{\sqrt{2}} \end{pmatrix} \qquad \text{and} \qquad \Phi_2 = \begin{pmatrix} \phi_2^+ \\ \dfrac{\rho_2 + i\eta_2}{\sqrt{2}} \end{pmatrix} . \tag{13.8}$$

The general finite temperature vacuum is then given by

$$\langle\Phi_1\rangle = \begin{pmatrix} 0 \\ \dfrac{\omega_1(T)}{\sqrt{2}} \end{pmatrix} \qquad \text{and} \qquad \langle\Phi_2\rangle = \begin{pmatrix} \omega_{CB}(T) \\ \dfrac{\omega_2(T) + i\omega_{CP}(T)}{\sqrt{2}} \end{pmatrix} . \tag{13.9}$$

We enforce that the charge breaking VEV ω_{CB} as well as the CP-violating VEV ω_{CP} have to vanish at $T = 0$, respectively. Further, we define $v_{1/2} \equiv \omega_{1/2}(T = 0)$ which fulfill the condition $v^2 = v_1^2 + v_2^2 \approx 246\,\text{GeV}$ at zero temperature. With this parameterization the minimum conditions at zero temperature can then be written as three equations,

$$m_{11}^2 v_1 + \frac{\lambda_1}{2}v_1^3 + \frac{\lambda_{345}}{2}v_1 v_2^2 = \text{Re}\left(m_{12}^2\right) v_2 , \tag{13.10}$$

$$m_{22}^2 v_2 + \frac{\lambda_2}{2}v_2^3 + \frac{\lambda_{345}}{2}v_1^2 v_2 = \text{Re}\left(m_{12}^2\right) v_1 , \tag{13.11}$$

$$2\,\text{Im}(m_{12}^2) = v_1 v_2 \text{Im}(\lambda_5) , \tag{13.12}$$

which, for non-zero VEVs v_1 and v_2, ensure one independent CP-violating phase if [147–149]

$$\text{Im}\left\{\lambda_5^* \left(m_{12}^2\right)^2\right\} \neq 0 . \tag{13.13}$$

Next, we proceed with the rotation into the Higgs basis via

$$\begin{pmatrix} \mathcal{H}_1 \\ \mathcal{H}_2 \end{pmatrix} = R_H^T \begin{pmatrix} \Phi_1 \\ \Phi_2 \end{pmatrix} \equiv \begin{pmatrix} c_\beta & s_\beta \\ -s_\beta & c_\beta \end{pmatrix} \begin{pmatrix} \Phi_1 \\ \Phi_2 \end{pmatrix} , \tag{13.14}$$

with

$$\tan\beta \equiv \frac{v_2}{v_1} . \tag{13.15}$$

The doublets in the Higgs basis can then be written, with the Goldstone bosons $G^\pm$ and G^0 in $\mathcal{H}_1$, as

$$\mathcal{H}_1 = \begin{pmatrix} G^\pm \\ \dfrac{1}{\sqrt{2}}(v + H^0 + iG^0) \end{pmatrix} \qquad \text{and} \qquad \mathcal{H}_2 = \begin{pmatrix} H^\pm \\ \dfrac{1}{\sqrt{2}}(R_2 + iI_2) \end{pmatrix} . \tag{13.16}$$

The mass matrix for the neutral Higgs states is defined for ρ_1, ρ_2 and $\rho_3 = I_2$ as

$$(\mathcal{M}^2)_{ij} = \left\langle \frac{\partial^2 V}{\partial\rho_i \partial\rho_j} \right\rangle , \tag{13.17}$$

which can be diagonalized by a general orthogonal matrix R via

$$R\mathcal{M}^2 R^T = \mathrm{diag}(m_1^2, m_2^2, m_3^2) \, , \tag{13.18}$$

with

$$R = \begin{pmatrix} c_1 c_2 & s_1 c_2 & s_2 \\ -(c_1 s_2 s_3 + s_1 c_3) & c_1 c_3 - s_1 s_2 s_3 & c_2 s_3 \\ -c_1 s_2 c_3 + s_1 s_3 & -(c_1 s_3 + s_1 s_2 c_3) & c_2 c_3 \end{pmatrix} , \tag{13.19}$$

where the notation $s_i \equiv \sin\alpha_i$, $c_i \equiv \cos\alpha_i$ ($i \in \{1,2,3\}$) was used and

$$-\pi/2 < \alpha_1 \leq \pi/2 \quad , \quad -\pi/2 < \alpha_2 \leq \pi/2 \quad , \quad -\pi/2 < \alpha_3 \leq \pi/2. \tag{13.20}$$

The model contains three neutral particles with no definite CP quantum numbers, h_1, h_2 and h_3, and two charged scalars $H^\pm$. The masses for the neutral Higgs bosons are ordered such that $m_1 \leq m_2 \leq m_3$. The set of independent parameters of the potential sector can be chosen as

$$\tan\beta \, , \, \lambda_1 \, , \, \lambda_2 \, , \, \lambda_3 \, , \, \lambda_4 \, , \, \mathrm{Im}(\lambda_5) \, , \, \mathrm{Re}(\lambda_5) \, , \, \mathrm{Re}(m_{12}^2) \, . \tag{13.21}$$

By imposing a $\mathbb{Z}_2$ symmetry we have the possibility to forbid tree-level flavor-changing neutral currents which are very constrained experimentally. The adopted natural flavor conservation mechanism [157,158] extends the symmetry to the Yukawa sector such that each of the three families of fermions couples to one and only one scalar field. We introduce the up-, down- and lepton-type fermion doublets as Φ_u, Φ_d and Φ_ℓ, which couple to up-type, down-type and charged leptons, respectively. This gives us four possible Yukawa types of the softly-broken $\mathbb{Z}_2$ symmetric 2HDM:

- Type-I: $\Phi_u = \Phi_d = \Phi_\ell \equiv \Phi_2$
- Type-II: $\Phi_u \equiv \Phi_2 \neq \Phi_d = \Phi_\ell \equiv \Phi_1$
- Lepton-Specific (LS) $\Phi_u = \Phi_d \equiv \Phi_2 \neq \Phi_\ell \equiv \Phi_1$
- Flipped $\Phi_u = \Phi_\ell \equiv \Phi_2 \neq \Phi_d \equiv \Phi_1$.

This lets us write the Yukawa Lagrangian as follows

$$\mathcal{L}_Y = -\sum_{i=1}^{3} \frac{m_f}{v} \bar{\psi}_f \left[c^e(h_i f f) + i c^o(h_i f f)\gamma_5 \right] \psi_f h_i \, , \tag{13.22}$$

where the coefficients of the CP-even and of the CP-odd part of the Yukawa coupling, $c^e(h_i f f)$ and $c^o(h_i f f)$, are presented in Tab. 13.1. The different families of fermions are identified by choosing f with the labels t, b and τ for up-type and down-type quarks and leptons, respectively. In this section we will only consider Type-I of the C2HDM.

13.2.1. VEV-Profile

In a model with a multi-dimensional VEV structure, such as the C2HDM, it becomes more challenging to determine the profile that interpolates between the false and the true vacuum. A common ansatz used in the literature [135,159,160] is to treat the VEVs as independent

	up-type	down-type	leptons
Type-I	$\frac{R_{i2}}{s_\beta} - i\frac{R_{i3}}{t_\beta}\gamma_5$	$\frac{R_{i2}}{s_\beta} + i\frac{R_{i3}}{t_\beta}\gamma_5$	$\frac{R_{i2}}{s_\beta} + i\frac{R_{i3}}{t_\beta}\gamma_5$
Type-II	$\frac{R_{i2}}{s_\beta} - i\frac{R_{i3}}{t_\beta}\gamma_5$	$\frac{R_{i1}}{c_\beta} - it_\beta R_{i3}\gamma_5$	$\frac{R_{i1}}{c_\beta} - it_\beta R_{i3}\gamma_5$
Lepton-Specific	$\frac{R_{i2}}{s_\beta} - i\frac{R_{i3}}{t_\beta}\gamma_5$	$\frac{R_{i2}}{s_\beta} + i\frac{R_{i3}}{t_\beta}\gamma_5$	$\frac{R_{i1}}{c_\beta} - it_\beta R_{i3}\gamma_5$
Flipped	$\frac{R_{i2}}{s_\beta} - i\frac{R_{i3}}{t_\beta}\gamma_5$	$\frac{R_{i1}}{c_\beta} - it_\beta R_{i3}\gamma_5$	$\frac{R_{i2}}{s_\beta} + i\frac{R_{i3}}{t_\beta}\gamma_5$

Table 13.1.: Yukawa couplings of the Higgs bosons h_i in the C2HDM, divided by the corresponding SM Higgs couplings. The expressions correspond to $[c^e(h_i ff) + ic^o(h_i ff)\gamma_5]$ from Eq. (13.22).

and assume a kink profile as we did with the benchmark model. The VEV profile is then given by

$$\phi_i(z) = \phi_{t,i} + (\phi_{f,i} - \phi_{t,i})\frac{1}{2}\left(1 + \tanh\left(\frac{z}{L_{w,i}}\right)\right) \quad \text{with} \quad i = 1, \cdots, n_{\text{Higgs}}\,, \tag{13.23}$$

where ϕ_t and ϕ_f are the true vacuum and false vacuum, respectively, and n_{Higgs} denotes the number of Higgs particles of the model.

In this thesis we will use a different approach where we solve the Equations Of Motion (EOM) of the fields. We begin by considering the EOM of a scalar field [34] in a plasma

$$\Box\phi_i + \nabla_{\phi_i} V(\boldsymbol{\phi}) + \sum_j (\nabla_{\phi_i} m_j) \int \frac{\mathrm{d}^3 p}{(2\pi)^3 2E_j} \delta f^j(p, z) = 0\,. \tag{13.24}$$

Solving these equations directly is beyond the scope of this thesis. Instead, we note that the last term in Eq.(13.24) acts as a friction term that stops the bubble from reaching the speed of light. We assume that the bubble wall has already reached a terminal velocity v_w and substitute the friction term with $\dfrac{\mu}{\gamma_w v_w}\partial_t\phi_i$, where μ is the friction coefficient [161]. If the wall has reached a terminal velocity it is clear that the profile can only depend on $z \equiv \gamma_w(\tilde{z} - v_w\tilde{t})$, where tilde refers to the coordinates in the plasma rest frame. Plugging $\phi_i(z) \equiv \phi_i(\gamma_w(\tilde{z} - v_w\tilde{t}))$ into the EOM gives

$$\frac{\mathrm{d}^2\phi_i}{\mathrm{d}z^2} + \mu\frac{\mathrm{d}\phi_i}{\mathrm{d}z} = \nabla_{\phi_i} V(\boldsymbol{\phi})\,. \tag{13.25}$$

To determine μ we can simply multiply the above equation by $\mathrm{d}\phi_i/\mathrm{d}z$ and integrate over z which gives

$$\mu\sum_i \int_{-\infty}^{\infty} \left[\frac{d\phi_i}{dz}\right]^2 dz = \Delta V\,, \tag{13.26}$$

where we used that the derivative of the field vanishes at $z \to \pm\infty$ and define $\Delta V \equiv V(\boldsymbol{\phi}(\infty)) - V(\boldsymbol{\phi}(-\infty))$. With this we obtain a recursive definition of μ, where we have to compute the profiles of the different $\phi_i(z)$ with an initial μ via Eq. (13.25) and insert the profiles into Eq. (13.26) to compute a new friction. We do these recursive steps until we obtain a constant μ and thus a stable VEV profile for the corresponding potential. As an initial guess for μ we use the kink profile.

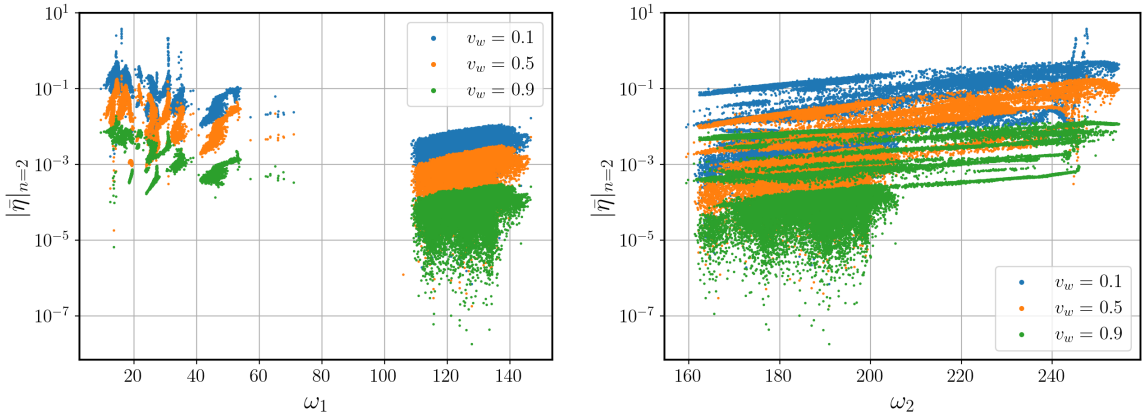

Figure 13.8.: Scatter plot of the normalized BAU for the C2HDM at $n = 2$ over the real VEV ω_1 (left) and ω_2 (right) at different wall velocities. The points fulfill all relevant experimental and theoretical constraints.

13.2.2. Parameter Impact on the BAU

We want to investigate how different parameters of the C2HDM affect the generated BAU. To do this, we generated a data sample which fulfills all relevant experimental and theoretical constraints using the tools `ScannerS` [112] and `BSMPT` [114]. Additionally, we use `BSMPT` to compute the percolation temperature T_p, which is the temperature where at least 29% of the false vacuum has tunneled into the true one. We use this temperature as our transition temperature to solve the transport equations and compute the BAU. For the parameter scan we compute the absolute value of the BAU for three wall velocities $v_w = 0.1, 0.5, 0.9$ and use the truncation scheme $R = -v_w$. We will comment further below on why we only consider the absolute value of the BAU and do not discard points with a negative sign in the BAU. Further, we only consider $n = 2$ equations per particle species since this is sufficient to draw conclusions about the parameter dependence of the BAU. As we saw in the benchmark model, this leads to an overestimation of the BAU in most scenarios.

First, we will look at the dependence of the BAU on the neutral VEVs ω_1 and ω_2 at T_p. The corresponding plots are shown in Fig. 13.8. In the left plot we observe a clear trend, namely that smaller values of ω_1 lead to a larger BAU. For ω_2 there is no such clear trend as the BAU remains relatively constant across the entire plotted ω_2 region with only a slight increase for larger ω_2 values. As we already saw in the benchmark model in Sec. 13.1 the magnitude of the BAU decreases as we increase the wall velocity. This is a phenomenon that we observe throughout the entire parameter space.

Next, we will investigate the dependence of the BAU on the complex parameters of the C2HDM, i.e. λ_5 and m_{12}^2, as these are the sources of CP-violation in this model. The corresponding plots are shown in Fig. 13.9, where on the left we show the normalized BAU over the absolute value of the ratio between the imaginary part and the real part of λ_5. In the right plot we do the same but for the ratio between the imaginary and real part of m_{12}^2 on the x-axis. Here, we see a clear correlation for both plots, namely that the normalized BAU goes to zero as the respective ratios go to zero. This is expected as these ratios are a measure of the complex phase of the respective parameters. As these complex phases go to zero, the model loses its CP-violating properties which ultimately leads to a constant θ such that the source terms in Eq. (11.48) vanish. This gives a clear prescription on how to maximize the BAU for future parameter searches. An interesting feature of this model is that a sign flip of the imaginary parts of λ_5, m_{12}^2 and a sign flip of ω_{CP} leaves the potential invariant. Therefore, flipping the signs of the imaginary parts is equivalent to flipping the

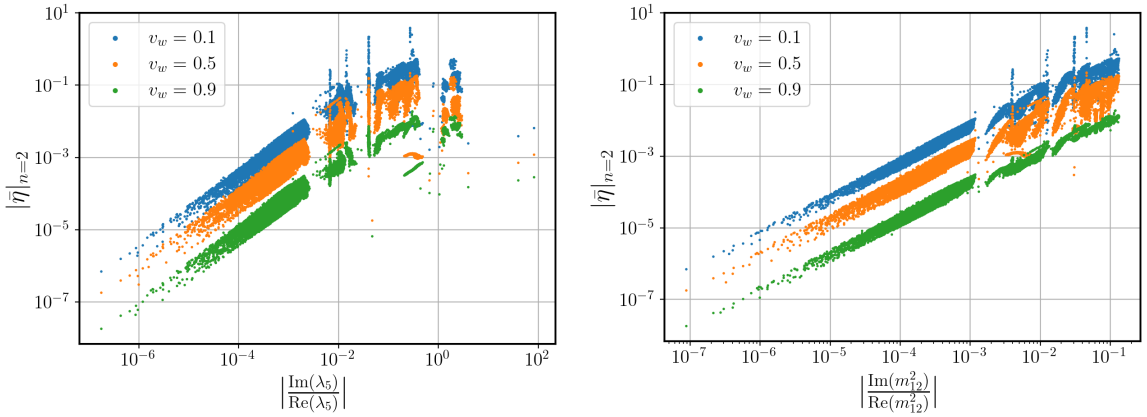

Figure 13.9.: Scatter plot of the normalized BAU for the C2HDM at $n = 2$ over the absolute value of the ratio between the imaginary and real part of λ_5 (m_{12}^2) on the left (right). The points fulfill all relevant experimental and theoretical constraints.

sign in ω_{CP}. Since, observables are not influenced by a constant complex phase, the change in the imaginary parts will leave them invariant. The key difference with the BAU is that the complex phase coming from ω_{CP} is z-dependent during the phase transition and therefore a sign flip of ω_{CP} will ultimately lead to a sign flip of the BAU. In short, if we obtain a negative BAU, we can simply flip the signs of the imaginary parts of λ_5 and m_{12}^2 to obtain a positive BAU without influencing other observables.[19]

In Fig. 13.10 we show the normalized BAU over the wall thickness and $L_w T_p$ as a color gradient for the wall velocity $v_w = 0.1$. Important to note is that in order to obtain a value for the wall thickness we use the approximation [159]

$$L_w \simeq \sqrt{\frac{\omega^2(T_p)}{8V_b}} \quad , \quad \omega^2(T_p) = \omega_1^2(T_p) + \omega_2^2(T_p) + \omega_{CP}^2(T_p) + \omega_{CB}^2(T_p) \, , \tag{13.27}$$

where V_b is the height of the potential barrier between the true and the false vacuum. This definition is valid for a kink profile, but as we will see in the next section, does not necessarily correspond to the wall thickness obtained from solving the field equations. Nevertheless, we see a strong correlation between the wall thickness and the generated BAU, i.e. small L_w lead to a large BAU. However, as we have shown in the case of the benchmark model, values of $L_w T \lesssim 100$ (keeping in mind that $T = T_n = 100\,\mathrm{GeV}$ in the benchmark model) lead to unreliable results and should be considered with caution. In general, we do not obtain a value of $L_w T_p$ that is larger than 10 throughout the entire parameter space, which according to the analysis we have done in the benchmark model, is not enough to obtain a stable BAU in the moment expansion. Therefore, our approach to compute the BAU might not be suitable for small velocities in this model.

13.2.3. Benchmark Points

To get a better picture of how our VEV profile and the kink profile differ in the C2HDM we will consider two Benchmark Points (BP). These two points are chosen such that the first has a large $L_w T_p$, while the second BP has a large BAU. The input parameters of these BPs are given in Tab. 13.2. We additionally provide the values for L_w, T_p, $L_w T_p$ and the VEVs at T_p

[19] When we talk about other observables we mean observables obtained in today's experiments where the VEV does not change over space and time. If we at some point deduce other early universe observables that rely on the VEV changing its phase, we have to be more careful.

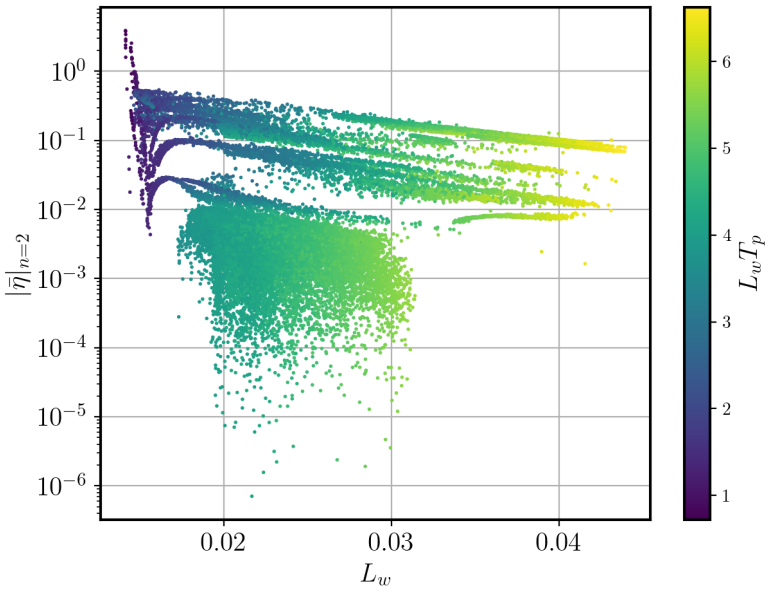

Figure 13.10.: Scatter plot of the normalized BAU for the C2HDM over the wall thickness and $L_w T_p$ as the color gradient. The points fulfill all relevant experimental and theoretical constraints.

as well as the computed normalized BAU, where in one case we use the kink profile and in the other case use the VEV profile obtained from solving the EOMs. In Fig. 13.11 we show the VEV profiles of ω_1, ω_2 and ω_{CP} of the presented BPs as a function of the bubble wall distance z. In blue we show the kink profile, where we used the same wall thickness for each VEV computed by `BSMPT` [113] and in orange we show the profile obtained by solving the EOMs given in Eq. (13.25). For BP1 we see that the field profiles match rather well with the exception of ω_{CP}, where we observe an additional dip before it reaches its true vacuum value. Defining a wall thickness for the EOM profiles is a bit more difficult than for the kink profiles, since we do not have an analytic expression for them. However, if we look at the z-values at which the VEV profiles reach a constant value in each z-direction and take the distance between the two, we can compare the kink and the EOM profiles. If we take this as our measure for the wall thickness, we find that the EOM profiles predict a larger wall thickness for each VEV compared the respective kink profiles. We know from our analysis in Sec. 13.1.2 that a larger L_w leads to a smaller BAU. This is consistent with the results obtained in the BP1 scenario where we obtain for the kink profile a normalized BAU of $|\bar{\eta}|^{\text{kink}}_{n=2} \approx 0.123$ and for the EOM profile a normalized BAU of $|\bar{\eta}|^{\text{EOM}}_{n=2} \approx 0.069$ (see Tab. 13.2). We observe a similar trend in the BP2 scenario. Here, the effect is even more drastic for ω_{CP}, where the wall thickness is off by roughly one order of magnitude. Another effect that naturally occurs when solving the EOMs, is that each VEV profile has their own wall thickness. As can be seen in the BP2 scenario, the wall thicknesses of the different VEVs do not have to be of the same order in magnitude.

Next, we want to check how the BAU evolves as we increase the number of considered moment equations per particle. We plot the normalized BAU over n for both BPs in Fig. 13.12. In blue we show the results obtained via the kink profile and in orange using the EOMs. For BP1 we observe a clear decrease of the absolute value of the BAU as we increase n. This is not surprising as we already saw this in Sec. 13.1. Further, consistent with our investigation in Sec. 13.1.2, $\bar{\eta}$ does not stabilize to constant value, even after taking into account $n = 50$ moment equations per particle. However, we observe that the results from the kink profile and the EOM profile move closer together as we increase n. This is a feature of BP1 and is

	BP1	BP2
$\tan\beta$	16.005	15.376
λ_1	0.027295	0.184255
λ_2	0.240944	0.242595
λ_3	6.87916	8.945212
λ_4	-2.88470	-3.21397
$\mathrm{Re}(\lambda_5)$	0.402294	1.710215
$\mathrm{Im}(\lambda_5)$	0.569051	0.460252
$\mathrm{Re}(m_{12}^2)$	17318.771	19800.915
L_w	0.047673	0.015447
T_p	150.82	51.1715
$L_w T_p$	7.190045	0.790438
$\omega_1(T_p)$	13.9098	15.9542
$\omega_2(T_p)$	162.214	247.473
$\omega_{CP}(T_p)$	-4.07453	0.074599
$\omega_{CB}(T_p)$	$2.98062 \cdot 10^{-9}$	$-1.3964 \cdot 10^{-8}$
$\lvert\bar{\eta}\rvert_{n=2}^{\mathrm{kink}}$	0.122611	10.711
$\lvert\bar{\eta}\rvert_{n=2}^{\mathrm{EOM}}$	0.0692125	3.888

Table 13.2.: Benchmark points for the C2HDM. The first 8 rows provide the input parameters, while the last 9 rows give the values for the wall thickness L_w, the percolation temperature T_p, $L_w T_p$ and the values of the VEVs at T_p as well as the absolute value of the normalized BAU using the kink profile or using the solution of the field equations. The L_w values provided in this table are computed using the approximation given in Eq. (13.27) and are only valid in the case of the kink solution (see text).

not true in general as we can see in the case of BP2. For BP2 we observe a strange behavior, namely that the BAU seems to diverge at $n = 42$ and then flips its sign and becomes negative for $n = 46, 50$. This indicates that this point is very unstable in the moment expansion and does not lead to conclusive results. We observe such a behavior only for large phase transition strengths, which in the case of BP2 is $\xi_p = \omega(T_p)/T_p \approx 4.846$ ($\xi_p \approx 1.08$ for BP1). However, it is not clear why this occurs for large ξ_p and further investigation is needed. A possible explanation could be that the phase transition is too strong and that the perturbative approach fails at this point.

To concluded this chapter, we want to say that one has to be cautious when computing the BAU in phenomenological models such as the C2HDM. We have shown that for wall thicknesses where $L_w T \lesssim 100$ there is no clear convergence of the BAU in the moment expansion using the current WKB method. A way to stabilize the moment expansion is to increase the wall velocity, however this will result in a decreased BAU, making it more challenging to find parameter regions which generate the observed BAU. However, we expect that the found correlations, e.g. the correlation between the imaginary part of λ_5 and BAU in Fig. 13.9, will still hold regardless of the precise value of the BAU.

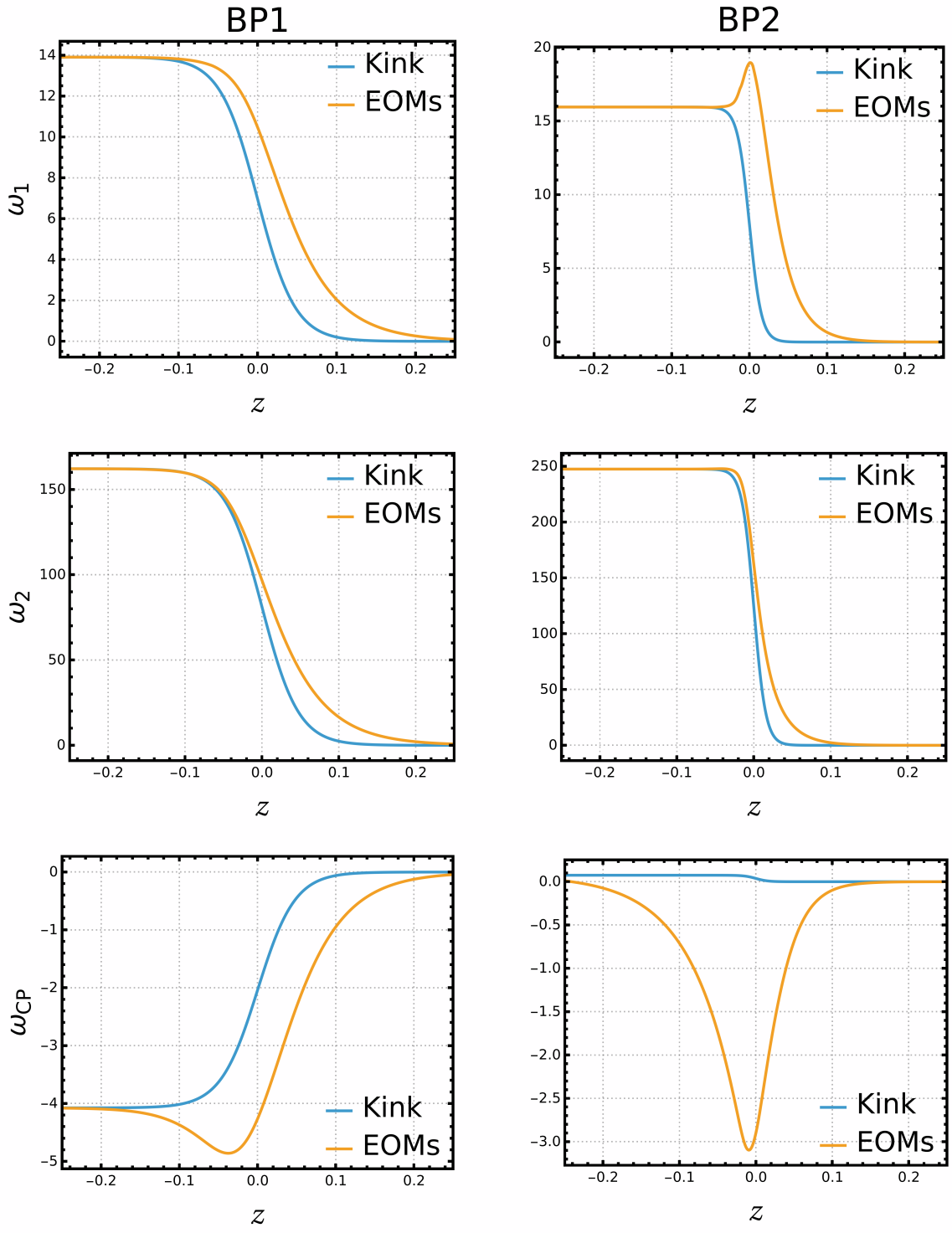

Figure 13.11.: VEV profiles for ω_1, ω_2 and ω_{CP} in terms of the bubble wall distance z for BP1 and BP2 presented in Tab. 13.2. In blue we show the kink profile and in orange the profile obtained by solving the EOMs in Eq. (13.25).

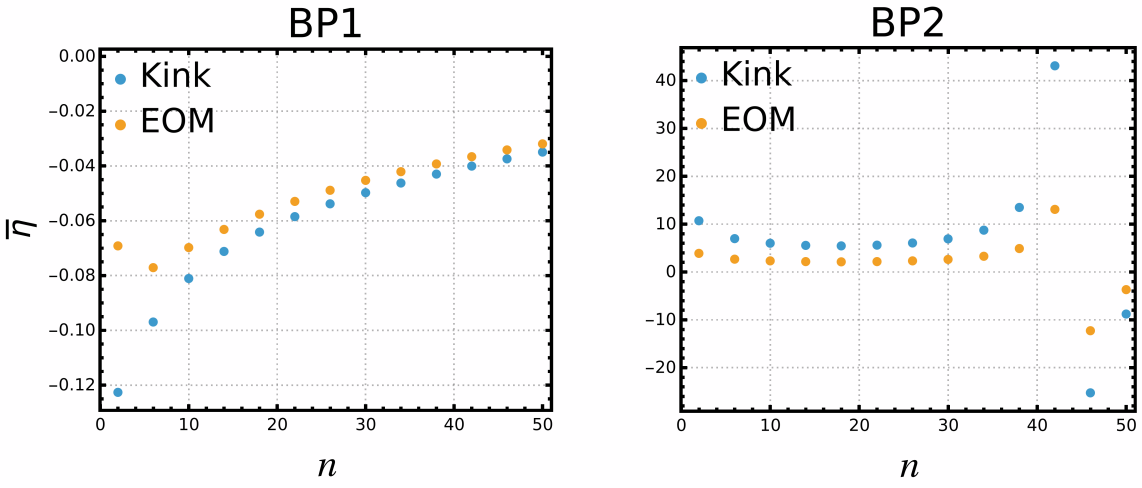

Figure 13.12.: The normalized BAU $\bar{\eta}$ over the number of moment equations n for the two BPs presented in Tab. 13.2. In blue: the results using a kink profile, in orange: the results using the profile obtained from the EOMs. We used a wall velocity of $v_w = 0.1$ and a constant truncation scheme with $R = -v_w$.

CHAPTER 14

Conclusions

In the second project of this thesis we have developed a code that is able to solve the transport equations and thus compute the BAU within in a given model. This code is not publicly available yet, but will be included in the next update of `BSMPT` [113, 114, 162]. We have performed a numerical investigation of the transport equations with respect to their moment expansion as well as a phenomenological investigation in the C2HDM. To this end, we have summarized the mechanism of EWBG which is required to obtain the matter anti-matter asymmetry. Further, we provided a derivation of how to compute the BAU in this framework. Doing so, we calculated the CP-violating force that emerges when considering a complex top-quark mass, derived the transport equations from the Boltzmann equation and gave the formula for the final BAU integration. In this context, we calculated the value of the top Yukawa rate which provides a new update compared to the previously available values from the literature, which gives a relative difference of roughly 41% compared to the most recent value where the leading log approximation was used [135].

With our code, we considered a benchmark model, where the relevant quantities such as the wall thickness L_w, VEVs, nucleation temperature and the wall velocity v_w are direct input parameters of the model. Our investigation suggests that as we increase the number of considered moments the BAU becomes truncation scheme independent. We observe this trend throughout our investigated region. This finding is in disagreement with the previous analysis done in this regard (see Ref. [13]), where it was found that the moment expansion has a large truncation scheme dependence for small wall velocities. Further, it is not clear that the BAU will always converge to a constant value for a large number of moment equations per particle n. We have shown that for values of $L_w \lesssim 1$ (i.e. $L_w T_n \lesssim 100$) or $v_w \lesssim 0.5$ there is no clear sign of convergence when taking into account $n = 50$ moment equations. We think what most likely causes this, is that the assumption that μ and δf are sufficiently small perturbations is not fulfilled in this regime.

For our investigation of the C2HDM, we used the tools `ScannerS` [112] and `BSMPT` [114] to generate a data sample that fulfills all relevant experimental and theoretical constraints. Further, we implemented an algorithm in BSMPT which solves the EOMs given in Eq. (13.25) to determine the VEV profile of the scalar fields. In our phenomenological investigation we observed a clear correlation between the BAU and the ratio between the imaginary part of λ_5 (m_{12}^2) and the real part of λ_5 (m_{12}^2) in Fig. 13.9. As this ratio goes to zero, so does the

computed BAU. This is explained by the fact that this ratio is measure of the complex phase which generates the CP-violation within this model. By setting this to zero, the source terms of the CP-odd transport equations vanish and no out of equilibrium force can be generated. Further, we showed that small values of L_w and $L_w T_p$ lead to a larger BAU. However, we did not find values for $L_w T_p > 10$ within our parameter search, which is not sufficient to obtain BAU values that are stable in the moment expansion and therefore have to be considered with caution.

Lastly, we compared the VEV profile stemming from the EOMs with a kink profile ansatz. To do so, we considered two benchmark scenarios and compared the VEV profiles of ω_1, ω_2 and ω_{CP} for the two approaches. We saw for both BPs, that the EOM profile predicts a larger wall thickness compared to the kink profile, which led to a smaller BAU. Further, we have found a strange behavior in the moment expansion of BP2, where the BAU seems to diverge and flips its sign at a specific value of n. We believe that this is due to the large phase transition strength of this BP, but further investigation has to be done in this regard.

We would like to remind the reader, that these results are new and have not been published previously. Our publication on this topic is in preparation.

CHAPTER 15

Final Conclusion and Outlook

The Standard Model of particle physics stands as one of the most successful achievements in modern science, with an unparalleled record of predictive power in collider experiments. Its precise quantitative predictions have been confirmed time and again, most notably through high-energy measurements at facilities such as the CERN and its Large Hadron Collider, where even subtle effects have been observed in remarkable agreement with theoretical expectations. This agreement with the collider data makes the identification of physics beyond the SM highly non-trivial. The absence of significant deviations from the predictions of the SM leave little room in the parameters space for models that attempt to describe new phenomena. At the same time, we know from cosmological observations that phenomena such as the existence of DM and the matter anti-matter asymmetry of the universe point toward the incompleteness of the SM.

To address these cosmological phenomena, i.e. DM and the observed BAU, it is necessary to consider the state of the early universe at which it was made up of a hot, dense plasma. During this time, particle interactions and out-of-equilibrium processes can lead through the evolution of the universe to the macroscopic structures and phenomena we observe today. These interactions provide a link between particles physics which we probe at colliders and through cosmological observables. In this context, the Boltzmann equation provides a useful tool to study the evolution of particle species as they undergo an out-of-equilibrium transition. The Boltzmann equation combines the microscopic particle interactions included in the collision operator, with the macroscopic evolution of the particle densities via the Liouville operator, thereby allowing us to make quantitative predictions with respect to relic abundances and asymmetries generated during the evolution of the universe.

The inclusion of additional particles besides the ones contained in the SM, can change the dynamics of the early universe plasma in a way that leads to the observed cosmological phenomena. In this thesis, we make use of this effect and study extensions of the SM that can accommodate the observed DM abundance as well as the observed BAU. More concretely, we developed tools which are able solve the Boltzmann equations for the given scenarios and performed phenomenological investigations using these tools.

In the context of DM we developed the tool `RelExt`, which assumes a DM model containing WIMPs that are stabilized by a $\mathbb{Z}_2$ symmetry and a single DM candidate. Although the

code is shipped with a few of such models, the user can load their own model into the code by providing the corresponding `FeynRules` model files. `RelExt` is then able to generate all relevant (co-)annihilation channels, compute the corresponding TACs and numerically solve the Boltzmann equation to obtain the DM relic density. Further, the code is able to perform efficient parameter scans within a given model, to determine parameter regions which are able to generate the observed DM abundance. In the first part of the thesis, we provided a detailed description of this tool and its algorithms as well as its usage. We showed that the parameter search techniques used in this code are able to determine the relevant parameter regions to obtain the observed DM abundance and are therefore able to generate phenomenologically relevant parameter points much faster than random searches. Further, we provided a validation of the numerical results obtained by our tool by comparing it with the well established code `MicrOMEGAs`.

In the next part of this thesis we finished a project that was already in the working, where we considered the DM model CP in the Dark. We showed that by setting the model parameter $\alpha_2 = \pi/2$, the model is able to obtain two DM candidates. One, which generates the DM abundance via freeze-out and one which generates the abundance via freeze-in. We have derived that the Boltzmann equations describing the density evolution of these particles can be decoupled and treated separately. For models that generate the relic density purely via freeze-in, it is challenging to provide predictions that can be measured in upcoming experiments. However, in our phenomenological investigation of this model, due to having two DM candidates, we have found that if the diphoton branching ratio re-scaled to the SM value is below one, the only way that this model is able to generate the observed relic abundance is via a sizable freeze-in contribution. This means, that in a scenario where this model accounts for the entire observed relic density, we would have a clear signal that could point us towards a relic density density that is mostly generated via freeze-in.

Within the third project we developed a code that is able to compute the BAU in the framework of EWBG by solving the necessary transport equations. We studied the stability of the BAU as we increase the number of moment equations in the transport network as well as performed a phenomenological investigation of the C2HDM with respect to the BAU. First, we introduced the mechanism of EWBG and presented the derivation of the CP-violating force as well as the transport equations. This includes the perturbative expansion in the chemical potentials of the involved particles as well as the average over arbitrarily large moments. For the collision rates appearing in the transport equations we have calculated an updated value for the top Yukawa rate, which gives a deviation to the most recent literature by roughly 41%. In our study of the stability of the BAU we considered a benchmark model, where the relevant parameters for the computation of the BAU are direct input parameters of the model. Our results suggest, that the BAU becomes independent of the chosen truncation scheme as we increase the number of moments. Further, we have found that for small bubble wall thicknesses and small bubble wall velocities the moment expansion does not converge to a constant value for the BAU and should therefore be considered with caution. In our phenomenological investigation of the C2HDM we were able to show clear correlations between certain parameters of the model and the generated BAU. We picked two BPs, for which we saw that the bubble wall thickness obtained from the EOMs is larger than the one obtained from the typically used kink ansatz for the VEV profile, which leads to a decrease in the computed BAU. The results obtained in this part are new and will be published soon.

Despite significant progress, the origins of DM and the observed matter–antimatter asymmetry remain unresolved, leaving key questions in fundamental physics open. Addressing these issues will require continued theoretical development on both the particle physics and astrophysical fronts, alongside increasingly precise observational and experimental input. Only

through the combined effort of experiment and theory we can hope to obtain answers on the fundamental questions about the universe we find ourselves in.

APPENDIX A

RelExt Structure and Algorithms

In the following, we describe the class structure of the code in more detail as well as explain the relevant algorithms used throughout `RelExt` mentioned in Chapter 4. Further, we will give a more detailed description on how these algorithms work.

A.1. Class Structure of RelExt

The class structure of `RelExt` is depicted in Fig. A.1. Each box represents a separate class of the code, except for the external `Mathematica` package, which feeds all the information about the model into the classes `ModelInfo` and `AnnihilationAmps`. We color coded the different classes based on the purposes they fulfill which are the following

Blue Highlights the classes which are responsible for running necessary computations and storing required information before the matrix elements are evaluated. This includes the `Mrun` class which computes the running quark masses, the class `Width` which computes the total decay widths of the s-channel mediator particles and `ModelInfo` which loads the denominator structure of a given process and the tokens used in the matrix elements.

Turquoise Highlights all classes which are responsible for the computation of the TAC given in Eq. (3.51). The class `AnnihilationAmps` is responsible for loading and evaluating the appropriate (co-)annihilation channels which are integrated over $\cos\theta$ by the class `SigvInt` which is also responsible for computing the remaining integrand of the TAC. Lastly, the `Tac` class is responsible for the s integration.

Green Highlights the classes which are responsible for solving the freeze-out Boltzmann equation. The class `BeqInfo` contains all the relevant information about the Boltzmann equation such as the value of the gravitational constant, the formula for Y_χ^{eq} and the effective degrees of freedom which are loaded via the `EffDof` class. This information is then used by the classes `FOCondition`, `FOAppr` and `FOFull`. The first of these classes contains the

formula for the freeze-out condition given in Eq. (4.10). The second class contains the formula for the integrand appearing in Eq. (4.11) and the third class contains the complete Boltzmann equation given in Eq. (3.33). These classes are then used by `FO1DM` to solve the Boltzmann equation and compute the relic density.

Steel blue Highlights the classes which are necessary to setup the search algorithms. The `OmegaGoal` class simply computes the difference between the desired relic density and the currently computed relic density. This class is used in every search algorithm to make sure that the next step step of these algorithms is taken into the correct direction. The class `MonteCarlo` is responsible for tracking the best cells as well as generating new parameters based on these cells.

Yellow These are the classes with which the user interacts directly. First, we have the `DataReader` class which reads the input files of the user, but is also used internally to load the necessary data for the effective degrees of freedom. The `Main` class contains all the functions to which the user has access and which the user can use throughout the `main.cpp` files.

In the shown class diagram we omitted the parts of the code that are responsible for the numerical algorithms since these are global functions and classes used throughout the code. The connections between the classes show their respective dependencies between each other. The important thing to note is that the `Main` class has a direct link to many of the other classes which allows the user to invoke them via the functions we provide within the `Main` class.

A.2. Key Algorithms of RelExt

In this section we describe in the detail the code for the algorithms described in Sec. 4.2. We will not discuss the numerical algorithms, as these are well known (see Ref. [109]) and instead will focus on the ones unique to `RelExt`.

A.2.1. Algorithms to compute the TAC

We start of with the functions that load in the requested (co-)annihilation channels and evaluate their matrix elements. These are provided in Listing A.1. The function `set_channels` takes in a vector of strings with the names of the channels we want to load and a boolean which determines if we want to include the flux factor of the given channel.[20] These strings are used to identify the corresponding (co-)annihilation functions via the maps `amp2fls` and `amp2s` which then fill the `cur_channel` vector with the functions of the channels we want to load. The difference between the two maps is that the former has the flux factors already included, while the latter does not. Next, we define a bracket operator for our AnnihilationsAmps class that evaluates the loaded matrix elements. Here, we simply iterate over all current channels and add them up for a given $\cos\theta$ and an s that can be set via a separate function. The sum of these channels is then returned.

Next, we will go through the algorithm that sorts the (co-)annihilation channels based on the prescription provided in Eq. (4.3). The corresponding function is given in Listing A.2. It takes a vector of strings as an input with the channel names that we want to include in the freeze-out process. In line 3 we assign memory to the vector `polK2s` with a size that is

[20] This is not the flux factor that is used in the calculation of a cross section.

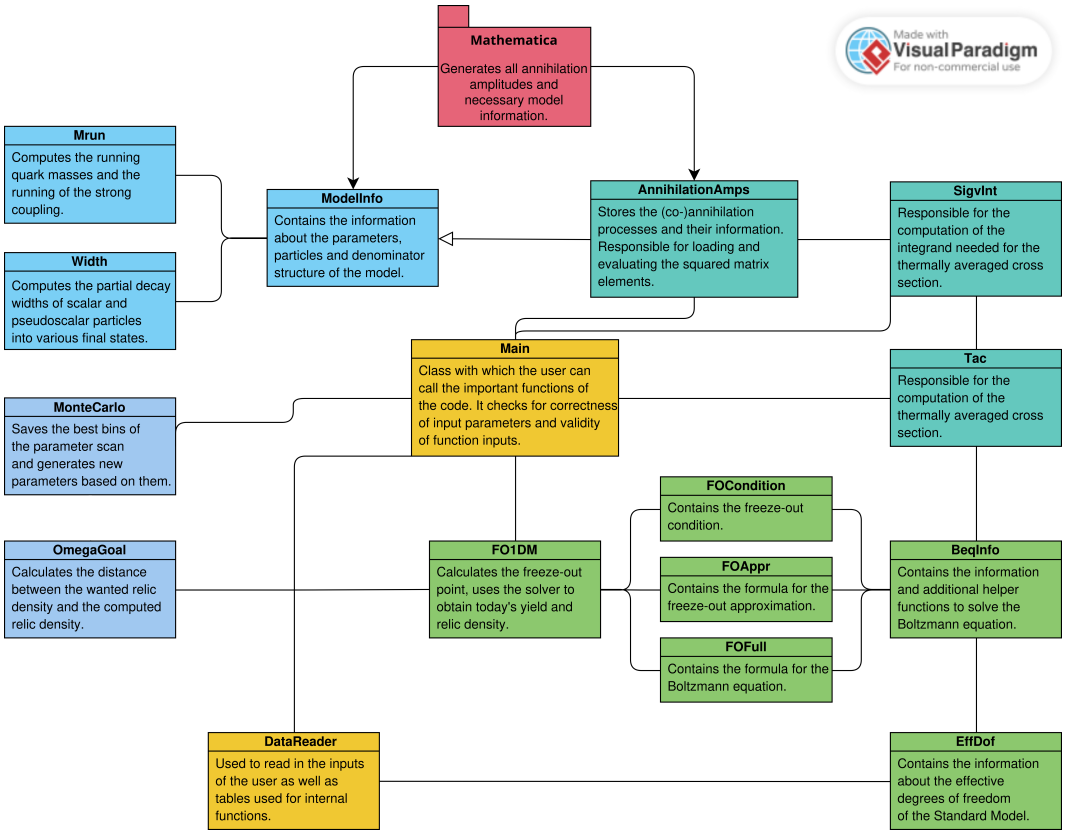

Figure A.1.: Class diagram showing the class dependencies of the `C++` part of `RelExt`. The figure has been made using the open source program `VisualParadigm`.

```
void AnnihilationAmps::set_channel(const VecString &ch_str, const
    bool flux) {
    cur_channel.clear();
    if (flux)
        for (auto it : ch_str) cur_channel.push_back(amp2fls[it]);
    else
        for (auto it : ch_str) cur_channel.push_back(amp2s[it]);
}

double AnnihilationAmps::operator()(const double cos_t) {
    double res = 0.;
    for (auto it : cur_channel) res += it(cos_t, s);
    return res;
}
```

Listing A.1: Code responsible for loading the wanted channels and evaluating the matrix elements.

```
1  bool Tac::sort_inimasses(const VecString &ch_str) {
2      double temp;
3      sigv.polK2s.resize(AA.bath_masses.size());
4      for (auto it : ch_str) {
5          AA.set_channel({it});
6          AA.assign_masses(m1, m2, it);
7          AA.set_s((m1 + m2) * (m1 + m2) * 100);
8          temp = AA(0.5);
9          if (std::isnan(temp) || std::isinf(temp)) {
10             std::cout << "The channel: " << it << " evaluates to non
                   numerical values.\n";
11             return false;
12         }
13         inimap[m1 + m2].push_back(it);
14     }
15     return true;
16 }
```

Listing A.2: Code responsible for sorting the (co-)annihlation channels.

equal to the number of DS particles involved in the DS thermal bath - more on this later. In lines 4-14 we loop over all channels. First we load the channel via the function shown in Listing A.1, then we call the function `assign_masses` which determines if the initial or final state masses are larger and assigns these to `m1` and `m2` for the given channel. In the lines 7-12 we test for a fixed s and $\cos\theta$ value if the channel results gives us nans or infinities and warn the user if this is the case. If we indeed find non-numerical results, the function returns false for this parameter point which ultimately leads the code to return a relic density of 0. However, if the channel passes the test it is sorted into the hashmap `inimap` which assigns the sum of the masses to a vector that contains the channel names for the given mass (see Tab. 4.1).

Now we move on to the integrand of the TAC given in Eqs. (4.6) and (4.7). The function `calc_polK2` precomputes the whole or parts of the denominator of the TAC. We first define `Tinv` via the formula $T^{-1} = x/m_{\rm DM}$ and also set a flag that we want to treat numerator and denominator as two separate parts of the calculation via `separate_num_den = true`. Next, in lines 7-16 we loop over the DS particles which are included in the DS thermal bath. In this loop we save the mass of the considered DS particle in line 8 and compute the corresponding denominator without the exponential function which we store in the vector `polK2s`. The map `DSdof` returns the internal degrees of freedom of the DS particle. Next, we check if the exponent of the exponential function is smaller than 700 to ensure that it is within the definition boundaries of the `C++` standard library. If it is, we treat the denominator separately as indicated by Eq. (4.6) and if not we then set the flag `separate_num_den` to false which will result in the code using Eq. (4.7) in the `lipsv` function. The `lipsv` function properly combines the denominator determined via `calc_polK2` with the Bessel function of the numerator. In this function, we first define the relevant variables in lines 20-25. With the `if`-case in line 27 we check if $x = m_{\rm DM}/T > 5$ to determine if the approximation given in Eq. (4.5) is valid or not. If it is, we proceed using Eq. (4.6) and Eq. (4.7) to compute the integrand. If not then we do not approximate the Bessel function in the denominator.[21] When we use the approximation we first check if the flag `seprate_num_den` is set to true and if the exponent of the exponential function is less than 700. If so, we use Eq. (4.6), otherwise we use Eq. (4.7). Lastly, we define a bracket operator for the `SigvInt` class that takes the variable $u \in (0, 1]$

[21] During the computation of the freeze-out relic density this case should never occur since we require that the freeze-out point should be at least $x_f = 5$.

as an input, converts it to the corresponding s-value and returns the entire TAC integrand, where `wij` is given by Eq. (3.40). The variable `lower_bound` stores the current lower boundary of the s integral as we will see later. Important is the multiplication by the Jacobian u^{-2} coming from the variable transformation between s and u.

Before we go over to the code responsible for the s integration, we will first look at the algorithms which set the internal boundaries around the resonance peaks preparing the integration over s. The corresponding functions are given in Listing A.4. We start with the function `peak_relevance`. It determines the x-value until which a given peak is relevant, i.e. it returns Eq. (4.8) inverted with respect to x. The variable `peakpos` stores the position of the peak (m_{med}) and `beps_eps` is the natural log of B_ϵ. In case the peak position matches the lower integral boundary it returns -1, making the peak irrelevant for additional boundaries. The next function, `peak_bounds`, sets the boundaries around the peak. As already stated in Sec. 4.2.2 we start with a boundary around the peak position with a size of $2 \cdot 20\Gamma_{\text{med}}$. In line 9 we check if the lower boundary of the peak is smaller than the lower boundary of the entire integral. While this is the case we keep reducing the size of the boundary by factors of 2. Once this is set, we assign 3 boundaries in lines 11-13, where the first and the third boundaries are specified via the width, while the second boundary is set exactly at the peak. These are converted from s space to u space using

$$u = \left(s - (m_i + m_j)^2 + 1\right)^{-1} \ . \tag{A.1}$$

The next function, `check_boundaries`, checks if the boundaries do not overlap. It is possible, that if the peaks are too close to each other, their boundaries might overlap leading the code to compute the same integral area twice. To avoid this, we ensure that subsequent boundary values are sorted in descending order (ascending in s space). For the boundary triplets returned by `peak_bounds` this is true by construction. However, for different boundary triplets the last boundary of the first triplet might be larger than the first boundary of the second triplet. In such a scenario they are set to the same boundary to resolve the overlap. This check only works if the boundaries are sorted. These functions are now combined in `set_boundaries` to set the inner boundaries of the s integral. In this function we keep track of the number of relevant peaks fulfilling the criterion in Eq. (4.8) via the variable `N_relevant_peaks`. From line 30-41 we loop over the number of possible resonances that can occur during the computation. In line 31, we determine the x-value up to which the peak is relevant, where `denstructures` contains the information about the width and the mass of the mediator particles. Next, we check in the if-case if the peak is relevant at the current x-value. If this is the case, we set peak boundaries, append them to the `boundaries` array and increase the number of relevant peaks. Lastly in lines 42 and 43, respectively, we sort the boundaries using an insertion sort algorithm and check these for overlaps.

Now that we are able to set the integration boundaries we move on to the integration over s. Here, we have two functions that are relevant shown in Listing A.5: `estimate_integrate_s` and `integrate_s`. As indicated by the function name, the former function is responsible for giving us a first estimate of the s integral. We keep track of the total result and current estimate by passing the `res` and `estimate` variables by reference. Although the purpose of this function is to estimate the integrand, the peaks are already precisely computed at this stage and are added to both the result and the estimate as can be seen in lines 4 and 5. In the for-loop in lines 7 and 8 we estimate the integrand between the peaks using the Kronrod 61-point method [109] and in line 10 we add the estimate of the integral between 0 and the first peak boundary as well as the integral between the last peak boundary and 1. This code is only executed if the number of relative peaks is greater than zero. In the case that the integrand contains no peaks, we estimate the integrand in a different manner via the loop shown in lines 19-26. During the first iteration we subdivide the integral into two subintegrals

```
void SigvInt::calc_polK2() {
    double Tinv = x / AA.MDM;
    double mtemp, cur;
    size_t i = 0;
    separate_num_den = true;
    den_save = 0.;
    for (auto it : AA.bath_masses) {
        mtemp = *AA.DSmasses[it];
        cur = AA.DSdof[it] * mtemp * mtemp * polK2(Tinv * mtemp);
        polK2s[i] = cur;
        if(Tinv * mtemp < 700. && separate_num_den)
            den_save += cur * exp(-Tinv * mtemp);
        else
            separate_num_den = false;
        i++;
    }
}

double SigvInt::lipsv(const double &s) {
    size_t i = 0;
    double num = 0.;
    double den = 0.;
    double mtemp;
    double sqs = sqrt(s);
    double Tinv = x / AA.MDM;

    if (x > 5) {
        if(sqs * Tinv < 700. && separate_num_den) {
            num += Tinv * exp(-sqs * Tinv) * polK1(sqs * Tinv);
            den += den_save;
        }
        else {
            num += Tinv * polK1(sqs * Tinv);
            for (auto it : AA.bath_masses) {
                mtemp = *AA.DSmasses[it];
                den += exp(-Tinv * (mtemp - sqs / 2)) * polK2s[i];
                i++;
            }
        }
    } else {
        num += Tinv * polK1(sqs * Tinv) * exp(-sqs * Tinv);
        for (auto it : AA.bath_masses) {
            mtemp = *AA.DSmasses[it];
            den += mtemp * mtemp * besselK2(Tinv * mtemp);
        }
    }

    return num / (den * den);
}

double SigvInt::operator()(const double &u) {
    double s = lower_bound * lower_bound + (1 - u) / u;
    return wij(s) * lipsv(s) / (u * u);
}
```

Listing A.3: Code responsible for computing the x dependent part of the TAC.

```
double Tac::peak_relevance(const double &peakpos) {
    if (peakpos == sigv.lower_bound) return -1.;
    return -beps_eps * AA.MDM / (peakpos - sigv.lower_bound);
}

double *Tac::peak_bounds(const double &peakpos, const double &width) {
    static double bounds[3];
    double n = 0.1;
    while (peakpos - 2 * width / n < sigv.lower_bound) n *= 2;

    bounds[0] = 1 / ((peakpos - 2 * width / n) * (peakpos - 2 * width
       / n) - sigv.lower_bound * sigv.lower_bound + 1);
    bounds[1] = 1 / (peakpos * peakpos - sigv.lower_bound *
       sigv.lower_bound + 1);
    bounds[2] = 1 / ((peakpos + 2 * width / n) * (peakpos + 2 * width
       / n) - sigv.lower_bound * sigv.lower_bound + 1);

    return bounds;
}

void Tac::check_boundaries() {
    for (size_t i = 0; i < boundaries.size() - 1; i++)
        if (boundaries[i] < boundaries[i + 1])
            boundaries[i + 1] = boundaries[i];
}

void Tac::set_boundaries(const double &x) {
    double peak_xf;
    double *b;

    N_relevant_peaks = 0;

    for (int j = 0; j < AA.N_widths; j++) {
        peak_xf = peak_relevance(*AA.denstructures.at(2 * j));

        if (peak_xf > 0 && x < peak_xf) {
            b = peak_bounds(*AA.denstructures.at(2 * j),
                            *AA.denstructures.at(2 * j + 1));
            boundaries[3 * N_relevant_peaks] = *b;
            boundaries[3 * N_relevant_peaks + 1] = *(b + 1);
            boundaries[3 * N_relevant_peaks + 2] = *(b + 2);
            N_relevant_peaks++;
        }
    }
    i_sort_boundaries();
    check_boundaries();
}
```

Listing A.4: Code responsible for assigning the integral boundaries on resonances.

```
void Tac::estimate_integrate_s(const double &x, double &res, double &estimate) {
    double error;
    if (N_relevant_peaks > 0) {
        res = res + integrate_peaks(x);
        estimate += res;

        for (size_t i = 1; i < N_relevant_peaks; i++)
            estimate += kronrod_61(sigv, boundaries[3 * i], boundaries[3 * i - 1], error);

        estimate += (kronrod_61(sigv, 0, boundaries[3 * N_relevant_peaks - 1], error) + kronrod_61(sigv, boundaries[0], 1, error));
    } else {
        double temp;
        double a = 1., b;
        size_t i, imax = 1;
        do {
            error = 0;
            temp = 0;
            b = 1.;
            for (i = 1; i < imax; i++) {
                a = (double)i * 1e-3 * b;
                temp += kronrod_61(sigv, a, b, error);
                b = a;
            }
            temp += kronrod_61(sigv, 0., a, error);
            imax++;
        } while ((error > 0.5 * std::abs(temp)) && (imax < 4));
        estimate += temp;
    }
}

void Tac::integrate_s(const double &x, double &res, double &estimate) {
    if (N_relevant_peaks > 0) {
        res +=
            h_adap_gauss_kronrod_15(sigv, 0, boundaries[3 * N_relevant_peaks - 1], estimate, gauss_kronrod_eps) +
            h_adap_gauss_kronrod_15(sigv, boundaries[0], 1, estimate, gauss_kronrod_eps);

        for (size_t i = 1; i < N_relevant_peaks; i++) {
            res +=
                h_adap_gauss_kronrod_15(sigv, boundaries[3 * i], boundaries[3 * i - 1], estimate, gauss_kronrod_eps);
        }
    } else {
        res +=
            h_adap_gauss_kronrod_15(sigv, 0, 1e-3, estimate, gauss_kronrod_eps);
        res +=
            h_adap_gauss_kronrod_15(sigv, 1e-3, 1, estimate, gauss_kronrod_eps);
    }
}
```

Listing A.5: Code responsible estimating and computing the s integral.

with boundaries $u \in \{(0, 10^{-3}), (10^{-3}, 1)\}$ and use the Kronrod 61-point method to obtain an estimate on the integral. If the relative error of this method is larger than 50 % we divide the integral into more subintegrals such that $u \in \{(0, 10^{-3n}), (10^{-3n}, 10^{-3(n-1)}), ..., (10^{-3}, 1)\}$ until the error is small enough or if a maximum number of $n = 3$ is reached.[22] The computed estimate is then used in the numerical algorithms to compute the integral value in the function `integrate_s`. This function works similar to the previous one, but instead of using an estimator, we use adaptive integration algorithms to compute the integral. In line 32, we first check if we have peaks that relevant in the integration region, then we integrate between 0 and the first peak boundary as well as the last peak boundary and 1. With the for-loop in lines 37-39 the areas between the peaks are integrated. In the case that there are no relevant peaks, we integrate the two subintegrals $u \in \{(0, 10^{-3}), (10^{-3}, 1)\}$.[23] With every integration the result is added to the total result saved in the variable `res`.

We are now at the stage where we can compute the TAC given in Eq. (3.51). The corresponding function is defined via the bracket operator shown in Listing A.6. In the lines 2-5 we prepare the computation by setting the total result as well as the estimate to 0. In line 4 we pass the x-value to the `SigvInt` instance `sigv` and in line 5 call the `calc_polK2` function used to initialize the denominator of the TAC. Next, we loop over the data structure that we set up in Listing A.2 in lines 6-14. During this loop we compute an estimate of the TAC. We do this by loading the channels that are assigned the same mass value via the condition given in Eq. (4.3) in line 7. Next, we assign the masses which correspond to aforementioned mass value to the variables `m1` and `m2` in line 8 and with them set the lower integration boundary in line 9. With the if-statement in line 10 we check if the criterion in Eq. (4.4) is fulfilled. If this is the case, we set the integral boundaries and estimate the contribution to the integral of the currently set channels in lines 11 and 12, respectively. The for-loop in lines 15-23 is identical to the previous one, except that we call `integrate_s` instead of `estimate_integrate_s`. At the end we return the result of the computed TAC.

A.2.2. Algorithm to compute the Relic Density

For the computation of the relic density we will only describe the function which returns the relic density but not the classes used within it. We do this, because the classes `FOCondition`, `FOAppr` and `FOFull` are straightforward implementations of Eq. (4.10), Eq. (4.11) and Eq. (3.33), respectively. The function to compute the relic density is shown in Listing A.7. First, the channels are sorted via `sort_inimasses` which returns `false` if the parameter point leads to problems. In that case the map with the sorted channels gets cleared via `clear_state` and a relic density of 0 is returned. With the for-loop in lines 10-18 we determine the freeze-out point via the freeze-out condition that is declared in the object `foc`. We start by computing the condition at $x = 50$ in line 9 and decrease it by 2 with each iteration. If we notice a sign flip between the current result `y1` and the previous result `y2` via the if-condition in line 12, we know the freeze-out point must be between the two corresponding x-values. We then apply a bisection algorithm to determine the freeze-out point. Next, we check if the freeze-out point is smaller than 5 in case the freeze-out point is not valid. In line 27 we define the initial starting value of the yield using $Y_{\mathcal{X}}(x_f) = (1 + \delta)Y_{\mathcal{X}}^{\mathrm{eq}}(x_f)$. We then check whether the freeze-out approximation should be used or not. If yes, an `FOAppr` object is instantiated in line 29, which contains the integrand of Eq. (4.11), and integrated over x using an adaptive integration method in line 30. The result is then combined with the initial yield to give the current yield in lines 31 and 32. In the case where the approximation is not used, the Boltzmann equation is instantiated via `FOFull` and used within the ODE solver

[22] In most cases the first iteration is sufficient.

[23] This acts as an artificial minimal recursion limit we set on the entire integral region.

```
double Tac::operator()(const double &x) {
    double res = 0.;
    double estimate = 0.;
    sigv.set_x(x);
    sigv.calc_polK2();
    for (auto &it : inimap) {
        AA.set_channel(it.second);
        AA.assign_masses(m1, m2, it.second[0]);
        sigv.set_lower_bound(m1 + m2);
        if (beps(x)) {
            set_boundaries(x);
            estimate_integrate_s(x, res, estimate);
        }
    }
    for (auto &it : inimap) {
        AA.set_channel(it.second);
        AA.assign_masses(m1, m2, it.second[0]);
        sigv.set_lower_bound(m1 + m2);
        if (beps(x)) {
            set_boundaries(x);
            integrate_s(x, res, estimate);
        }
    }
    return res;
}
```

Listing A.6: Code responsible for computing the thermally averaged cross section.

`Odeint` to compute today's yield in the lines 34-37. At the end we clear the map of sorted channels and return the relic density via the function `omega`.

A.2.3. Parameter Search Algorithms

Lastly, we will present the algorithms used to search the parameter space to obtain the desired relic density. We start with the Monte Carlo based algorithm where we have the two main functions. The first, `set_weight`, is responsible for keeping track of the best cells and the second, `generate_new_pars`, generates new parameters based on these cells. Both functions are presented in Listing A.8. In the `set_weight` function we need to provide the current parameter values `pars` and the computed relic density `relic` with these parameters. With the relic density we compute the weight given by Eq. (4.12) in line 2. Next, we convert the parameters into a vector of bins that uniquely assign a cell to the parameter point and convert it to a cell ID in lines 3 and 4, respectively. The conversion prescription from a bin to an ID in the example of 4 parameters is given by

$$\texttt{[b1,b2,b3,b4]} \rightarrow \texttt{"b1,b2,b3,b4"},$$

where `bi` is the bin number of the corresponding parameter. In lines 5 and 6 we check if this cell ID already exists among the best cells and if it does, we update its weight in case it is larger than the currently saved one. With the else if-condition that follows we check if the number of best cells has already reached the user requested size. If this is not the case we add the new cell to the best cells and update the worst cell. The last else if-statement is only reached if the `best_cells` map is full. In that case we check if the weight of the current cell is larger than the worst cell. If it is, we remove the worst cell and insert the new one. After that, we search for the new worst cell and save it for the next time the function

```
double FO1DM::operator()(const VecString &channels) {
    if (!BI.tac.sort_inimasses(channels)) {
        BI.tac.clear_state(true);
        return 0.;
    }

    double res;
    double x1 = 50., x2 = 50.;
    double y1, y2 = foc(x2);
    for (x1 = 48.; x1 > 3.; x1 -= 2.) {
        y1 = foc(x1);
        if (y1 * y2 < 0) {
            x1 = bisec_to_x(foc, x1, x2, secant_eps);
            break;
        }
        x2 = x1;
        y2 = y1;
    }

    if (x1 < 5.) {
        if (!suppress)
            std::cout << "Freeze-out temperature could not be
                found.\n";
        BI.tac.clear_state(true);
        return 0.;
    }

    double yfo = (1. + foc.del) * BI.yeq(x1);
    if (appr) {
        FOAppr foa(BI);
        res = adap_gauss_kronrod_15(foa, x1, xtoday, 1e-4);
        res = 1. / yfo - res;
        res = 1. / res;
    } else {
        FOFull fof(BI);
        Output out;
        Odeint<StepperDopr853<FOFull>> ode(yfo, x1, xtoday, 0., 1e-6,
            0.1, 0., out, fof);
        ode.integrate();
        res = yfo;
    }
    BI.tac.clear_state(true);
    return omega(res);
}
```

Listing A.7: Code responsible for the computatoin of the relic density.

```
void MonteCarlo::set_weight(const VecDoub &pars, const double &relic)
    {
    double weight = relic > target ? pow(target / relic, 2) :
        pow(relic / target, 2);
    std::vector<int> bins = get_bins(pars);
    std::string ID = bins_to_ID(bins);
    if (best_cells.count(ID) != 0) {
        best_cells[ID] = (best_cells[ID] > weight) ? best_cells[ID] :
            weight;
    } else if (best_cells.size() < N_best) {
        best_cells[ID] = weight;
        if (worst_cell > weight) {
            worst_cell = weight;
            worst_cell_ID = ID;
        }
    } else if (weight > worst_cell) {
        best_cells.erase(worst_cell_ID);
        best_cells[ID] = weight;
        double new_worst = 2.;
        std::string new_worst_ID = "";
        for (auto it : best_cells) {
            if (it.second < new_worst) {
                new_worst = it.second;
                new_worst_ID = it.first;
            }
        }
        worst_cell = new_worst;
        worst_cell_ID = new_worst_ID;
    }
}

VecDoub MonteCarlo::generate_new_pars() {
    VecDoub res(N_pars);
    double rand = generate_random(0., 1.);
    if ((best_cells.size() == N_best) && (rand > p_random)) {
        std::string cell_ID = select_random_cell_ID();
        std::vector<int> bins = ID_to_bins(cell_ID);
        for (size_t i = 0; i < lbounds.size(); i++) {
            double dx = (ubounds[i] - lbounds[i]) / (double)N_bins;
            res[i] = generate_random(lbounds[i] + dx *
                (double)bins[i], lbounds[i] + dx * ((double)bins[i] +
                1.));
        }
    } else {
        for (size_t i = 0; i < N_pars; i++)
            res[i] = generate_random(lbounds[i], ubounds[i]);
    }
    return res;
}
```

Listing A.8: Code responsible for tracking the best cells and generating new parameters during the Monte Carlo search.

```
1  template <class FUNC>
2  VecDoub RandomWalk::walk(FUNC &f) {
3      size_t cur_step = 0;
4      VecDoub xnew(f.get_parvals());
5      ynew = f(xnew);
6      do {
7          yold = ynew;
8          xold = xnew;
9          if (is_good) {
10             same_step(xnew);
11         } else {
12             random_step(xnew);
13         }
14         ynew = f(xnew);
15         if (std::abs(ynew) >= std::abs(yold)) {
16             xnew = xold;
17             ynew = yold;
18             is_good = false;
19         } else
20             is_good = true;
21         if ((cur_step % 100) == 0) {
22             std::cout << "Current Step: " << cur_step
23                       << " Omega: " << f.get_omega() << "\n";
24         }
25         cur_step++;
26     } while (std::abs(ynew) > eps && (cur_step < maxit));
27     std::cout << "Steps taken: " << cur_step << "\n";
28     return xnew;
29 }
```

Listing A.9: Code repsonsible for the random walk.

is called. As already mentioned we can also generate new parameters from the best cells via the `generate_new_pars` function. In this function we first prepare in line 30 a vector `res` where we will save the new set of parameters. Next, we generate a random number between 0 and 1 which will be used to determine if we will generate a parameter point from the best cells or a random one. In line 32 we therefore first check if the best cells vector is already full and then check if the generated random number `rand` is larger than one set by the user `p_random` (p_r). If this is the case we generate a parameter point from the best cells. We do this by first selecting a random cell from the best cells in line 33 and converting it to a vector of bin numbers in line 34. Next, in the for loop in lines 35-41 we loop over the parameters and define `dx` to be the size of a single bin for the given parameter boundaries. With this `dx`, we generate a new random parameter value inside the given bin and save it in the `res` vector in line 38. In the case that `rand` is smaller than the user specified value `p_random` we generate a random parameter between the given parameter boundaries in lines 40 and 41. Finally, we return the new parameters in line 43.

The search algorithm we will discuss next, is the random walk. We give the corresponding code in Listing A.9. The template function `walk` takes a functor `f` as an input. For our purposes, this functor will return the difference between the computed relic density and the desired relic density (i.e. $\Delta\Omega h^2$) when called via the bracket operator. We start in line 4, where we get the current parameter values of the model and save them in a vector `xnew`. In line 5 we compute $\Delta\Omega h^2$ and save it in the variable `ynew`. Now, we enter the while loop in which we first save the current value of $\Delta\Omega h^2$ in `yold` and the current parameter values in `xold`. In line 9 we check if the previous step was a good step, i.e. reduced $\Delta\Omega h^2$. If this is

the case, we take the same step via `same_step` and if not then we take a random step via `random_step`. In line 14 we compute a new $\Delta\Omega h^2$ and in line 15 check if its larger than the previous one. If the computed $\Delta\Omega h^2$ is larger, then we load the old parameter values and the old $\Delta\Omega h^2$ value as well as set `is_good` to false. Otherwise it was a step in the right direction and we set `is_good` to true. In lines 21 to 24 we print the relic density after every 100 steps taken and update the number of steps taken in line 25. The loop keeps going until either the desired accuracy `eps` or the maximum iteration number `maxit` is reached. Once it exits the loop, it returns the found parameter values.

The last algorithm we will describe in this section will be single parameter search with the code given in Listing A.10. As already stated in Sec. 4.2.4 the single parameter search consists of three search modes: vanguard, descent and bisect. The algorithm always starts in the vanguard mode. With the function `update_mode` we update the current mode after each step. As an input it takes the current step of the parameter search and the current $\Delta\Omega h^2$. In line 2 we check if the sign between the previous $\Delta\Omega h^2$ and the current one has flipped. If it has, we switch to the bisect mode via line 3. In line 7 we check if this was the first step of the parameter search to ensure the next if statement is consistent. There, we compare the signs between the previous step and the current step. If the signs are different, we must be in a local minimum and switch to the descent mode in line 14. Now we move on to the actual search algorithm which is provided in the template function `find`. As with the random walk we need to provide a functor that calculates $\Delta\Omega h^2$ and a starting value of the parameter we want to search for. In line 20 we define the maximum allowed number of iterations and compute the initial $\Delta\Omega h^2$ in line 21. During the while loop that starts in line 23, we first increase the number of iterations, save the parameter value and the corresponding $\Delta\Omega h^2$ in lines 24, 25 and 26, respectively. Moving on to the switch case, we have three possible cases - one for each search mode. If we are in the vanguard mode we first determine the direction which minimizes $\Delta\Omega h^2$ in line 29. We then define a step multiplier based on how large $\Delta\Omega h^2$ is, i.e. for large $\Delta\Omega h^2$ the multiplier becomes large but is bounded by a maximum size of 1. The step itself is then defined in lines 32 and 33 where we multiply the direction with the multiplier, the default vanguard step size (0.5) and the absolute value of the parameter. The addition with 10^{-5} acts as minimum step size. With this step, the new parameter is computed in line 34 and checked if it differs from the previous one in line 35. Using this parameter, we compute the next $\Delta\Omega h^2$ in line 37. Based on this new $\Delta\Omega h^2$ and the current step we update the search mode in line 38. We save the current step in line 39 and return the parameter value in line 40 if we have already reached the desired accuracy in $\Delta\Omega h^2$. In the case that we are in the descent mode we first compute the gradient in line 43 and adjust the parameter accordingly in line 44. With the new parameter we compute $\Delta\Omega h^2$ in line 45. We update the mode in the following line since it can still happen that the sign flips. Lastly, we check if the relative difference between the previous and current $\Delta\Omega h^2$ is smaller than the desired accuracy and if that is the case we return the parameter value. In the bisect mode we simply call the bisection algorithm between the previous parameter value and the current one.

```
void FindRoot::update_mode(const double step, const double y) {
    if (std::signbit(yold) != std::signbit(y)) {
        searchmode = bisect;
        std::cout << "Switch to bisect mode.\n";
        return;
    }
    if (first_step) {
        first_step = false;
        return;
    }
    if (std::signbit(stepold) != std::signbit(step)) {
        if (!(searchmode == descent)) {
            std::cout << "Switch to descent mode.\n";
            searchmode = descent;
        }
    }
}
template <class FUNC>
double FindRoot::find(FUNC &f, double xstart) {
    static const int MAXIT = 500;
    double y = f(xstart);
    int it = 0;
    while (it != MAXIT) {
        ++it;
        xold = xstart;
        yold = y;
        switch (searchmode) {
            case vanguard: {
                double dir = absgradient(f, xstart, y) > 0 ? 1. : -1.;
                double step =
                    std::abs(y) / scale > 1 ? 1. : std::abs(y) /
                       scale;
                step =
                    dir * (step * vanguard_step_size + 1e-5) *
                       std::abs(xstart);
                xstart = next_x(f, xstart - step);
                if (std::abs(xstart - xold) < 1e-14 * std::abs(xold))
                    return xstart;
                y = f(xstart);
                update_mode(step, y);
                stepold = step;
                if (std::abs(y) < eps) return xstart;
            } break;
            case descent: {
                double grad = descent_rate * absgradient(f, xstart,
                   y);
                xstart = next_x(f, xstart - grad);
                y = f(xstart);
                update_mode(grad, y);
                stepold = grad;
                if (std::abs(y - yold) < eps * std::abs(yold)) return
                   xstart;
            } break;
            case bisect:
                return bisec_to_y(f, xold, xstart, eps);
                break;
            default:
                break;
        }
    }
    return xstart;
}
```

Listing A.10: Code repsonsible for the single parameter search.

APPENDIX B

Model Parameters

In this appendix we provide the parameters of the potential of the models we used in the thesis in terms of their input parameters.

B.1. CxSM Model Parameters

The CxSM model, introduced in Sec. 5.1, has the following set of input parameters,

$$v\,,\ v_S\,,\ \alpha\,,\ m_{h_1}\,,\ m_{h_2}\,,\ m_A\,. \tag{B.1}$$

We can express the remaining parameters from this set of inputs to obtain

$$\lambda = \frac{m_{h_1}^2 + m_{h_2}^2 + \cos 2\alpha \left(m_{h_1}^2 - m_{h_2}^2\right)}{v^2}\,, \tag{B.2}$$

$$d_2 = \frac{m_{h_1}^2 + m_{h_2}^2 + \cos 2\alpha \left(m_{h_2}^2 - m_{h_1}^2\right)}{v_S^2}\,, \tag{B.3}$$

$$\delta_2 = \frac{\sin 2\alpha \left(m_{h_1}^2 - m_{h_2}^2\right)}{v v_S}\,, \tag{B.4}$$

$$m^2 = \frac{1}{2}\left(\cos 2\alpha \left(m_{h_2}^2 - m_{h_1}^2\right) - \frac{v\left(m_{h_1}^2 + m_{h_2}^2\right) + v_S \sin 2\alpha \left(m_{h_1}^2 - m_{h_2}^2\right)}{v}\right)\,, \tag{B.5}$$

$$b_2 = \frac{1}{2}\left(2m_A^2 - m_{h_1}^2 - m_{h_2}^2 + \cos 2\alpha \left(m_{h_1}^2 - m_{h_2}^2\right) - \frac{v \sin 2\alpha \left(m_{h_1}^2 - m_{h_2}^2\right)}{v_S}\right)\,, \tag{B.6}$$

$$b_1 = -m_A^2\,. \tag{B.7}$$

B.2. CP in the Dark Model Parameters

The model CP in the Dark was introduced in Sec. 5.2 with the following input parameters,

$$v\,,\, m_h\,,\, m_{h_1}\,,\, m_{h_2}\,,\, m_{H^+}\,,\, \alpha_1\,,\, \alpha_2\,,\, \alpha_3\,,\, \lambda_2\,,\, \lambda_6\,,\, \lambda_8\,,\, m_{22}\,,\, m_s\,. \tag{B.8}$$

With these the remaining parameters are given by

$$m_{h_3}^2 = -\frac{m_{h_1}^2 R_{11}R_{12} + m_{h_2}^2 R_{21}R_{22}}{R_{31}R_{32}}\quad, \tag{B.9}$$

$$\lambda_3 = 2\frac{m_{H^\pm}^2 - m_{22}^2}{v^2}\quad, \tag{B.10}$$

$$\begin{aligned}\lambda_4 =& \frac{(m_{h_2}^2 + m_{h_3}^2 - 2m_{H^\pm}^2)(R_{13} - 2R_{21}R_{32}) + (m_{h_2}^2 - m_{h_1}^2)(2R_{12}R_{22}R_{23} + R_{13}R_{23}^2)}{v^2(R_{13} - 2R_{21}R_{32})} \\ &+ \frac{(m_{h_1}^2 - m_{h_3}^2)(2R_{12}R_{32}R_{33} + R_{13}R_{33}^2)}{v^2(R_{13} - 2R_{21}R_{32})}\quad,\end{aligned} \tag{B.11}$$

$$\lambda_5 = \frac{R_{13}(m_{h_3}^2 - m_{h_1}^2 R_{23}^2 + m_{h_2}^2(R_{23}^2 - 1) + (m_{h_1}^2 - m_{h_3}^2)R_{33}^2)}{v^2(R_{13} - 2R_{21}R_{32})}\quad, \tag{B.12}$$

$$\begin{aligned}\lambda_7 =& -\frac{2(m_{h_2}^2 R_{23}(2R_{12}R_{22} + R_{13}R_{23}) + m_S^2(R_{13} - 2R_{21}R_{32}) + m_{h_3}^2(R_{11}R_{31} - R_{12}R_{32})R_{33})}{v^2(R_{13} - 2R_{21}R_{32})} \\ &- \frac{2m_{h_1}^2(2R_{12}(R_{22}R_{23} - R_{32}R_{33}) + R_{13}(1 + R_{23}^2 - R_{33}^2) - 2R_{21}R_{32})}{v^2(R_{13} - 2R_{21}R_{32})}\quad,\end{aligned} \tag{B.13}$$

$$\mathrm{Re}(A) = \frac{R_{11}((m_{h_2}^2 - m_{h_1}^2)R_{21}^2 + (m_{h_1}^2 - m_{h_3}^2)R_{31}^2)}{v^2(R_{13} - 2R_{21}R_{32})}\quad, \tag{B.14}$$

$$\mathrm{Im}(A) = \frac{R_{12}((m_{h_2}^2 - m_{h_1}^2)R_{22}^2 + (m_{h_1}^2 - m_{h_3}^2)R_{32}^2)}{v^2(R_{13} - 2R_{21}R_{32})}\quad. \tag{B.15}$$

APPENDIX C

Universal Transport Functions

In this appendix we want to derive explicit expressions for the universal functions defined in Eqs. (11.47), (11.49) and (11.66). We start by considering the generic integral form

$$\begin{aligned}\mathcal{K}(V,n,m,k) &\equiv \left\langle \frac{p_z^n}{E^m} V(E,p_z)\mathcal{F}_{0w}^k \right\rangle \\ &= \frac{1}{N_1}\int \mathrm{d}^3p \frac{p_z^n}{E^m} V\mathcal{F}_{0w}^k[\gamma_w(E+v_w p_z)]\end{aligned} \tag{C.1}$$

where $V(E,p_z)$ is an arbitrary function of E and p_z, N_1 is a normalization constant given by Eq. (11.43) and

$$\mathcal{F}_{0w}^k \equiv \frac{\partial^k f_{0w}}{\partial(\gamma_w(E+v_w p_z))^k}\ , \tag{C.2}$$

where f_{0w} is defined in Eq. (11.28). First, we perform a Lorentz transformation

$$E=\gamma_w(E'-v_w p_z') \quad , \quad p_z=\gamma_w(p_z'-v_w E') \quad , \quad p_x=p_x' \quad , \quad p_y=p_y'\ , \tag{C.3}$$

where our new variables E' and p_z' are the energy and momentum in the plasma frame resulting in

$$\mathcal{K}(V,n,m,k)=\frac{1}{N_1}\int \frac{\mathrm{d}^3p'}{E'}\frac{(\gamma_w(p_z'-v_wE'))^n}{(\gamma_w(E'-v_wp_z'))^{m-1}} V\mathcal{F}_0^k[E']\ . \tag{C.4}$$

Next, we do the coordinate transformation $(p_x',p_y',p_z')\to(E',p_z',\theta)$ via

$$E'=\sqrt{p_x'^2+p_y'^2+p_z'^2+m^2} \quad , \quad \tan(\theta)=\frac{p_y'}{p_x'} \quad , \quad p_z'=p_z'\ . \tag{C.5}$$

This leads to the Jacobian $\det(J)=E'$ and turns Eq. (C.4) into

$$\begin{aligned}\mathcal{K}(V,n,m,k) &= \frac{1}{N_1}\int_m^\infty \mathrm{d}E' \int_{-p_{E'}}^{p_{E'}} \mathrm{d}p_z' \int_{-\pi}^{\pi}\mathrm{d}\theta \frac{(\gamma_w(p_z'-v_wE'))^n}{(\gamma_w(E'-v_wp_z'))^{m-1}} V\mathcal{F}_0^k \\ &= \frac{2\pi}{N_1}\int_m^\infty \mathrm{d}E \int_{-p_E}^{p_E}\mathrm{d}p_z \frac{(\gamma_w(p_z'-v_wE'))^n}{(\gamma_w(E'-v_wp_z'))^{m-1}} V\mathcal{F}_0^k\ ,\end{aligned} \tag{C.6}$$

where $p_{E'} \equiv \sqrt{E'^2 - m^2}$. Next, we make the substitutions $p'_z = y p_{E'}$ and $E' = \omega T$ to arrive at the final expression

$$\mathcal{K}(V, n, m, k) = -\frac{3}{\pi^2 \gamma_w} T^{n-m-k+1} \int_x^\infty \mathrm{d}\omega \int_{-1}^1 \mathrm{d}y \frac{\tilde{p}_\omega \tilde{p}_z^n}{\tilde{E}^{m-1}} V \mathcal{F}_0^k[\omega] \,, \tag{C.7}$$

with

$$x = m/T \quad , \quad \tilde{p}_\omega = \sqrt{\omega^2 - x^2} \quad , \quad \tilde{p}_z = \gamma_w (y\tilde{p}_\omega - v_w \omega) \quad , \quad \tilde{E} = \gamma_w (\omega - v_w y \tilde{p}_\omega) \,. \tag{C.8}$$

We can now define the universal functions in terms of $\mathcal{K}$ as follows

$$K_\ell = T^{-1} \mathcal{K}(1, \ell, \ell, 0) \,, \tag{C.9}$$

$$D_\ell = \mathcal{K}(1, \ell, \ell, 1) \,, \tag{C.10}$$

$$Q_\ell = \frac{T^2}{2} \mathcal{K}(1, \ell - 1, \ell, 2) \,, \tag{C.11}$$

$$Q_\ell^{8o} = \frac{T^2}{2} \mathcal{K}(V_{s/h}, \ell - 2, \ell, 1) \,, \tag{C.12}$$

$$Q_\ell^{9o} = \frac{T^4}{4} \left[\mathcal{K}(V_{s/h}, \ell - 2, \ell + 2, 1) - \gamma_w \mathcal{K}(V_{s/h}, \ell - 2, \ell + 1, 2) \right] \,, \tag{C.13}$$

where $V_{s/h}$ are functions that depend on if we use the spin or helicity basis and are given by [135]

$$V_s = \frac{|\tilde{p}_z|}{\sqrt{\tilde{p}_z^2 + x^2}} \quad , \quad V_h = V_s^2 \left(1 - \frac{x^2}{\omega^2} \right)^{-1/2} \,. \tag{C.14}$$

Note that the T dependence of the universal functions cancels, making them dimensionless and solely dependent on x and v_w.

Acknowledgements (Danksagungen)

First and foremost, I want to thank my supervisor Prof. Dr. Milada M. Mühlleitner. She gave me the opportunity to work on amazing topics and her guidance throughout my thesis was invaluable. Through our weekly meetings, our many discussions, and her encouragement she taught me how to be a strong researcher and tackle challenging problems. I truly enjoyed my time at the institute and admire the positive atmosphere she has created, and hope that it continues for years to come.

The next person I want to thank, is my second supervisor Prof. Dr. Rui Santos. It was a real pleasure to work and discuss with him. What I admire most about him is his uncanny ability to pinpoint potential mistakes in my approach and flaws in my arguments, constantly pushing me to improve.

I would further like to thank all those with whom I collaborated on my projects. Thank you for the many insightful and fruitful discussions Karim, Rodrigo, João, Tim, Felix, Matrin, Rafael and Prof. Dr. Thi Nhung Dao.

I also want to thank all my colleagues at the institute who were willing to discuss and answer my questions patiently. Special thanks to Sauro and Christoph for my IT needs and trouble. A big thank you to all my (ex-)office mates: Felix, who always gave me great practical advice for my problems. Karim, who was always there for fundamental discussions and my Tayloring needs. Pavao and Maurice, who were always ready to discuss everything with me, inside and outside of physics.

Moreover I want to thank my family for supporting me all these years and always believing in me. My dad Konstantin, who always shared my interest in physics with me. My mom Natalia, who always cared and continues to care for my well being. My sister Maria, who has a bright future ahead of her. My wife Annika, who always patiently listened to my problems, and supported me through difficult times. And last but not least, my cats Kiki and Theodor, who got many ”oohs” and ”ahhs” as they walked past the camera in my online meetings.

References

[1] M. Baak, M. Goebel, J. Haller, A. Hoecker, D. Kennedy, R. Kogler, K. Mönig, M. Schott, and J. Stelzer, "The electroweak fit of the standard model after the discovery of a new boson at the lhc," *The European Physical Journal C* **72** no. 11, (Nov., 2012) . http://dx.doi.org/10.1140/epjc/s10052-012-2205-9.

[2] **ATLAS Collaboration and CMS Collaboration** Collaboration, G. e. a. Aad, "Combined measurement of the higgs boson mass in pp collisions at $\sqrt{s} = 7$ and 8 tev with the atlas and cms experiments," *Phys. Rev. Lett.* **114** (May, 2015) 191803. https://link.aps.org/doi/10.1103/PhysRevLett.114.191803.

[3] G. Hinshaw *et al.*, "Nine-year wilkinson microwave anisotropy probe (wmap) observations: Cosmological parameter results," *The Astrophysical Journal Supplement Series* **208** no. 2, (Sept., 2013) 19. http://dx.doi.org/10.1088/0067-0049/208/2/19.

[4] N. Aghanim *et al.*, "Planck2018 results: Vi. cosmological parameters," *Astronomy & Astrophysics* **641** (Sept., 2020) A6. http://dx.doi.org/10.1051/0004-6361/201833910.

[5] J. e. a. Aalbers, "First dark matter search results from the lux-zeplin (lz) experiment," *Physical Review Letters* **131** no. 4, (July, 2023) . http://dx.doi.org/10.1103/PhysRevLett.131.041002.

[6] J. Aalbers *et al.*, "Dark matter search results from 4.2 tonne years of exposure of the lux-zeplin (lz) experiment," *Physical Review Letters* **135** no. 1, (July, 2025) . http://dx.doi.org/10.1103/4dyc-z8zf.

[7] A. D. Sakharov, "Violation of CP Invariance, C asymmetry, and baryon asymmetry of the universe," *Pisma Zh. Eksp. Teor. Fiz.* **5** (1967) 32–35.

[8] K. Kajantie, M. Laine, K. Rummukainen, and M. Shaposhnikov, "A non-perturbative analysis of the finite-t phase transition in su (2) × u (1) electroweak theory," *Nuclear Physics B* **493** no. 1–2, (May, 1997) 413–438. http://dx.doi.org/10.1016/S0550-3213(97)00164-8.

[9] Z. Fodor, J. Hein, K. Jansen, A. Jaster, and I. Montvay, "Simulating the electroweak phase transition in the su (2) higgs model," *Nuclear Physics B* **439** no. 1-2, (Apr., 1995) 147–186. http://dx.doi.org/10.1016/0550-3213(95)00038-T.

[10] J. M. Cline, M. Joyce, and K. Kainulainen, "Supersymmetric electroweak baryogenesis," *Journal of High Energy Physics* **2000** no. 07, (July, 2000) 018–018. http://dx.doi.org/10.1088/1126-6708/2000/07/018.

[11] L. Fromme and S. J. Huber, "Top transport in electroweak baryogenesis," *Journal of High Energy Physics* **2007** no. 03, (Mar., 2007) 049–049. http://dx.doi.org/10.1088/1126-6708/2007/03/049.

[12] J. M. Cline and K. Kainulainen, "Electroweak baryogenesis at high bubble wall velocities," *Phys. Rev. D* **101** (Mar, 2020) 063525. https://link.aps.org/doi/10.1103/PhysRevD.101.063525.

[13] K. Kainulainen and N. Venkatesan, "Systematic moment expansion for electroweak baryogenesis," 2024. https://arxiv.org/abs/2407.13639.

[14] S. L. Glashow, "Partial-symmetries of weak interactions," *Nuclear Physics* **22** no. 4, (1961) 579–588. https://www.sciencedirect.com/science/article/pii/0029558261904692.

[15] S. Weinberg, "A model of leptons," *Phys. Rev. Lett.* **19** (Nov, 1967) 1264–1266. https://link.aps.org/doi/10.1103/PhysRevLett.19.1264.

[16] A. Salam, *Weak and electromagnetic interactions*, pp. 244–254. https://www.worldscientific.com/doi/abs/10.1142/9789812795915_0034.

[17] P. D. Group, Workman, *et al.*, "Review of particle physics," *Progress of Theoretical and Experimental Physics* **2022** no. 8, (08, 2022) 083C01. https://doi.org/10.1093/ptep/ptac097.

[18] J. C. ROMÃO and J. P. SILVA, "A resource for signs and feynman diagrams of the standard model," *International Journal of Modern Physics A* **27** no. 26, (Oct., 2012) 1230025. http://dx.doi.org/10.1142/S0217751X12300256.

[19] D. J. Gross and F. Wilczek, "Ultraviolet behavior of non-abelian gauge theories," *Phys. Rev. Lett.* **30** (Jun, 1973) 1343–1346. https://link.aps.org/doi/10.1103/PhysRevLett.30.1343.

[20] K. G. Wilson, "Confinement of quarks," *Phys. Rev. D* **10** (Oct, 1974) 2445–2459. https://link.aps.org/doi/10.1103/PhysRevD.10.2445.

[21] G. 't Hooft, "Symmetry breaking through bell-jackiw anomalies," *Phys. Rev. Lett.* **37** (Jul, 1976) 8–11. https://link.aps.org/doi/10.1103/PhysRevLett.37.8.

[22] V. Baluni, "CP Violating Effects in QCD," *Phys. Rev. D* **19** (1979) 2227–2230.

[23] E. Gildener, "Gauge-symmetry hierarchies," *Phys. Rev. D* **14** (Sep, 1976) 1667–1672. https://link.aps.org/doi/10.1103/PhysRevD.14.1667.

[24] G. Hooft, *Naturalness, Chiral Symmetry, and Spontaneous Chiral Symmetry Breaking*, pp. 135–157. Springer US, Boston, MA, 1980. https://doi.org/10.1007/978-1-4684-7571-5_9.

[25] Y. Fukuda *et al.*, "Evidence for oscillation of atmospheric neutrinos," *Physical Review Letters* **81** no. 8, (Aug., 1998) 1562–1567. http://dx.doi.org/10.1103/PhysRevLett.81.1562.

[26] **SNO Collaboration** Collaboration, Q. R. Ahmad *et al.*, "Direct evidence for neutrino flavor transformation from neutral-current interactions in the sudbury neutrino observatory," *Phys. Rev. Lett.* **89** (Jun, 2002) 011301. https://link.aps.org/doi/10.1103/PhysRevLett.89.011301.

[27] J. Ellis and D. Wands, "Inflation (2023)," 2023. https://arxiv.org/abs/2312.13238.

[28] A. Maleknejad, M. Sheikh-Jabbari, and J. Soda, "Gauge fields and inflation," *Physics Reports* **528** no. 4, (July, 2013) 161–261. http://dx.doi.org/10.1016/j.physrep.2013.03.003.

[29] S. Hannestad, "What is the lowest possible reheating temperature?," *Physical Review D* **70** no. 4, (Aug., 2004) . http://dx.doi.org/10.1103/PhysRevD.70.043506.

[30] E. W. Kolb and M. S. Turner, *The Early Universe*, vol. 69. Taylor and Francis, 5, 2019.

[31] D. Brout *et al.*, "The pantheon+ analysis: Cosmological constraints," *The Astrophysical Journal* **938** no. 2, (Oct, 2022) 110. https://doi.org/10.3847/1538-4357/ac8e04.

[32] E. Di Valentino, O. Mena, S. Pan, L. Visinelli, W. Yang, A. Melchiorri, D. F. Mota, A. G. Riess, and J. Silk, "In the realm of the hubble tension—a review of solutions," *Classical and Quantum Gravity* **38** no. 15, (July, 2021) 153001. http://dx.doi.org/10.1088/1361-6382/ac086d.

[33] D. E. Morrissey and M. J. Ramsey-Musolf, "Electroweak baryogenesis," *New Journal of Physics* **14** no. 12, (Dec., 2012) 125003. http://dx.doi.org/10.1088/1367-2630/14/12/125003.

[34] G. D. Moore and T. Prokopec, "How fast can the wall move? a study of the electroweak phase transition dynamics," *Physical Review D* **52** no. 12, (Dec., 1995) 7182–7204. http://dx.doi.org/10.1103/PhysRevD.52.7182.

[35] G. C. Dorsch, S. J. Huber, and T. Konstandin, "A sonic boom in bubble wall friction," *Journal of Cosmology and Astroparticle Physics* **2022** no. 04, (Apr., 2022) 010. http://dx.doi.org/10.1088/1475-7516/2022/04/010.

[36] L. Husdal, "On effective degrees of freedom in the early universe," *Galaxies* **4** no. 4, (Dec., 2016) 78. http://dx.doi.org/10.3390/galaxies4040078.

[37] P. F. Depta, M. Hufnagel, K. Schmidt-Hoberg, and S. Wild, "Bbn constraints on the annihilation of mev-scale dark matter," *Journal of Cosmology and Astroparticle Physics* **2019** no. 04, (Apr., 2019) 029–029. http://dx.doi.org/10.1088/1475-7516/2019/04/029.

[38] A. Bazavov, T. Bhattacharya, M. Cheng, C. DeTar, H.-T. Ding, S. Gottlieb, R. Gupta, P. Hegde, U. M. Heller, F. Karsch, E. Laermann, L. Levkova, S. Mukherjee, P. Petreczky, C. Schmidt, R. A. Soltz, W. Soeldner, R. Sugar, D. Toussaint, W. Unger, and P. Vranas, "Chiral and deconfinement aspects of the qcd transition," *Physical Review D* **85** no. 5, (Mar., 2012) . http://dx.doi.org/10.1103/PhysRevD.85.054503.

[39] C. Pitrou, A. Coc, J.-P. Uzan, and E. Vangioni, "Precision big bang nucleosynthesis with improved helium-4 predictions," *Physics Reports* **754** (Sept., 2018) 1–66. http://dx.doi.org/10.1016/j.physrep.2018.04.005.

[40] S. Seager, D. D. Sasselov, and D. Scott, "How exactly did the universe become neutral?," *The Astrophysical Journal Supplement Series* **128** no. 2, (June, 2000) 407–430. http://dx.doi.org/10.1086/313388.

[41] A. Hosseinzadeh and S. A. Jafari, "Semiclassical transport in two-dimensional dirac materials with spatially variable tilt," 2024. https://arxiv.org/abs/2303.06030.

[42] S. Enomoto, Y.-H. Su, M.-Z. Zheng, and H.-H. Zhang, "Boltzmann equation and its cosmological applications," 2023. https://arxiv.org/abs/2301.11819.

[43] A. K. Das, *Finite Temperature Field Theory*. World Scientific, New York, 1997.

[44] J. Rammer, *Quantum Field Theory of Non-equilibrium States*. 2011.

[45] M. Le Bellac, *Thermal Field Theory*. Cambridge Monographs on Mathematical Physics. Cambridge University Press, 1996.

[46] A. Salvio, "Introduction to thermal field theory: From first principles to applications," *Universe* **11** no. 1, (Jan., 2025) 16. http://dx.doi.org/10.3390/universe11010016.

[47] M. E. Peskin and D. V. Schroeder, *An Introduction to quantum field theory*. Addison-Wesley, Reading, USA, 1995.

[48] J. I. Kapusta and C. Gale, *Finite-temperature field theory: Principles and applications*. Cambridge Monographs on Mathematical Physics. Cambridge University Press, 2011.

[49] B. Carr and F. Kühnel, "Primordial black holes as dark matter candidates," *SciPost Physics Lecture Notes* (May, 2022) . http://dx.doi.org/10.21468/SciPostPhysLectNotes.48.

[50] M. Milgrom, "Mond theory," *Canadian Journal of Physics* **93** no. 2, (Feb., 2015) 107–118. http://dx.doi.org/10.1139/cjp-2014-0211.

[51] M. Cirelli, A. Strumia, and J. Zupan, "Dark matter," 2024. https://arxiv.org/abs/2406.01705.

[52] J. L. Feng, "The wimp paradigm: Theme and variations," *SciPost Physics Lecture Notes* (June, 2023) . http://dx.doi.org/10.21468/SciPostPhysLectNotes.71.

[53] M. Pospelov, A. Ritz, and M. Voloshin, "Secluded wimp dark matter," *Physics Letters B* **662** no. 1, (Apr., 2008) 53–61. http://dx.doi.org/10.1016/j.physletb.2008.02.052.

[54] R. T. D'Agnolo and J. T. Ruderman, "Light dark matter from forbidden channels," *Physical Review Letters* **115** no. 6, (Aug., 2015) . http://dx.doi.org/10.1103/PhysRevLett.115.061301.

[55] D. Pappadopulo, J. T. Ruderman, and G. Trevisan, "Dark matter freeze-out in a nonrelativistic sector," *Physical Review D* **94** no. 3, (Aug., 2016) . http://dx.doi.org/10.1103/PhysRevD.94.035005.

[56] R. T. D'Agnolo, D. Pappadopulo, and J. T. Ruderman, "Fourth exception in the calculation of relic abundances," *Physical Review Letters* **119** no. 6, (Aug., 2017) . http://dx.doi.org/10.1103/PhysRevLett.119.061102.

[57] E. D. Kramer, E. Kuflik, N. Levi, N. J. Outmezguine, and J. T. Ruderman, "Heavy thermal dark matter from a new collision mechanism," *Physical Review Letters* **126** no. 8, (Feb., 2021) . http://dx.doi.org/10.1103/PhysRevLett.126.081802.

[58] E. Kuflik, M. Perelstein, N. R.-L. Lorier, and Y.-D. Tsai, "Elastically decoupling dark matter," *Physical Review Letters* **116** no. 22, (June, 2016) . http://dx.doi.org/10.1103/PhysRevLett.116.221302.

[59] P. J. Fitzpatrick, H. Liu, T. R. Slatyer, and Y.-D. Tsai, "New pathways to the relic abundance of vector-portal dark matter," *Physical Review D* **106** no. 8, (Oct., 2022) . http://dx.doi.org/10.1103/PhysRevD.106.083517.

[60] Y. Hochberg, E. Kuflik, T. Volansky, and J. G. Wacker, "Mechanism for thermal relic dark matter of strongly interacting massive particles," *Physical Review Letters* **113** no. 17, (Oct., 2014) . http://dx.doi.org/10.1103/PhysRevLett.113.171301.

[61] **CMS Collaboration** Collaboration, A. Tumasyan *et al.*, "Search for invisible decays of the higgs boson produced via vector boson fusion in proton-proton collisions at

$\sqrt{s} = 13$ TeV," *Phys. Rev. D* **105** (May, 2022) 092007. https://link.aps.org/doi/10.1103/PhysRevD.105.092007.

[62] T. Binder, T. Bringmann, M. Gustafsson, and A. Hryczuk, "Dark matter relic density revisited: The case for early kinetic decoupling," 2018. https://arxiv.org/abs/1805.00526.

[63] J. Edsjö and P. Gondolo, "Neutralino relic density including coannihilations," *Physical Review D* **56** no. 4, (Aug., 1997) 1879–1894. http://dx.doi.org/10.1103/PhysRevD.56.1879.

[64] P. D. Group, "Review of particle physics," *Progress of Theoretical and Experimental Physics* **2020** no. 8, (08, 2020) 083C01, https://academic.oup.com/ptep/article-pdf/2020/8/083C01/34673722/ptaa104.pdf. https://doi.org/10.1093/ptep/ptaa104.

[65] M. Abramowitz and I. A. Stegun, "Handbook of mathematical functions with formulas, graphs and mathematical tables." Washington: U.S. Department of Commerce. xiv, 1046 pp. (1964)., 1964.

[66] R. Capucha, K. Elyaouti, M. Mühlleitner, J. Plotnikov, and R. Santos, "Relext: A new dark matter tool for the exploration of dark matter models," *Computer Physics Communications* **320** (2026) 109968. https://www.sciencedirect.com/science/article/pii/S0010465525004692.

[67] A. Arbey, F. Mahmoudi, and G. Robbins, "SuperIso Relic v4: A program for calculating dark matter and flavour physics observables in Supersymmetry," *Comput. Phys. Commun.* **239** (2019) 238–264, arXiv:1806.11489 [hep-ph].

[68] T. Bringmann, J. Edsjö, P. Gondolo, P. Ullio, and L. Bergström, "DarkSUSY 6 : An Advanced Tool to Compute Dark Matter Properties Numerically," *JCAP* **07** (2018) 033, arXiv:1802.03399 [hep-ph].

[69] G. Belanger, F. Boudjema, A. Pukhov, and A. Semenov, "MicrOMEGAs: A Program for calculating the relic density in the MSSM," *Comput. Phys. Commun.* **149** (2002) 103–120, arXiv:hep-ph/0112278.

[70] G. Belanger, F. Boudjema, A. Pukhov, and A. Semenov, "micrOMEGAs: Version 1.3," *Comput. Phys. Commun.* **174** (2006) 577–604, arXiv:hep-ph/0405253.

[71] G. Belanger, F. Boudjema, A. Pukhov, and A. Semenov, "MicrOMEGAs 2.0: A Program to calculate the relic density of dark matter in a generic model," *Comput. Phys. Commun.* **176** (2007) 367–382, arXiv:hep-ph/0607059.

[72] G. Belanger, F. Boudjema, A. Pukhov, and A. Semenov, "micrOMEGAs_3: A program for calculating dark matter observables," *Comput. Phys. Commun.* **185** (2014) 960–985, arXiv:1305.0237 [hep-ph].

[73] G. Belanger, F. Boudjema, and A. Pukhov, "micromegas : a code for the calculation of dark matter properties in generic models of particle interaction," 2014. https://arxiv.org/abs/1402.0787.

[74] G. Belanger, F. Boudjema, A. Goudelis, A. Pukhov, and B. Zaldivar, "micrOMEGAs5.0 : Freeze-in," *Comput. Phys. Commun.* **231** (2018) 173–186, arXiv:1801.03509 [hep-ph].

[75] M. Backovic, K. Kong, and M. McCaskey, "MadDM v.1.0: Computation of Dark Matter Relic Abundance Using MadGraph5," *Physics of the Dark Universe* **5-6** (2014) 18–28, arXiv:1308.4955 [hep-ph].

[76] M. Backović, A. Martini, O. Mattelaer, K. Kong, and G. Mohlabeng, "Direct Detection of Dark Matter with MadDM v.2.0," *Phys. Dark Univ.* **9-10** (5, 2015) 37–50, arXiv:1505.04190 [hep-ph].

[77] F. Ambrogi, C. Arina, M. Backovic, J. Heisig, F. Maltoni, L. Mantani, O. Mattelaer, and G. Mohlabeng, "MadDM v.3.0: a Comprehensive Tool for Dark Matter Studies," *Phys. Dark Univ.* **24** (2019) 100249, arXiv:1804.00044 [hep-ph].

[78] M. Palmiotto, A. Arbey, and F. Mahmoudi, "Darkpack: A modular software to compute bsm squared amplitudes for particle physics and dark matter observables," 2023. https://arxiv.org/abs/2211.10376.

[79] A. Belyaev, N. D. Christensen, and A. Pukhov, "Calchep 3.4: for collider physics within and beyond the standard model," *Computer Physics Communications* **184** no. 7, (July, 2013) 1729–1769. http://dx.doi.org/10.1016/j.cpc.2013.01.014.

[80] J. Alwall, M. Herquet, F. Maltoni, O. Mattelaer, and T. Stelzer, "Madgraph 5: going beyond," *Journal of High Energy Physics* **2011** no. 6, (June, 2011) . http://dx.doi.org/10.1007/JHEP06(2011)128.

[81] G. Uhlrich, F. Mahmoudi, and A. Arbey, "– odern tificial heoretical phsicist a c++ framework automating theoretical calculations beyond the standard model," *Computer Physics Communications* **264** (July, 2021) 107928. http://dx.doi.org/10.1016/j.cpc.2021.107928.

[82] C. Arina, "Review on dark matter tools," 2021. https://arxiv.org/abs/2012.09462.

[83] W. R. Inc., "Mathematica, Version 14.1." https://www.wolfram.com/mathematica. Champaign, IL, 2024.

[84] A. Alloul, N. D. Christensen, C. Degrande, C. Duhr, and B. Fuks, "Feynrules 2.0— a complete toolbox for tree-level phenomenology," *Computer Physics Communications* **185** no. 8, (Aug., 2014) 2250–2300. http://dx.doi.org/10.1016/j.cpc.2014.04.012.

[85] R. Coimbra, M. O. P. Sampaio, and R. Santos, "ScannerS: Constraining the phase diagram of a complex scalar singlet at the LHC," *Eur. Phys. J. C* **73** (2013) 2428, arXiv:1301.2599 [hep-ph].

[86] R. Costa, M. Mühlleitner, M. O. P. Sampaio, and R. Santos, "Singlet Extensions of the Standard Model at LHC Run 2: Benchmarks and Comparison with the NMSSM," *JHEP* **06** (2016) 034, arXiv:1512.05355 [hep-ph].

[87] V. Barger, P. Langacker, M. McCaskey, M. Ramsey-Musolf, and G. Shaughnessy, "Complex Singlet Extension of the Standard Model," *Phys. Rev. D* **79** (2009) 015018, arXiv:0811.0393 [hep-ph].

[88] M. Gonderinger, H. Lim, and M. J. Ramsey-Musolf, "Complex Scalar Singlet Dark Matter: Vacuum Stability and Phenomenology," *Phys. Rev. D* **86** (2012) 043511, arXiv:1202.1316 [hep-ph].

[89] M. Mühlleitner, M. O. P. Sampaio, R. Santos, and J. Wittbrodt, "Phenomenological Comparison of Models with Extended Higgs Sectors," *JHEP* **08** (2017) 132, arXiv:1703.07750 [hep-ph].

[90] C.-W. Chiang, M. J. Ramsey-Musolf, and E. Senaha, "Standard Model with a Complex Scalar Singlet: Cosmological Implications and Theoretical Considerations," *Phys. Rev. D* **97** no. 1, (2018) 015005, arXiv:1707.09960 [hep-ph].

[91] F. Egle, M. Mühlleitner, R. Santos, and J. a. Viana, "One-loop corrections to the Higgs boson invisible decay in a complex singlet extension of the SM," *Phys. Rev. D* **106** no. 9, (2022) 095030, arXiv:2202.04035 [hep-ph].

[92] F. Egle, M. Mühlleitner, R. Santos, and J. a. Viana, "Electroweak corrections to Higgs boson decays in a Complex Singlet extension of the SM and their phenomenological impact," *JHEP* **11** (2023) 116, arXiv:2306.04127 [hep-ph].

[93] I. Engeln, P. Ferreira, M. M. Mühlleitner, R. Santos, and J. Wittbrodt, "The Dark Phases of the N2HDM," *JHEP* **08** (2020) 085, arXiv:2004.05382 [hep-ph].

[94] D. Azevedo, P. Gabriel, M. Muhlleitner, K. Sakurai, and R. Santos, "One-loop corrections to the Higgs boson invisible decay in the dark doublet phase of the N2HDM," *JHEP* **10** (2021) 044, arXiv:2104.03184 [hep-ph].

[95] D. Azevedo, P. M. Ferreira, M. M. Muhlleitner, S. Patel, R. Santos, and J. Wittbrodt, "CP in the dark," *JHEP* **11** (2018) 091, arXiv:1807.10322 [hep-ph].

[96] L. Biermann, M. Mühlleitner, and J. Müller, "Electroweak phase transition in a dark sector with cp violation," *The European Physical Journal C* **83** no. 5, (May, 2023) . http://dx.doi.org/10.1140/epjc/s10052-023-11612-w.

[97] K. Ghorbani and H. Ghorbani, "Scalar split WIMPs in future direct detection experiments," *Phys. Rev. D* **93** no. 5, (2016) 055012, arXiv:1501.00206 [hep-ph].

[98] T. Robens, T. Stefaniak, and J. Wittbrodt, "Two-real-scalar-singlet extension of the SM: LHC phenomenology and benchmark scenarios," *Eur. Phys. J. C* **80** no. 2, (2020) 151, arXiv:1908.08554 [hep-ph].

[99] D. Huang, A. P. Morais, and R. Santos, "Anomalies in B-meson decays and the muon $g-2$ from dark loops," *Phys. Rev. D* **102** no. 7, (2020) 075009, arXiv:2007.05082 [hep-ph].

[100] R. Capucha, D. Huang, T. Lopes, and R. Santos, "Impact of electroweak group representation in models for B and g-2 anomalies from dark loops," *Phys. Rev. D* **106** no. 9, (2022) 095032, arXiv:2207.11556 [hep-ph].

[101] T. Hahn, "Feynman diagram calculations with feynarts, formcalc, and looptools," 2010. https://arxiv.org/abs/1006.2231.

[102] V. Shtabovenko, R. Mertig, and F. Orellana, "Feyncalc 10: Do multiloop integrals dream of computer codes?," 2023. https://arxiv.org/abs/2312.14089.

[103] V. Shtabovenko, R. Mertig, and F. Orellana, "Feyncalc 9.3: New features and improvements," *Computer Physics Communications* **256** (Nov., 2020) 107478. http://dx.doi.org/10.1016/j.cpc.2020.107478.

[104] A. Djouadi, J. Kalinowski, and M. Spira, "HDECAY: A Program for Higgs boson decays in the standard model and its supersymmetric extension," *Comput. Phys. Commun.* **108** (1998) 56–74, arXiv:hep-ph/9704448.

[105] A. Djouadi, J. Kalinowski, M. Muehlleitner, and M. Spira, "HDECAY: Twenty$_{++}$ years after," *Comput. Phys. Commun.* **238** (2019) 214–231, arXiv:1801.09506 [hep-ph].

[106] M. Spira, "QCD effects in Higgs physics," *Fortsch. Phys.* **46** (1998) 203–284, arXiv:hep-ph/9705337.

[107] M. Spira, "Higgs Boson Production and Decay at Hadron Colliders," *Prog. Part. Nucl. Phys.* **95** (2017) 98–159, arXiv:1612.07651 [hep-ph].

[108] G. Alguero, G. Bélanger, F. Boudjema, S. Chakraborti, A. Goudelis, S. Kraml, A. Mjallal, and A. Pukhov, "micromegas 6.0: N-component dark matter," *Computer Physics Communications* **299** (June, 2024) 109133. http://dx.doi.org/10.1016/j.cpc.2024.109133.

[109] W. H. Press, S. A. Teukolsky, W. T. Vetterling, and B. P. Flannery, *Numerical Recipes 3rd Edition: The Art of Scientific Computing*. Cambridge University Press, USA, 3 ed., 2007.

[110] P. Gondolo and G. Gelmini, "Cosmic abundances of stable particles: Improved analysis," *Nuclear Physics B* **360** no. 1, (1991) 145–179. https://www.sciencedirect.com/science/article/pii/0550321391904384.

[111] L. Biermann, M. Mühlleitner, and J. Müller, "Electroweak phase transition in a dark sector with CP violation," *Eur. Phys. J. C* **83** no. 5, (2023) 439, arXiv:2204.13425 [hep-ph].

[112] M. Mühlleitner, M. O. P. Sampaio, R. Santos, and J. Wittbrodt, "Scanners: Parameter scans in extended scalar sectors," 2020. https://arxiv.org/abs/2007.02985.

[113] P. Basler, M. Mühlleitner, and J. Müller, "BSMPT v2 a tool for the electroweak phase transition and the baryon asymmetry of the universe in extended Higgs Sectors," *Comput. Phys. Commun.* **269** (2021) 108124, arXiv:2007.01725 [hep-ph].

[114] P. Basler, L. Biermann, M. Mühlleitner, J. Müller, R. Santos, and J. Viana, "Bsmpt v3 a tool for phase transitions and primordial gravitational waves in extended higgs sectors," 2025. https://arxiv.org/abs/2404.19037.

[115] R. Capucha, K. Elyaouti, M. Mühlleitner, J. Plotnikov, and R. Santos, "Freeze-in as a complementary process to freeze-out," 2024. https://arxiv.org/abs/2407.04809.

[116] L. J. Hall, K. Jedamzik, J. March-Russell, and S. M. West, "Freeze-in production of fimp dark matter," *Journal of High Energy Physics* **2010** no. 3, (Mar., 2010) . http://dx.doi.org/10.1007/JHEP03(2010)080.

[117] N. Bernal, K. Deka, and M. Losada, "Thermal dark matter with low-temperature reheating," 2024. https://arxiv.org/abs/2406.17039.

[118] N. Bernal, E. Cervantes, K. Deka, and A. Hryczuk, "Freezing-in cannibals with low-reheating temperature," *JHEP* **09** (2025) 083, arXiv:2506.09155 [hep-ph].

[119] G. Bélanger and J.-C. Park, "Assisted freeze-out," *Journal of Cosmology and Astroparticle Physics* **2012** no. 03, (Mar, 2012) 038. https://doi.org/10.1088/1475-7516/2012/03/038.

[120] G. Alguero, G. Bélanger, S. Kraml, and A. Pukhov, "Co-scattering in micromegas: A case study for the singlet-triplet dark matter model," *SciPost Physics* **13** no. 6, (Dec., 2022) . http://dx.doi.org/10.21468/SciPostPhys.13.6.124.

[121] M. Trodden, "Electroweak baryogenesis," *Reviews of Modern Physics* **71** no. 5, (Oct., 1999) 1463–1500. http://dx.doi.org/10.1103/RevModPhys.71.1463.

[122] W. Bernreuther, "Cp violation and baryogenesis," 2002. https://arxiv.org/abs/hep-ph/0205279.

[123] S. L. Adler, "Axial-vector vertex in spinor electrodynamics," *Phys. Rev.* **177** (Jan, 1969) 2426–2438. https://link.aps.org/doi/10.1103/PhysRev.177.2426.

[124] D. J. Gross and R. Jackiw, "Construction of covariant and gauge invariant t* products," *Nucl. Phys. B* **14** (1969) 269–284.

[125] A. Belavin, A. Polyakov, A. Schwartz, and Y. Tyupkin, "Pseudoparticle solutions of the yang-mills equations," *Physics Letters B* **59** no. 1, (1975) 85–87. https://www.sciencedirect.com/science/article/pii/037026937590163X.

[126] F. R. Klinkhamer and N. S. Manton, "A saddle-point solution in the weinberg-salam theory," *Phys. Rev. D* **30** (Nov, 1984) 2212–2220. https://link.aps.org/doi/10.1103/PhysRevD.30.2212.

[127] V. A. Rubakov and M. E. Shaposhnikov, "Electroweak baryon number non-conservation in the early universe and in high-energy collisions," *Physics-Uspekhi* **39** no. 5, (May, 1996) 461–502. http://dx.doi.org/10.1070/PU1996v039n05ABEH000145.

[128] M. D'Onofrio, K. Rummukainen, and A. Tranberg, "Sphaleron rate in the minimal standard model," *Phys. Rev. Lett.* **113** (Oct, 2014) 141602. https://link.aps.org/doi/10.1103/PhysRevLett.113.141602.

[129] J. H. Christenson, J. W. Cronin, V. L. Fitch, and R. Turlay, "Evidence for the 2π decay of the k_2^0 meson," *Phys. Rev. Lett.* **13** (Jul, 1964) 138–140. https://link.aps.org/doi/10.1103/PhysRevLett.13.138.

[130] B. e. a. Aubert, "Observation of b0 meson system," *Physical Review Letters* **87** no. 9, (Aug., 2001) . http://dx.doi.org/10.1103/PhysRevLett.87.091801.

[131] K. Rummukainen, M. Tsypin, K. Kajantie, M. Laine, and M. Shaposhnikov, "The universality class of the electroweak theory," *Nuclear Physics B* **532** no. 1–2, (Oct., 1998) 283–314. http://dx.doi.org/10.1016/S0550-3213(98)00494-5.

[132] Z. Fodor, "Electroweak phase transitions," *Nuclear Physics B - Proceedings Supplements* **83–84** (Apr., 2000) 121–125. http://dx.doi.org/10.1016/S0920-5632(00)91603-7.

[133] J. van de Vis, J. de Vries, and M. Postma, "Bubble trouble: a review on electroweak baryogenesis," 2025. https://arxiv.org/abs/2508.09989.

[134] T. Prokopec, M. G. Schmidt, and S. Weinstock, "Transport equations for chiral fermions to order h and electroweak baryogenesis: Part i," *Annals of Physics* **314** no. 1, (Nov., 2004) 208–265. http://dx.doi.org/10.1016/j.aop.2004.06.002.

[135] G. Barni, "Electroweak baryogenesis with baryonet: a self-contained review of the wkb approach," 2025. https://arxiv.org/abs/2510.21915.

[136] G. C. Dorsch, T. Konstandin, E. Perboni, and D. A. Pinto, "Non-singular solutions to the boltzmann equation with a fluid ansatz," 2024. https://arxiv.org/abs/2412.09266.

[137] S. D. Curtis, L. D. Rose, A. Guiggiani, Ángel Gil Muyor, and G. Panico, "Non-linearities in cosmological bubble wall dynamics," 2024. https://arxiv.org/abs/2401.13522.

[138] A. Ekstedt, O. Gould, J. Hirvonen, B. Laurent, L. Niemi, P. Schicho, and J. van de Vis, "How fast does the WallGo? A package for computing wall velocities in first-order phase transitions," *JHEP* **04** (2025) 101, arXiv:2411.04970 [hep-ph].

[139] P. Huet and A. E. Nelson, "Electroweak baryogenesis in supersymmetric models," *Physical Review D* **53** no. 8, (Apr., 1996) 4578–4597. http://dx.doi.org/10.1103/PhysRevD.53.4578.

[140] J. de Vries, M. Postma, J. van de Vis, and G. White, "Electroweak baryogenesis and the standard model effective field theory," *Journal of High Energy Physics* **2018** no. 1, (Jan., 2018) . http://dx.doi.org/10.1007/JHEP01(2018)089.

[141] G. D. Moore, "Computing the strong sphaleron rate," *Physics Letters B* **412** no. 3–4, (Oct., 1997) 359–370. http://dx.doi.org/10.1016/S0370-2693(97)01046-0.

[142] G. D. Moore and M. Tassler, "The sphaleron rate in su(n) gauge theory," *Journal of High Energy Physics* **2011** no. 2, (Feb., 2011) . http://dx.doi.org/10.1007/JHEP02(2011)105.

[143] J. M. Cline and B. Laurent, "Electroweak baryogenesis from light fermion sources: A critical study," *Physical Review D* **104** no. 8, (Oct., 2021) . http://dx.doi.org/10.1103/PhysRevD.104.083507.

[144] H. A. Weldon, "Effective fermion masses of order gT in high-temperature gauge theories with exact chiral invariance," *Phys. Rev. D* **26** (Nov, 1982) 2789–2796. https://link.aps.org/doi/10.1103/PhysRevD.26.2789.

[145] A. Peshier, K. Schertler, and M. H. Thoma, "One-loop self energies at finite temperature," *Annals of Physics* **266** no. 1, (June, 1998) 162–177. http://dx.doi.org/10.1006/aphy.1997.5781.

[146] T. Hahn, "Cuba—a library for multidimensional numerical integration," *Computer Physics Communications* **168** no. 2, (June, 2005) 78–95. http://dx.doi.org/10.1016/j.cpc.2005.01.010.

[147] I. F. Ginzburg, M. Krawczyk, and P. Osland, "Two Higgs doublet models with CP violation," in *International Workshop on Linear Colliders (LCWS 2002)*, pp. 703–706. 11, 2002. arXiv:hep-ph/0211371.

[148] J. F. Gunion and H. E. Haber, "The CP conserving two Higgs doublet model: The Approach to the decoupling limit," *Phys. Rev. D* **67** (2003) 075019, arXiv:hep-ph/0207010.

[149] A. Barroso, P. M. Ferreira, R. Santos, and J. P. Silva, "Probing the scalar-pseudoscalar mixing in the 125 GeV Higgs particle with current data," *Phys. Rev. D* **86** (2012) 015022, arXiv:1205.4247 [hep-ph].

[150] I. F. Ginzburg and M. Krawczyk, "Symmetries of two Higgs doublet model and CP violation," *Phys. Rev. D* **72** (2005) 115013, arXiv:hep-ph/0408011.

[151] A. W. El Kaffas, W. Khater, O. M. Ogreid, and P. Osland, "Consistency of the two Higgs doublet model and CP violation in top production at the LHC," *Nucl. Phys. B* **775** (2007) 45–77, arXiv:hep-ph/0605142.

[152] A. Arhrib, E. Christova, H. Eberl, and E. Ginina, "CP violation in charged Higgs production and decays in the Complex Two Higgs Doublet Model," *JHEP* **04** (2011) 089, arXiv:1011.6560 [hep-ph].

[153] S. Inoue, M. J. Ramsey-Musolf, and Y. Zhang, "CP-violating phenomenology of flavor conserving two Higgs doublet models," *Phys. Rev. D* **89** no. 11, (2014) 115023, arXiv:1403.4257 [hep-ph].

[154] D. Fontes, J. C. Romão, and J. P. Silva, "$h \to Z\gamma$ in the complex two Higgs doublet model," *JHEP* **12** (2014) 043, arXiv:1408.2534 [hep-ph].

[155] B. Grzadkowski, O. M. Ogreid, and P. Osland, "Measuring CP violation in Two-Higgs-Doublet models in light of the LHC Higgs data," *JHEP* **11** (2014) 084, arXiv:1409.7265 [hep-ph].

[156] D. Fontes, M. Mühlleitner, J. C. Romão, R. Santos, J. P. Silva, and J. Wittbrodt, "The C2HDM revisited," *JHEP* **02** (2018) 073, arXiv:1711.09419 [hep-ph].

[157] S. L. Glashow and S. Weinberg, "Natural Conservation Laws for Neutral Currents," *Phys. Rev. D* **15** (1977) 1958.

[158] E. A. Paschos, "Diagonal Neutral Currents," *Phys. Rev. D* **15** (1977) 1966.

[159] L. Fromme, S. J. Huber, and M. Seniuch, "Baryogenesis in the two-higgs doublet model," *Journal of High Energy Physics* **2006** no. 11, (Nov., 2006) 038–038. http://dx.doi.org/10.1088/1126-6708/2006/11/038.

[160] T. Gent, S. Huber, K. Mimasu, and J. M. No, "Towards precise baryogenesis in the 2HDM+a," arXiv:2512.22081 [hep-ph].

[161] B. H. Liu, L. McLerran, and N. Turok, "Bubble nucleation and growth at a baryon-number-producing electroweak phase transition," *Phys. Rev. D* **46** (Sep, 1992) 2668–2688. https://link.aps.org/doi/10.1103/PhysRevD.46.2668.

[162] P. Basler and M. Mühlleitner, "Bsmpt (beyond the standard model phase transitions): A tool for the electroweak phase transition in extended higgs sectors," *Computer Physics Communications* **237** (Apr., 2019) 62–85. http://dx.doi.org/10.1016/j.cpc.2018.11.006.